

Intra-Cortical Microelectrode Arrays for Neuro-Interfacing

by

Salam Ramy Gabran

A thesis
presented to the University of Waterloo
in fulfillment of the
thesis requirement for the degree of
Doctor of Philosophy
in
Electrical and Computer Engineering

Waterloo, Ontario, Canada, 2012

©Salam Ramy Gabran 2012

Author's Declaration

I hereby declare that I am the sole author of this thesis. This is a true copy of the thesis, including any required final revisions, as accepted by my examiners.

I understand that my thesis may be made electronically available to the public.

Abstract

Neuro-engineering is an emerging multi-disciplinary domain which investigates the electrophysiological activities of the nervous system. It provides procedures and techniques to explore, analyze and characterize the functions of the different components comprising the nervous system. Neuro-engineering is not limited to research applications; it is employed in developing unconventional therapeutic techniques for treating different neurological disorders and restoring lost sensory or motor functions. Microelectrodes are principal elements in functional electric stimulation (FES) systems used in electrophysiological procedures. They are used in establishing an interface with the individual neurons or in clusters to record activities and communications, as well as modulate neuron behaviour through stimulation. Microelectrode technologies progressed through several modifications and innovations to improve their functionality and usability. However, conventional electrode technologies are open to further development, and advancement in microelectrodes technology will progressively meliorate the neuro-interfacing and electrotherapeutic techniques.

This research introduced design methodology and fabrication processes for intra-cortical microelectrodes capable of befitting a wide range of design requirements and applications. The design process was employed in developing and implementing an ensemble of intra-cortical microelectrodes customized for different neuro-interfacing applications. The proposed designs presented several innovations and novelties. The research addressed practical considerations including assembly and interconnection to external circuitry.

The research was concluded by exhibiting the Waterloo Array which is a high channel count flexible 3-D neuro-interfacing array. Finally, the dissertation was concluded by demonstrating the characterization, in vitro and acute in vivo testing results of the Waterloo Array. The implemented electrodes were tested and benchmarked against commercial equivalents and the results manifested improvement in the electrode performance compared to conventional electrodes. Electrode testing and evaluation were conducted in the Krembil Neuroscience Centre Research Lab (Toronto Western Hospital), and the Neurosciences & Mental Health Research Institute (the Sick Kids hospital).

The research results and outcomes are currently being employed in developing chronic intra-cortical and electrocorticography (ECoG) electrode arrays for the epilepsy research and rodents nervous system investigations. The introduced electrode technologies will be used to develop customized designs for the clinical research labs collaborating with CIRFE Lab.

Acknowledgements

I would like to express my gratitude and appreciation to my supervisors Prof. Raafat Mansour and Prof. Magdy Salama for their support, guidance, patience and providing a productive atmosphere for doing research.

I would also like to thank my committee members and research associates for the valuable information, knowledge and support:

Prof. Roman Genov, Tariq AlSalam, Hossein Kassiri: Intelligent Sensory Microsystems Lab, University of Toronto

Prof. Peter Carlen, Josh Dian, Youssef El-Hayek, Carlos Florez: Krembil Neuroscience Centre, Toronto Western Hospital, University of Toronto

Prof. Jose Luis Perez-Velazquez, Yana Adamchik: Neurosciences & Mental Health Research Institute, Sick Kids Hospital

Prof. Mary Nagai: Rehabilitation Engineering Lab, University of Toronto

Prof. Mandar Jog: Movements Disorder Clinic, University of Western Ontario

Special thanks to:

The Natural Sciences and Engineering Research Council of Canada (NSERC)

Canada Foundation for Innovation (CFI)

The Centre for Integrated RF Engineering (CIRFE) Lab, University of Waterloo

Canadian Microelectronics Corporation (CMC)

Quantum and Nano Centre (QNC), Waterloo Institute for Nanotechnology (WIN), University of Waterloo

Nanofabrication Laboratory, University of Western Ontario

Giga-to-Nano electronics Centre (G2N Lab), University of Waterloo

Finally, I would love to thank my Heavenly Father, family, friends and CIRFE Lab colleagues who shared with me the ups and downs of this long journey:

Ramy, Nedal and Wesam Gabran, George and Christen Shaker, Michael Gad, Mina Farid, John and Sally Saad, Tony Salib, Wafik Moussa, Michael Mounir, Albert and Marian Wasef, Mina AbdelMalek, Michael and Sally Ayoub, Ahmed Bayoumy, Karim El-Rayes, Ahmed Abdel-Aziz, Hany Lewis, Ayad and Evon Barsoum, Michael Ibrahim, Mikhail Shenouda, Sara Attar, Siamak Fouladi, Oliver Wong, Scott Shen, Bill Joley, Sepehr Forouzanfar, Saeed Fatholouloumi.

Dedication

To my father, mother and brother.

We did it again, without your unconditional love, support, sacrifice and prayers I wouldn't have gone so far, and yet more to come.

Table of Contents

Author's Declaration	ii
Abstract.....	iii
Acknowledgements.....	iv
Dedication.....	v
Table of Contents.....	vi
List of Figures.....	x
List of Tables	xvi
Chapter 1 Introduction.....	1
1.1 Defining Neuro-Engineering	1
1.2 Motivation.....	3
1.3 Research Objective	3
1.4 Thesis Outline.....	4
Chapter 2 Literature Survey.....	5
2.1 Introduction to Cortical Recording	5
2.2 Applications of Electrotherapeutic Techniques	5
2.3 The Evolution of Intra-Cortical Electrode Design.....	7
2.3.1 Electrode categories	7
2.3.2 Micropipettes	7
2.3.3 The quest for multisite recording.....	8
2.3.4 Micro-wire bundle electrodes	8
2.3.5 Thin-film electrodes technology	11
2.3.6 Single shaft multi-channel electrodes	11
2.3.7 Needle arrays	14
2.3.8 Multi-shaft electrodes	16
2.3.9 Flexible substrate electrodes	18
2.4 Practical Considerations.....	20
2.4.1 Tissue displacement.....	20
2.4.2 Pad size and separation	21
2.4.3 Shaft width.....	21

2.4.4 Mechanical strength	22
2.4.5 Neuro-compatibility and foreign body response	22
2.4.6 Electrode material.....	22
2.4.1 Electrode failure	24
2.4.2 Reliable chronic recording	25
2.5 Summary of the Survey	27
Chapter 3 Microelectrode Design Methodology	28
3.1 Introduction	28
3.2 Design Methodology	28
3.3 Design Guidelines	29
3.4 Single Shaft Electrodes	30
3.5 Pad Geometry	31
3.6 Modified Pad Layout.....	31
3.7 Double Metallization Layer Stimulation Electrodes	33
3.8 Modified Vias.....	36
3.9 Short Shaft Electrodes	38
3.10 Electrical Analysis and Design Optimization.....	38
3.11 Recording/Stimulation Electrodes.....	41
3.12 Multi-Composite Layer Recording Electrodes.....	42
3.13 Carrier Wafers and Interconnect Cables.....	46
3.14 Electrode with Integrated Cables for 3-D Assembly: The Waterloo Array	49
3.15 Implantation Assistive Devices	50
3.16 Conclusion.....	51
Chapter 4 Electromagnetic Analysis of Intra-Cortical Microelectrodes	52
4.1 Introduction	52
4.2 Modeling Medtronic 3387 DBS Electrode.....	52
4.3 Brain Tissue Modeling	53
4.4 Simulation Setup and Stimulation Pulses.....	55
4.5 Simulation Results.....	57
4.5.1 Stimulation pulse parameters	57
4.5.2 Tissue dielectric properties.....	60

4.6 Modeling Miniature Electrodes	63
4.7 Metal Planes.....	69
4.8 Conclusion	71
Chapter 5 Structural Analysis of Intra-Cortical Microelectrodes	72
5.1 Introduction.....	72
5.2 Forces Acting on the Electrode.....	72
5.3 Electrode Mechanical Failure Modes	72
5.4 Buckling Analysis.....	74
5.4.1 Buckling analysis simulation model	74
5.4.2 Analyses results	74
5.5 Electrode Fracture.....	80
5.5.1 Axial and shear loading	80
5.5.2 Simulation results.....	81
5.5.3 Array shear loading.....	91
5.6 Mechanical Modeling of Brain Tissue.....	95
5.7 Strain Relief Cross-sections.....	98
5.8 Conclusion	100
Chapter 6 Electrode Fabrication	102
6.1 Introduction.....	102
6.2 Electrode Materials	102
6.3 Simple Single Shaft Recording Electrodes	102
6.4 Recording and Stimulation Electrodes.....	104
6.5 Double Metallization Layer Stimulation Electrode	106
6.5.1 Silicon electrodes.....	106
6.5.2 Stainless steel.....	111
6.5.3 Electrode DC resistance measurement.....	112
6.6 Polyimide Electrodes with Integrated Cables (Flex Electrodes).....	113
6.7 Multi-composite layer Recording Electrodes	114
6.7.1 Fabrication procedure	115
6.8 Carrier Wafers and Interconnect Cables	116
6.9 The Waterloo Array: 3-D Electrodes Arrays	118

6.10 Pad post processing	120
6.11 Conclusion.....	121
Chapter 7 Electrode Characterization and Testing.....	123
7.1 Introduction	123
7.2 Electrode Electrical Characterization	123
7.3 In Vitro Testing of the Flex Electrode.....	124
7.4 Acute In Vivo Testing of the Flex electrode	127
7.5 Conclusion.....	130
Chapter 8 Thesis Conclusion.....	131
8.1 Research Summary	131
8.2 Future Work	131
Appendix A Acronyms.....	132
Appendix B Foreign Body Response	134
Appendix C Brain Tissue Dielectric Properties and Dispersion Modes.....	135
Appendix D Material Properties.....	139
Appendix E Brain Tissue Mechanical Modeling	140
Bibliography	142

List of Figures

Figure 2-1. Applications of electrotherapeutic techniques	9
Figure 2-2. Classification of microelectrodes	10
Figure 2-3. Micro-wire bundle electrodes, Left: Niotrode, Right: Niotrode array [63]	11
Figure 2-4. 4 channel silicon microprobe [25].....	12
Figure 2-5. Left: Molybdenum thin film electrode [77], Right: Molybdenum thin film electrode with 2x12 sites [70].....	12
Figure 2-6. Ceramic thin film electrode [16].....	13
Figure 2-7. Tapered electrode tip using non-continuous seed layer, Left: Seed layer sketch, Right: Fabricated electrode tip [181]	13
Figure 2-8. Judy’s lab electrode fabrication steps [181].....	14
Figure 2-9. Needle array electrode [21].....	15
Figure 2-10. Left: Active electrode array, Right: CMOS cell schematic [53]	15
Figure 2-11. Left: 10x10 EDM array electrode, Right: titanium electrode with 1141 pins [11]	16
Figure 2-12. Left: Utah array, Right: Sloped Utah array [74]	17
Figure 2-13. Left: MEA electrode array [178], Right: Close up view of a single needle	17
Figure 2-14. Multi-shaft silicon recording electrodes [47]	17
Figure 2-15. Active multi-shank silicon electrodes [73].....	18
Figure 2-16. Left: Microscale Implantable Neural Interface (MINI), Right: Single probe [23].....	19
Figure 2-17. Caltech dual sided electrode [179].....	19
Figure 2-18. Flexible parylene electrode [64].....	20
Figure 2-19. Flexible electrode with integrated microfluidic channel [78]	20
Figure 2-20. Modes of electrode failure	26
Figure 3-1. Electrode design process flow.....	29
Figure 3-2. Basic simple recording electrode with 4 pads (Layout A)	30
Figure 3-3. Basic simple recording electrode layout with 7 pads (Layout B)	30
Figure 3-4. Exploded assembly of simple recording electrodes, Left: Layout A, Right: Layout B.....	31
Figure 3-5. Current density distribution for different stimulation pad models	32
Figure 3-6. Voltage distribution	32
Figure 3-7. Modified trapezium recording pads on tapered shaft	33
Figure 3-8. Electrode array with tapered alternating shafts	33
Figure 3-9. Comparison between conventional stimulation electrode layout (top) and the proposed architecture with double metallization layers (bottom).....	34

Figure 3-10. Electrode top view	34
Figure 3-11. Top view showing the superimposed metallization layers, first metallization layer is shown in black and the exposed pads are in yellow	35
Figure 3-12. Exploded assembly view of the double metallization layer stimulation electrode.....	35
Figure 3-13. Sectional view of the stimulation electrode with (Left) and without (Right) insulation and passivation layers. The figure reveals the tracks in metal-2 layer (yellow), buried via (green), and part of the stimulation pad (yellow). The red contour (Right) represents the stimulation pad footprint.	36
Figure 3-14. Double metallization layer stimulation electrode – Modified vias – Tapered shaft.....	37
Figure 3-15. Double metallization layer stimulation electrode – Modified vias – Step shaft.....	37
Figure 3-16. Double metallization layer stimulation electrode – Modified design – 4 shafts electrode array.....	37
Figure 3-17. FEM model for the electrode metal structure	38
Figure 3-18. Sensitivity analysis: Current vs. track width and thickness for 1mm track.....	40
Figure 3-19. Sensitivity analysis: Current vs. track width and thickness for 3.5mm track.....	40
Figure 3-20. Post processing results, Left: Current sensitivity analysis of parametric model, Right: Correlation matrix of current vs. design parameters	41
Figure 3-21. Joule heating post processing results, Left: Joule heating sensitivity analysis of parametric model, Right: Correlation matrix of Joule heating vs. design parameters	41
Figure 3-22. Preliminary layout of stimulation/recording electrode, Left: Electrode layout, Right: Pads and tracks.....	43
Figure 3-23. Stimulation/recording electrode with improved pad packing	43
Figure 3-24. Cross sectional layout of a composite layer	44
Figure 3-25. Three stacked composite layers	44
Figure 3-26. Multi-composite layer electrode layout	45
Figure 3-27. Multi-composite layer electrode, Layout A: 7 pads per layer	45
Figure 3-28. Multi-composite layer electrode, Layout B: 4 pads per layer	45
Figure 3-29. Pad layout for recording and stimulation.....	45
Figure 3-30. Multi-composite layer electrode with optimized mechanical design	46
Figure 3-31. Multi-composite layer electrode with optimized mechanical design: Metallization layers	46
Figure 3-32. Carrier wafer for the two shaft double metallization layer stimulation electrode, Top: Carrier wafer with pads, tracks and alignment groove, Bottom: Carrier wafer and electrode assembly.....	47
Figure 3-33. Carrier wafer for quad shaft electrode customized for Omnetics A79050 socket.....	48
Figure 3-34. 3-D electrode assembly using carrier wafers	48
Figure 3-35. Electrode-cable assembly.....	49
Figure 3-36. 3-D flexible electrodes stacked using silicon carrier wafers.....	50

Figure 3-37. Flexible electrode shaft layout, Green: Buried vias, Blue: Routing tracks, Red: Exposed tracks, Brown: Electrode contour	50
Figure 3-38. Implantation assistive device	51
Figure 4-1. Medtronic 3387 DBS electrode layout.....	53
Figure 4-2. Medtronic 3387 DBS electrode simulation model.....	53
Figure 4-3. Stimulation patterns, Left: Normalized Gaussian pulse, Right: Normalized anodic monophasic rectangular pulse (t, 0, 1e-11)	55
Figure 4-4. Simulation results for Gaussian and monophasic pulses with very fine-4 meshing.....	56
Figure 4-5. Electric field distribution of Gaussian pulse stimulation @ $\sigma = 0.3\text{S.m}^{-1}$	56
Figure 4-6. Electric field intensity vs. simulation pulse amplitude (A) for $\epsilon_r = 1 \times 10^4$ and 1×10^5 @ $\sigma = 0.15\text{S.m}^{-1}$	58
Figure 4-7. Electric field intensity vs. simulation pulse width @ $\epsilon_r = 1 \times 10^5$ and $\sigma = 0.15\text{S.m}^{-1}$	59
Figure 4-8. Current steering and field shaping for 2 rings firing	59
Figure 4-9. Maximum electric field vs. current steering ratio for different permittivity @ $\epsilon_r = 1 \times 10^4$ and $\epsilon_r = 1 \times 10^5$ at $\sigma = 0.15\text{S.m}^{-1}$	60
Figure 4-10. Maximum electric field intensity (V/m) vs. conductivity for different relative permittivities	61
Figure 4-11. Electric field intensity vs. permittivity @ $\sigma = 0.1\text{S.m}^{-1}$	62
Figure 4-12. Maximum electric field intensity vs. capsule thickness (T_{Capsule}) for tissue permittivity of $\epsilon_r = 5 \times 10^4$ and $\sigma_{\text{Gray Tissue}} = 0.15\text{S.m}^{-1}$, $\sigma_{\text{Capsule}} = 0.1\text{S.m}^{-1}$	63
Figure 4-13. Maximum electric field intensity vs. gray matter thickness (T_{Capsule}) for tissue permittivity of $\epsilon_{\text{Gray Tissue}} = 1 \times 10^5$ and $\sigma_{\text{Gray Tissue}} = 0.1\text{S.m}^{-1}$, $\epsilon_{\text{White Tissue}} = 2 \times 10^4$, $\sigma_{\text{White Tissue}} = 0.1\text{S.m}^{-1}$	64
Figure 4-14. Medtronic 3387 DBS electrode planar model.....	65
Figure 4-15. Electric field distribution of the planar model for Medtronic 3387 DBS electrode	65
Figure 4-16. Electric field distribution of Medtronic 3387 DBS electrode	66
Figure 4-17. Normal plane field values for intra-cortical microelectrode	67
Figure 4-18. Electric field distribution for different electrode widths, Left: $50\mu\text{m}$, Right: $1600\mu\text{m}$. The blue line represents the electrode width	67
Figure 4-19. Effect of electrode width on field distribution	68
Figure 4-20. Effect of vertical pad gap on the electric field intensity.....	68
Figure 4-21. Electric field distribution for different pads layouts	69
Figure 4-22. Electric field distributions: Left: single side stimulation without an intermediate metal plane, Middle: with intermediate metal plane, Right: with two intermediate metal planes	70
Figure 4-23. Microelectrode model with variable width metal strips	70
Figure 5-1. Forces acting on the electrode [146]	73

Figure 5-2. Fixed-free Eigen buckling model.....	75
Figure 5-3. Histogram of critical loads for different electrode layouts: Fixed-free Eigen buckling analysis – Silicon	78
Figure 5-4. Failure analysis models, Left: Axial loading, Right: Shear loading.....	82
Figure 5-5. Array shear loading model, Left: Base edge loading, Right: Base sides loading.....	92
Figure 5-6. Electrode-skin penetration model	97
Figure 5-7. Simulation results for silicon shaft, Left: Deformation, Right: Safety factor distribution	97
Figure 5-8. Modified cross-sections for strain relief	98
Figure 5-9. Flex cable simulation model	99
Figure 5-10. Total deformation of different modified cross-sections	99
Figure 5-11. Comparing deformation ratios of different cross-section modifications.....	100
Figure 6-1. Single shaft polyimide recording electrode with 12 channels: $\tau = 12\mu\text{m}$, $w = 550\mu\text{m}$	103
Figure 6-2. Single shaft polyimide recording electrode with 40 channels: $\tau = 12\mu\text{m}$, $w = 830\mu\text{m}$	103
Figure 6-3. Simple single shaft silicon electrodes	104
Figure 6-4. Single narrow shaft electrode with 4 channels (Layout A), Top: Before release, Left: Electrode tip, Right: SEM picture for the electrode tip	105
Figure 6-5. Single narrow shaft electrode with 7 channels (Layout B), Top: Before release, Left: Electrode base, Right: SEM picture for the electrode tip	105
Figure 6-6. Single shaft silicon recording/stimulation electrode with 24 recording and 6 stimulation channels, $w = 1.1\text{mm}$	106
Figure 6-7. Optimized pad layout for stimulation/recording electrodes with 9 recording and 8 stimulation channels, $w = 380\mu\text{m}$, Top: Released electrode, Bottom: Electrode tip	106
Figure 6-8. Metal-1 patterning, Left and Middle: Photoresist mask (tracks), Right: Metal-1 after etching (interconnect pads).....	107
Figure 6-9. Patterned vias, Left: dry etching using RIE, Right: wet BHF etching	108
Figure 6-10. Photoresist mask for modified Metal-1 track tips	108
Figure 6-11. Modified via patterned using RIE in dielectric-2.....	108
Figure 6-12. Modified vias and patterned pads, Left: Before electrode release, Right: After electrode release	108
Figure 6-13. Patterned metal layers demonstrating stimulation pads and routing tracks	109
Figure 6-14. Double metallization layer stimulation electrode: SEM pictures for the electrode shaft demonstrating stimulation pads, vias and routing tracks	109
Figure 6-15. Double metallization layer stimulation electrode: SEM pictures.....	110
Figure 6-16. Double metallization layer stimulation electrode: Quad shafts (aluminum pads), $\ell_{\text{shaft}} = 3\text{mm}$, $w = 130\mu\text{m}$, pads = $110 \times 110\mu\text{m}$	110

Figure 6-17. Double metallization layer stimulation electrode: Single and quad shafts (gold pads).....	110
Figure 6-18. Double metallization layer stimulation electrode: Double shaft electrode for small rodents (gold pads), $\ell_{\text{shaft}} = 1\text{mm}$	111
Figure 6-19. Double metallization layer stimulation electrode: Ensemble of different layouts	111
Figure 6-20. I-V characteristic measurements for p-doped silicon wafer without passivation.....	113
Figure 6-21. Laser diced Flex quad shaft stimulation electrode	114
Figure 6-22. Close up views of the electrode shaft, the bottom figure is a dark field image for the shaft showing the pads, tracks and modified vias	114
Figure 6-23. Multi-composite layer recording electrode, Left: Interconnect pads, Right: Recording pads.....	115
Figure 6-24. Exposed recording pads with etched windows in the oxide layers	115
Figure 6-25. SEM pictures for the multi-composite layer electrode, Left: Electrode tip with the bottom most composite layer, Right: Electrode shaft with tracks belonging to the bottom most composite layer and pads of the intermediate layer	116
Figure 6-26. Left: Quad shaft electrode carrier with through holes and alignment groove, the electrode surface is passivated with oxide layer, Right: Exposed pads with through holes drilling cross-hair markers	117
Figure 6-27. SEM pictures of dual shaft electrode carrier wafer, Left: Released carrier wafer with patterned metallization layer and etched alignment groove, Right: Electrode-wafer assembly before gold wire bonding	117
Figure 6-28. Flexible interconnect cables, Top: Single shaft electrode, Bottom left: Quad shaft electrode, Bottom right: Double shaft electrode carrier wafer.....	119
Figure 6-29. Single (Top) and Quad (Bottom) shaft electrode-cable assemblies	119
Figure 6-30. Left: 2.4 and 5mm 3-D stacking carrier wafers, Right: SEM picture of the 2.4mm 3-D stacker...	119
Figure 6-31. The Waterloo Array: 3-D Flex electrode assembly with 12 shafts and 72 stimulation pads	120
Figure 6-32. SEM pictures of the pads on different electrodes showing the surface roughness. RSE: Rough surface electrode (modified Flex electrode), SSE: Smooth surface electrode (original Flex electrode), CME: Commercial microelectrode (Neuro Nexus), CMW: Commercial microwire electrode	121
Figure 7-1. Left: AC impedance characterization setup showing the two-electrode standard electrochemical cell, electrolyte and cables. Right: Circuit schematic	124
Figure 7-2. FRA of electrode-electrolyte interface: Pad impedance magnitude	124
Figure 7-3. Flex electrodes mounted on in vitro PCB's with 12 and 24 channel connections	125
Figure 7-4. Electrode connection and mounting assembly	125
Figure 7-5. In vitro testing setup, Krembil Neuroscience Centre Research Lab, Toronto Western Hospital (TWH).....	126
Figure 7-6. Stimulation pulse and the resultant evoked potential	126

Figure 7-7. Dual shaft Flex electrode in vivo testing assembly	128
Figure 7-8. Measured noises: (a) instrumentation noise and microelectrodes system noise densities and (b) microelectrodes noise densities of the presented and commercial electrodes [209]	129
Figure 7-9. Measured mean signal-to-noise ratio for the presented and commercial electrodes [209]	129
Figure 7-10. Measured neural signal and microelectrodes noise spectral densities of the presented and commercial electrodes [209].....	130
Figure D-1. Dielectric parameters of human brain grey matter based on Gabriel model (solid and dashed lines) and pre-1996 literature (triangles and circles) [154]	136
Figure D-2. Conductivity of white and grey matter (10Hz – 100MHz)	137
Figure D-3. Loss tangent of white and grey matter (10Hz – 100MHz).....	137
Figure D-4. Relative permittivity of white and grey matter (10Hz – 100MHz).....	138
Figure L-1. Curve fitting of the experimental stress-strain of brain tissue	141

List of Tables

Table 1-1. Current and upcoming neuro-modulation and neural augmentation practices	2
Table 2-1. Different materials and their suitability for electrode fabrication	23
Table 3-1. Comparison between electrode dimensions	33
Table 3-2. Parametric model variables	39
Table 3-3. Connector cables for electrodes and carrier wafers	48
Table 4-1. Mean values for brain tissue conductivity	54
Table 4-2. Maximum electric field intensity [V/m] for different tissue dielectric properties	61
Table 5-1. Young moduli of different human tissue [146]	73
Table 5-2. Proposed electrode layouts	76
Table 5-3. Critical loads [mN] for different layouts: Fixed-free Eigen buckling analysis.....	78
Table 5-4. Eigen buckling analysis: Deformation of different layouts – Silicon.....	79
Table 5-5. Safety factor distribution for axial loading – Silicon.....	83
Table 5-6. Safety factor distribution for axial loading – Stainless steel	84
Table 5-7. Safety factor distribution for axial loading – Polyimide	86
Table 5-8. Safety factor distribution for shear loading – Silicon.....	87
Table 5-9. Safety factor distribution for shear loading – Stainless steel.....	89
Table 5-10. Safety factor distribution for shear loading – Polyimide.....	90
Table 5-11. Minimum thickness recommended for different electrode designs and materials (safety factor = 10)	91
Table 5-12. Safety factor distribution for shear loading of electrode array – Silicon.....	92
Table 5-13. Safety factor distribution for shear loading of electrode array – Stainless steel.....	94
Table 5-14. Safety factor distribution for shear loading of electrode array – Polyimide.....	95
Table 5-15. Three parameters Mooney-Rivlin hyper elastic model	97
Table 7-1. FRA of electrode-electrolyte interface impedance: minimum recorded values	126
Table L-1. Fresh brain tissue curve fitted stress-strain curve	140

Chapter 1

Introduction

1.1 Defining Neuro-Engineering

Neuro-engineering is a multi-disciplinary research area which utilizes engineering techniques in neuro-physiology and neuro-sciences. It investigates the functions of the central and peripheral nervous systems, and provides techniques to manipulate their behaviour through intra-cortical recording and stimulation. Neuro-engineering involves two main research venues; the first studies neurological functions using computational and experimental methods to quantify and model coding and information processing in sensory and motor systems. The second stream employs functional electrical stimulation (FES) in developing therapeutic techniques to treat neurological disorders and restore impaired functions through neural augmentation and neuro-modulation [1][2][3][4][5]. FES provides treatment for psychological and encephalon disorders as well as therapeutic technologies to restore motor functions and regulate organ functionality.

Neuro-modulation is a medical intervention technique developed to stimulate peripheral nerves, the spinal cord, or the brain in order to regulate the activity of neuron clusters. It can be performed surgically by lesioning specific regions in the nervous system, pharmacologically by drug infusion into cerebrospinal fluid or electrically through delivering an electric charge to the targeted neurons. Electrical stimulation of the central, peripheral and autonomic nervous systems is currently a standard clinical practice for investigating and treating several diseases and disorders.

Unlike conventional neural ablation and lesioning; electric stimulation is reversible and non-destructive. The first forms of electric neuro-modulators were galvanic [6][7] and chronic cardiac pacemakers [8]. Furthermore, intermittent deep brain stimulation (DBS) of the subthalamic nucleus (STN) exhibited improvements in patients with Parkinson's disease and torsion dystonia [9][10]. Stimulation targets include Vagus nerve, deep brain, cortical and intra-cortical structures. In general, the cerebral cortex provides easy access to motor intent and sensory perception, and is readily regarded as an interface for restoring neurological functions lost due to degenerative muscular diseases, stroke, or spinal cord injury [11][12][13]. FES also has the potential to develop treatments for the restoration of sensory functions including tactile, visual, and vestibular senses, as well as treating psychological disorders including depression and Obsessive-Compulsive Disorder (OCD). Table 1-1 lists the current and upcoming neuro-modulation and neural augmentation procedures.

Neuro-interfacing electrodes possess eminent role in the progress of neuro-engineering and FES-based therapeutic techniques. Advancements in electrode design will meliorate the delivered therapy by improving the electrode functionality and biocompatibility. This motivated the development of cranial and sub-cranial electrodes during the past three decades for neural recording starting with simple glass micropipettes, followed by metallic needles, wire electrodes and finally, micromachined microelectrodes [14][15][16][17]. Present electrode technologies and electrotherapeutic procedures are yet far from being mature, and created a milieu for multitude of

research activities accommodating diverse fields including engineering design, microfabrication, computational neurology, material science and neurophysiology.

This research tackled the electrode design problem from engineering perspective. The research explored different parameters attributing to electrode performance. Several designs were proposed in pursuit of reliable long-term recording and stimulation electrodes. Wide range of materials was experimented in fabricating different electrode components. Surface modifications were applied to improve the electrode electrical properties, and various electrode geometries were explored to minimize tissue trauma and displacement.

Table 1-1. Current and upcoming neuro-modulation and neural augmentation practices

Status	Neuro-modulation	Neural Augmentation
FDA Approved	Pain (SCS ¹) Epilepsy (VNS ²) Parkinson's disease (DBS ³) Essential Tremor (DBS) Dystonia ⁴ (DBS) Depression (VNS)	Quadraparesis (Ambulation) Quadraparesis (C5-6 function) Blindness Bladder dysfunction
Investigational	Neuropathic pain (DBS, CS ⁵) Epilepsy (DBS) Occipital neuralgia (PNS ⁶) Migraine headache (PNS) Cluster headache (DBS) Obsessive-compulsive disorder ⁷ (DBS) Obesity, Depression (DBS, CS) Tourette's Disease (DBS) Hypertension Stroke rehabilitation (CS) Minimally-conscious state (DBS) Addiction (DBS) Aphasia (CS) Tinnitus (CS, PNS) Parkinson's disease, tremor (CS)	Deafness Foot drop

¹ SCS: spinal cord stimulation

² VNS: vagus nerve stimulation

³ DBS: deep brain stimulation

⁴ Humanitarian Device Exemption (HDE) status

⁵ CS: cortical stimulation

⁶ PNS: peripheral nerve stimulation

⁷ HDE status pending

1.2 Motivation

This research progressed through collaboration with several engineering and medical research groups: Intelligent Sensory Microsystems Laboratory (UoT), Krembil Neuroscience Centre Research, Toronto Western Hospital (UoT), Sick Kids Hospital and Rehabilitation Engineering Laboratory (UoT). Working with medical research groups revealed the inevitable need to develop new generation of electrode arrays that would offer enhanced functionality in terms of adding more capabilities, and improved biocompatibility to create electrodes suitable for in vivo and chronic applications. The developed electrodes should provide access to neurons with minimal tissue damage, high positional accuracy and allow high dense multisite recording and stimulation of cortical columns [17][24][25]. The delivered electrodes have to be suitable for chronic implantation and capable of satisfying the stringent constraints to maintain proper functionality and biocompatibility [26][27][28][29][30][31].

Cortical recording allowed studying the electrophysiological functions of the nervous system, it is also utilized in neuro-prosthetics and brain-machine interfaces (BMI) to restore or augment lost motor and sensory functions [23]. Moreover, functional electrical stimulation (FES) of the central nervous system (CNS) has the potential to provide irreplaceable therapeutics and procedures for diagnosis and treatment, as well as developing neuron interfaces for medical prosthesis [2][18][19][20][21][22]. Cortical and intra-cortical electrode design progressed through many innovations aiming to develop neuro-interfacing electrodes for stimulation and recording. The lack of knowledge urges to study the population dynamics and information coding across ensembles of neurons which requires simultaneous multisite recording of neural activities over extended recording periods.

1.3 Research Objective

The primary goal of this research was to design, fabricate and test intra-cortical microelectrodes capable of satisfying a wide range of constraints and design requirements. Developing electrodes with improved functionality and biocompatibility required reworking the conventional electrode technology through fulfilling the following objectives:

- Develop design methodology for intra-cortical microelectrodes
- Create electromagnetic (EM) and mechanical models for the electrode and brain tissue to study the electrode electric performance and improve its design
- Create novel electrode layouts and architectures to implement proposed designs
- Integrate multiple functions on the electrode including simultaneous recording and stimulation, and current steering
- Develop fabrication processes for the different electrode designs
- Develop assembly techniques to create 3-D electrode arrays
- Develop insertion procedure to minimize tissue displacement and damage
- Electrode characterization and clinical testing

The research objectives were successfully fulfilled, and in conclusion; electrodes are tools, and advancements in electrode technology will meliorate the delivered procedures and therapies.

1.4 Thesis Outline

The first chapter presents a brief introduction highlighting the applications of neuro-modulation in medical procedures and outlines the research motivation and objectives. Chapter two provides an elaborate survey on the evolution of intra-cortical electrode design and demonstrates the history of cortical recording and stimulation. The design methodology and an elaborate illustration of the proposed designs are introduced in chapter three. The electromagnetic modeling and simulation of the implanted electrodes using finite difference time domain (FDTD) is discussed in chapter four discusses. Chapter five presents the structural analysis and mechanical design optimization for the proposed electrode layouts using finite element analysis and modeling (FEM). Electrode fabrication is illustrated in chapter six, and the characterization, in vitro and in vivo testing results are presented in chapter seven. Finally, the thesis is concluded and the future work is presented in chapter eight.

Chapter 2

Literature Survey

2.1 Introduction to Cortical Recording

Electrotherapeutic techniques

The application of electric charges in therapeutic practices has been exercised ever since mankind discovered features of electricity. Chronic clinical electrotherapeutic techniques were first introduced in cardiac pacemakers in the 50's. In the same time, experiments on sound perception arising from electrode implantation inspired the development of cochlear prosthesis. The stimulation of the visual cortex started in 1966 [34], and in the 70's the treatment of chronic pain was demonstrated through spinal cord stimulation (SCS). In 1972, The Neural Prosthesis Program launched a multidisciplinary research for developing technologies to restore motor function to paralyzed individuals. The main goals were to study electrode-tissue interaction, biomaterials and neural interface development to develop cochlear and visual prosthesis, and the control of motor functions. Deep brain stimulation (DBS) was introduced by Benabid et al in France 1987 [2] and research exhibited the relation between subthalamic-nucleus (STN) in the basal ganglia and movement disorders. Further research showed that applying lesions to the STN can reverse Parkinson-like effects induced by MPTP (1-methyl-4-phenyl-1, 2, 3, 6-tetrahydropyridine) treated monkeys [18]. In 1997, stimulation of the thalamus was approved by the FDA for the treatment of movement disorders and it was implemented in about 20,000 patients using electrodes and stimulators supplied by Medtronic [18][35].

Neurophysiologic investigation

Neurophysiologic investigation studies the neural system architecture and information processing, and requires long-term simultaneous recording of cortical neuron populations. The exploration of brain functions was limited to single cell recording due to technological constraints which prevented producing multi-channel recording electrodes. Thus, the instantaneous behaviour of neuron populations had to be inferred from the time-averaged responses of individual cells recorded through several sessions [36]. The progress in this field was impeded by the limitations of conventional microelectrodes [37] which introduced variability in electrical impedance levels and was limited to single channel recording. The advancement of microelectronics industry and silicon microfabrication introduced thin-film electrodes which allowed the production of multisite recording microprobes. Information about the functional anatomy of the nervous system can be elaborately reviewed in [39][40][41][42].

2.2 Applications of Electrotherapeutic Techniques

Nervous system recording and stimulation provide therapeutic techniques for the diagnosis and treatment of several disorders through neuro-modulation and neural augmentation. A short list of the FDA approved electrotherapeutic techniques includes:

- Deep brain stimulation: Parkinson's disease, essential tremor, dystonia
- Spinal cord stimulation: Chronic pain
- Vagus nerve stimulation: Epilepsy, depression

Biomedical and neuro-physiologic research is progressing to create therapies and develop neuro-prosthetics for neural augmentation. Different applications of electrotherapeutic techniques are listed in Figure 2-1, and were categorized as follows:

- Cortical stimulation
- Neuropathic pain
- Obesity
- Depression
- Hypertension Stroke rehabilitation
- Parkinson's disease, tremor
- Aphasia
- Tinnitus
- Brain-machine-interfaces [43][23]
- Blindness
- Deafness

Deep brain stimulation

- Neuropathic pain
- Tourette's Disease

Peripheral nerve stimulation

- Migraine headache
- Epilepsy
- Cluster headache
- Minimally-conscious state
- Addiction
- Obsessive-compulsive disorder
- Neuro-prosthetics control for paralyzed patients [21][23][44][45][46]. Providing tools for multisite neural recordings which is required for studying and analysing neural interactions [47][44]

2.3 The Evolution of Intra-Cortical Electrode Design

Intra-cortical electrodes were designed to capture neural electrical activities in the brain for studying neural interactions. Various concepts steered the design of intra-cortical electrodes starting with simple architectures in the form of glass micropipettes [14][46][48] and silicon needles [15]. These electrodes were designed to be stiff enough to penetrate through the dura (tough fibrous membrane covering the brain, spinal cord and the inner surface of the skull) and the pia (innermost of the three layers covering the brain and spinal cord) without buckling [16][17]. Micro electrodes were introduced to shrink the electrode dimensions and minimize brain tissue trauma, tissue displacement and chronic damage [16][43][49]. Surface coating the electrodes with biologically anti-fouling polymers was investigated to counteract the nonspecific affinity of proteins and cells to attach to surfaces [50][51][52]. Electrode surface modifications were investigated to reduce tissue adhesion [45]. In addition, increasing the number of available channels brought in more challenges [11][23][47][53]. Other designs aimed to integrate amplifiers onto the electrode structure to improve signal-to-noise ratio and signal quality by amplifying the signal at its source [53][54][58].

2.3.1 Electrode categories

Research produced multitude of electrode designs with diverse characteristics. The electrodes were classified according to various design features including geometry, number of channels, application and anatomical position [55], and detailed classification is listed in Figure 2-2. Glass micropipettes electrodes were the earliest technology that provided single channel recording. These electrodes are not suitable for implantation or long-term applications, however, they are currently being used for single site clinical recording of brain slice activities due to their low cost and ease of fabrication. Micro-wire bundle electrodes replaced glass micropipettes in rodent and primate signal recording procedures. The tetrodes and niotrodes are two versions of micro-wire bundles providing four and six recording spots respectively. Microelectrode design benefited from the advancement of microfabrication technologies, and thin film electrodes were introduced with the potential to increase the number of recording spots.

2.3.2 Micropipettes

Glass micropipettes and insulated metallic needles (e.g. tungsten wires with diameters ranging from 25 to 50 μ m) were the early tools used in single-unit recording and provided a great deal of knowledge at the individual cell level [46]. The electrode was designed to penetrate into the brain tissue and the recording pad located at its tip allowed single channel recording from deep brain structures. Glass micropipettes were designed for intracellular recording by penetrating through the cell membrane resulting in better signal pickup (>10mV) [56]. These electrodes are fabricated by pulling heated glass capillary tubes into a diameter of 1 to 2 mm [57]. The heated electrode is split by stretching forming sharp tips and the dimensions can be controlled by the temperature and the pulling force [58]. The micropipette is filled with conductive solution (e.g. potassium chloride KCL) and poked through the cell membrane. Negative pressure is applied to create a continuum of conductive medium by

mixing the KCL solution with intracellular fluids. Glass micropipette electrodes are low cost and easy to fabricate in house according to the desired dimensions. However, they have major disadvantages. The capacitive loading of the high tip resistances (~ 2 to $8\text{M}\Omega$) [59] together with the series glass wall capacitance [60] form a low pass filter which limits the recording bandwidth [60]. Moreover, the electrode has brittle and narrow tip which is susceptible to breakage and blockage [61]. The brittle nature of micropipette electrodes aggravates tissue trauma and damage due to the electrode dislocation within the brain and is not suitable for chronic in vivo applications [63]. Glass micropipette electrodes are currently used in recording the evoked responses of brain tissue slices in neuron stimulation experiments. Metal microelectrodes are made from insulated metallic shafts (usually platinum, gold or tungsten) with exposed tips [60][62]. In general, metal microelectrodes are used for extracellular recording while glass micropipettes are for intracellular recording [14]. These electrodes exhibit high tissue displacement, and the traumatizing effect is estimated as the ratio of number of recording sites to the brain volume displaced [63].

2.3.3 The quest for multisite recording

Single channel recording provide relatively little information about the organization and function of neural circuits and systems. Simultaneous multisite recording is more beneficial in studying neural interaction, topographic organization and functional relationships of neuron populations [53][64]. It is also essential for implementing closed-loop neural prostheses and neural augmentation systems [51]. Acquiring data through single site recording is done by successive recordings which require repetitive stimulation which is a time consuming procedure and may produce non correlated results.

2.3.4 Micro-wire bundle electrodes

Micro-wire electrodes are made of Nickel-Chrome wires ($\Phi 25\mu\text{m}$) coated with a $3.5\mu\text{m}$ insulating layer (e.g. Teflon). The wires are spun on helical trace around a platinum/iridium wire ($\Phi 38\mu\text{m}$ with a $6.5\mu\text{m}$ insulation layer), then fixed using epoxy resin (Epo-Tek 302-3M, Polytec PT, Germany). The wire assembly is cut and the tip is bevelled at 45° to expose the metal cores creating recording sites. The final niotrode electrode array has a total diameter $<100\mu\text{m}$ providing 9 recording channels as shown in Figure 2-3-Left with channel impedance of $300\text{k}\Omega$ at 1KHz [63]. Niotrodes improved tissue displacement of single wire electrode by a factor of 4.5 and a single shaft of the Utah array by a factor of 9. These electrodes are currently used in rodents and primates intra-cortical recording experiments. In order to increase the recording density; hypothetically, several niotrodes can be integrated in 2-D matrix as shown in Figure 2-3-Right, but it will be challenging to control the inter-electrode spacing precisely. A major drawback of this electrode is limiting the recording to the electrode tip which is in contact with the most damaged cells [65]. Other drawbacks include low positional accuracy, mechanical vulnerability structure and difficulty in controlling array layout [65][66]. In conclusion, wire and glass micropipettes offer low cost and simple tool for single-site recording with low ratio of recording sites to displaced tissue.

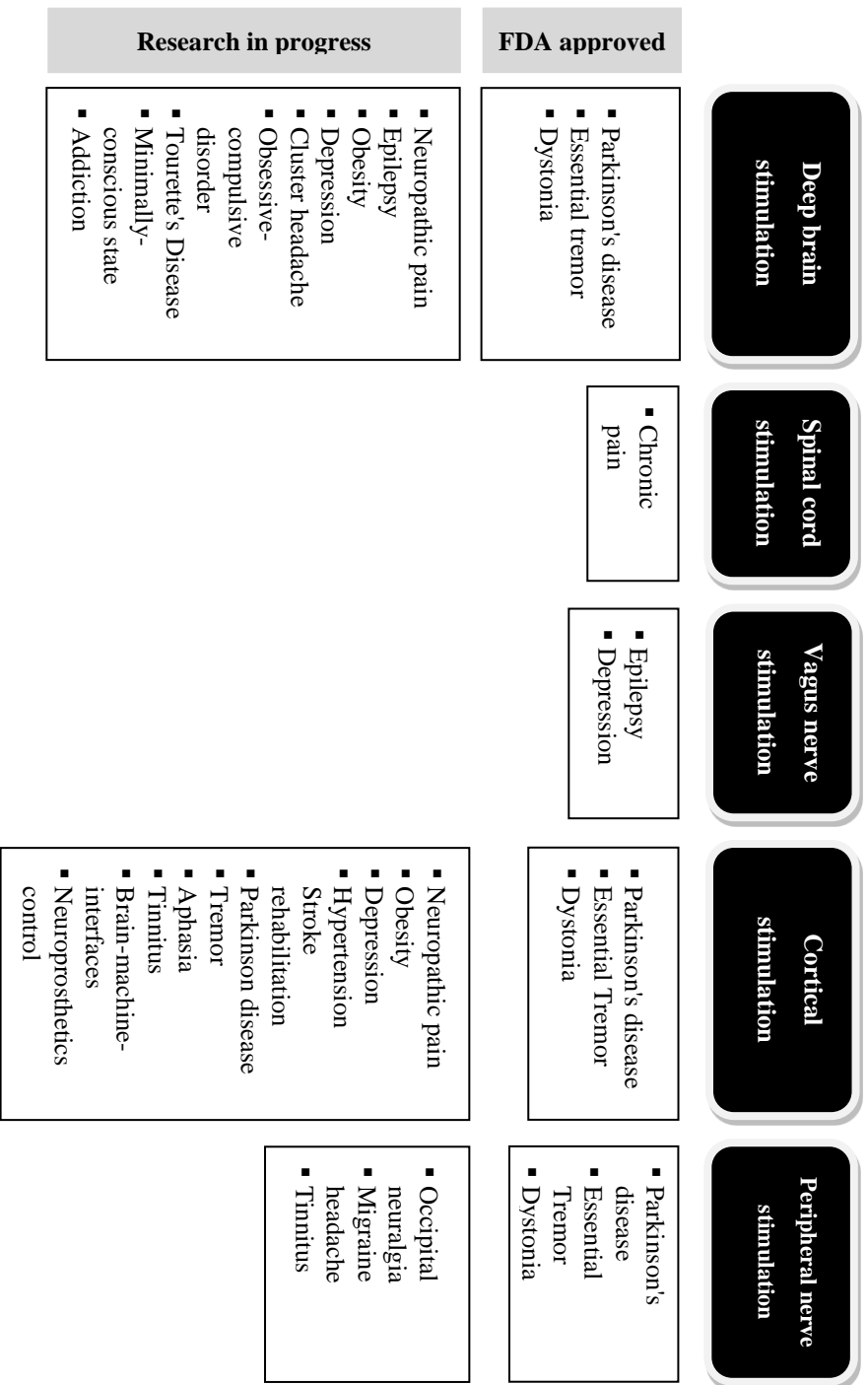


Figure 2-1. Applications of electrotherapeutic techniques

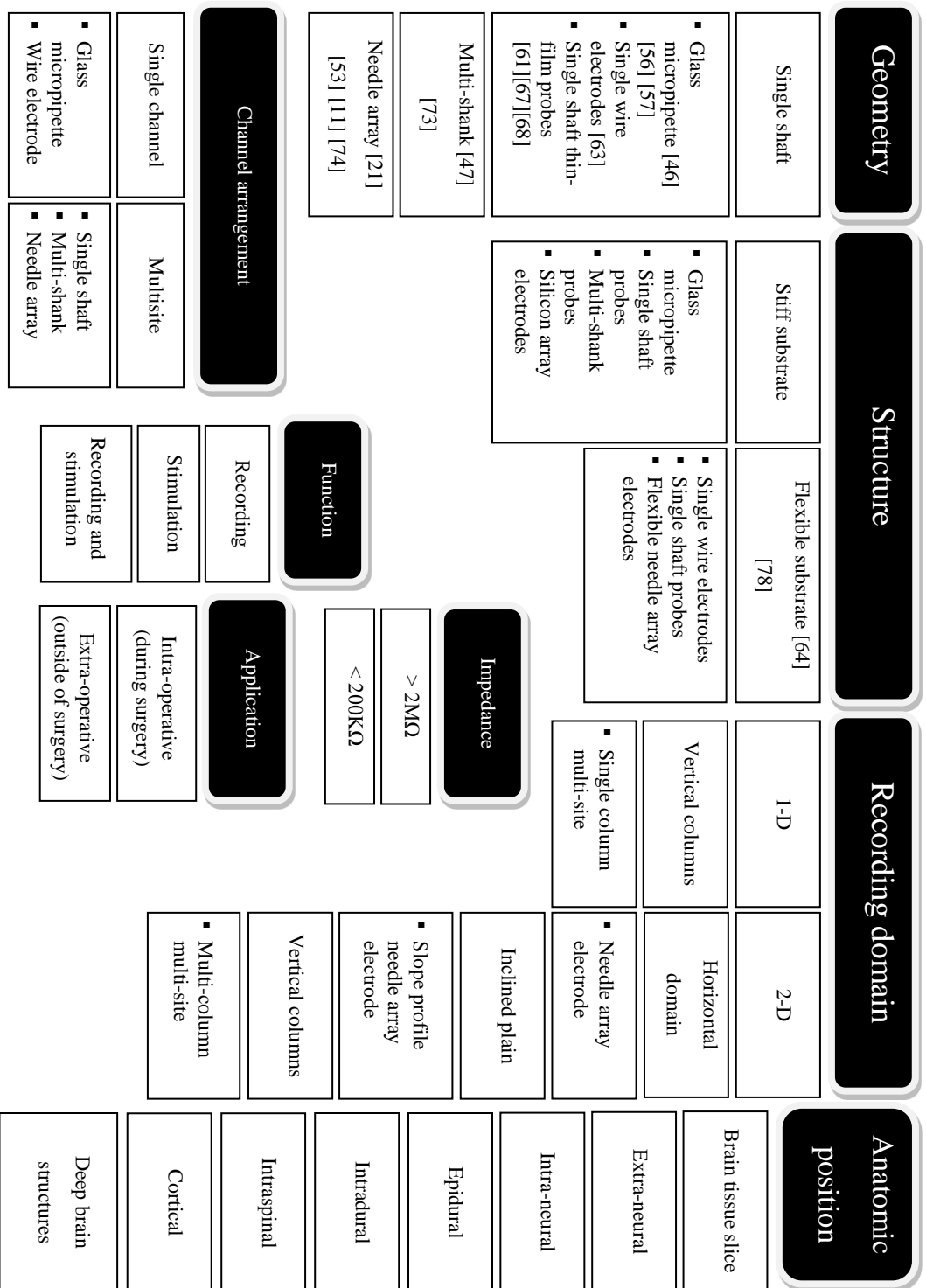


Figure 2-2. Classification of microelectrodes

2.3.5 Thin-film electrodes technology

Thin-film technology employs microfabrication and photolithography techniques to create high precision multisite recording electrodes for the simultaneous sampling of multiple neurons. Conductive layers are deposited and patterned on dielectric substrate and a dielectric layer provides electric insulation and maintains biocompatibility [61][67][68]. Thin film electrode technology progresses with the advancement of microfabrication processes, and introduced a remarkable leap in intra-cortical electrode technology.

2.3.6 Single shaft multi-channel electrodes

Single shaft thin film electrodes have a planar structure, and the slender shaft carries several pads representing the interface channels. The electrodes are designed for multisite recording in order to increase the spatial resolution as well as increase the number of recording sites per displaced volume of tissue. Silicon fabrication processes were used in implementing multisite microelectrodes with an array of recording pads. The electric connections were formed using metal thin film deposition and patterning techniques on silicon substrate which forms the electrode shaft. Figure 2-4 shows a 4 channel microprobe fabricated on 15 μm thick silicon shaft. The shaft was 3mm long, and the tapered profile started with a width of 90 μm at the base that narrowed to 20 μm at the tip. Gold recording sites were deposited at different spacing (30 to 200 μm) and polysilicon (or tantalum) was used for interconnections. Finally, the structure was insulated by a layer of silicon-oxide and silicon-nitride. The areas of the recording sites ranged between 100 to 400 μm^2 and the impedance ranged from 2M to 8M Ω at 1KHz. The stability of this electrode was tested by immersion in physiological saline and rats, and they were functional for 12 days then the output lead insulation failed [25]. Another silicon electrode provided 9 recording sites with 300 μm separation while keeping the 9th pad 1mm deeper. Each recording site was 50x50 μm^2 and the structure was insulated by a 3 μm of silicon-nitride [69].

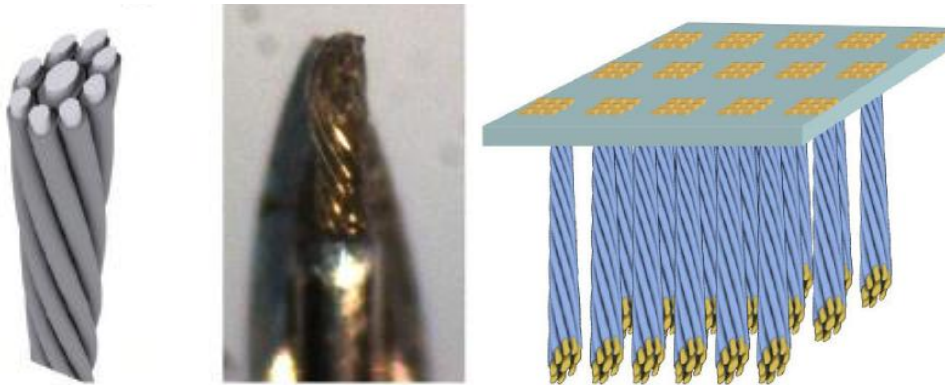


Figure 2-3. Micro-wire bundle electrodes, Left: Niotrode, Right: Niotrode array [63]

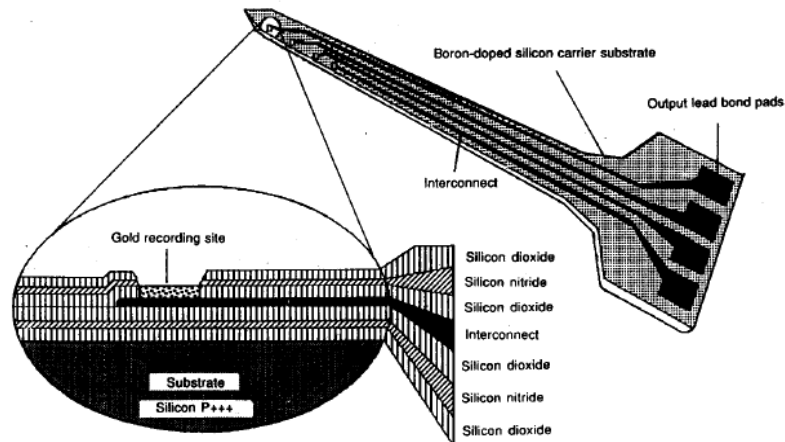


Figure 2-4. 4 channel silicon microprobe [25]

Molybdenum was also used as a shaft material to support two layers of polyimide sandwiching gold metallization layer (Figure 2-5-Left). Windows were etched in the upper polyimide layer to expose the $30 \times 30 \mu\text{m}$ gold recording sites with $500 \mu\text{m}$ separation. The electrode was 3.75 mm long and the tapered shaft width was $135 \mu\text{m}$ at the tip [77]. Another molybdenum single shaft electrode provided 24 channels arranged in 1×24 or 2×12 arrays by patterning gold on $17 \mu\text{m}$ thick molybdenum substrate (Figure 2-5-Right). The electrode impedance was $100 \text{ K}\Omega$ at 1 KHz with 3 to 4 pF shunt capacitance. Ceramic was proposed to replace silicon and the electrode presented in Figure 2-6 had 4 recording sites ($22 \times 80 \mu\text{m}$) separated by $200 \mu\text{m}$ patterned on a ceramic shaft. Alumina was used to passivate the electrode surface [16] and the electrode was stable for 180 days in a saline solution [16]. Ceramic substrates do not allow the creation of tips with cross-section areas as small as that of metal substrates [70], which restrain the implementation of different electrode geometries.

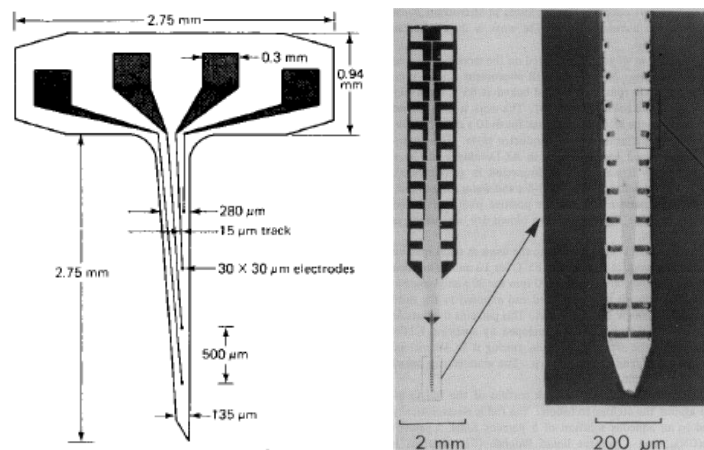


Figure 2-5. Left: Molybdenum thin film electrode [77], Right: Molybdenum thin film electrode with 2×12 sites [70]

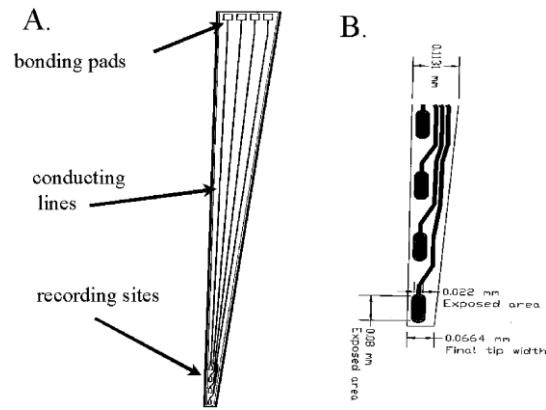


Figure 2-6. Ceramic thin film electrode [16]

Judy's lab in UCLA presented a single shaft electrode with a nickel structural layer. The electrode shaft was fabricated using nickel electroplating on non-continuous seed layer to generate a tapered tip design which facilitates penetration as shown in Figure 2-7. The seed layer was patterned on carrier wafer coated with oxide for release and nickel was coated with gold for biocompatibility [181]. The fabrication steps and electrode layout are shown in Figure 2-8.

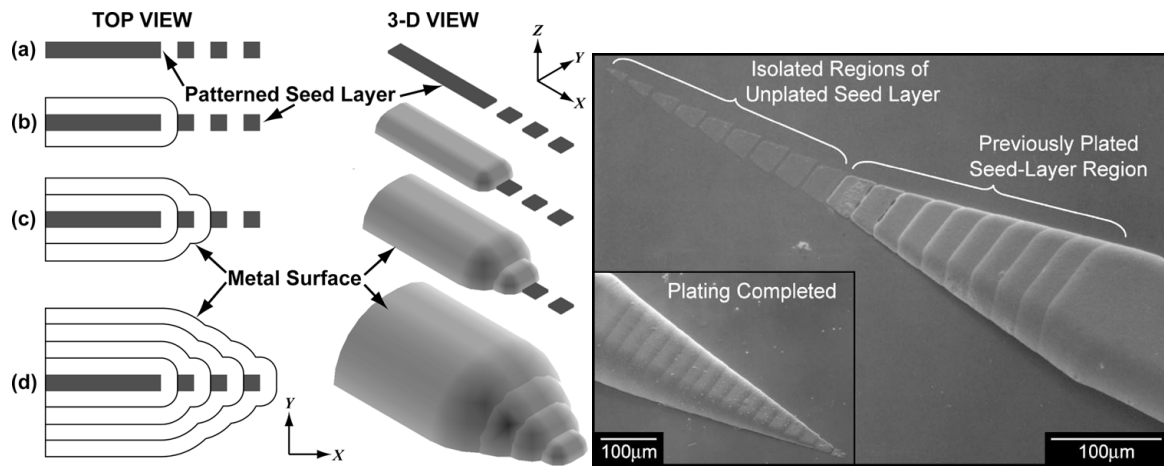


Figure 2-7. Tapered electrode tip using non-continuous seed layer, Left: Seed layer sketch, Right: Fabricated electrode tip [181]

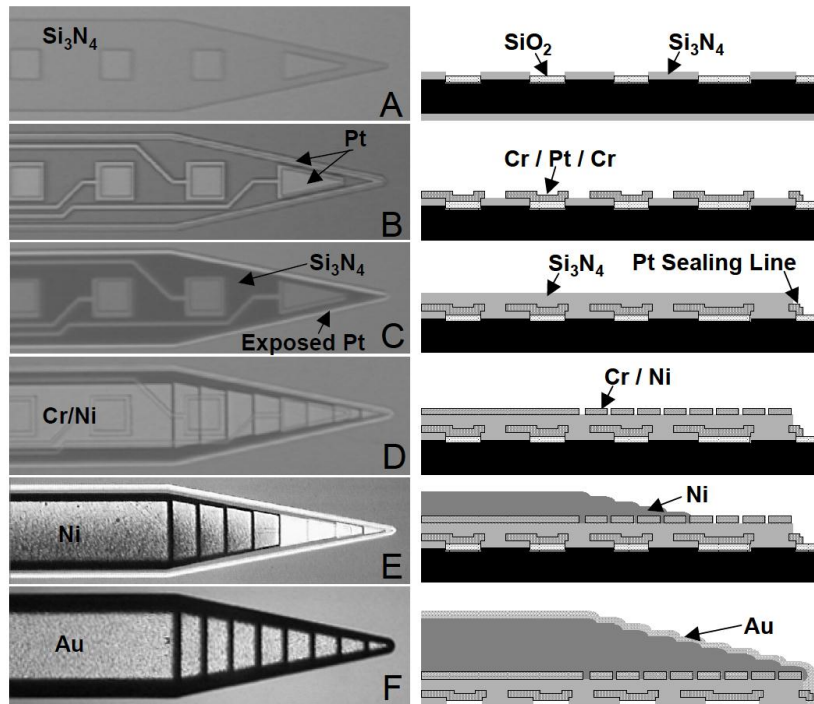


Figure 2-8. Judy's lab electrode fabrication steps [181]

2.3.7 Needle arrays

Single shaft electrodes allow recording the electrical activity of neural columns but larger areas have to be covered for a comprehensive perception of neural interactions. In order to increase the density of recording sites, 3-D microelectrode arrays were developed to provide simultaneous multisite recording from a large population of neurons. These electrodes can be used for controlling neural prosthetics [21].

Needle arrays can be in the form of a matrix of micro-needles, each allocates a recording channel at its tip. The needles could have the same length or patterned into a sloped contour. This architecture limits the recording to a planar field. On the other hand, the electrode can be constructed from several shafts, each carrying multiple recording spots. This allows recording the neural activity of neighbouring neural columns. A silicon needle array intra-cortical electrode was fabricated on a silicon substrate to have a 10x10 matrix of 1mm brittle needles with a pitch of 400 μ m. The platinum tips were coated with silicon-nitride and the needle rows were isolated using silicon-oxide. This electrode was designed for flip-chip integration with on-chip circuitry for amplification and wireless transmission [21].

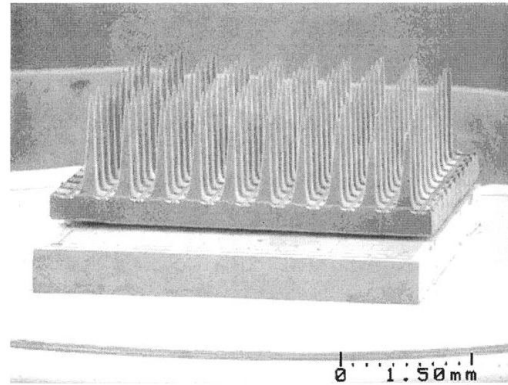


Figure 2-9. Needle array electrode [21]

A similar architecture was implemented as an active electrode with onboard bioamplifier and additional circuitry for signal pre-processing. The active array had 256 channels (Figure 2-10) suitable for in vitro was fabricated on a single die [53] with 16x16 array of signal pre-processing CMOS cells, and the needles were post-fabricated on the die using gold wire bonding. Signal pre-processing includes amplification, band-pass filtering and storage in the in-channel analogue memory. The electrode base was 3x4.5mm, and the tapered needles were 100 μ m long and had a diameter of 80 μ m [53].

Electrical discharge machining (EDM) was applied in fabricating high density array electrode for intra-cortical recording of brain activity [11]. Several metals were used including titanium, titanium-aluminum -vanadium alloy (Ti90-Al6-V4), stainless steel, and tungsten-carbide, and the needles were coated with platinum for biocompatibility. The electrode was designed to have 1mm long needles with a pitch of 400 to 500 μ m and pictures of the fabricated electrodes are shown in Figure 2-11. The same technique was able to produce 5mm long needles with spacing of 250 μ m. The electrode impedance was spread along wide range due to poor soldering resulted by adhesion problems of titanium alloys [49].

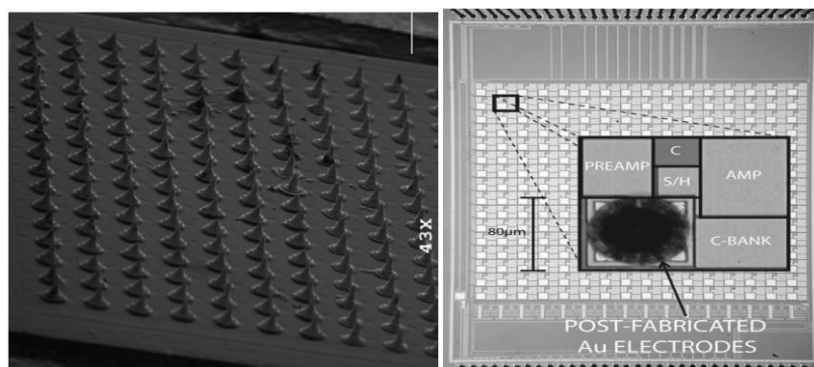


Figure 2-10. Left: Active electrode array, Right: CMOS cell schematic [53]

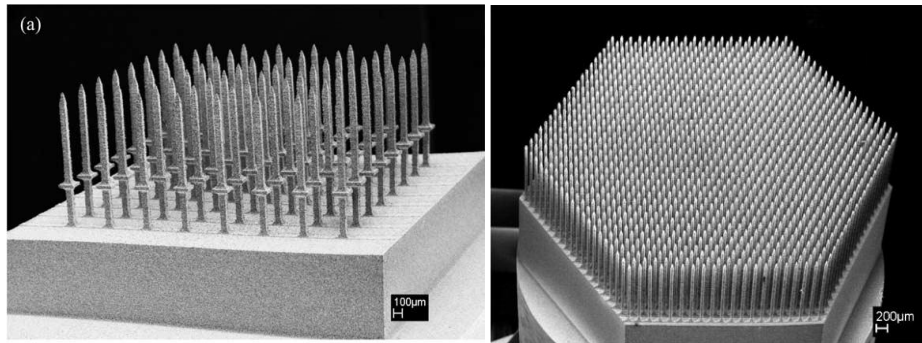


Figure 2-11. Left: 10x10 EDM array electrode, Right: titanium electrode with 1141 pins [11]

Utah array

Utah array was a part of DARPA-supported project to develop a bionic arm (Figure 2-12). The electrode consisted of 100 silicon needles arranged in a two-dimensional array, each needle represented a recording site [46] precisely spaced and this provided an advantage compared to micro-wires [63]. The needles were 1mm long and had tip diameter of 50µm.

Microelectrode Arrays (MEA)

The ESIEE Neurocom group designed silicon needle array providing 64, 256 or 1024 recording sites. The needles were fabricated using isotropic and anisotropic silicon etching to create 80µm needles with 50µm pitch and the electrode is shown in Figure 2-13 [178].

2.3.8 Multi-shaft electrodes

Needle array electrodes limited the recording in a planar domain, and some electrodes had a sloped profile to record from different depths, and each needle provided single recording site located at its tip. In order to investigate closely-spaced columnar organization and layering of cortical tissue, it is required to develop electrodes with 3-D architecture. High channel count electrode was designed to accommodate up to 128 channels distributed among several shafts. The shafts had tapered tips and several designs were fabricated with shaft lengths ranging from 4 mm to 15mm as shown in Figure 2-14 [47]. Figure 2-15 presents an electrode with integrated 8 channel amplifier and 64:8 multiplexer to access the 64 recording sites consuming 756µW (Figure 2-15). The recording sites were made of 100µm² iridium pads spaced at 200µm [73].

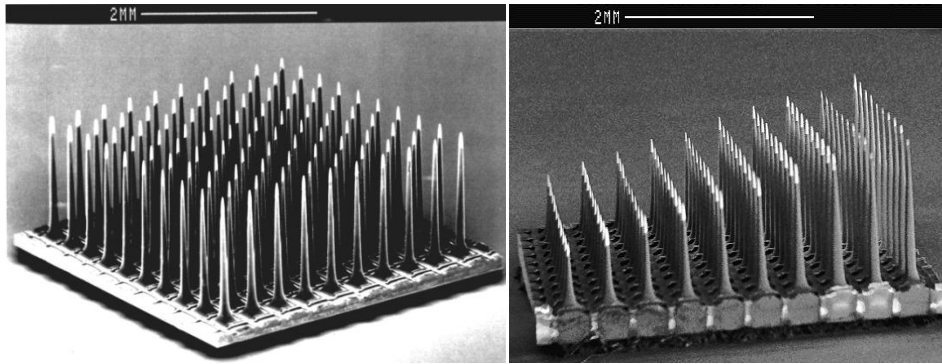


Figure 2-12. Left: Utah array, Right: Sloped Utah array [74]

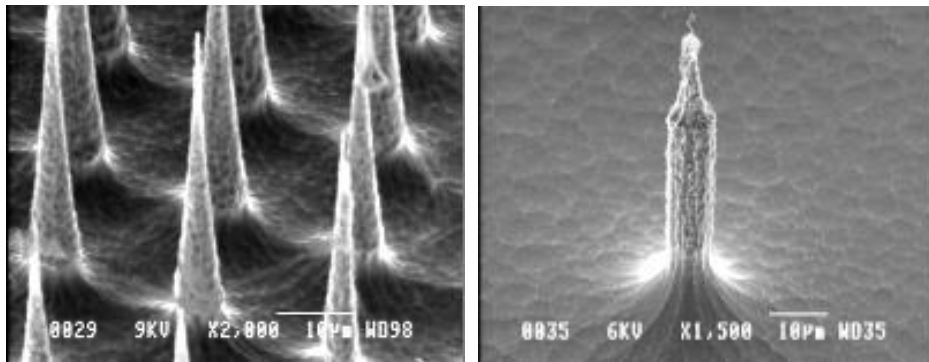


Figure 2-13. Left: MEA electrode array [178], Right: Close up view of a single needle

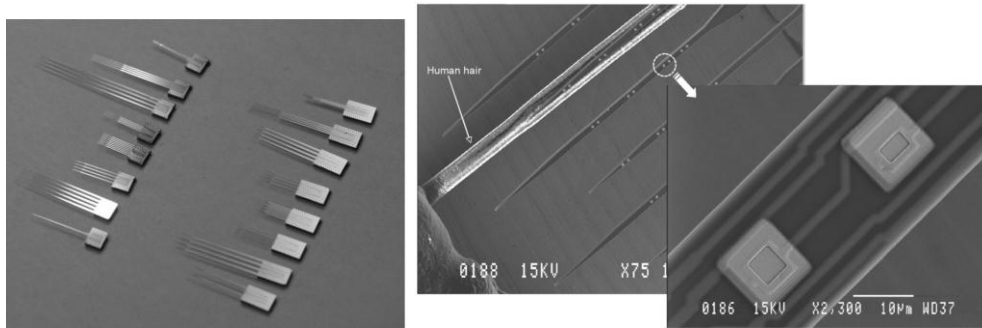


Figure 2-14. Multi-shaft silicon recording electrodes [47]

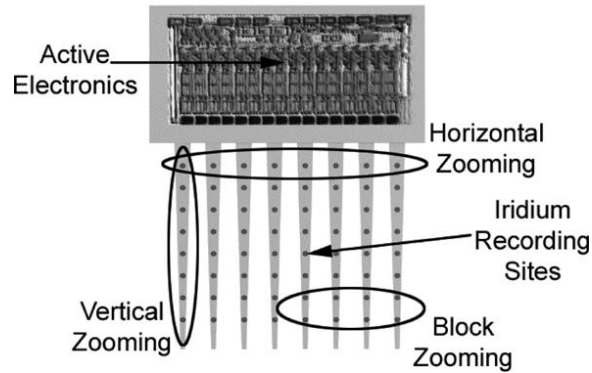


Figure 2-15. Active multi-shank silicon electrodes [73]

In order to simplify electrode assembly and integration, a modular design for multi-probe cortical assembly was implemented by stacking 2-D probes to provide 3-D constellation of recording sites. The Microscale Implantable Neural Interface (MINI) was made up of 16 channel probes yielding a total of 96 channels (Figure 2-16). Each 3mm probe carried 4 recording spots with an area of $1250\mu\text{m}^2$ and a pitch of $400\mu\text{m}$. The probes were stacked $250\mu\text{m}$ apart and had $20\times 60\mu\text{m}$ perforations to allow tissue integration. The probe assembly was then connected to a module for signal acquisition through flexible interconnects [23]. Laurent lab and Roukes group in Caltech developed a dual-side recording electrodes. The electrode comprised two silicon shafts with pads on both sides. A single electrode unit was assembled to form a 3-D electrode array [179] as shown in Figure 2-17 [180].

2.3.9 Flexible substrate electrodes

Numerous designs for electrodes were developed on silicon and ceramic substrates; however, stiff electrodes would potentially cause significant trauma due to the displacement of rigid structures within brain tissue. Furthermore, brittle shafts are prone to fracture and would release debris in the brain. Flexible substrates were introduced to overcome the drawbacks of brittle electrodes and brought in several design challenges involving the mechanical design, fabrication and tissue penetration [31][43][49][75][76].

A sketch of a flexible Parylene-based electrode array is presented in Figure 2-18; this design had 6 shanks each was 1.2mm in height and $160\mu\text{m}$ in width with 3 recording pads each was $20\times 20\mu\text{m}$. The electrode was coated with a stiff layer of polyethylene glycol (PEG) to assist during insertion, the PEG layer would eventually dissolve into the tissue fluid after insertion [64]. A microfluidic channel could be integrated in the electrode for injecting chemicals (Figure 2-19). The channel was also a part of the insertion mechanism as it was filled with PEG which would dissolve after insertion [78].

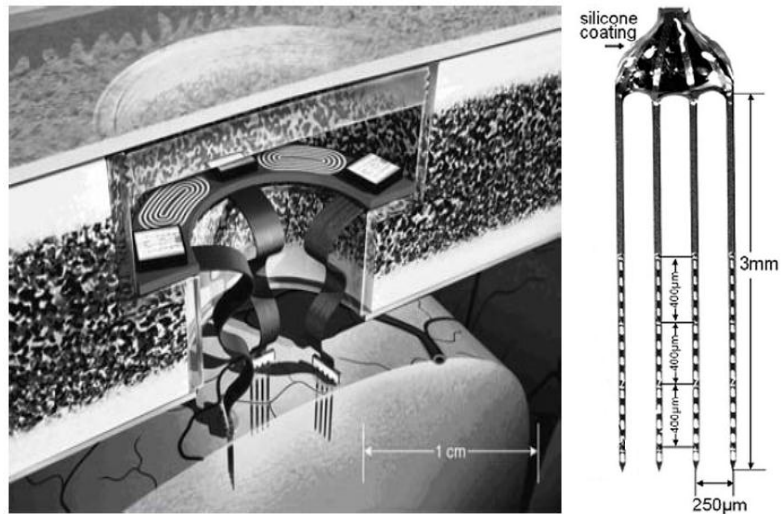


Figure 2-16. Left: Microscale Implantable Neural Interface (MINI), Right: Single probe [23]

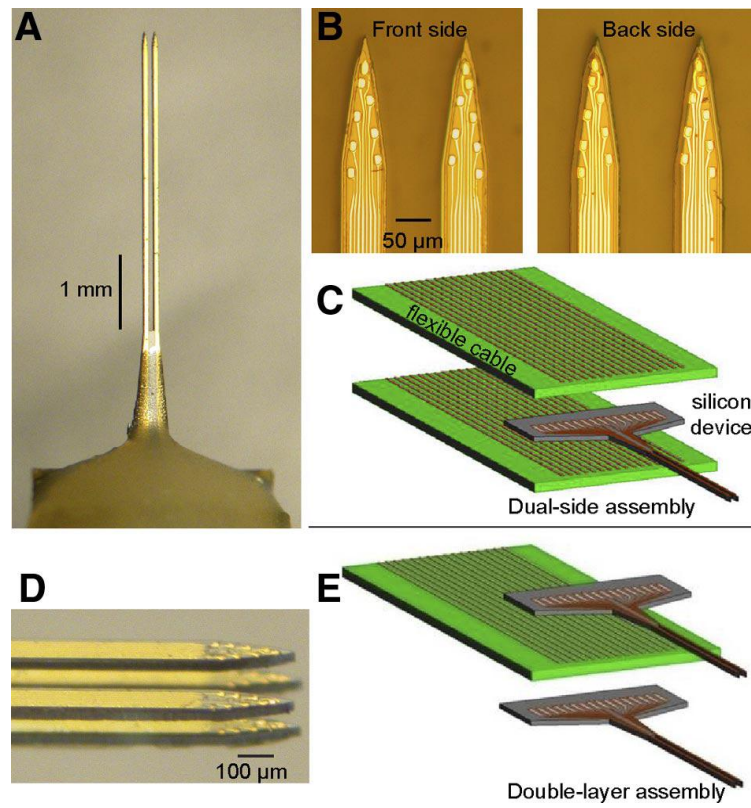


Figure 2-17. Caltech dual sided electrode [179]

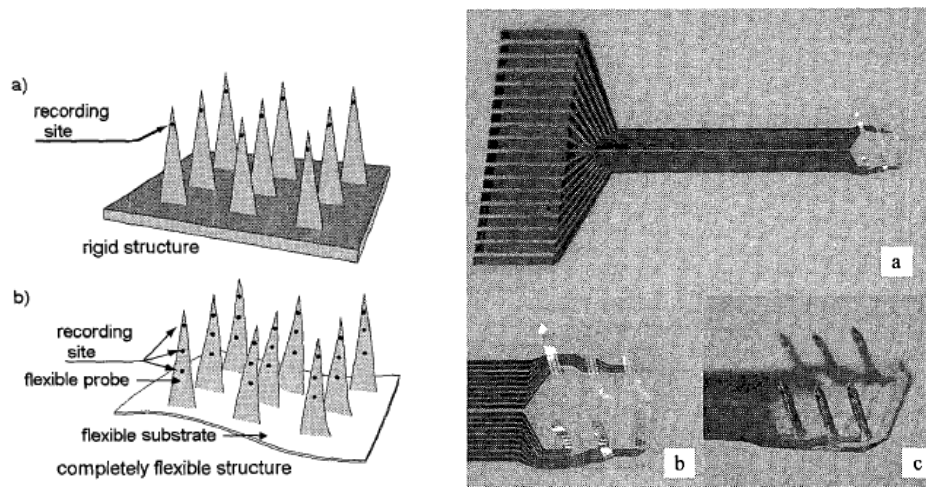


Figure 2-18. Flexible parylene electrode [64]

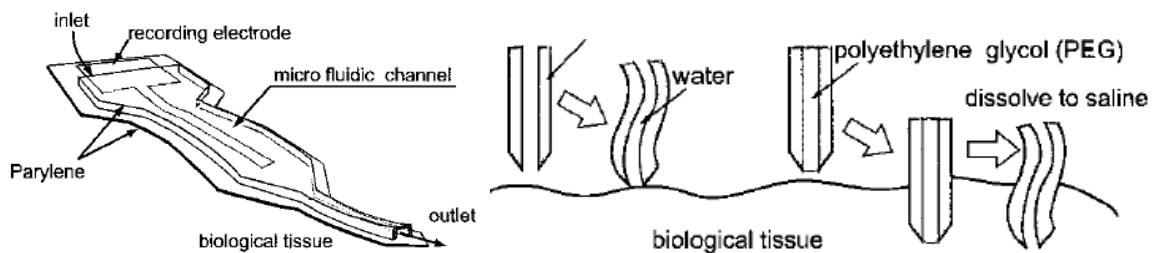


Figure 2-19. Flexible electrode with integrated microfluidic channel [78]

2.4 Practical Considerations

There are several practical considerations that contribute to proper electrode operation and failure. They involve various topics including but not limited to physiological, electrical, and mechanical, chemical considerations. These topics can be incorporated in the design process in the form of guidelines and constraints.

2.4.1 Tissue displacement

Brain tissue can be displaced through cortical dislocation and rotational acceleration of the head. Cortical dislocation is a result of the forces generated by the circulatory and respiratory systems and pulsate the cortex perpendicularly with respect to the skull [79]. Rotational acceleration of the head causes cortical displacement relative to the overlying bone and dura. If a probe was rigidly connected to the skull, it would transfer the displacement forces to its shaft and would eventually deflect the tips away from the targeted location, and the dislocation would lead to further tissue trauma. Thus,

chronic electrodes are preferred to have flexible structures, and should be tethered to other elements using flexible interconnect cables.

It is required to design microprobes virtually invisible to the tissue in order to minimize tissue damage and displacement. During insertion, the electrode destroys some neurons within the kill zone and this might limit discrimination of individual neurons [26][44]. Tissue displacement can be estimated by the ratio of number of recording sites to the brain volume displaced [63] and should be kept below 1%. Cortical recording requires large number of recording sites covering large neural area. Increasing the recording sites density is not in favour of the electrode size, and therefore the electrode geometry is a principal factor affecting tissue displacement.

2.4.2 Pad size and separation

Pad size and spacing determine the channel density and electrode dimensions, which in turn influences the electrode functionality (number of channels) and biocompatibility (intensity of tissue trauma), thus they are considered critical design parameters. Pad size controls its impedance and charge capacity which dictates the electrode application. Large pads provide lower impedance ($\sim 300\Omega$) and are used for stimulation and local field potential (LFP) recording, while smaller pads with higher impedance ($>2M\Omega$) are used for single neuron isolation and spike recording. Neural stimulation electrodes can be divided into two major categories according to surface area:

Macroelectrodes

These electrodes are characterized by high-charge-per-phase thresholds and low charge density thresholds. They deliver the charge to the surface of the target tissue and have geometric surface area (GSA) larger than $100,000\mu\text{m}^2$ (0.001cm^2). The low charge-injection densities inhibit corrosion and avoid stimulation-induced electrode degradation, but the high-charge-per-phase levels may induce tissue damage.

Microelectrodes

Microelectrodes have low-charge-per-phase thresholds and high charge density thresholds. They penetrate the target and have surface areas smaller than $10,000\mu\text{m}^2$ allowing high selectivity in stimulating small volumes of tissue. The elevated levels of charge densities evoke electrode degradation and tissue damage thus charge-per-phase and charge density must be kept low to prevent tissue and electrode damage.

2.4.3 Shaft width

Decreasing the electrode dimensions is constrained by its mechanical strength and the ability to penetrate through the pia and the dura layers of the brain [46]. It was reported that the shaft width could influence the extracellular current flow blinding the recording spots at the back side of the electrode if the width was more than $100\mu\text{m}$ [25]. Thus, if the recording spots were to be placed on both sides, it is preferred to keep the electrode width narrower than $30\mu\text{m}$ such that the recording field of a site becomes more spherical [15].

2.4.4 Mechanical strength

The electrode must be capable of handling the mechanical forces applied during insertion and operation. Flexible shafts provide strain relief and conform to the surrounding tissue, thus they improve the electrode biocompatibility. However, they are prone to buckling failure and may collapse during insertion. On the other hand, stiff and brittle electrodes would survive insertion forces without failing, but would cause more post-operative tissue damage due to electrode dislocation and micromotion. Moreover, when a brittle electrode fails mechanically, it will fracture and disperse debris in the brain. An electrode competent for chronic in vivo interfacing should have a flexible structure capable of surviving axial loading during implantation to maintain the design biocompatibility.

2.4.5 Neuro-compatibility and foreign body response

Neuro-compatibility represents the quality of electrode-tissue interface influenced by the tissue reactive response (host response) and bio-fouling. The presented electrodes are intended for prolonged application, and bio-fouling has to be considered due to the tendency of proteins and cells to adhere to foreign bodies inserted in the human body. Electrodes are foreign bodies and will encourage further protein adhesion forming unexcitable organic layer that encapsulates the needles and degrades the electrode functionality. The capsule thickness depends on the degree of reactivity of tissue to the implanted material as well its shape and surface condition. These responses result due to electrode biocompatibility issues evoked by cytotoxicity and electrode geometry (refer to Appendix B).

2.4.6 Electrode material

Foreign bodies introduced to a living system evoke changes in the homeostatic mechanisms which stabilize the internal body equilibrium. Biocompatible materials result in minimal biological response and do not produce toxic, injurious, or immunological response when come in contact with tissue. Biological performance of materials is evaluated by the host and material responses. The host response is a local or systemic reaction of living systems to the foreign material other than the intended therapeutic response. Inert electrodes do not impose irreversible chemical changes on the ambient environment [101]. In brief, material biocompatibility can be described in terms of the acute and chronic inflammatory responses and the fibrous capsule formation. There are several factors that limit the choice of electrode materials:

- Foreign body response (refer to Appendix B)
- Allergic responses
- Electric isolation
- Mechanical strength
- Biocompatibility

- Impedance
- Radiographic visibility

Table 2-1 lists different materials and their suitability for electrode fabrication

Table 2-1. Different materials and their suitability for electrode fabrication

	Considerations in favour	Arguments against
Gold	<ul style="list-style-type: none"> ▪ Biocompatible 	
Platinum	<ul style="list-style-type: none"> ▪ More tissue response than gold and stainless steel ▪ No gliosis after 30 days 	<ul style="list-style-type: none"> ▪ Produces denser capsule
Stainless steel	<ul style="list-style-type: none"> ▪ Very low tissue response 	<ul style="list-style-type: none"> ▪ Allergenic to some individuals
Aluminum	<ul style="list-style-type: none"> ▪ Biocompatible 	
Copper		<ul style="list-style-type: none"> ▪ Toxic
Silver		<ul style="list-style-type: none"> ▪ Toxic
Tantalum	<ul style="list-style-type: none"> ▪ Biocompatible ▪ Mild response after 30 days 	<ul style="list-style-type: none"> ▪ More tissue response than gold and stainless steel
Polyimide	<ul style="list-style-type: none"> ▪ Non-toxic ▪ Biocompatible ▪ Very little tissue response ▪ Flexible ▪ Strong ▪ Resistant to heat and chemicals 	
Parylene	<ul style="list-style-type: none"> ▪ Biocompatible ▪ Good insulator ▪ Transparent 	
Iridium	<ul style="list-style-type: none"> ▪ Highly resistant to corrosion ▪ Iridium oxide has high charge capacity 	
Nickel		<ul style="list-style-type: none"> ▪ Allergenic ▪ Severe local necrosis
Nichrome (80% Ni – 20% Cr)	<ul style="list-style-type: none"> ▪ Recommended for medical implants 	
Tungsten	<ul style="list-style-type: none"> ▪ Biocompatible ▪ No gliosis after 30 days 	<ul style="list-style-type: none"> ▪ More tissue response than gold and stainless steel
Silicon	<ul style="list-style-type: none"> ▪ Easily fabricated and processed ▪ Mild tissue response 	<ul style="list-style-type: none"> ▪ Brittle
Sapphire	<ul style="list-style-type: none"> ▪ Superior stiffness compared to silicon 	
Pyrex	<ul style="list-style-type: none"> ▪ Mild response after 30 days 	
Boron	<ul style="list-style-type: none"> ▪ Non-toxic 	

2.4.1 Electrode failure

The electrode fails when it loses the ability to efficiently perform its functions. Different forms of failure were identified and summarized into structural and electrical failures. Structural failure is device-oriented, while electrical failure reflects the neuro-compatibility which can be defined as the viability of the working interface between the metal electrode site and its target neurons.

Structural failure

Structural failure is an irreversible physical damage to the electrode and results due to excessive mechanical loading, physical contact or chemical interaction with the ambient environment. In general, the principal sources of different forms of structural failures are:

- Mechanical
 - Buckling: This failure mode is caused by excessive compressive forces applied on slender probes and needles. It can either damage a poorly designed probe or prevent it from penetrating the dura and pia layers
 - Stress corrosion cracking (SCC): Failure of structures subjected to constant tensile stress in a corrosive environment
 - Mechanical failure due to intrinsic stresses in deposited layers
 - Delamination: The electrode is constructed of composite materials layered together and this structure makes it susceptible to repeated cyclic stresses generated by vascular pulsatility
- Physical
 - Multi-layer electrodes might delaminate or fracture due to water uptake
- Chemical
 - Corrosion: The extended exposure to saline solution can damage metallic pads, insulation layers as well as connection leads
 - Delamination and corrosion attack passivation layers designed for insulation and not protection against corrosion [103]

Electrochemical decomposition

Electrochemical corrosion attacks single metal as well as multi-metal electrodes, and DC current flow leads to electrolytic decomposition. According to Faraday's law: the passage of one Faraday removes or deposits 1g equivalent of monovalent element [91], and this is effective in stimulation electrodes. DC currents can be avoided through capacitive coupling or using balanced bipolar waveforms; the later does not perfectly eliminate electrode corrosion due to the nonlinear nature of the electrode-electrolyte interface. As for multi-metal structures; bimetal junctions immersed in saline solution creates short-circuited galvanic cell and the current flow will generate unstable potential adding noise to the acquired signal in case of recording electrode.

Electrical failure

Electrical failure is the loss of contact with neurons which degrades or inhibits recording the neural activities. Electrical failure can result due to disruption of the electrode-electrolyte interface, tissue reactive responses, and tissue damage or electrode dislocation.

Micromotion

Micromotion and electrode dislocation are caused by several disturbances:

- Physiological: Including cardiac, respiratory (2 to 25 μ m in cats) and vascular pulsations (1 to 3 μ m in cats) [130]
- Behavioural: Spontaneous head and trunk movement
- Mechanical: Displacement of the lead wire is transferred to the electrode if the design lacks enough strain relief between the implanted electrode and other circuitry or additional structures mounted on the skull

2.4.2 Reliable chronic recording

Intra-cortical electrodes capable of chronic recording and stimulation are key players in neuro-modulation and functional electrical stimulation. Realizing such electrodes is challenged by:

- Foreign body response
- Stimulant artifacts
- Electrode displacement
- Recording density
- Fabrication technology limitations
- Electrochemical electrode damage

In vitro experiments showed the effect of bio-molecular and cellular interactions on increasing the impedance of recording microelectrodes [80][81][82]. In order to overcome the lack of consistent performance of single-site recordings, multi-site recording methods were proposed [83][84].

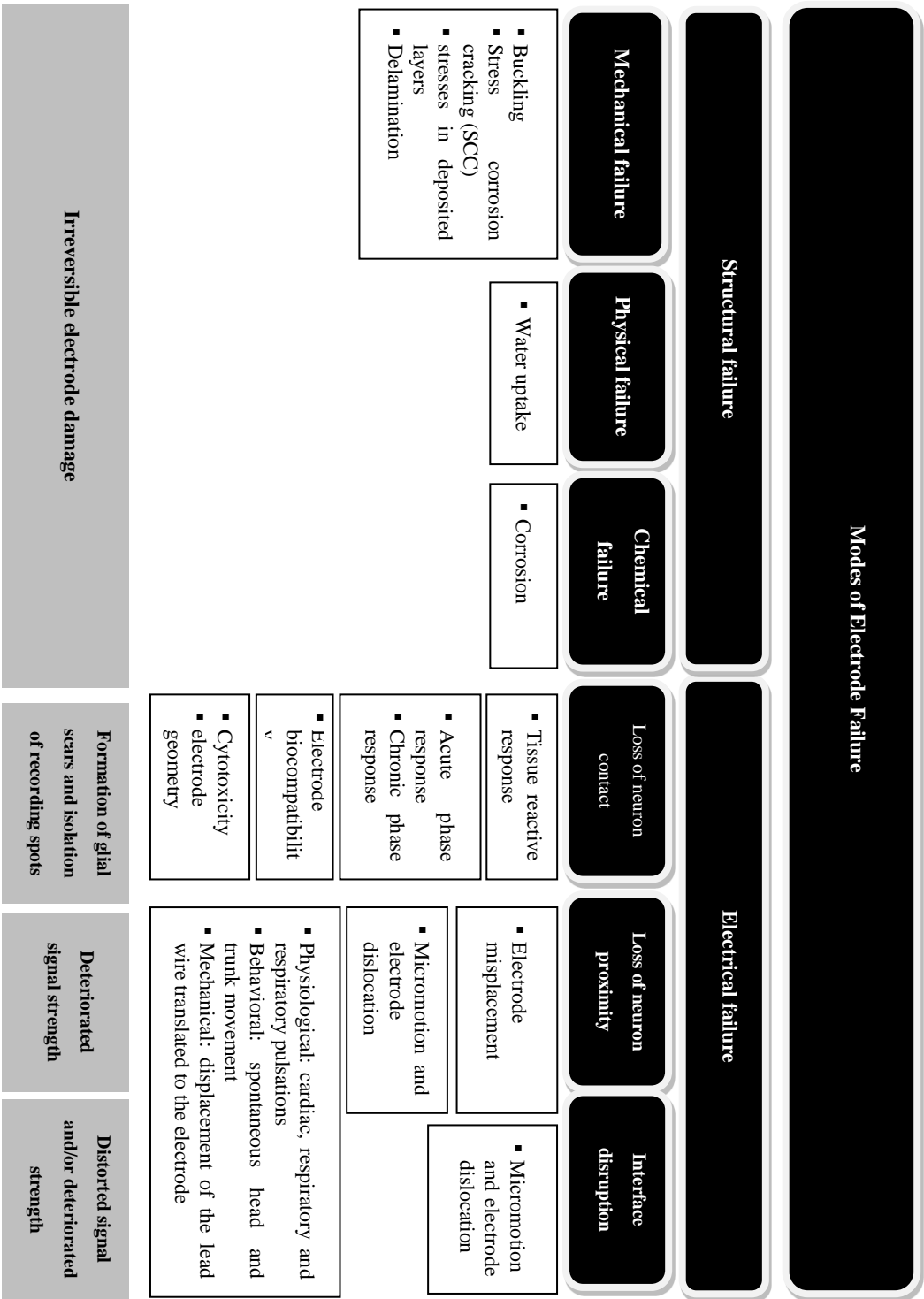


Figure 2-20. Modes of electrode failure

2.5 Summary of the Survey

Neuro-engineering and functional electrical stimulation (FES) are emerging multi-disciplinary research areas aiming to develop therapeutic techniques for treating neurological disorders and restore impaired functions through neural augmentation and neuro-modulation. The progress of neuro-engineering relies primarily on recording electric activities of cortical tissues and neural clusters in the brain and requires simultaneous multisite long-term recording of neurons. The brain cortex provides access to motor and sensory perception and is an attractive region for neural interfacing to restore lost neurological functions. The small size and large population of neurons in the cortex region necessitates efficient multisite recording and stimulation with minimal tissue displacement and damage. This defines the objective of cortical electrode design to construct high channel density electrode arrays providing access to the cortical columns with minimal tissue damage and high positional accuracy.

Cortical electrodes can be classified into several groups based on different criteria, this guides in identifying the appropriate configuration required for different applications. Several electrode designs were proposed and technologies emerged in pursuit of reliable long-term recording and stimulation electrodes. New materials were introduced to fabricate different electrode elements, surface modification processes were applied to improve biocompatibility, and electrode geometry was experimented to minimize tissue trauma and displacement. Research is active to identify and explore the different parameters attributing to the design of implantable electrodes. Increasing the number of available channels brings in more challenges. A competent intra-cortical electrode should be designed to provide high recording channel count arranged in multi-dimensional array for the comprehensive visualization of neural interactions.

Chapter 3

Microelectrode Design Methodology

3.1 Introduction

The quest for advanced neuro-interfacing electrodes with improved functionality motivated the development of multi-shaft microelectrode arrays. Working with medical research groups revealed the need to create electrode arrays capable of providing tightly packed constellation of stimulation and recording pads to improve the positional accuracy and extend the electrode usability. This research introduced an ensemble of microelectrodes designed to fulfil various requirements and applications. Electrode development commenced with simple single shaft electrodes for design and fabrication processes development and optimization, and progressed into more complicated layouts and architectures. In the context of this dissertation, electrode layout refers to its geometrical design and can be recognized by its top view, while the electrode architecture defines its composition including the different layers and materials. The objective of the design methodology is to develop electrode layouts capable of maximizing the number of channels per shaft and minimizing the shaft width and the electrode footprint. The layouts would be implemented using architectures that would satisfy the mechanical and biomedical design constraints as well as microfabrication process rules. This chapter illustrates the electrode development through a sequence of layouts and architectures developed to satisfy different requirements and applications, and thorough mechanical analysis of the different designs is presented in Chapter 5.

3.2 Design Methodology

The design and implementation of reliable chronic electrode is a comprehensive process that integrates several domains. Electrode design flow is presented in Figure 3-1 and commences with identifying the design requirements and constraints to maintain reliable and safe operation. Design requirements identified application, anatomical position and interface duration; while the constraints included tissue properties, implant volume, mechanical requirements, electrical requirements and material toxicity. This information was acquired from experts in the field. Electrode layout design began with simple and abstract contours that complied with electrode size limitations dictated by the anatomic position, and pad requirements defined by the application.

The electrode shaft is implanted within the tissue to position the pads at the targeted location; consequently, it is a critical component which manipulates the design process. The shaft is a pad carrier, and it was required to minimize its size in order to reduce tissue trauma associated with implantation. It also had to provide the required structural strength to survive the mechanical forces experienced during implantation and operation. Complex architectures were developed to implement the required electrode layouts; these included multiple layer designs and stiffening metal layers. The preliminary electrode geometry was modeled to analyze its mechanical performance and identify the competent layouts. Mechanically challenged electrodes would required an insertion device which would aggravate tissue trauma, thus the electrodes presented in this research were designed to survive

implantation while having a small footprint to improve its biocompatibility. Fabrication processes were, and finally, the electrode were characterized and tested.

3.3 Design Guidelines

A competent intra-cortical interfacing electrode should satisfy the following guidelines [40][46][59][63][85][91][100]:

- Small footprint to minimize tissue trauma and displacement, and foreign body response
- Geometric surface area of recording pads less than $1000\mu\text{m}^2$ to record single unit action potential [90]
- Stimulation electrodes should have large pads to deliver the required charge and the electric structures should handle currents of up to 1mA
- Sampling cortical activities requires spatial recording site distribution of 50 to $100\mu\text{m}$
- Leads connecting the electrode to the supra-dural platform or percutaneous plug have to be flexible to relief the strain caused by brain motion
- Exposed materials must be biocompatible and have no water uptake if used in chronic applications
- Flexible electrode structures are preferred to brittle especially for chronic in vivo applications

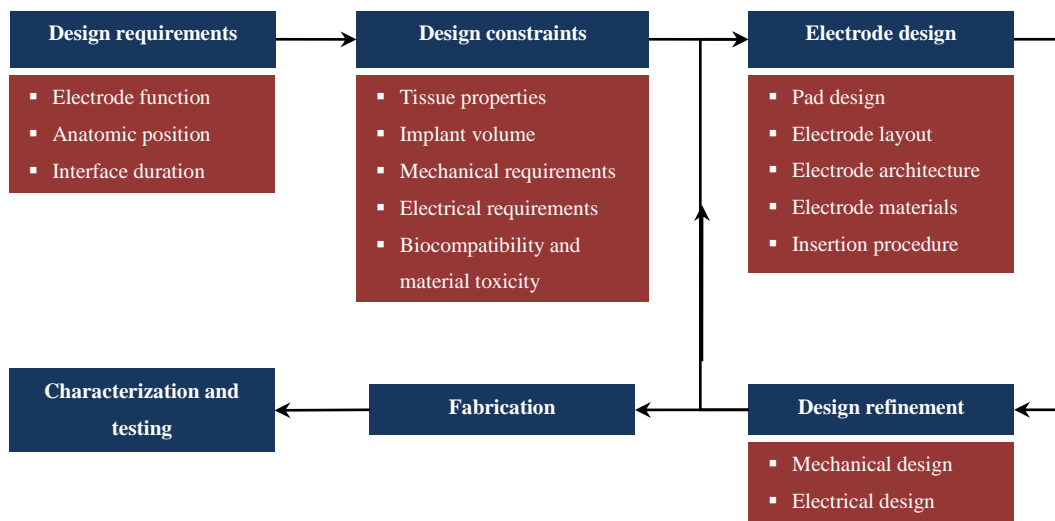


Figure 3-1. Electrode design process flow

3.4 Single Shaft Electrodes

Electrode development started with creating simple designs providing low number of interfacing channels. A single shaft electrode was designed to provide 4 recording channels on a narrow shaft (identified as Layout A) having a 6mm shaft with width of $110\mu\text{m}$. The electrode metallization layer was made of aluminum and coated with chrome and gold layers for adhesion and biocompatibility respectively. The electrode surface was passivated with silicon-oxide and $15\times 15\mu\text{m}$ windows were patterned to expose the $20\times 20\mu\text{m}$ electrode pads. The electrode width was expanded to accommodate 7 channels (Layout B) on a $200\mu\text{m}$ shaft. The electrodes were implemented on silicon-on-chip (SOI) wafer with $50\mu\text{m}$ device layer. The electrode layouts are shown in Figure 3-2 (Layout A) and Figure 3-3 (Layout B), and Figure 3-4 shows the exploded assembly of the electrode exhibiting the structural (grey), metallization (yellow) and passivation (amber) layers. This electrode was designed to develop and optimize the fabrication process for implementing further designs and its mechanical design was not optimized to withstand the insertion forces or maximize channel packing.

Dimensions of the simple recording electrode

- Recording pad: $20\times 20\mu\text{m}$, (exposed: $15\times 15\mu\text{m}$)
- Track width: $10\mu\text{m}$
- Track spacing: $10\mu\text{m}$
- Electrode length: 6.5mm
- Contact pad: $100\times 500\mu\text{m}$
- Shaft width: layout A: $110\mu\text{m}$, layout B: $200\mu\text{m}$



Figure 3-2. Basic simple recording electrode with 4 pads (Layout A)



Figure 3-3. Basic simple recording electrode layout with 7 pads (Layout B)

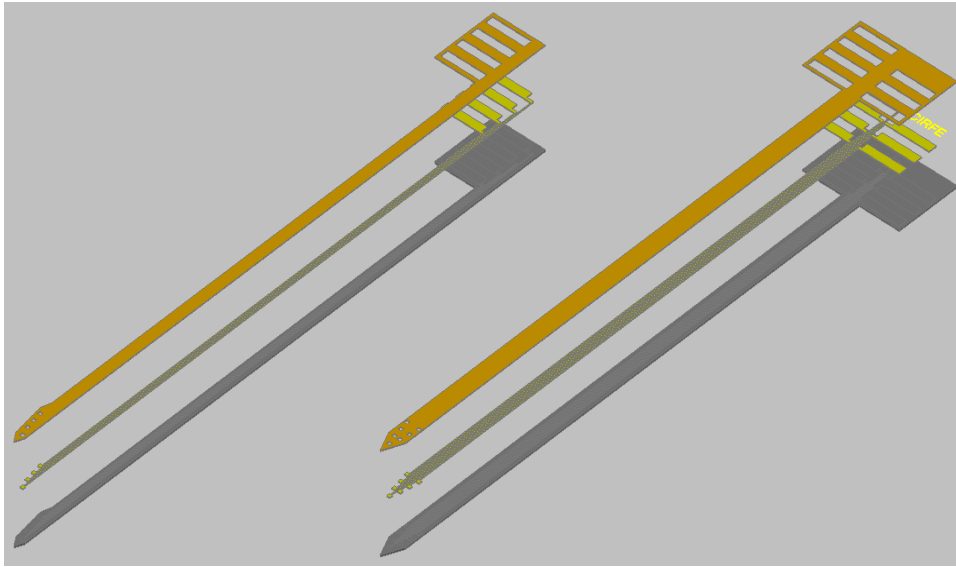


Figure 3-4. Exploded assembly of simple recording electrodes, Left: Layout A, Right: Layout B

3.5 Pad Geometry

Improving channel packing on some electrode shafts required modifying the pad geometry while maintaining its area to provide reliable electric performance. Several pad geometries were modeled and analyzed to investigate the current density distribution and resistance, and the different geometries included square, circular and triangular cross-sections. Half symmetric pad models were created and voltage was applied at the track base while the pad surface was grounded. Current density patterns associated with the different pad layouts are shown in Figure 3-5, and the results showed that the voltage drop was similar for different pad designs and the voltage gradient along a track and square pad is demonstrated in Figure 3-6. The results inferred that pad geometries had indistinguishable effect on the electric performance provided that the cross-section surface area was preserved.

3.6 Modified Pad Layout

Recording pad geometry was modified to achieve dense packing and reduce the shaft width. Figure 3-7 shows trapezoidal pads accommodated on narrow tapered shaft tip, and the pad dimensions preserved the surface area provided by the conventional recording pads. The modified pad layout allowed packing 6 channels on a 130 μm wide shaft, while the conventional pad design was limited to 7 channels per 200 μm as demonstrated in Figure 3-3, and a comparison between the electrode dimensions is listed in Table 3-1. The tapered tip facilitates electrode penetration and the shafts can be stacked alternatively as shown in Figure 3-8 to create a two dimensional array and reduce the lateral displacement during insertion for precise insertion.

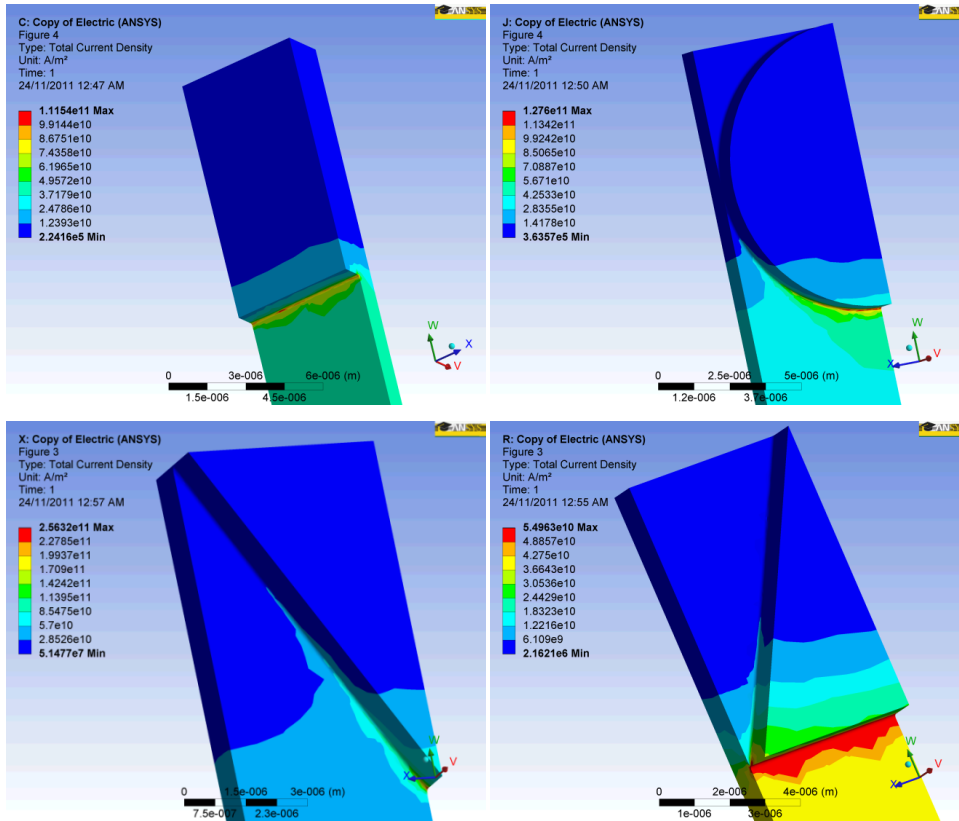


Figure 3-5. Current density distribution for different stimulation pad models

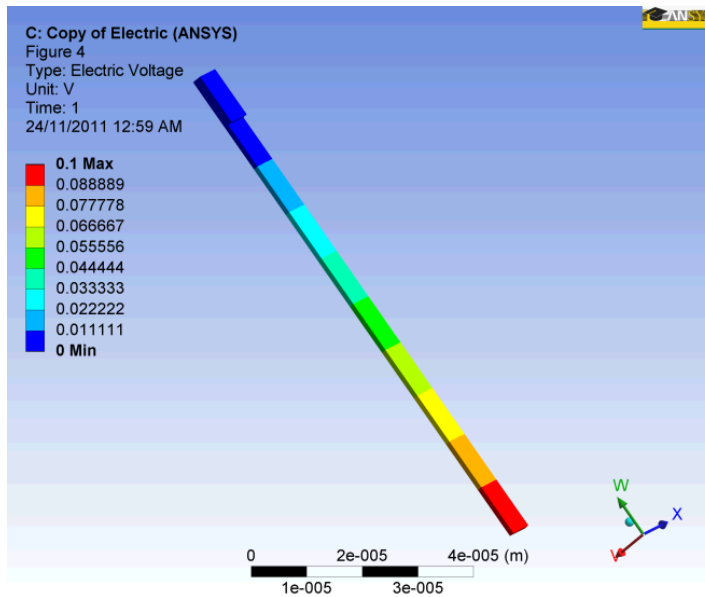


Figure 3-6. Voltage distribution

Table 3-1. Comparison between electrode dimensions

Layout	Conventional pads (B)	Modified pads
Channels	7	6
Recording pads	20x20 μm	Trapezium: 35 μm x 18 μm x 10 μm
Recording pads area	400 μm^2	420 μm^2
Track width	10 μm	10 μm
Track spacing	10 μm	10 μm
Shaft width	200 μm	130 μm



Figure 3-7. Modified trapezium recording pads on tapered shaft

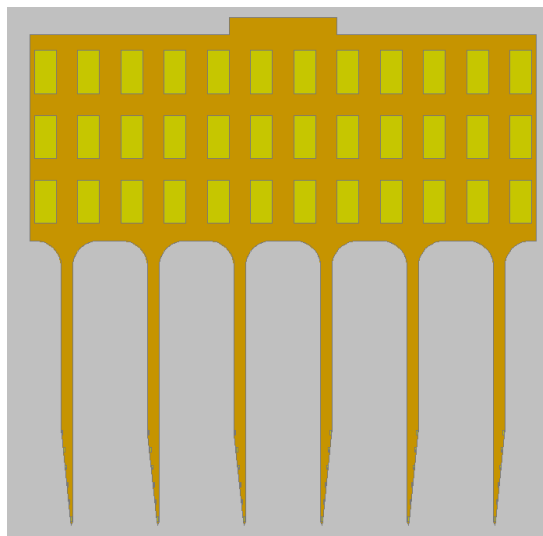


Figure 3-8. Electrode array with tapered alternating shafts

3.7 Double Metallization Layer Stimulation Electrodes

An electrode has two sets of pads; the interfacing pads come in contact with neurons, and the interconnect pads connect the electrode to external circuits, and each pad pair is connected by a routing track. Stimulation pads are characterized by having larger areas ($\sim 10,000\mu\text{m}^2$) compared to neural spike recording pads ($\sim 400\mu\text{m}^2$) to be able to deliver an electric charge that suffices stimulation, and this area constraint leads to low channel count for a given shaft width. The large stimulation pads can also be used for local field potential (LFP) recording from a cluster of neurons.

The functionality of stimulation electrodes can be improved through adding more channels; however, the number of channels per shaft is limited by the area of stimulation pads and electrode dimensions.

In conventional electrodes, the shafts accommodate the pads and tracks on a single layer offering limited channel packing. The routing tracks and pads share the shaft width as shown in Figure 3-9-Top; accordingly, the tracks can be considered an overhead which consume the available electrode surface. The minimum track width is controlled by the lithography process resolution, and reducing the width would raise its impedance. Stacking more tracks on a shaft would expand its width beyond the dimensions allowed by the biocompatibility requirements. In conclusion, the number of channels on a shaft is constrained by its width.

The double metallization layer stimulation electrode architecture introduced in this section was developed to increase the number of channels per shaft for a given set of electrode dimensions. This novel architecture comprises two metallization layers; the first accommodates the routing tracks and the second forms the exposed interconnect and stimulation pads. The two layers are electrically isolated by a dielectric film and the pads are connected to the associated tracks through buried vias. Figure 3-9 demonstrates a comparison between the conventional electrode and the proposed design with double metallization layers. The electrode layout is illustrated in Figure 3-10 showing the exposed pads, and Figure 3-11 demonstrates the two metallization layers superimposed to reveal the electrode internal structure. The introduced design has 3mm shaft with a width of $130\mu\text{m}$, and each stimulation pad is $110\times 110\mu\text{m}$. The electrode thickness is determined according to the material mechanical properties and electrode structural analysis discussed in Chapter 5.

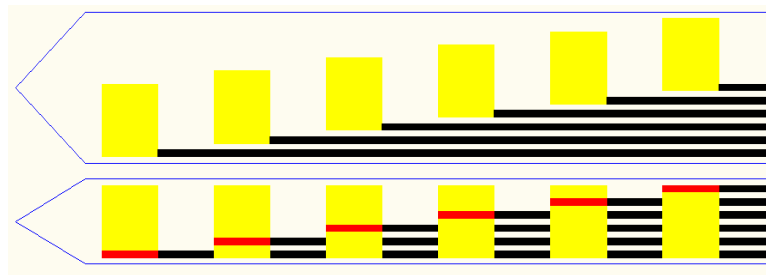


Figure 3-9. Comparison between conventional stimulation electrode layout (top) and the proposed architecture with double metallization layers (bottom)

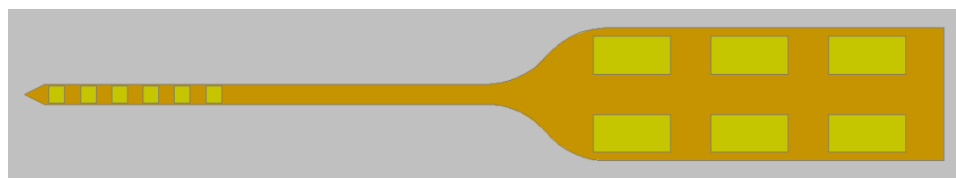


Figure 3-10. Electrode top view

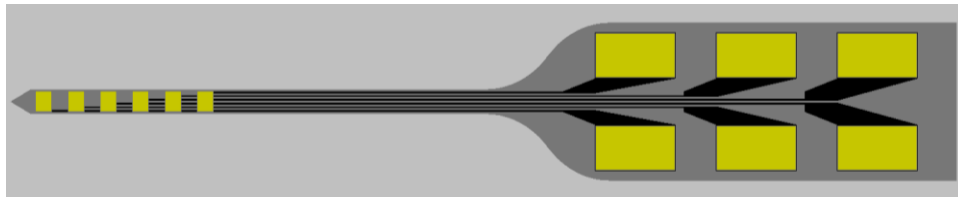


Figure 3-11. Top view showing the superimposed metallization layers, first metallization layer is shown in black and the exposed pads are in yellow

The electrode architecture is demonstrated in the exploded assembly diagram in Figure 3-12 showing the substrate (grey), the bottom first metallization layer (metal-1) forming the interconnect pads and tracks (yellow), the stimulation and interconnect pads reside in the top metallization layer (metal-2), while the buried vias (green) connects each pad to the associated track. A dielectric layer (red) insulates the metallization layers, and finally, the electrode is passivated with top a dielectric layer (amber). The sectional view (Figure 3-13) reveals the electrode anatomy demonstrating a portion of a stimulation pad (yellow) in contact with the associated track through the via (green). Figure 3-13-Left includes the dielectric insulation (red) and passivation (amber) layers, while the metal structure is shown in Figure 3-13-Right and the pad footprint is represented by the red contour. (US provisional patent 61/657,810 "Implantable Neuro-Interfacing Stimulation and/or Recording Electrodes with Multiple Metallization, Dielectric and Passivation Layers, and Multi-Dimensional Electrode Arrays ")

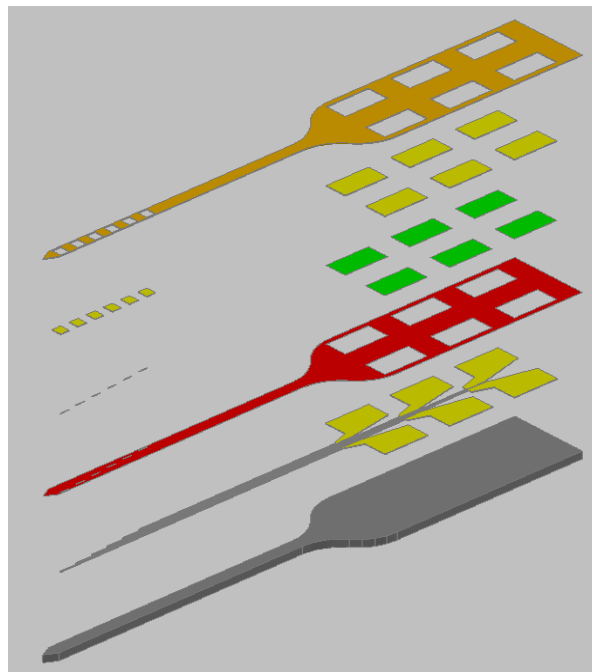


Figure 3-12. Exploded assembly view of the double metallization layer stimulation electrode

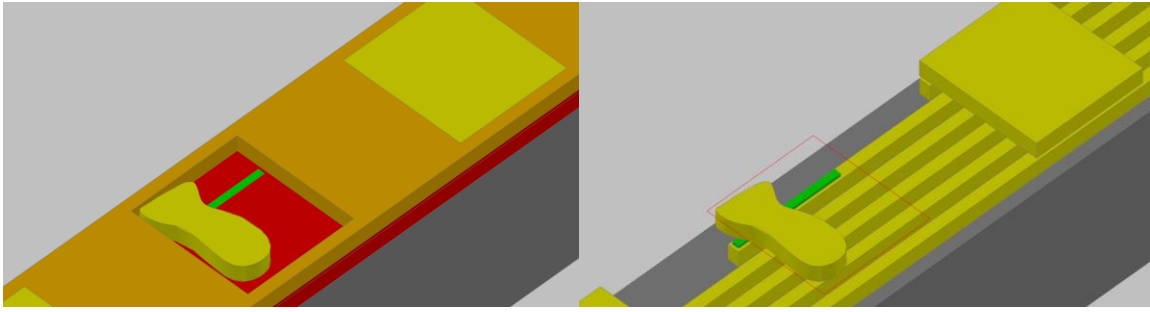


Figure 3-13. Sectional view of the stimulation electrode with (Left) and without (Right) insulation and passivation layers. The figure reveals the tracks in metal-2 layer (yellow), buried via (green), and part of the stimulation pad (yellow). The red contour (Right) represents the stimulation pad footprint.

Dimensions of the double metallization layer stimulation electrode

- Stimulation pad: 110x110 μ m
- Interconnect pad: 250x500 μ m
- Track width: 10 μ m
- Track pitch: 10 μ m
- Shaft length: 3mm
- Shaft width: 130 μ m
- Shaft pitch: 1mm

3.8 Modified Vias

The experimental results of the electrode DC resistance measurement (discussed in section 6.5.3) recommended that the electrical connection between the metallization layers had to be improved. The vias were expanded from 6x100 μ m to 30x100 μ m and redesigned to maintain dense channel packing. This modification enhanced the electrical connection between the metallic layers and achieved the anticipated resistance (calculated in section 3.10). The electrode shaft was altered to accommodate the modified vias and two modifications were proposed having a tapered (Figure 3-14) or stepped layout (Figure 3-15). The optimized single shaft electrode was used for creating multi-shaft arrays according to various design requirements and applications. One of the designs was customized for implantation in animal brain and its layout is shown in Figure 3-16. The quad shaft electrode had 3mm shafts providing a total of 24 stimulation channels.

Dimensions of the double metallization layer stimulation electrode – modified vias

- Stimulation pad: 110x110 μ m
- Interconnect pad: 250x500 μ m

- Track width: 10 μ m
- Track pitch: 10 μ m
- Shaft length: 3mm
- Shaft width: 130 μ m
- Shaft pitch: 1mm

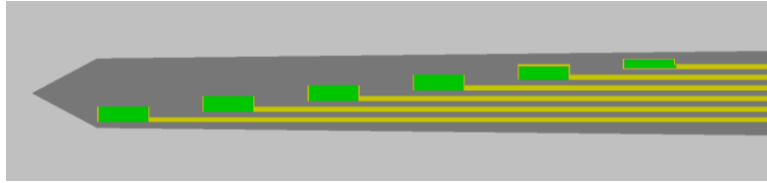


Figure 3-14. Double metallization layer stimulation electrode – Modified vias – Tapered shaft

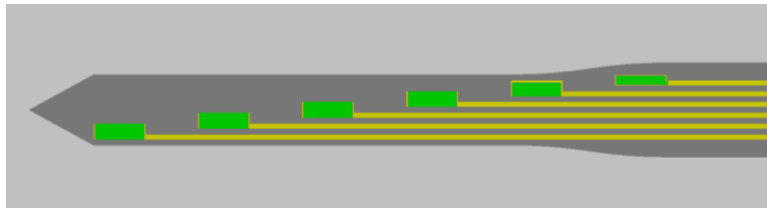


Figure 3-15. Double metallization layer stimulation electrode – Modified vias – Step shaft

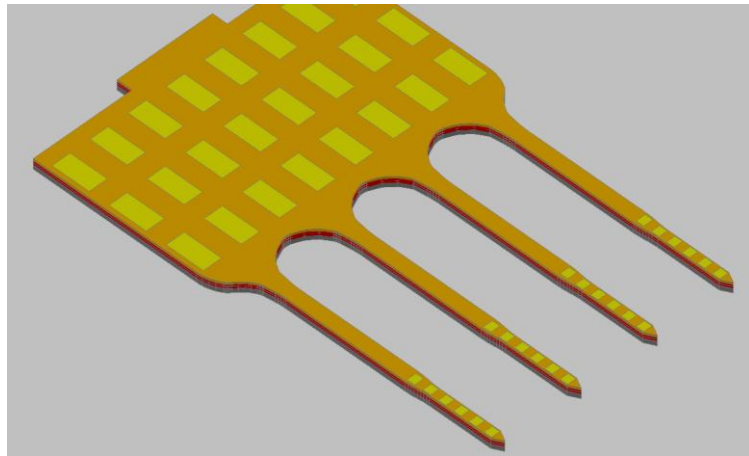


Figure 3-16. Double metallization layer stimulation electrode – Modified design – 4 shafts electrode array

3.9 Short Shaft Electrodes

The double metallization layer stimulation electrode architecture was used for developing a modified electrode with shorter shafts for small rodents. The electrode was designed to have two short shafts to fit within the tight dimensions of the rodents and maintain reliable contact. It was custom designed for the Rehabilitation Engineering Lab (REL) – University of Toronto.

3.10 Electrical Analysis and Design Optimization

Finite element modeling and analysis was used in estimating the electrode DC resistance and explore the effect of different design parameters on its value. The electrode metal structure was made up of routing tracks, stimulation pads, interconnect pads, and vias. Components with narrow cross-sections, e.g. routing tracks and stimulation pad vias, were anticipated to significantly contribute to the resistance. Figure 3-17 shows the metal structure model, and the components are illustrated in different colours. Unity voltage was applied to the interconnect pad and the surface of the stimulation pad was grounded. Current flow through the structure was calculated, and the resistance was estimated to be 70.94Ω , and was in good agreement with the experimental value (72Ω). Parametric model was created to manipulate several variables including dimensions, material types, and temperature. Component dimensions were varied to cover a range of practical fabrication values, and two temperatures were used representing ambient lab (20°C) and human body (37°C) conditions and the values of design parameters are listed in Table 3-2. The results were post processed and sensitivity analysis was executed to investigate the effect of different parameters on the resistance.

The effect of a short track (1mm) cross-section area on current flow is illustrated in Figure 3-18, and the results exhibited the dominance of track thickness in controlling the current flow. As the track length increased; it introduced higher resistance, and the influence of track thickness resided as shown in Figure 3-19 for 3.5mm shaft.

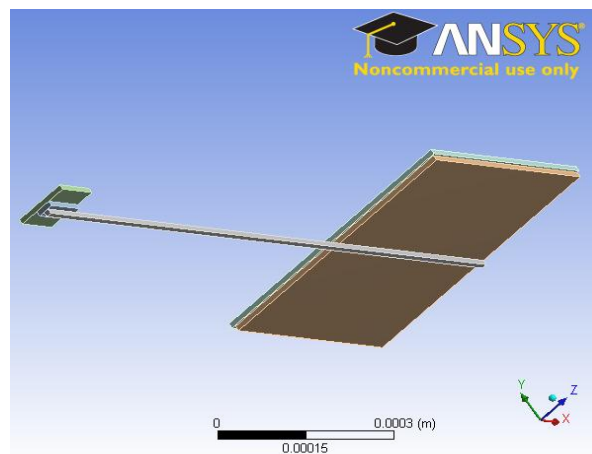


Figure 3-17. FEM model for the electrode metal structure

The effect of electrode dimensions on its resistance was verified by results post processing and sensitivity analysis. The histogram in Figure 3-20-Left illustrates the dominance of track length on the metal structure resistance, while track cross-section and via width exhibited moderate effect, and other parameters were negligible. The correlation matrix in Figure 3-20-Right confirmed the results showing that the track length acquired the highest correlation with current compared to other parameters. The stimulation circuit to be integrated with the electrodes produced a current of 1mA yielding voltage drop of 76mV across the electrode metallic structure. Accordingly, the unity voltage source in the simulation model was replaced by 76mV and the results reproduced the resistance values taking in consideration thermal effects modulating the resistivity.

Joule heating

Thermoelectric model was developed to estimate joule heating and the associated temperature rise generated by current flow in the metallic structure. The simulation was executed at 20°C and repeated at 37°C, and the resulting temperatures were 37.19°C and 20.84°C respectively. The sensitivity analyses results in Figure 3-21 showed that the track length was the effective parameter on temperature rise which was less than 1°C satisfying biocompatibility constraints.

Table 3-2. Parametric model variables

	Minimum		Maximum
Routing track length	1000μm		6000μm
Routing track width	1μm		10μm
Routing track thickness	300nm		1μm
Pad via width	2μm		30μm
Pad via length	50μm		100μm
Pad via thickness	50μm		100μm
Temperature (discrete)	20°C		37°C
Aluminum resistivity [Ω.m]	2.43e-8 @ 0°C	2.67e-8 @ 20°C	3.63e-8 @ 100°C
Gold resistivity [Ω.m]	2.051e-8 @ 0°C	2.214e-8 @ 20°C	2.87e-8 @ 100°C

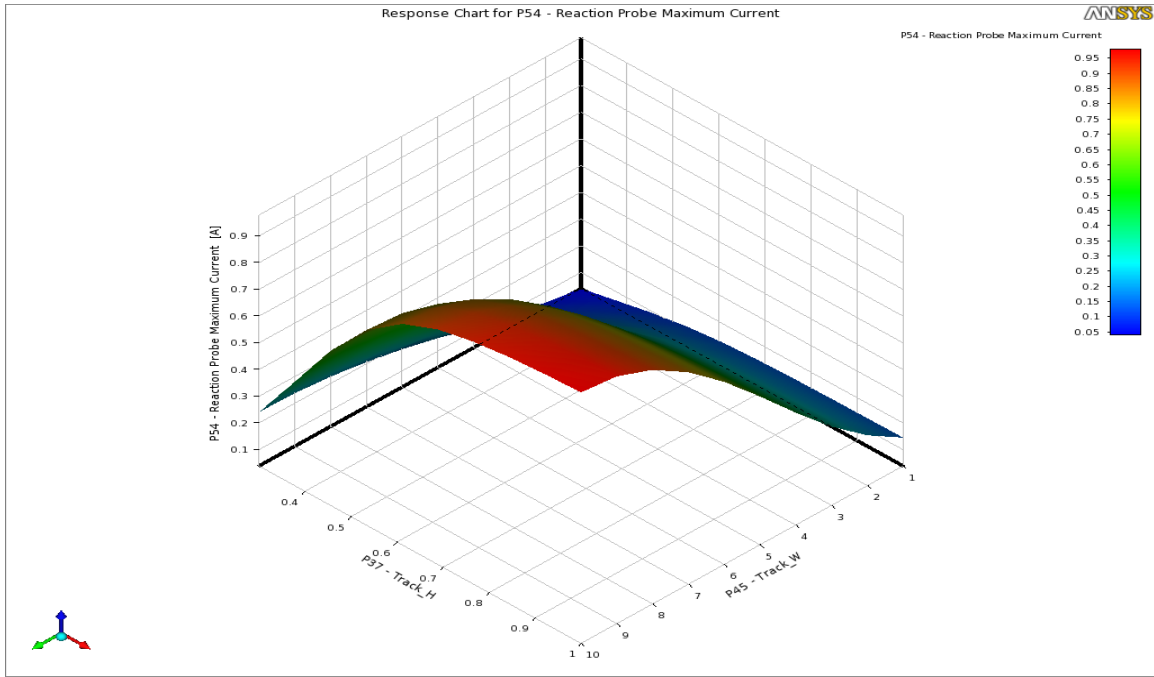


Figure 3-18. Sensitivity analysis: Current vs. track width and thickness for 1mm track

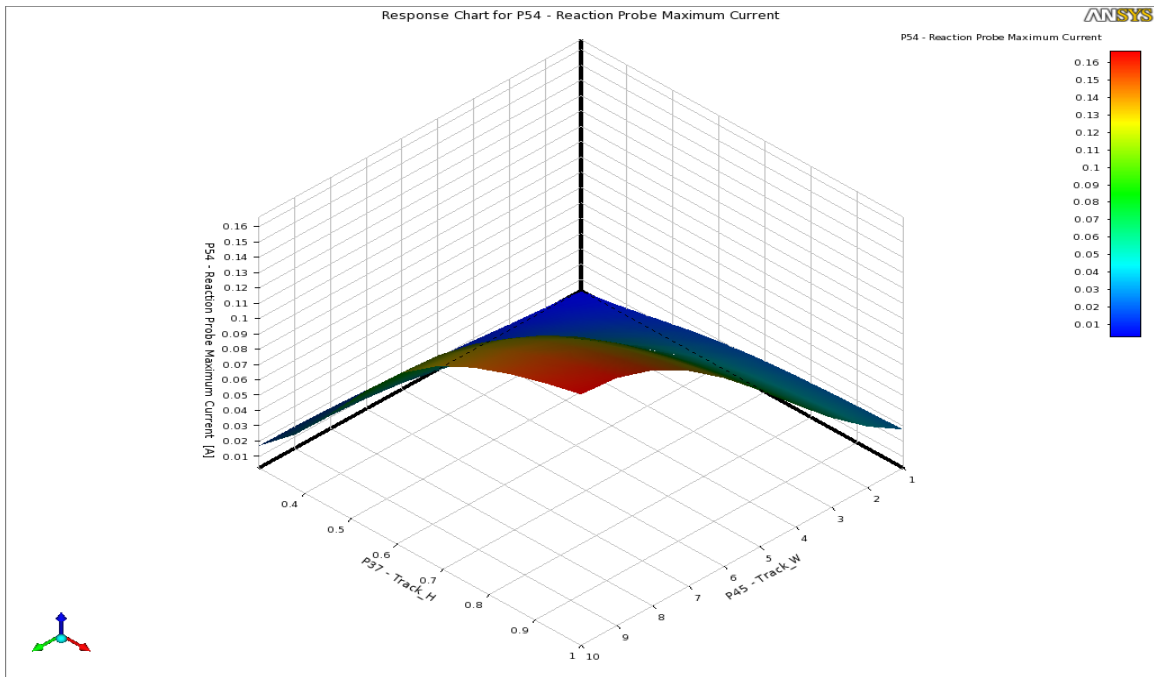


Figure 3-19. Sensitivity analysis: Current vs. track width and thickness for 3.5mm track

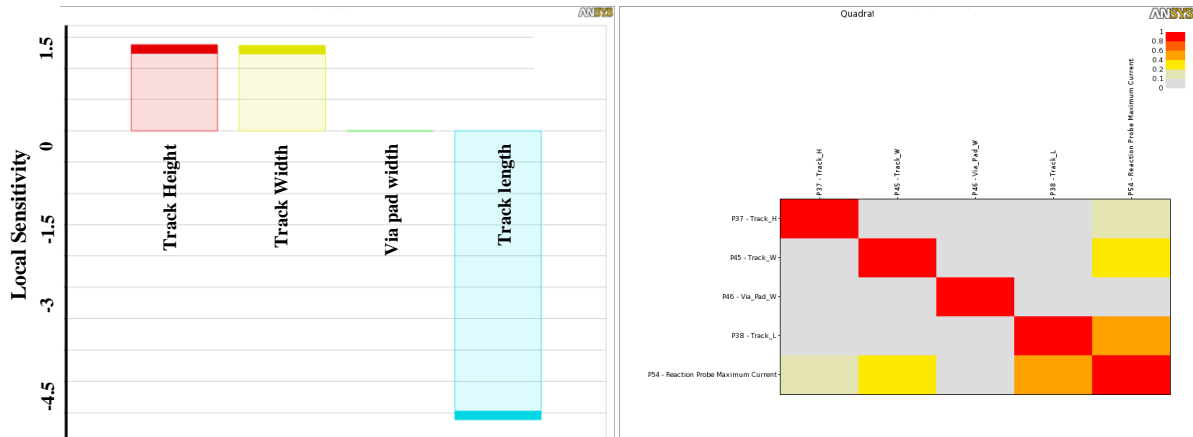


Figure 3-20. Post processing results, Left: Current sensitivity analysis of parametric model, Right: Correlation matrix of current vs. design parameters

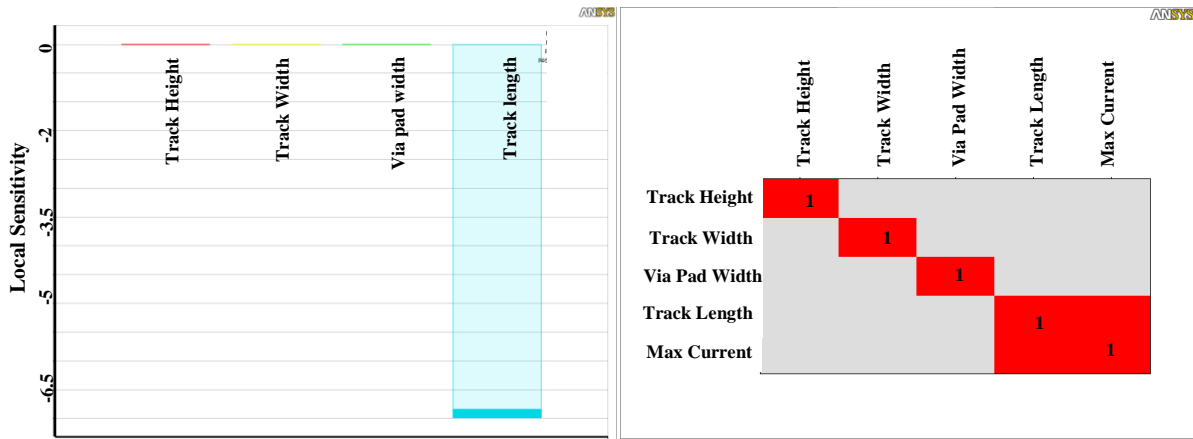


Figure 3-21. Joule heating post processing results, Left: Joule heating sensitivity analysis of parametric model, Right: Correlation matrix of Joule heating vs. design parameters

3.11 Recording/Stimulation Electrodes

Integrating recording and stimulation pads on a single shaft is required for several applications including simultaneous recording and stimulation and closed loop neuro-interfacing. It can also improve the spatial accuracy of electrode implantation by identifying the targeted spot through monitoring neural activity patterns during insertion (a standard procedure in DBS electrode implantation). A preliminary layout presented in Figure 3-22 was designed to provide 6 stimulation and 24 recording channels. The implemented electrode had 15 μ m tracks with spacing of 15 μ m yielding a shaft width of 1100 μ m. Squeezing the tracks and spacing to 10 μ m would shrink the electrode width down to 910 μ m which is beyond the design requirements.

Dimensions of the preliminary recording/stimulation electrode

- Recording pad: 22x22 μm
- Stimulation pad: 9500 μm^2
- Track width: 15 μm
- Track spacing: 15 μm
- Electrode length: 5.6mm
- Contact pad: 500x50 μm
- Shaft width: 1100 μm

Improved packing of stimulation and recording pads

A novel pad layout was developed to exploit area utilization and improve the tip design of stimulation/recording electrodes. Stimulation and recording pads were arranged in an alternating scheme along the edge of the shaft to allow forming a tapered tip and facilitate tissue penetration. The pads layout is shown in Figure 3-23 and was used in packing 8 stimulation and 9 recording pads along a tapered shaft. The demonstrated design had track width and spacing of 15 μm and a shaft width of 382 μm which dropped to 200 μm by reducing the routing tracks to 10 μm . (US provisional patent 61/405,195 "Multi-layer Intracortical Electrodes: Design Methodology, Layout Optimization and Fabrication Process".)

Dimensions of the improved recording/stimulation electrode

- Recording pad: 22x22 μm
- Stimulation pad: 11610 μm^2
- Track width: 15 μm
- Track spacing: 15 μm
- Electrode length: 5.6mm
- Contact pad: 500x50 μm
- Shaft width: 382 μm

3.12 Multi-Composite Layer Recording Electrodes

Tracks are considered an overhead which consume the available area on the electrode shaft, and the number of channels is limited by track width and spacing which makes the vertical space appealing for utilization. One approach to increase channel packing was through narrowing down tracks using a higher resolution photolithography process. This solution is not economical and also narrow tracks introduce higher electrical resistance and mechanical vulnerability. This design presents a multi-

composite layer electrode architecture which multiplies the channel count by exploiting the vertical space while keeping shaft width unchanged.

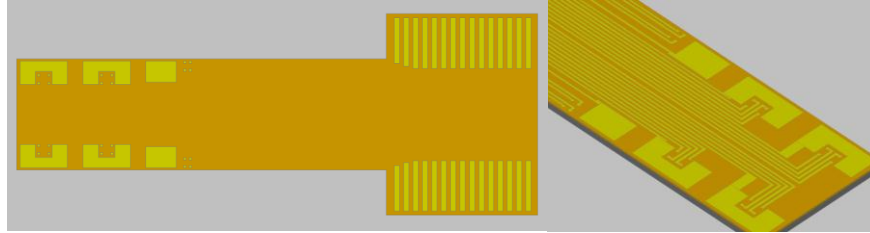


Figure 3-22. Preliminary layout of stimulation/recording electrode, Left: Electrode layout, Right: Pads and tracks

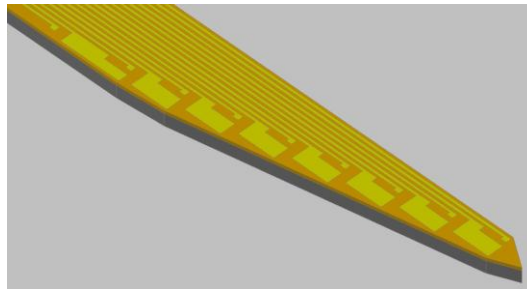


Figure 3-23. Stimulation/recording electrode with improved pad packing

The multi-composite layer electrode architecture was based on vertically stacking composite layers, where each layer accommodated a group of pads and tracks, thus increasing the number of channels without changing the electrode width. The stacked composite layers are made of thin films and do not contribute significantly to the shaft thickness. A composite layer consisted of a metallization film forming the tracks and pads, and dielectric coating to provide electrical insulation between the different composite layers, and a cross sectional layout is illustrated in Figure 3-24. The composite layers were formed to have descending lengths and create a stepped structure as shown in Figure 3-25. The stepped architecture exposes the pads on one layer without overlapping with others. The electrode tip was tapered to facilitate insertion and Figure 3-26 shows the electrode layout where the first, second and third metallization layers are represented in black, red and blue respectively. The total thickness of the composite layers was small compared to that of the electrode structural material and do not aggravate tissue trauma and displacement. The design methodology was employed to create different electrodes; Figure 3-27 and Figure 3-28 demonstrate layouts A and B providing 7 and 4 recording channels per layer respectively. It was also used to design multifunction electrode with recording and stimulation channels sharing the same shaft (Figure 3-29) adopting the pad packing scheme introduced in section 3.11 and outlined in Figure 3-23. Silicon was used as the structural layer for its mechanical strength and suitability for the multi-composite layer processing and the metal layers were made of aluminum and the exposed pads were coated with gold for biocompatibility. (US

provisional patent 61/405,195 "Multi-layer Intracortical Electrodes: Design Methodology, Layout Optimization and Fabrication Process")

Dimensions of the multi-composite layer recording electrode (Figure 3-27 and Figure 3-28)

- Recording pad: 20x20 μm , (exposed: 15x15 μm)
- Track width: 10 μm
- Track spacing: 10 μm
- Electrode length: 6.5mm
- Contact pad: 100x500 μm
- Shaft width: layout A: 110 μm , layout B: 200 μm



Figure 3-24. Cross sectional layout of a composite layer

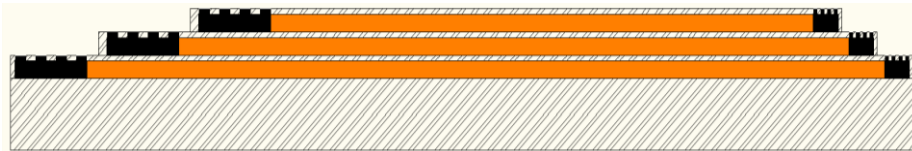


Figure 3-25. Three stacked composite layers

Modified multi-composite layer electrode layout

The mechanical design analysis recommended using the electrode layout shown in Figure 3-30 and the multi-composite layer electrode layout was modified accordingly. The patterned metallization layers are shown in Figure 3-31 in different colours. Pads (yellow) belonging to different layers vary in height to compensate for the difference in elevation with respect to the electrode substrate.

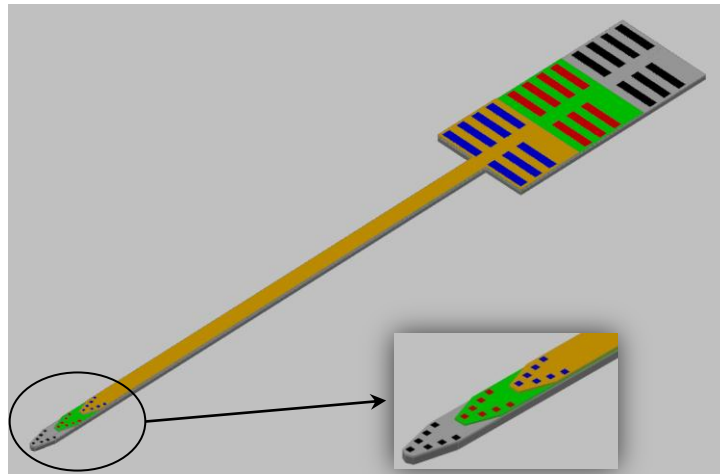


Figure 3-26. Multi-composite layer electrode layout



Figure 3-27. Multi-composite layer electrode, Layout A: 7 pads per layer



Figure 3-28. Multi-composite layer electrode, Layout B: 4 pads per layer

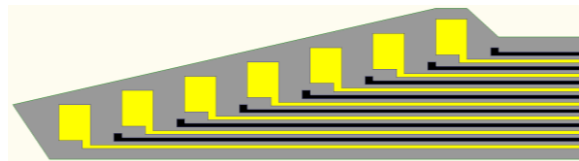


Figure 3-29. Pad layout for recording and stimulation

Dimensions of the multi-composite layer recording electrode – modified layout (Figure 3-30)

- Recording pad: 20x20 μm , (exposed: 15x15 μm)
- Track width and spacing: 10 μm
- Electrode length: 6.5mm
- Contact pad: 100x250 μm , (exposed: 80x230 μm)

- Shaft width: 170 μ m

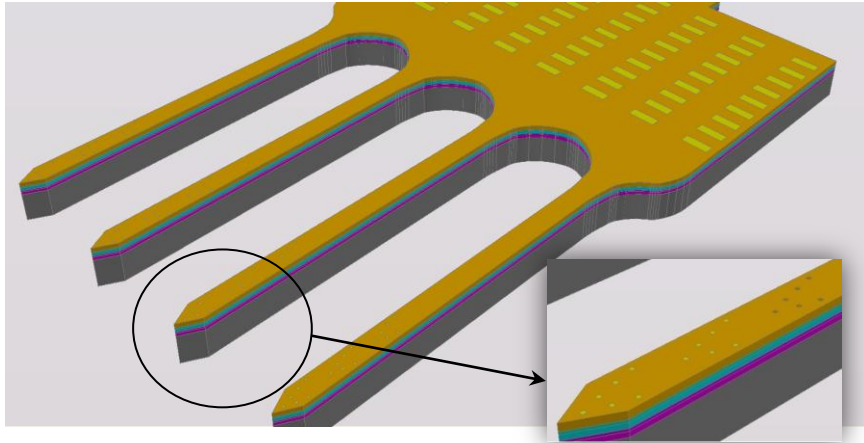


Figure 3-30. Multi-composite layer electrode with optimized mechanical design

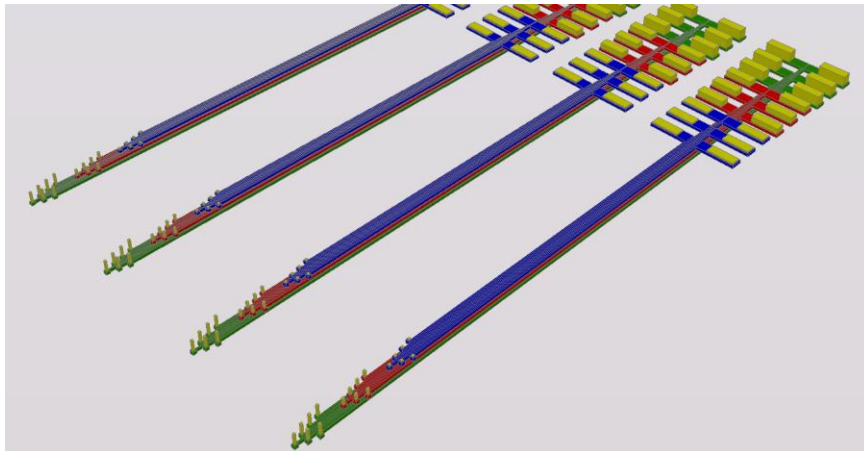


Figure 3-31. Multi-composite layer electrode with optimized mechanical design: Metallization layers

3.13 Carrier Wafers and Interconnect Cables

Carrier wafers

Carrier wafers were designed to facilitate electrode handling and coupling to external circuitry through the wide bases and large pads. The number and layout of pads were customized to accommodate different electrode designs, and two carrier wafers were implemented for application with multi-shaft electrodes. The first wafer was designed for the double shaft stimulation electrode introduced in section 3.9. The wafer layout is shown in Figure 3-32 with 12 interconnect pads and a groove to align the electrode. Other carrier wafers were created for the quad shaft electrode providing

24 interconnect pads, and one of the designs was customized to accommodate commercial connectors for example the Omnetics A79050 micro-cable pin header as shown in Figure 3-33. The carrier wafers can also be stacked to create 3-D electrode arrays as shown in Figure 3-34. Due to size limitations, this design would not fit in a rodent skull and was not implemented.

Interconnect cables

Due to small interconnect pad dimensions and tight spacing; it was not practical to attach individual lead wires to the pads. Flexible interconnect cables were custom designed for different electrodes and carrier wafers layouts and presented in Table 3-3. The pads on the cable have triangular layout, this facilitates bonding to the interconnect pads on the electrodes or carrier wafers using conductive glues (e.g. silver epoxy) as shown in Figure 3-35.

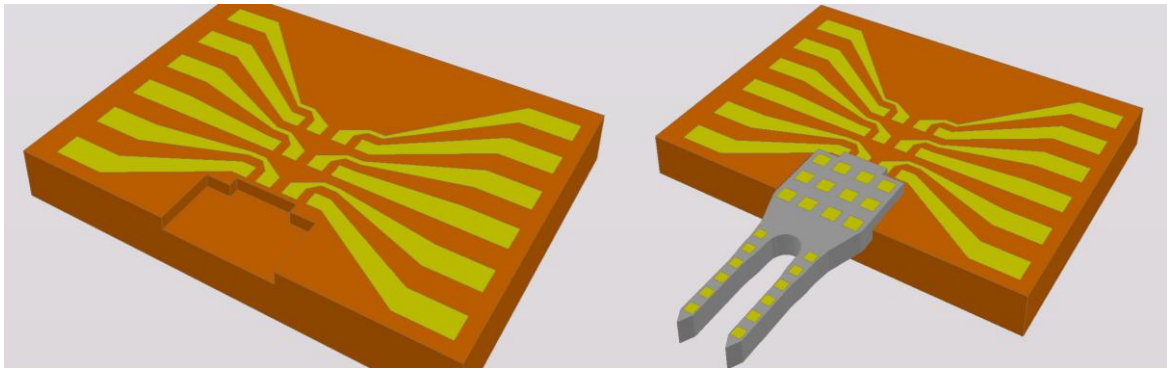


Figure 3-32. Carrier wafer for the two shaft double metallization layer stimulation electrode, Top: Carrier wafer with pads, tracks and alignment groove, Bottom: Carrier wafer and electrode assembly

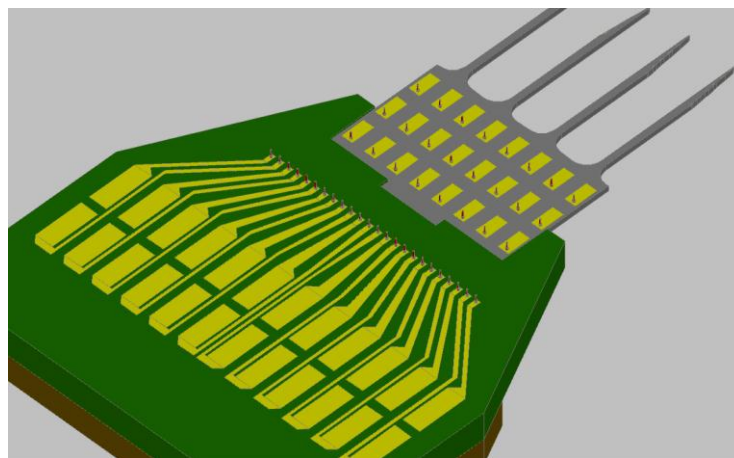


Figure 3-33. Carrier wafer for quad shaft electrode customized for Omnetics A79050 socket

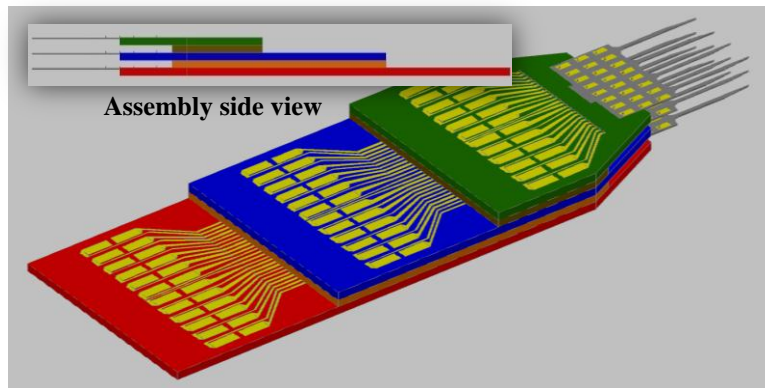


Figure 3-34. 3-D electrode assembly using carrier wafers

Table 3-3. Connector cables for electrodes and carrier wafers

Quad shaft electrode		
Dual shaft electrode carrier		

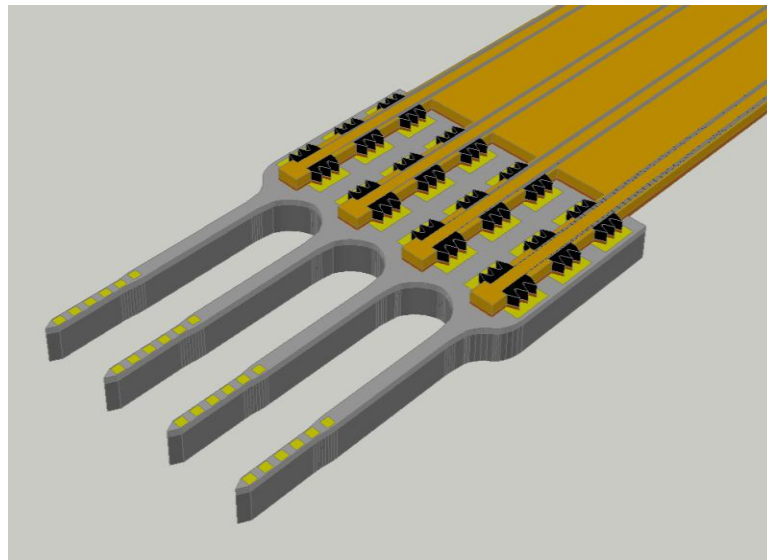
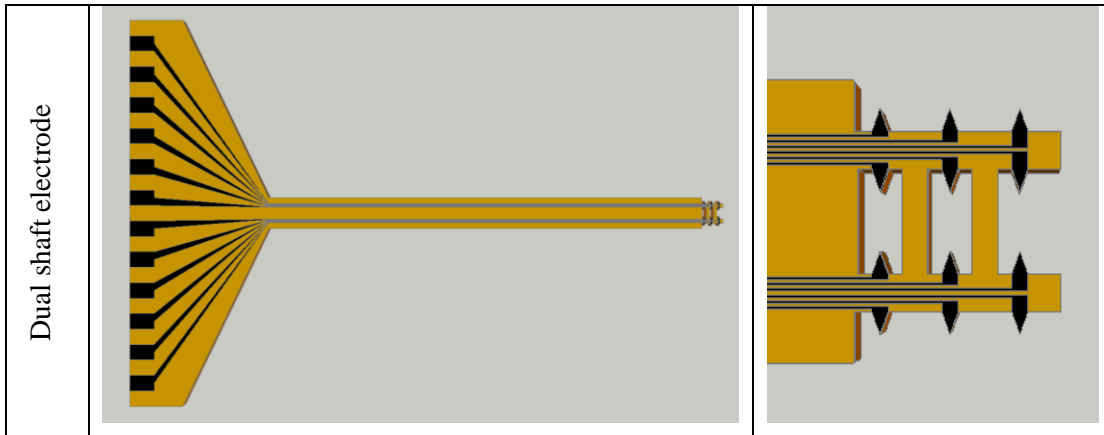


Figure 3-35. Electrode-cable assembly

3.14 Electrode with Integrated Cables for 3-D Assembly: The Waterloo Array

The double metallization layer stimulation electrode introduced in section 3.7 was expanded to include an integrated interconnect cable. This electrode was designed to be implemented on flexible substrates and provided two major advantages compared with the original design. The total electrode length was 2.5mm and waived the need for attaching separate interconnects cable, thus simplifying the assembly steps. Moreover, the electrode was designed for stacking using silicon carrier wafers to create the 3-D Waterloo Array as shown in Figure 3-36. The via design was modified to tolerate the flexible substrate expansion during fabrication and overcome misalignment, and the shaft layout is shown in Figure 3-37.

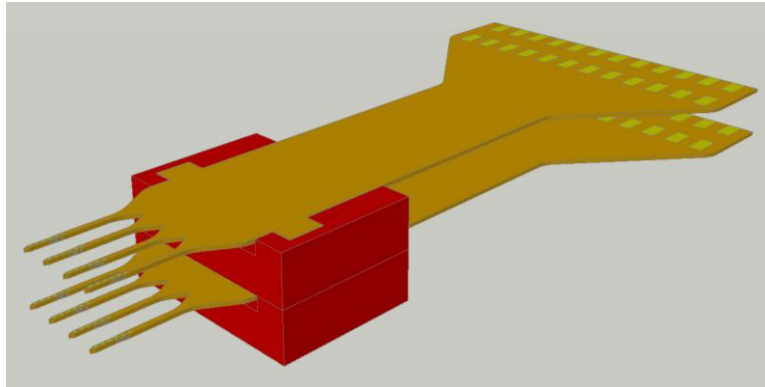


Figure 3-36. 3-D flexible electrodes stacked using silicon carrier wafers

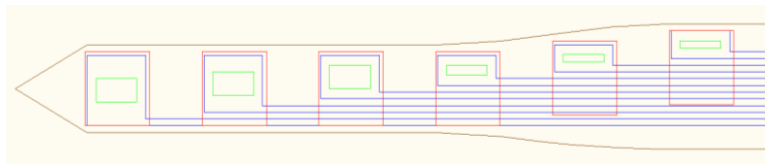


Figure 3-37. Flexible electrode shaft layout, Green: Buried vias, Blue: Routing tracks, Red: Exposed tracks, Brown: Electrode contour

3.15 Implantation Assistive Devices

A competent electrode design would have a flexible structure to conform to the tissue and acquire small footprint to reduce trauma, nevertheless, these features would compromise the rigidity required for tissue penetration. Assistive insertion techniques can be used to compensate the lack of rigidity during penetration and avoid mechanical failure. During penetration, the force is dispersed to the underlying tissue due to its elasticity, thus an initial rapid prick exploits the viscoelastic properties and confines the force within the tissue surface leading to rupture [31].

Implantation can be assisted chemically using collagenase enzymes to break up the collagen networks of the pia mater; this technique can reduce the required penetration force by 40% [189][190]. There are several mechanical assistive techniques, for example, attaching a stiffening backplane [205], or creating a hollow electrode structure to house a stylus. These approaches increase the electrode volume which is an undesired overhead that aggravates tissue trauma. Another technique involves coating the flexible electrode with biodegradable polymers to temporarily stiffen the probe shaft [206], and as the coating dissolves, it releases chemicals into the brain. The insertion technique adopted in this research was based on developing electrodes with a mechanical design that provides the required axial rigidity to survive penetration while maintain the flexibility to shear forces.

The electrodes introduced in this thesis were designed to survive the forces experienced during implantation. This allowed successful tissue penetration without the need for implantation apparatus

and avoid further tissue trauma. An implantation assistive device in the form of a block with a flange was designed to be used with more vulnerable electrodes. The flange rests on the brain surface to support the block, and the electrode slides along a trench as shown in Figure 3-38. This tool is designed to keep the electrode straight during insertion and supports it during propagation through the tissue to minimize the shaft effective length and avoid buckling failure.

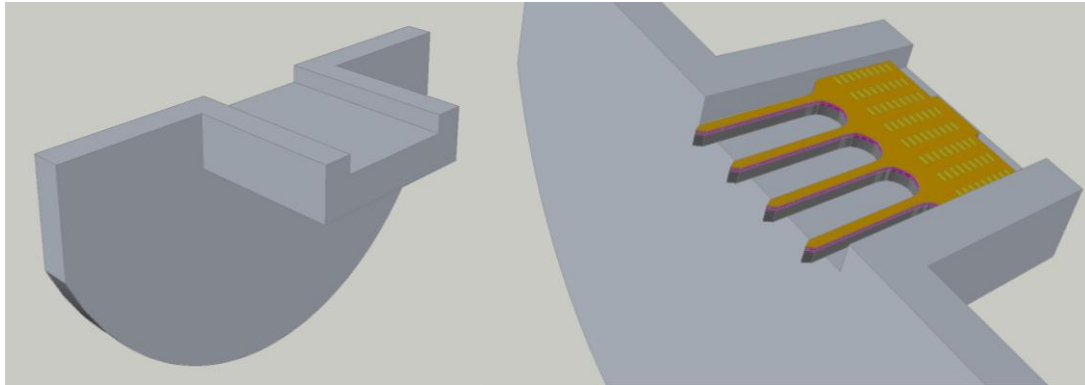


Figure 3-38. Implantation assistive device

3.16 Conclusion

This chapter introduced the intra-cortical microelectrode design methodology developed to benefit a wide range of design requirements and applications. The design guidelines and constraints were acquired from literature and experts in the field. The design methodology was employed in developing several electrodes customized for different recording and stimulation applications. An ensemble of microelectrodes was introduced and the discussion presented the progress of electrodes starting with simple single shaft designs which then evolved into more complicated designs, and finally concluded by the “Waterloo Array”. The discussion also introduced novel electrode architectures and modifications to increase the number of channels for stimulation as well recording electrodes while reduce the electrode footprint. Other designs and pad layout schemes were developed to increase the channel count on stimulation/recording electrodes while minimizing the shaft dimensions. Several components were also designed to facilitate the electrode handling and operation including carrier wafers, stacking wafers and interconnect cables.

The electrodes to be implemented were developed to satisfy the design requirements and constraints according to the application. The shaft layout used in the final implementation was qualified by the mechanical analysis as discussed in Chapter 5 and was designed for proper skin penetration without the need for implantation assistive devices. This helps to reduce tissue trauma and improve the electrode biocompatibility. Pad layouts and dimensions were designed according to the acquired design requirements as well as guidelines extracted from the electromagnetic modeling of the electrodes to be introduced in Chapter 4.

Chapter 4

Electromagnetic Analysis of Intra-Cortical Microelectrodes

4.1 Introduction

Electromagnetic modeling and analysis was used for investigating the influence of electrode design parameters and tissue properties on the electric field distribution within the brain tissue, study the effect of miniaturizing electrode dimensions, and explore methods of current steering. Finite difference time domain (FDTD) models were created and simulated using Empire XCcel 5.3 (IMST GmbH, Kamp-Lintfort Germany) [182]. Due to the lack of experimental data identifying the operation levels of the electric field intensities in the tissue, the Medtronic 3387 DBS electrode (Medtronic Inc, Minneapolis, MN) was modeled to provide reference benchmark data to be used for the microelectrode design.

Models for brain tissue (white and grey matters) representing the environment encompassing the electrode were created based on Gabriel model [152][153] assuming homogenous medium, and were further modified to heterogeneous tissue structure comprising white and grey matters. The electrode and tissue models were integrated to represent the implanted electrode and surrounding brain tissue. Several microelectrode designs were modeled to explore the effects of electrode and pads layout on electric field intensity distribution used in evaluating the volume of tissue activated (VTA). Finally, pad arrays were modeled to explore current steering. The analysis also studied the effect of integrated metal reinforcement planes on the electric field distribution within the brain tissue. Results verified ability of miniature microelectrodes to replicate electric field distribution generated by FDA approved and commercially available stimulation electrodes.

4.2 Modeling Medtronic 3387 DBS Electrode

The Medtronic 3387 DBS electrode was designed for chronic stimulation with no recording capabilities. It had a cylindrical core encapsulating wires feeding four equidistant platinum rings which represent the stimulation pads on the electrode perimeter. The electrode shaft was 1.28mm in diameter and each ring had a length and thickness of 0.5mm and 0.08mm respectively as shown in Figure 4-1. It is FDA approved and was modeled to provide reference data for the field intensity and distribution within the brain tissue to be used for designing intra-cortical electrodes. The Medtronic 3387 had macro sized ring pads and an alternative model with planar pads was developed to evaluate and verify the field distribution of planar pads. The planar pads model was further modified into a miniature layout to model microelectrodes and this model was employed in the analysis of the intra-cortical microelectrodes. The Medtronic 3387 electrode model is shown in Figure 4-2 and perfect geometric approximation (PGA) algorithm was used to model the circular features of the electrode [182][187]. PGA allowed modeling the dome tip and it avoids yielding very high dense discretization mesh and consuming memory resources [185]. The electrode was made of polyurethane and modeled to have relative permittivity $\epsilon_r = 4.3$ and tangent delta $\delta = 4 \times 10^{-3}$. The contact rings were platinum with conductivity $\sigma = 9.3 \times 10^6 \text{S.m}^{-1}$. The knowledge elicited from the simulation results provided:

- Reference benchmark data from FDA approved DBS electrode
- Guidelines for the design and development of DBS and intra-cortical electrodes as well as optimizing electrode design and pad geometry and layout
- Data required to evaluate the volume of tissue activated (VTA) by stimulation
- Simulations for current steering methods

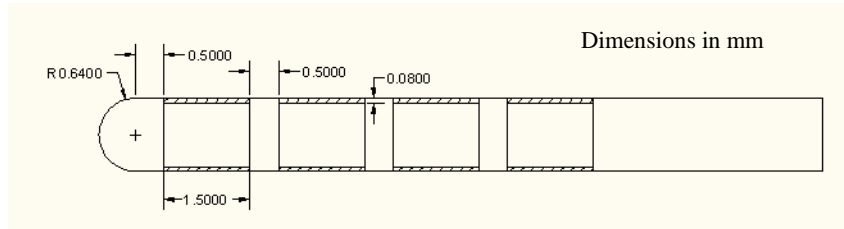


Figure 4-1. Medtronic 3387 DBS electrode layout

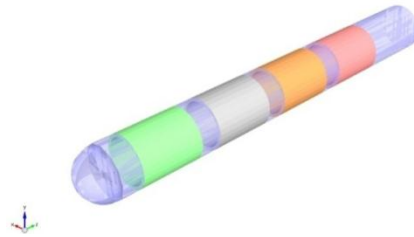


Figure 4-2. Medtronic 3387 DBS electrode simulation model

4.3 Brain Tissue Modeling

Brain tissue represents the ambient medium in which the electrode is implanted and its dielectric properties affect the electric field distribution within tissue and influence the neurons responses to external applied electric fields produced by stimulation. Referring to DBS; the electrode resides in the internal globus pallidus (GPi) or subthalamic nucleus (STN) located in the basal ganglia which is composed of grey matter (relative permittivity $\epsilon_r = 2.46 \times 10^6$ and conductivity $\sigma = 0.16329 \text{ S.m}^{-1}$ at 130Hz [184]), surrounded by white matter (relative permittivity $\epsilon_r = 1.06904 \times 10^6$ and conductivity $\sigma = 0.059 \text{ S.m}^{-1}$ [184]). As a result of foreign body reaction (refer to section 2.4.5 and Appendix B), the electrode was encapsulated by unexcitable tissue with a mean conductivity of 0.1 S.m^{-1} ranging between 0.05 to 0.2 S.m^{-1} [155][188].

To investigate the effect of different tissue layers and dielectric properties on the field distribution, several tissue models with different complexities and levels of detail were developed [187]. Brain tissue was modeled with three levels of complexity: Model-I was a simple representation of brain gray tissue as a homogenous lossy dielectric with isotropic and frequency independent

characteristics disregarding the anatomical details of the brain [128][145]. However, the homogenous brain tissue model limited the results accuracy due to ignoring biophysical based conductivities [147]. Model-II included the encapsulation tissue layer with permittivity similar to grey tissue ($\epsilon_r = 5 \times 10^4$) and a lower conductivity ($\sigma = 0.1 \text{ S.m}^{-1}$). Model-III comprised two layers representing the gray ($\epsilon_{r\text{-Gray}} = 1 \times 10^5$, $\sigma_{\text{Gray}} = 0.1 \text{ S.m}^{-1}$) and white tissue ($\epsilon_{r\text{-White}} = 2 \times 10^4$, $\sigma_{\text{White}} = 0.1 \text{ S.m}^{-1}$).

Several models were proposed in [128][147] assuming homogeneous tissue structure and included fixed thickness encapsulation of 0.5mm. The encapsulation layer thickness varies from 0.1 to 1mm [155] depending on the electrode material biocompatibility and implant duration. To investigate the effect of encapsulation layer thickness on field distribution, a comprehensive model with inhomogeneous layers and variable thickness encapsulation layer was developed. The results exhibited the effect of encapsulation layer on the electric field intensity and distribution which accordingly controlled the spatial penetration of the electric field. Table 4-1 lists the average low frequency conductivity values used in modeling brain tissue as extracted from literature. More information about the biological tissue dielectric properties, modeling and dispersion modes is provided in Appendix B.

Table 4-1. Mean values for brain tissue conductivity

Tissue	σ [S.m^{-1}]	Reference
Bulk neural tissue (average value)	0.2	Buston et al [128][155][188]
encapsulation layer (0.5mm thick)	0.1	Buston et al [155][188]
encapsulation layer (0 – 1 thick)	0.05 – 0.2	Grill and Mortimer (2004) [155][188]
White matter	0.15	Geddes and Baker, Malmivuo and Plonsey [155][188]
Grey matter	0.45	Geddes and Baker, Malmivuo and Plonsey [155][188]
Grey matter	0.28	Sotiropoulos [156]
Internal capsule (IC) along primary fibre direction	1.17	Sotiropoulos [156]
Internal capsule (IC) along orthogonal axis	0.125	Sotiropoulos [156]
Average head conductivity	0.33	[157][158]
Grey matter	0.1	Gabriel [152], Nicholson [159] Apollonio [160][161]
Internal capsule (IC) along primary fibre direction	1	Gabriel [152], Nicholson [159] Apollonio [160]
Internal capsule (IC) along orthogonal axis	0.1	Gabriel [152], Nicholson [159]

4.4 Simulation Setup and Stimulation Pulses

DBS pattern is a sequence of cathodic monophasic rectangular pulses with amplitude ranging between 1 and 4 volts and can reach up to 10 volts [2]. Stimulation pulses have a period of $0.1\mu\text{s}$ and the firing frequency is 130Hz [128][129][156][162] which classifies the simulation procedure as quasistatic electric field simulation. Simulations were executed using two sets of stimulation patterns; Gaussian (Figure 4-3-Left) and cathodic monophasic rectangular (Figure 4-3-Right) pulses. Unlike rectangular pulses, Gaussian pulse does not have sharp transients in the time domain and is preferred for FDTD modeling. Simulations were iterated using several data sets and the Gaussian pulses underestimated the electric field intensity by 0.27 to 2.7% [187]. The purpose of the calibration was to explore the effect of simulator configuration on the results accuracy and model stability.

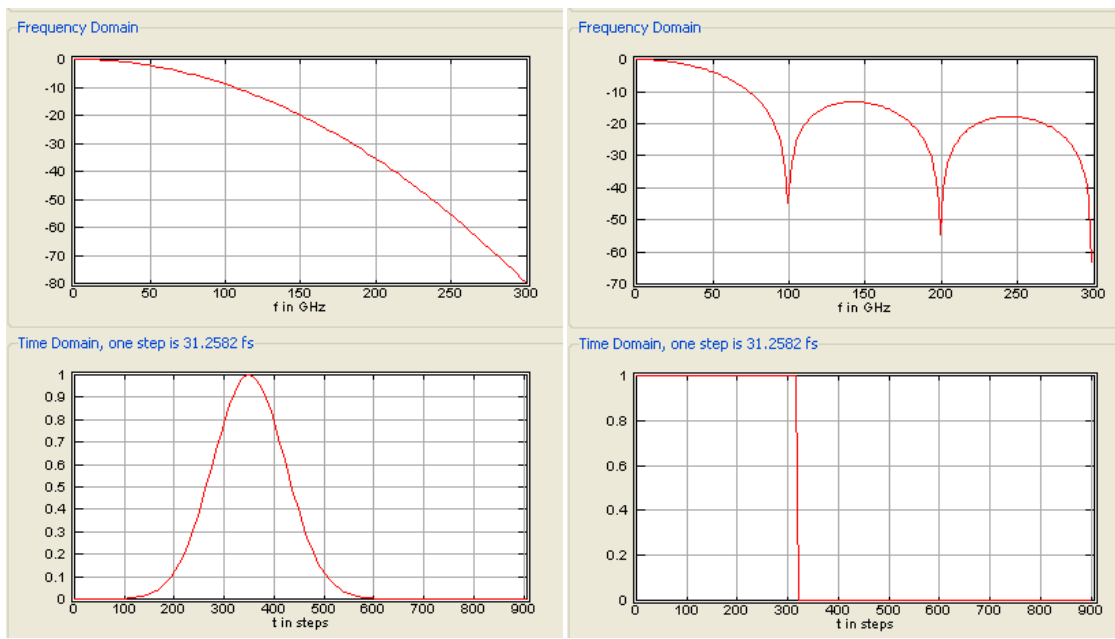


Figure 4-3. Stimulation patterns, Left: Normalized Gaussian pulse, Right: Normalized anodic monophasic rectangular pulse ($t, 0, 1e-11$)

The electric field distribution for Gaussian pulse simulation with brain tissue conductivity of $0.3\text{S}\cdot\text{m}^{-1}$ is shown in Figure 4-4. The simulation results for very fine-4 meshing density are represented in Figure 4-5 listing the maximum and minimum electric field values.

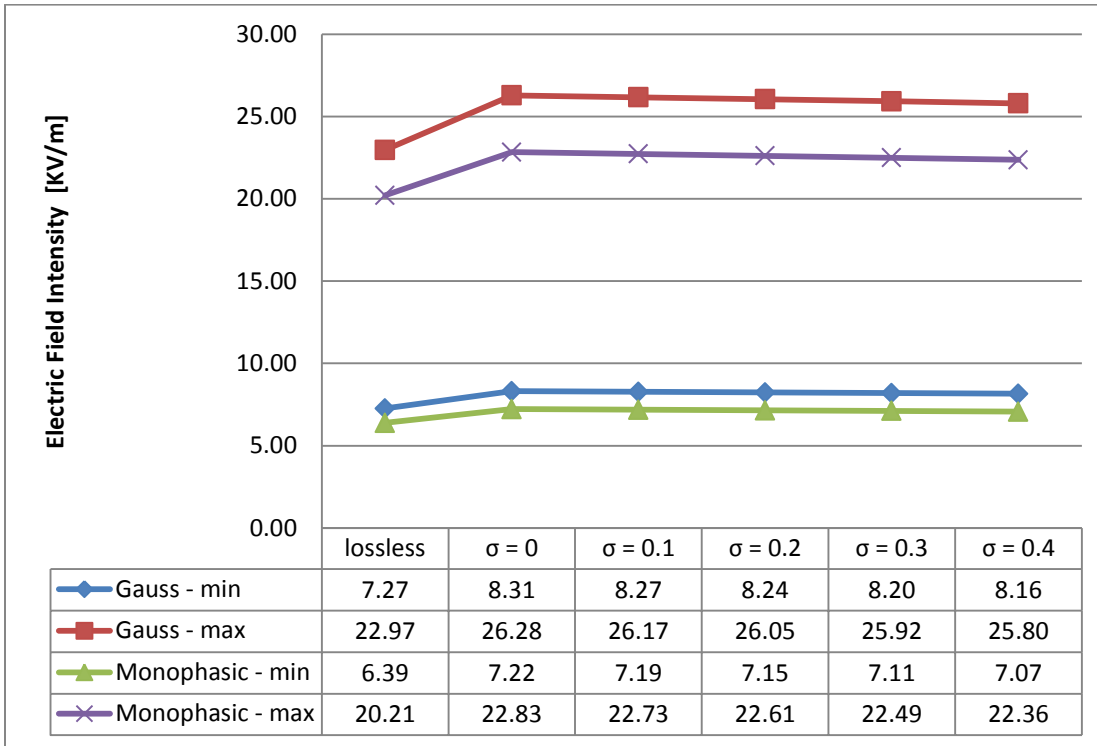


Figure 4-4. Simulation results for Gaussian and monophasic pulses with very fine-4 meshing

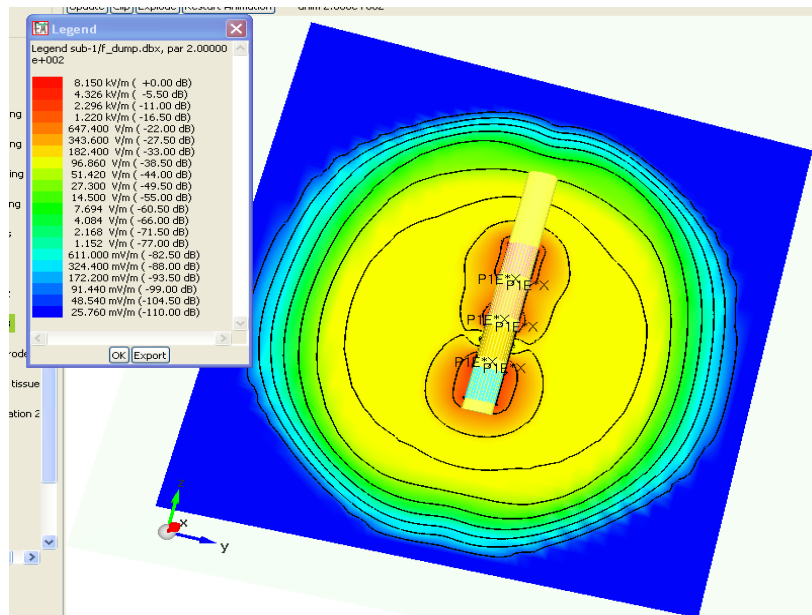


Figure 4-5. Electric field distribution of Gaussian pulse stimulation @ $\sigma = 0.3\text{S.m}^{-1}$

4.5 Simulation Results

4.5.1 Stimulation pulse parameters

Pulse amplitude and width

The stimulation pulse had two degrees of freedom; amplitude and width. These two parameters were varied to study the effect of pulse characteristics on field distribution. Model-I with single homogenous tissue layer was used and the simulation was iterated for two different values of relative permittivity (1×10^4 and 1×10^5) and conductivity $\sigma = 0.15 \text{S.m}^{-1}$. Sweeping the pulse amplitude (A) from 1 to 10 had no effect on the depth of field penetration within the tissue while directly affected the levels of field intensity which is shown in Figure 4-6. The results were modeled using a linear relationship with a minimum RMSE = 18.2 and 5.88 for $\epsilon_r = 1 \times 10^4$ and $\epsilon_r = 1 \times 10^5$ respectively (equation 3.1 and equation 3.2), and $R^2 = 99.8\%$ and the extracted model equation is plotted in Figure 4-6.

$$@\epsilon_r = 1 \times 10^4 \rightarrow E_{\max}(A) = 162 * A \quad \dots (3.1)$$

$$@\epsilon_r = 1 \times 10^5 \rightarrow E_{\max}(A) = 53 * A \quad \dots (3.2)$$

The results showed the dominance of pulse amplitude on the field intensity at lower tissue permittivity, and where the slope at $\epsilon_r = 1 \times 10^4$ is almost 3 times that of $\epsilon_r = 1 \times 10^5$.

To study the effect of pulse width on the electric field distribution, a constant amplitude pulse of 5V and width (PW) varying from 52 to 52000 steps (time step is set to 0.5psec due to computational limitations) was defined for the stimulation pattern using Model-I with $\epsilon_r = 1 \times 10^5$ and $\sigma = 0.15 \text{S.m}^{-1}$. It was found that the electric field spatial depth was controlled by changing the simulation pulse width rather than its amplitude (top left corner of Figure 4-7 represents the effect of pulse width on field distribution for 52 and 52000 steps respectively). Accordingly, the amplitude of the stimulation current injected can be reduced by increasing the pulse width to obtain the same effect on the spatial distribution of the electric field. The results were represented by a power relation (equation 3.3) with RMSE = 131 and $R^2 = 98\%$ and plotted in Figure 4-7.

$$E_{\max}(W) = 21.6(\text{PW})^{0.4} \quad \dots (3.3)$$

Firing Pattern

In order to improve the effectiveness of DBS it was required to enhance the spatial precision of charge delivery and minimize the risk of undesired stimulation of non-targeted regions. Current steering mechanisms can be employed to control spatial distribution of the electric field within the brain tissue [127]. Several parameters can be manipulated to achieve current steering and electric field shaping; these include contacts shape and distribution, stimulation pulse waveform and tissue dielectric properties.

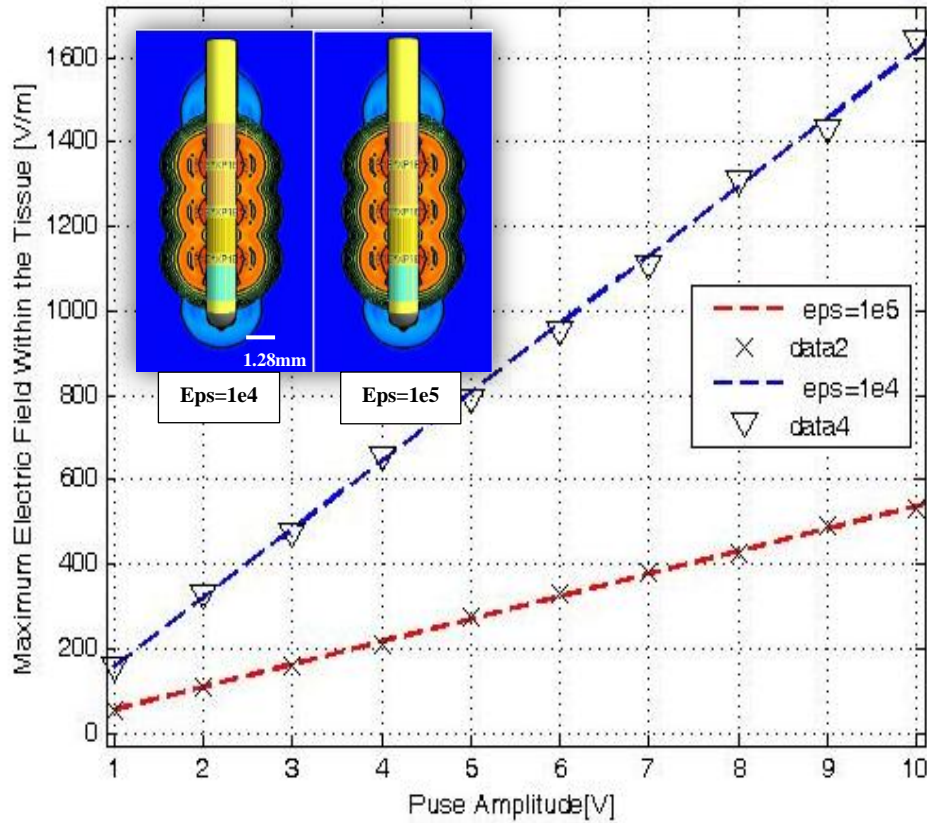


Figure 4-6. Electric field intensity vs. simulation pulse amplitude (A) for $\epsilon_r = 1 \times 10^4$ and 1×10^5 @ $\sigma = 0.15 \text{ S.m}^{-1}$

To investigate the influence of current steering on sculpting the electric field, a variable firing pattern was applied as differential a current between contact ring pairs. Constant current source was modeled for stimulation, and the ratio between the differential current components applied between the rings was controlled to yield different ratios. Homogenous single layer model was assumed ($\epsilon_r = 1 \times 10^5$, $\sigma = 0.15 \text{ S.m}^{-1}$) and the electric field distribution for different firing patterns is plotted in Figure 4-8. The results illustrated the ability of controlling the electric field distribution by using a simple array of firing rings and manipulate the ratio between current components between ring pairs. It is possible to shape the electric field distribution within the brain tissue by changing the stimulation pattern as well as the pads distribution. However, ring pads are not suitable for delivering charges with appropriate spatial accuracy and prevent undesired stimulation of non-targeted neurons. Figure 4-9 shows the maximum electric field versus current steering ratio for conductivity $\sigma = 0.15 \text{ S.m}^{-1}$ and different permittivities ($\epsilon_r = 1 \times 10^4$ and $\epsilon_r = 1 \times 10^5$).

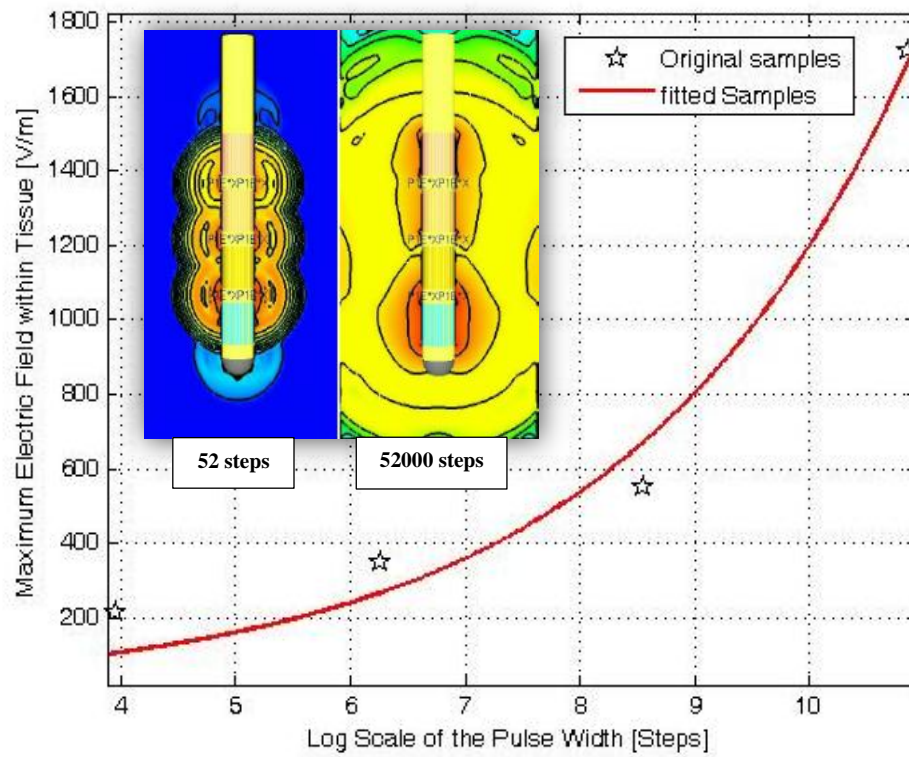


Figure 4-7. Electric field intensity vs. simulation pulse width @ $\epsilon_r = 1 \times 10^5$ and $\sigma = 0.15 \text{ S.m}^{-1}$

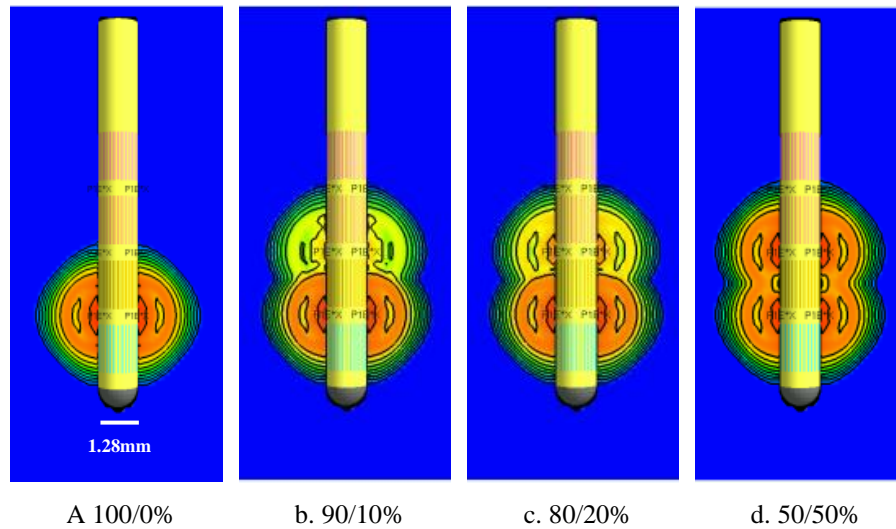


Figure 4-8. Current steering and field shaping for 2 rings firing

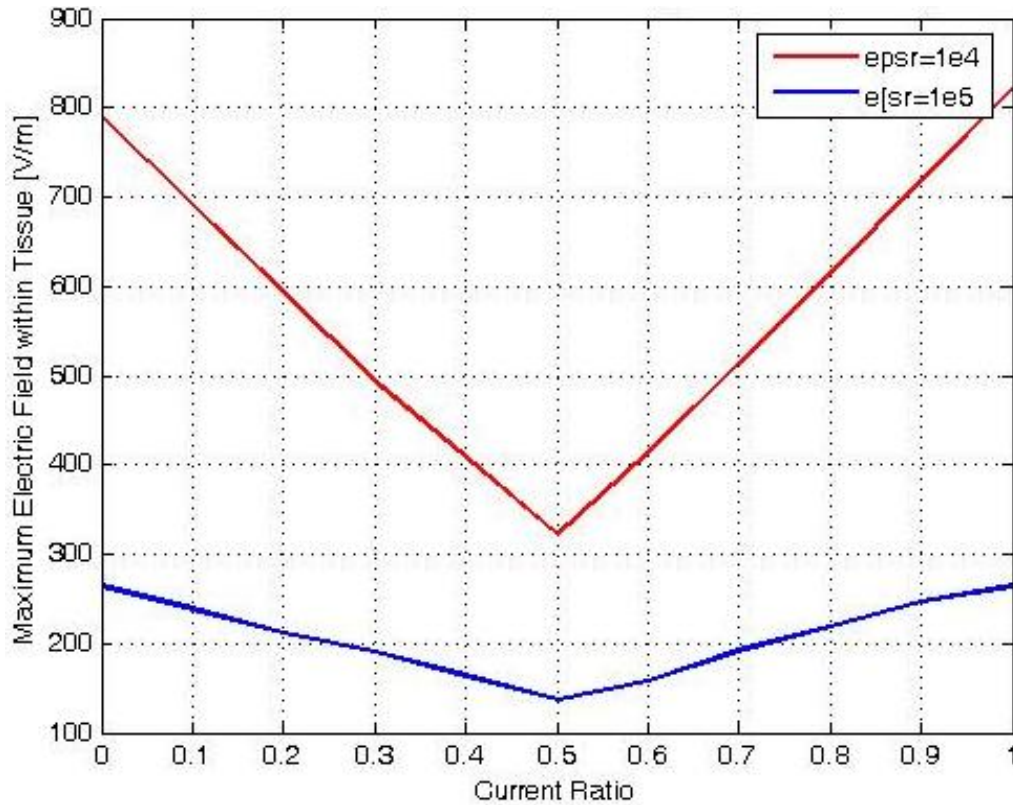


Figure 4-9. Maximum electric field vs. current steering ratio for different permittivity @ $\epsilon_r = 1 \times 10^4$ and $\epsilon_r = 1 \times 10^5$ at $\sigma = 0.15 \text{S.m}^{-1}$

4.5.2 Tissue dielectric properties

Model-I

The tissue exhibited significant increase in dielectric permittivity and drop in conductivity near DC (10 – 1000Hz) demonstrating the characteristics of poor conductor which attenuates the field intensity and its penetration depth. The electric field intensity associated with different dielectric properties values are plotted in Figure 4-10 exhibiting the dominant effect of elevated permittivity values on the field distribution. On the other hand, tissue conductivity had negligible effect, and the maximum field values are listed in Table 4-1. Field penetration depth reached 1.5mm at relative permittivity $\epsilon_r = 1 \times 10^5$ which dropped to 1mm at $\epsilon_r = 1 \times 10^6$, and increased to 6mm when the relative permittivity drops to 1×10^4 .

Table 4-2. Maximum electric field intensity [V/m] for different tissue dielectric properties

Permittivity	Conductivity					
	00.02	00.04	00.06	00.1	00.2	00.3
$\epsilon_r = 1 \times 10^4$	948	948	946	946	946	946
$\epsilon_r = 5 \times 10^4$	502	502	502	502	502	502
$\epsilon_r = 1 \times 10^5$	369	369	369	369	369	369
$\epsilon_r = 5 \times 10^5$	134	134	134	134	134	134

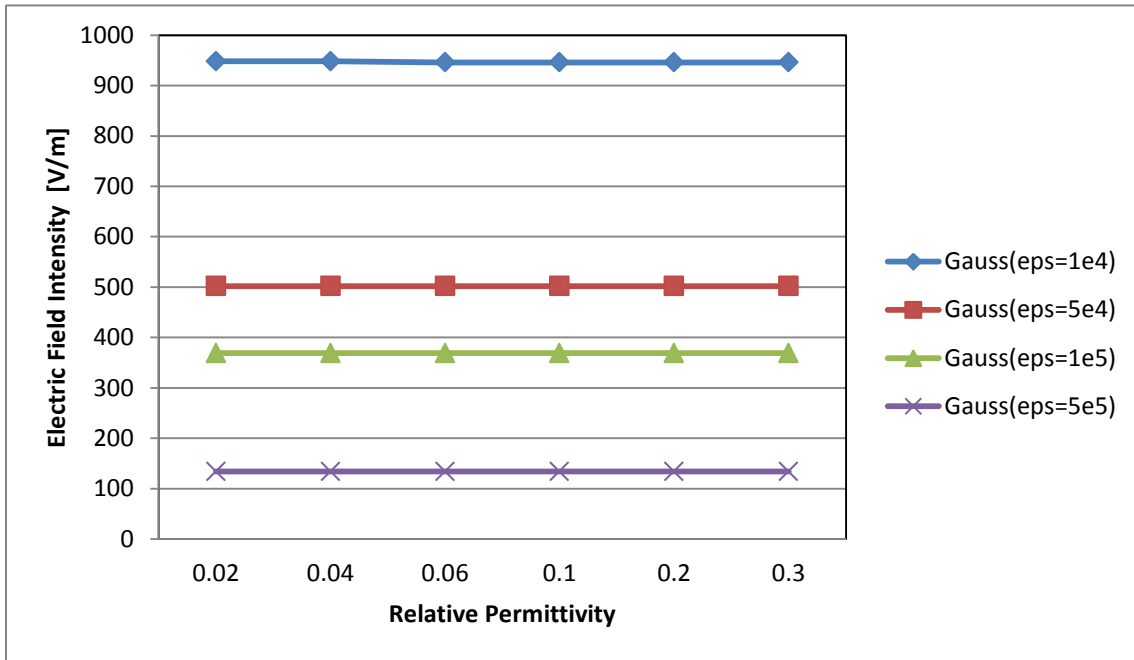


Figure 4-10. Maximum electric field intensity (V/m) vs. conductivity for different relative permittivities

The effect of tissue dielectric constant on the field intensity distribution for relative permittivity $\epsilon_r = 1 \times 10^4$ up to $\epsilon_r = 1 \times 10^6$ was modeled using power relation with confidence bounds of 95% and modeled in equation 3.4 with RMSE = 64.56 and maximum coefficient of determination $R^2 = 94\%$, the model is plotted in Figure 4-11.

$$E_{\max}(\epsilon_r) = (4.499 \times 10^4)(\epsilon_r)^{-0.4157} \quad \dots (3.4)$$

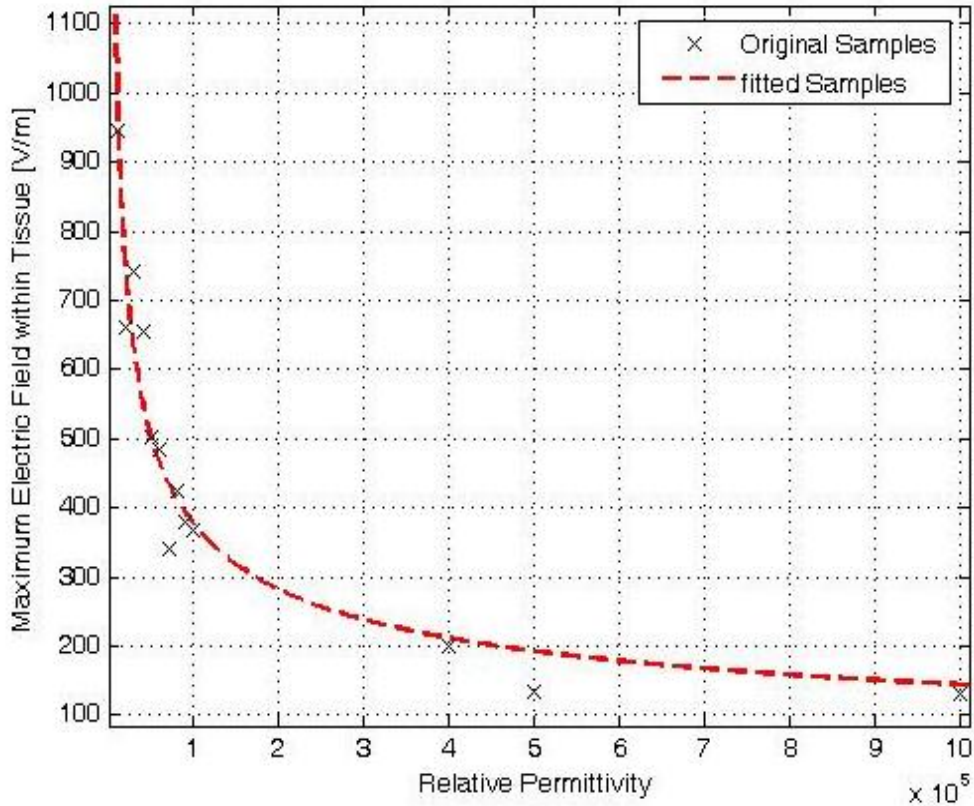


Figure 4-11. Electric field intensity vs. permittivity @ $\sigma = 0.1\text{S.m}^{-1}$

Model-II

This model included the encapsulation tissue layer and its thickness was varied from 0.1 to 1mm with 0.1mm increments to investigate its effect on the field distribution. Figure shows the gray box representing gray tissue, and the red box representing the encapsulation layer. The results inferred that field intensity was inversely proportional to the capsule thickness. In order to compensate for the field attenuation due to the formation of the capsule, the stimulation pulse was modified to maintain the targeted depth of the electric field. The results were modeled to demonstrate the effect of capsule thickness (T_{Capsule}) on the field distribution and the extracted model equation is:

$$E_{\text{max}}(T_{\text{Capsule}}) = 47.6(T_{\text{Capsule}})^{-1.01} + 401 \quad \dots (3.5)$$

With $R^2 = 91\%$, and RMSE = 47.1

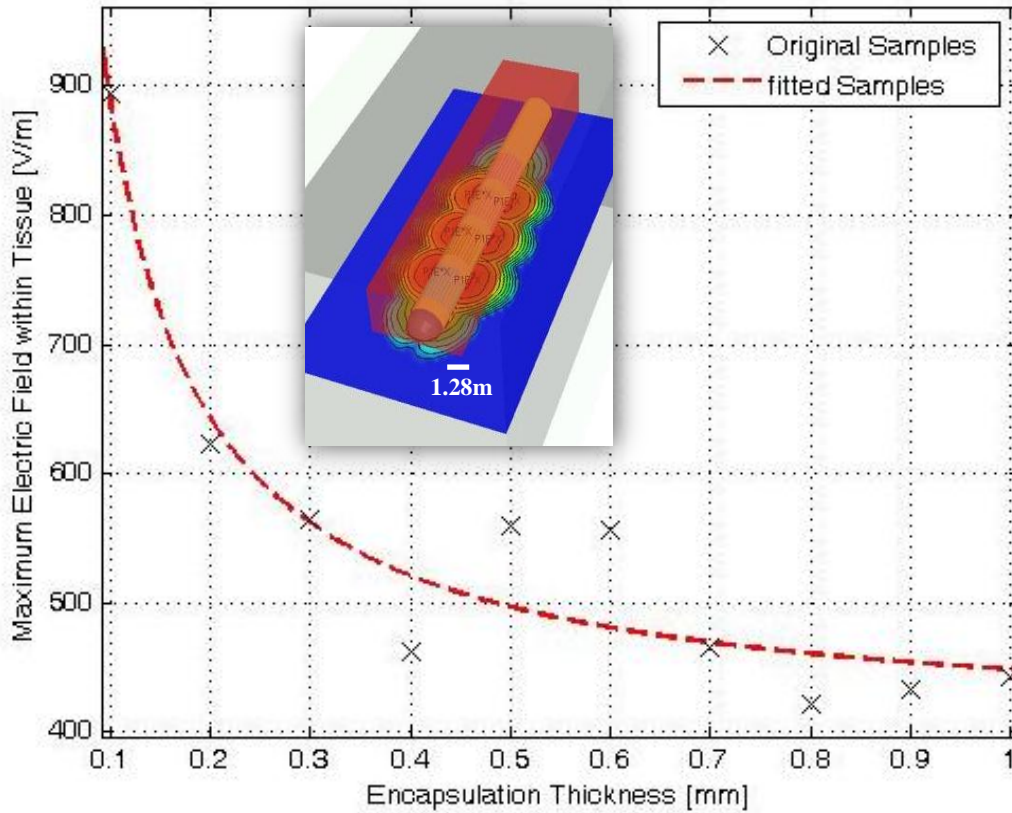


Figure 4-12. Maximum electric field intensity vs. capsule thickness (T_{Capsule}) for tissue permittivity of $\epsilon_r = 5 \times 10^4$ and $\sigma_{\text{Gray Tissue}} = 0.15 \text{S.m}^{-1}$, $\sigma_{\text{Capsule}} = 0.1 \text{S.m}^{-1}$

Model-III

The electrode displacement within the tissue was included by changing the gray tissue layer thickness (T_{Gray}) from 0 to 2mm; this simulated the change of the electrode proximity to the gray-white tissue boundary. The results in Figure 4-13 exhibited a pinch in the field lines at the gray-white matter boundary (red-gray boxes respectively) associated with more dense distribution of the field equipotential lines. As a result; electric field penetration within the gray matter dropped. The effect of gray tissue thickness (T_{Gray}) on the field intensity was modeled by equation 3.6 with $R^2 = 98.5\%$, and $\text{RMSE} = 34.6$.

$$E_{\text{max}}(T_{\text{Gray}}) = 200.3(T_{\text{Gray}})^{-0.452} + 139.2 \quad \dots (3.6)$$

4.6 Modeling Miniature Electrodes

It is required to miniaturize the electrode, increase its recording density and integrate current steering capabilities. Miniaturizing electrode dimensions and pad size should maintain the proper and safe electrical performance of the electrodes. The Medtronic 3387 electrode model was used as a reference

electrode, and its cylindrical structure was modified into a planar layout with stimulation pads at both sides, each representing a stimulation channel. The planar model is shown in Figure 4-14 and had cross-section of 1280x280 μm and pad length, width and thickness of 2000x1280x20 μm respectively. The 11.5mm electrode model had 8 pads on both sides 500 μm apart. The electric field distribution is shown in Figure 4-15 and the maximum values were estimated to be 2.348KV/m and 2.06KV/m in the normal and horizontal directions respectively with respect to the stimulation pads. These values were in good agreement with the original Medtronic 3387 electrode with cylindrical shaft in Figure 4-16. The higher electric field values along the normal plane was justified by the superposition of stimulation pulses generated by the pad located at the back of the electrode.

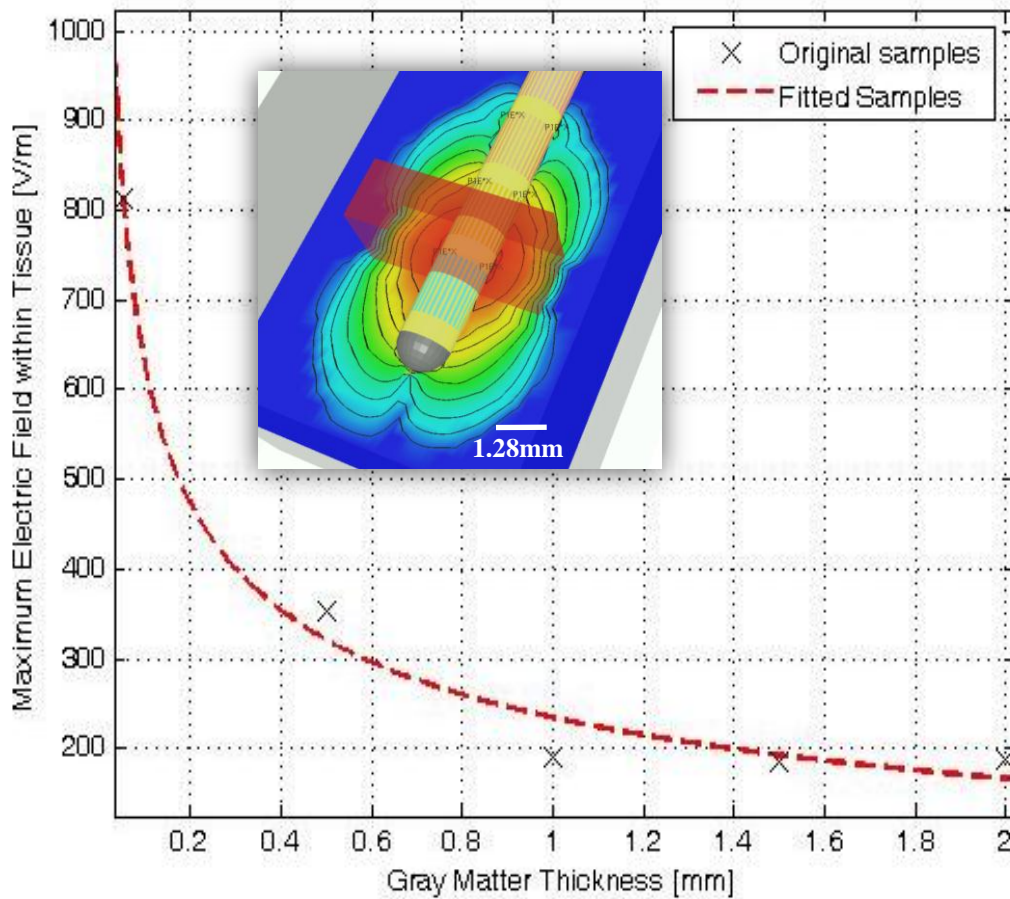


Figure 4-13. Maximum electric field intensity vs. gray matter thickness (T_{Capsule}) for tissue permittivity of $\epsilon_{\text{Gray Tissue}} = 1 \times 10^5$ and $\sigma_{\text{Gray Tissue}} = 0.1 \text{S.m}^{-1}$, $\epsilon_{\text{White Tissue}} = 2 \times 10^4$, $\sigma_{\text{White Tissue}} = 0.1 \text{S.m}^{-1}$

However, miniaturizing the pads to 50x117 μm significantly raised the electric field to 9.19KV/m along the horizontal plane and 44.68KV/m along the normal plane as shown in Figure

4-17. This implied that conventional stimulation patterns had to be adjusted, otherwise electric field values would drastically increase and the physiological response and tissue safety might be compromised. Furthermore, superimposed fields generated by the backside pads would interfere with proper localized distribution of electric fields. The voltage level of the stimulation pattern was downscaled tenfold and the electric field levels were comparable to the Medtronic 3387 electrode simulations.

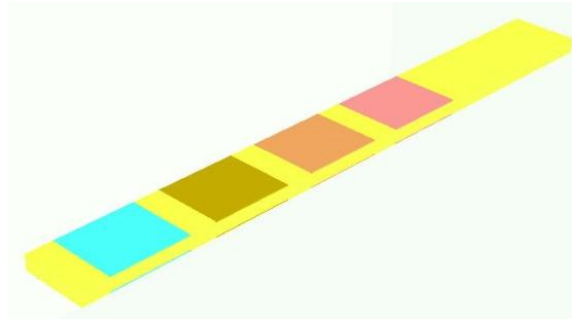


Figure 4-14. Medtronic 3387 DBS electrode planar model

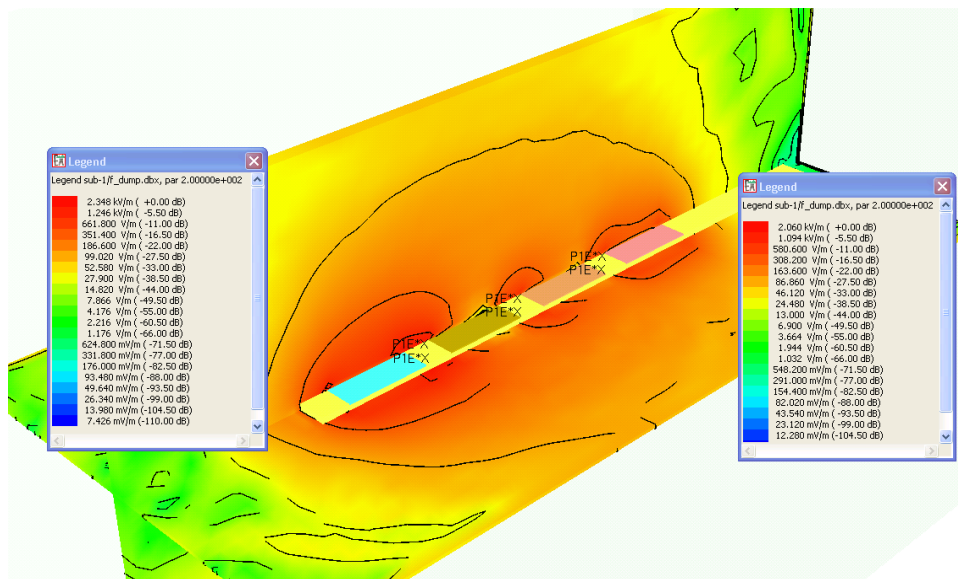


Figure 4-15. Electric field distribution of the planar model for Medtronic 3387 DBS electrode

Electrode Design Parameters

Electrode width

The electrode width was varied from 50 to 1600 μm to study its effect on the electric field distribution. An electrode with small width within the same order of magnitude as the pad dimensions produced higher field intensities compared to that with larger width. In addition, it exhibited less field penetration depth within the brain tissue (in Figure 4-18: blue rectangle represents the electrode width). The low field values associated with small electrode width was a result of high tissue permittivity at quasistatic stimulation frequencies. This lead to shallow penetration within brain tissue as the field was intensified near the pads. The relationship between the electrode width and field intensity for given pad width (50x50 μm) was plotted in Figure 4-19.

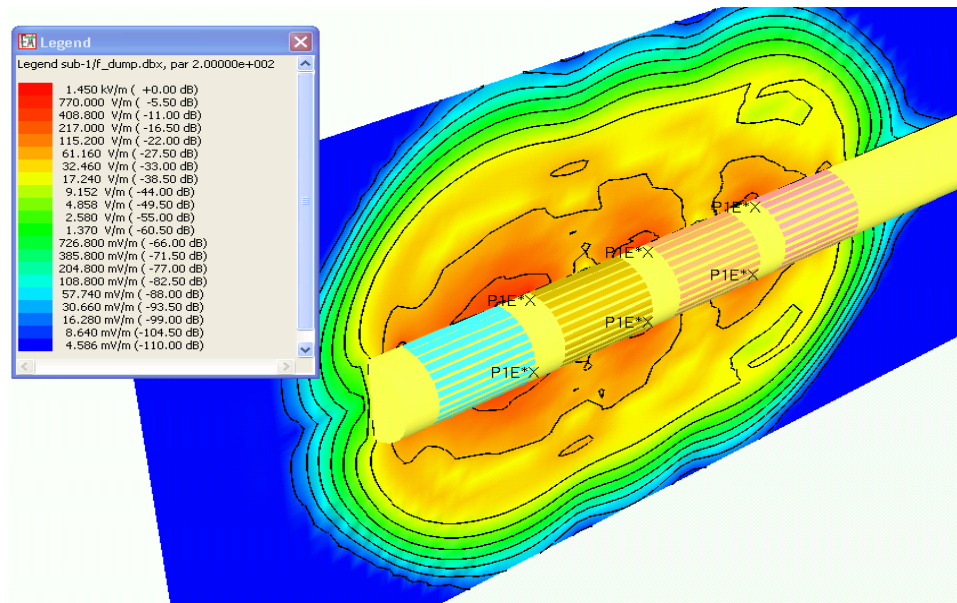


Figure 4-16. Electric field distribution of Medtronic 3387 DBS electrode

Pad Size

The rectangular pads modeled for this analysis had a length of 50 μm , and the width was varied from 20 to 100 μm . Small area pads yielded higher intensities and shallower field penetration. This can be exploited to modulate the field distribution and intensity within brain tissue by controlling the effective pad width relative to the electrode width. A practical implementation was an array of closely packed pads that can be fired in phase to form a single wide stimulation port with adjustable dimensions [186]. However, maximum pad dimensions were limited by electrode size limitations as well as safe charge densities delivered [26] which constrained the geometrical surface area between 1000 μm^2 and 2500 μm^2 to maintain the functionality of a stimulation electrode [91].

Pads layout

The relationship between the pad gaps and the electric field intensity was plotted in Figure 4-20, and the results showed that the drop in maximum field intensity resulting due to gap variation was not

significant. The vertical gap between the pads was varied from 50 to 550 μm and Figure 4-21 shows a layout with a 4x4 pads matrix. The results also inferred that pads spacing should be 2 to 4 times its dimensions for optimal packing. This was in agreement with experimental results for single neuron spike recording reported in [17], in which the 50 μm pads were spaced by 100 to 150 μm to avoid overlap between recording channels.

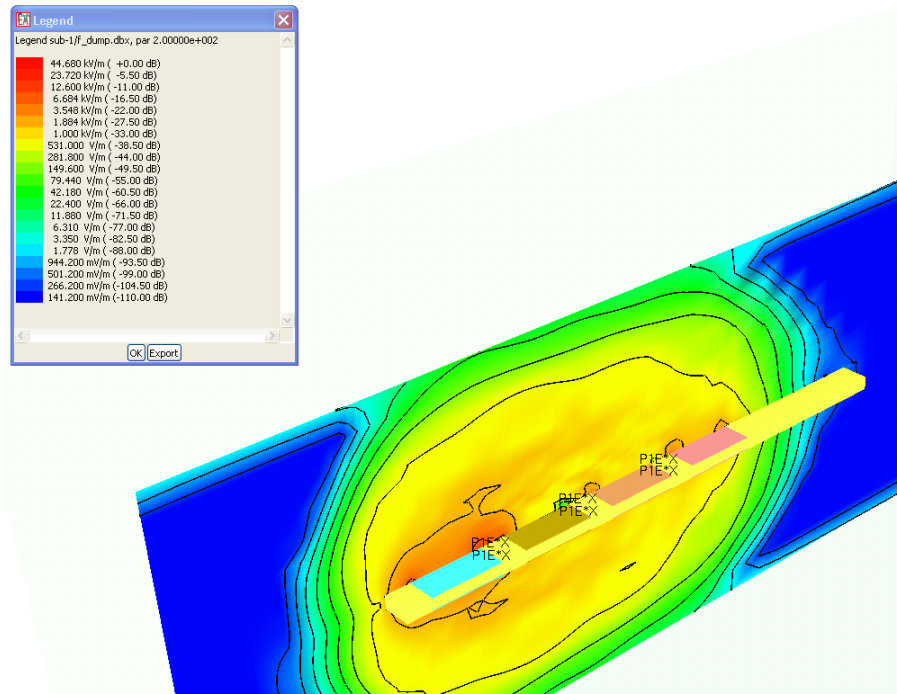


Figure 4-17. Normal plane field values for intra-cortical microelectrode

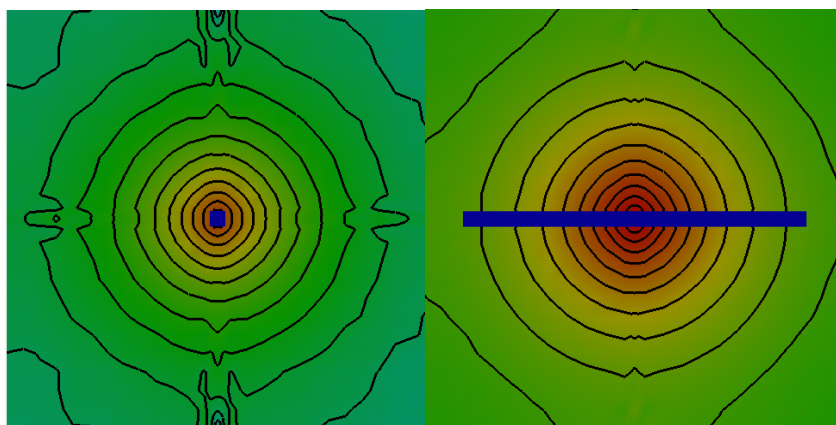


Figure 4-18. Electric field distribution for different electrode widths, Left: 50 μm , Right: 1600 μm . The blue line represents the electrode width

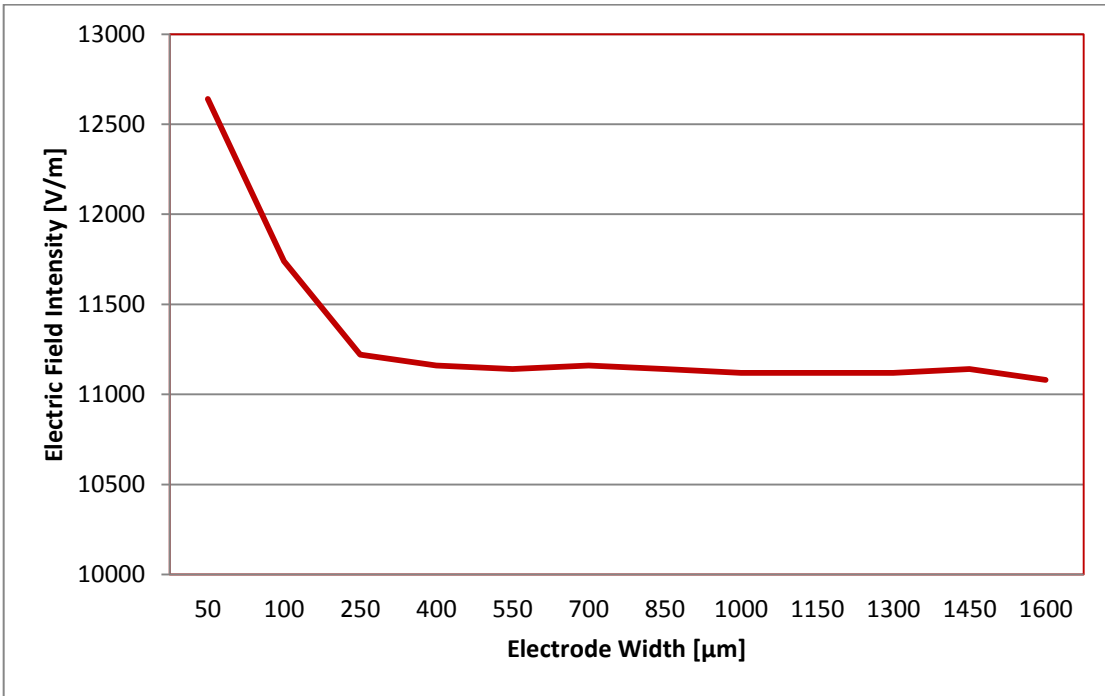


Figure 4-19. Effect of electrode width on field distribution

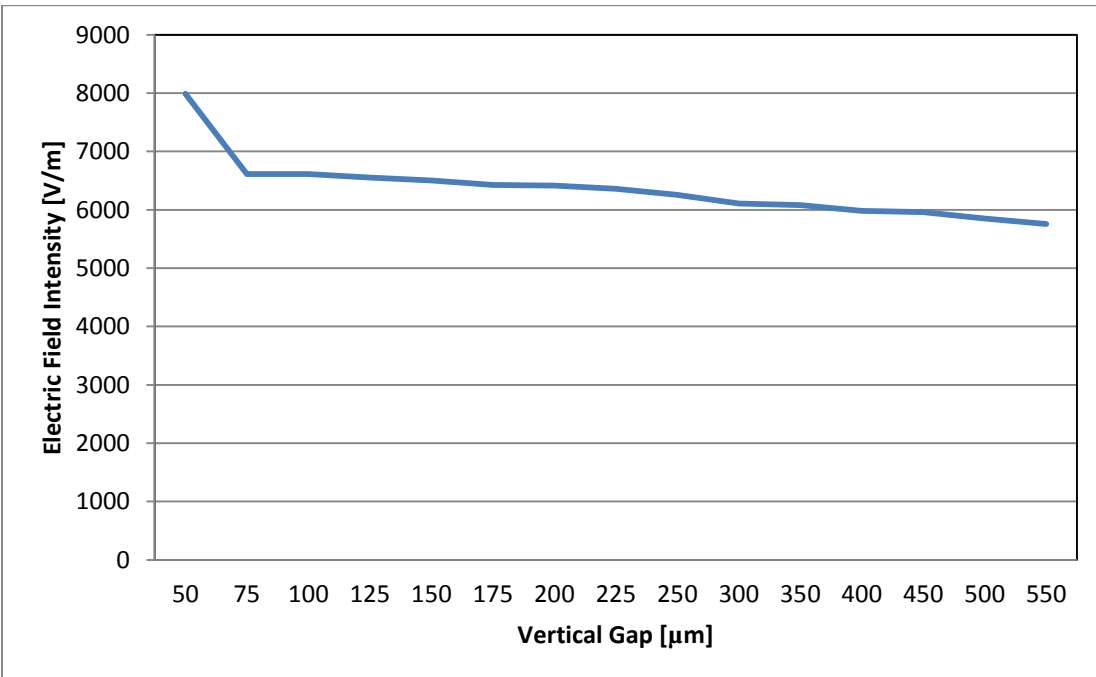
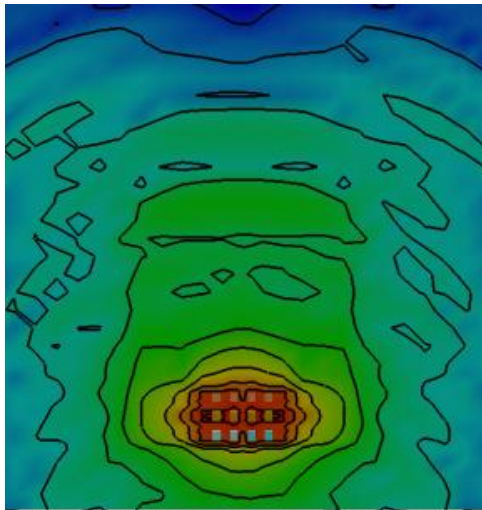
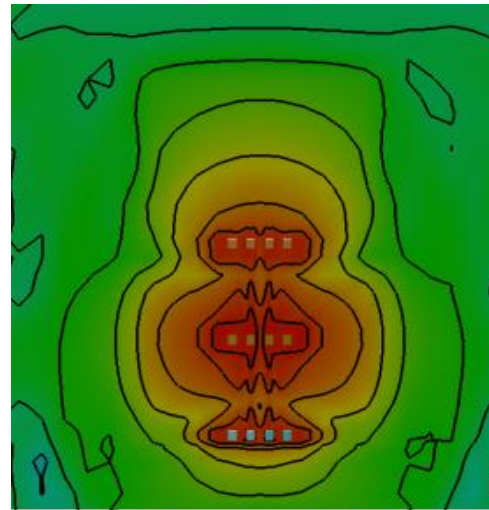


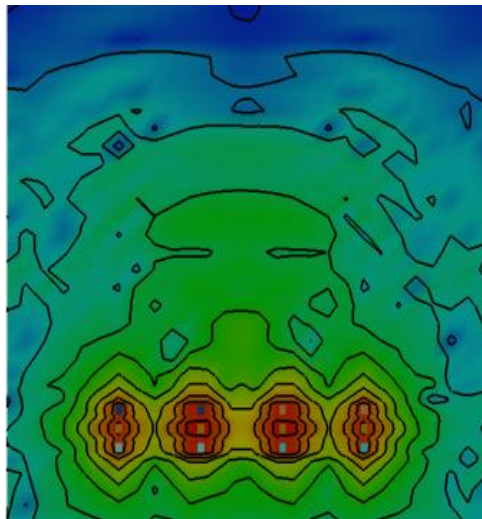
Figure 4-20. Effect of vertical pad gap on the electric field intensity



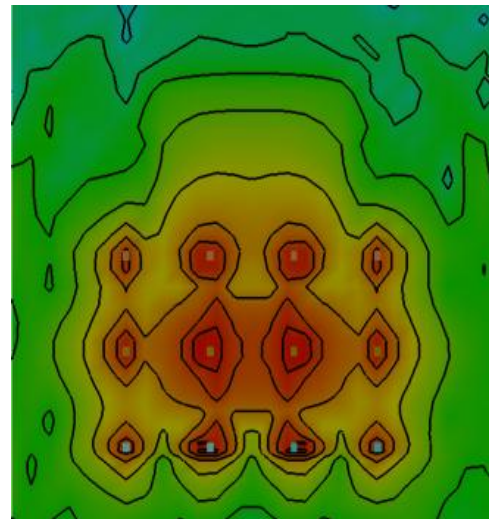
Horizontal gap: 50µm, vertical gap: 50µm



Horizontal gap: 50µm, vertical gap: 450µm



Horizontal gap: 450µm, vertical gap: 50µm



Horizontal gap: 500µm, vertical gap: 450µm

Figure 4-21. Electric field distribution for different pads layouts

4.7 Metal Planes

Metal planes can be integrated within the electrode shaft to provide structural rigidity and mechanical support during electrode insertion and operation. This section investigates the influence of electrically floating metal plane on the electrode electrodynamics. Several electrode designs with different metal layer configurations were modeled and simulated, and the results were compared with a control design of an electrode without metal reinforcement. The stimulation signals were fired from the pads at one side of the electrode (active zone) while the pads at the back side were not activated (idle

zone). The field intensity was estimated at both sides of the electrode to investigate the effect of the metal plane in isolating the field at the idle plane. The electric field distributions for regular electrode and another with metallic plane are presented in Figure 4-22. The results exhibited that single metallic layer attenuated the field in the idle zone resulting in shallower field penetration and less intensity values. Adding a second metal plane improved the field isolation and attenuation in the idle zone as shown in Figure 4-22, however, a third metal plane did not contribute significantly to the field attenuation. To investigate the efficacy of the metal plane in blocking the electric field propagation, the plane was divided into strips as shown in Figure 4-23 and the width was swept from zero and increased to form a solid plane, and the results showed that metal strips of different widths yielded attenuation similar to solid a metallic plane.

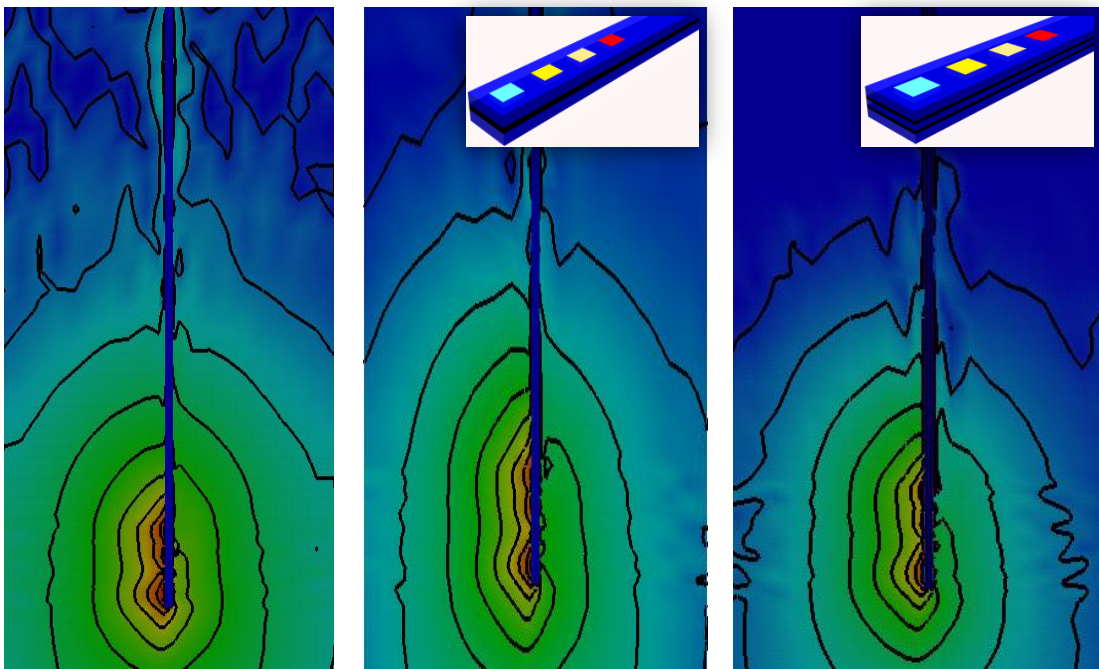


Figure 4-22. Electric field distributions: Left: single side stimulation without an intermediate metal plane, Middle: with intermediate metal plane, Right: with two intermediate metal planes

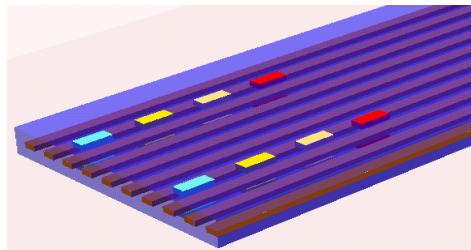


Figure 4-23. Microelectrode model with variable width metal strips

4.8 Conclusion

The objective of the electromagnetic analysis was to investigate the effect of microelectrode design parameters and tissue properties on the electric field distribution and intensity within the brain tissue, study the effect of miniaturizing electrode dimensions, and explore methods of current steering. Finite difference time domain (FDTD) was used for modeling and simulating the microelectrodes and brain tissue. The tissue models were created based on Gabriel biological tissue models. Due to the lack of low frequency data illustrating the operation levels of the electric field intensity and distribution associated with intra-cortical stimulation, the Medtronic 3387 DBS electrode was modeled and analyzed to provide reference data for developing the intra-cortical microelectrode design. The Medtronic 3387 electrode had ring pads and a modified model was created with planar pads to validate planar models which were then miniaturized to investigate the performance of microelectrodes. Miniaturizing the stimulation electrodes exhibited a remarkable increase in the electric field intensity, and the stimulation voltage levels had to be customized for microelectrodes.

The simulation results exhibited that the electric field distribution in ambient brain tissue was affected by: pad size and layout, stimulation pulse characteristics and firing pattern, tissue dielectric properties, electrode dimensions and non-homogenous tissue structure. Expanding the pulse width produced higher field levels, and the pulse amplitude affected the field intensity without changing its distribution. The electrode width affected the field intensity such that widths of the same order of magnitude as the stimulation pad dimensions yielded high field intensities and less penetration within the tissue compared to wider electrodes. Pad size exhibited inverse relation with field intensity, and expanding the gap between pads increased the field penetration within the tissue. The encapsulation tissue layer created in response to implanting a foreign body attenuated the electric field.

Pad arrays were also modeled to investigate their efficacy in manipulating the spatial accuracy of charge delivery and field shaping through current steering. The simulation results exhibited the ability to manipulate the electric field distribution within brain tissue through controlling the ratios of the differential stimulation signal components between pad pairs.

Finally, the study explored the effect of integrating metal reinforcement planes on the distribution of the electric fields within the brain tissue. Simulations verified the ability to improve the spatial charge delivery by adding electrically floating metal planes at the backside of the electrode which attenuate the field intensity at the idle zone (the region to the back of the stimulation pad), and accordingly, can be used for controlling the field distribution and avoiding stimulation of untargeted neural structures.

In conclusion, the electromagnetic modeling and simulation results verified the ability of microelectrodes with miniature pads to replicate the electric field distribution generated by the FDA approved and commercially available stimulation electrodes. However, due to the scarcity of low frequency experimental data for the tissue dielectric properties, the available models require further refinement, and the data provided in this chapter will be considered qualitatively.

Chapter 5

Structural Analysis of Intra-Cortical Microelectrodes

5.1 Introduction

The electrode mechanical performance is influenced by several parameters including the electrode layout, architecture and material. It was required to develop an electrode with a rigid structure capable of penetrating through the tissue without the need for insertion assistive device to minimize tissue trauma. Yet, its structure has to be flexible and match the ambient tissue stiffness to minimize post implantation tissue trauma. These mechanical properties had to be provided through a small footprint design to improve the electrode biocompatibility. Achieving flexibility and rigidity introduced design challenges, and finite element mechanical modeling and analysis using Ansys Workbench 12 was employed in the design process. Several layouts were modeled (Table 5-2) and analyzed to identify the competent designs capable of satisfying the mechanical requirements.

The insertion force was estimated from literature and the mechanical failure modes were identified for brittle and ductile materials. The electrode would fail buckling due to axial loading and fracture due shear forces. Safety factor of 5 was assumed and the different proposed layouts were modeled to estimate the failure loads and the minimum electrode dimensions. The main degree of freedom was the shaft thickness, and the recommended thicknesses for the different layouts and materials were calculated. Finally, strain relief sections were modeled and investigated to improve the electrode mechanical performance and enhance its biocompatibility.

5.2 Forces Acting on the Electrode

During insertion, the electrode is subjected to three mechanical forces outlined on the free body diagram in Figure 5-1 [146]. The tip force represents the axial reaction acting on the electrode tip during penetration, and the clamping force acts normal to the electrode surface. The friction force is exerted along on the electrode surface and estimated as the product of the normal force acting on the surface and the coefficient of friction. These forces are superimposed to form the total axial reaction force acting on the electrode during insertion. The applied insertion force should overcome the total reaction force for successful penetration without driving the electrode into any of the various mechanical failure modes. The mechanical properties of various types of tissue define a wide range of penetration forces, and experimental results documented in literature estimated the penetration force to range between 1 to 10mN [189][190][191][79], which is 2 to 3 orders of magnitude lower than the penetration force of epidermal tissue estimated to be 1N [164][165][166].

5.3 Electrode Mechanical Failure Modes

The electrode is prone to mechanical failure during insertion through two modes: buckling and fracture [170]. Several materials were tested for implementing the electrode structural layer, and the various material mechanical properties introduced different failure modes. Brittle materials (e.g.

silicon, SU-8) experiencing uniaxial stresses undergo elastic deformation and when the stress level exceeds yield strength, they exhibit negligible plastic deformation followed by fracture. Therefore; ultimate tensile strength (UTS) is the design parameter considered as the maximum loading limit for brittle structures. On the contrary, ductile materials (e.g. metals and flexible polymers) respond to uniaxial stress by elastic deformation until yield is reached, followed by plastic deformation and eventually cracking leading to fracture. Ductile material would fail if the maximum shear stress exceeds the maximum shear yield strength of the material.

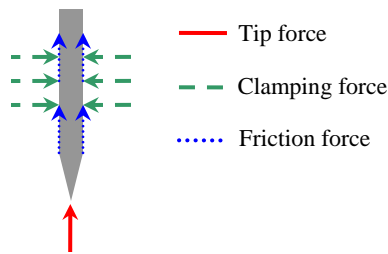


Figure 5-1. Forces acting on the electrode [146]

Table 5-1. Young moduli of different human tissue [146]

Layer	Young modulus [MPa]
Stratum corneum	12000
Viable epidermis	16
Dermis	12
Average value for brain tissue	8.863

Miniature brittle structures

The probability of defect existence deteriorates the fracture strength of brittle materials, and for silicon it is estimated to be 7GPa [192]. However; anisotropic etched silicon membranes with sharp edges exhibit fracture of strength of 300MPa [193], inferring stress concentration factor of 33 at sharp walls and corners. Taechung Yi reported fracture strength of <110> silicon samples to be 0.6 to 1.2GPa and is affected by the etching process [194]. Miniaturizing silicon structures diminishes the probability of existence of critical crack and will push the material properties to the defect free theoretical limit, consequently; increasing the structure's fracture strength. Experiments [195] reported increase in the fracture strength of polysilicon associated by length decrease, and this was a result of a drop in the probability of critical crack.

Experimental results in [15] reported that silicon shafts with cross-sectional area below $2000\mu\text{m}^2$ were much more flexible and compared to bulk silicon, its fracture stress increased by a factor of 6. The fracture stress significantly increased for a width of $150\mu\text{m}$ and saturated for smaller

dimensions. Small structures exhibited magnified stress endurance because the probability of occurrence of surface defects and imperfections drops [15].

5.4 Buckling Analysis

Buckling is a failure mode that occurs in slender structures when the axial force exerted on the shaft exceeds a threshold value identified as the critical load and disturbs its structural equilibrium. This drives the column into an unstable state and the electrode shaft geometry will collapse into buckling modes. The critical instance during electrode insertion is just before tissue penetration at which the axial load and the electrode effective length are at their maximum values [171]. The value of the critical load is function of electrode geometry and material as well as end supports configurations. Buckling resistance drops with the presence of material defects, geometrical asymmetry, and eccentric loading which introduces bending moments and promotes curvature. In order to avoid buckling failure, the electrode should be designed to have a critical load beyond the force required for tissue penetration; otherwise; an insertion support tool will be required.

During penetration, the electrode base is held by tweezers while the tip propagates through the tissue and its displacement is restricted along the penetration direction. This is a fixed-pinned loading condition, however; the more stringent fixed-free configuration was assumed. Shafts with uniform cross-sections were modeled to calibrate the simulator using analytical techniques.

5.4.1 Buckling analysis simulation model

The electrode was modeled for Eigen buckling analysis, and different layouts were modeled and analyzed. The critical loads were estimated to represent the forces provoking buckling failure, and the simulation model for a sample electrode layout is shown in Figure 5-2. Unity axial force was applied to the electrode base, while the tip was constrained in all directions to create fixed-free loading condition. The force was ramped and the critical load was estimated, and finally the buckling mode was extracted and plotted.

5.4.2 Analyses results

Rectangular cross-sections

A shaft with uniform rectangular cross-section was modeled to investigate the influence of different electrode parameters on its mechanical performance. The shaft width was fixed at 130 μm while the thickness was varied from 20 to 200 μm . A 3mm silicon or stainless steel shaft with thickness of 20 μm had a critical load of ~5mN, which dropped to ~0.9mN for 6mm shaft. Safety factor of 10 (~10mN) was acquired for 3mm shaft with a thickness of 30 μm , and 50 μm for 6mm shaft. Electrodes designed for application in rodents had 1mm shafts yielding a critical load of 40mN for a thickness of 20 μm . Polyimide sheet and SU-8 epoxy photoresist were modeled as the structural material. Polyimide rectangular shaft required a thickness of 140 μm to survive a critical load of 10mN for a 6mm shaft which dropped to 92 μm for 3mm shaft. As for SU-8, 6mm shaft provided critical load of 8mN for a thickness of 200 μm , and 10mN for 3mm shaft with a thickness of 105 μm .

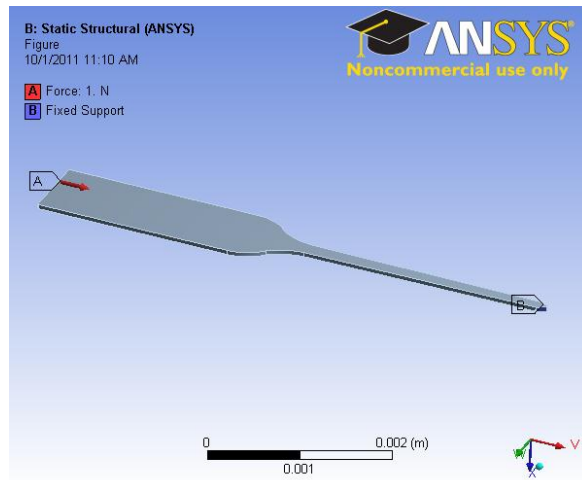


Figure 5-2. Fixed-free Eigen buckling model

Proposed electrode layouts

Several electrode layouts were proposed in pursuit of a design that would accommodate large number of channels and satisfy the mechanical requirements and the proposed layouts are presented in Table 5-2. In general, the prototypes had shafts long enough to reside within 3mm inside the tissue and carry the interface pads, while the bases were large to facilitate handling and provide large interconnect pads for easy connections. The shafts in prototypes A, B, E, and F had lengths of 3mm and were extended in C and D, in general, the total electrode length was about 6mm. The interconnect pads on prototypes C, E and F were arranged transversely while in A, B and D were longitudinal. The electrodes models were analyzed to explore their mechanical performance, and parametric modeling and sensitivity analysis were employed to determine the effect of electrode dimensions and material properties on the critical load. The implantable shafts had fixed lengths of 3mm and the thickness was swept from 50 to 200 μ m. Several materials were modeled and the critical loads were estimated assuming fixed-free loading conditions.

Critical loads for the different layouts and materials are listed in

Thin silicon and stainless steel structures satisfied the mechanical requirements to avoid buckling failure scoring a minimum safety factor of 23 for layout D with thickness of 50 μ m. On the other hand; the minimum thickness of a polyimide electrode to barely survive buckling was 100 μ m with a minimum safety factor of 2.2.

Table 5-3, and plotted on the histogram in Figure 5-3. The first buckling modes of silicon electrodes are shown in Table 5-4 to illustrate shaft deformation due to axial forces. Results comparison showed that layouts E and F were the most stable, while layout C was the most vulnerable to buckling failure due to the abrupt change in the cross-section. Layouts E and F had wider shafts which explain their high resistance to buckling, and electrode dimensions are provided in Chapter 3. Silicon and stainless steel electrodes exhibited superior performance to resistant buckling failure, and 50µm silicon would survive the applied axial forces. The moduli of elasticity for silicon and stainless steel are of close values ($E_{\text{Silicon}} = 180\text{GPa}$, $E_{\text{Stainless-Steel}} = 200\text{GPa}$), accordingly; the critical loads for both materials were within proximity demonstrating. On the other hand, the critical loads associated with polyimide and SU-8 structures were very low due to their mediocre moduli of elasticity, and 50µm shafts would fail. The safety factor was calculated according to equation 5.1 [196]:



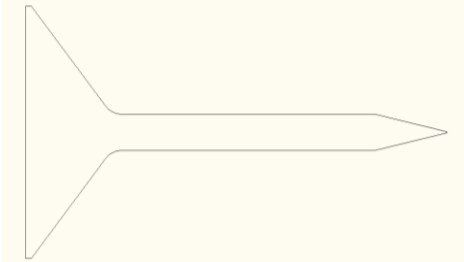

$$\text{Safetyfactor} = \frac{\text{Failureload}}{\text{Designload}} \quad \dots (5.1)$$

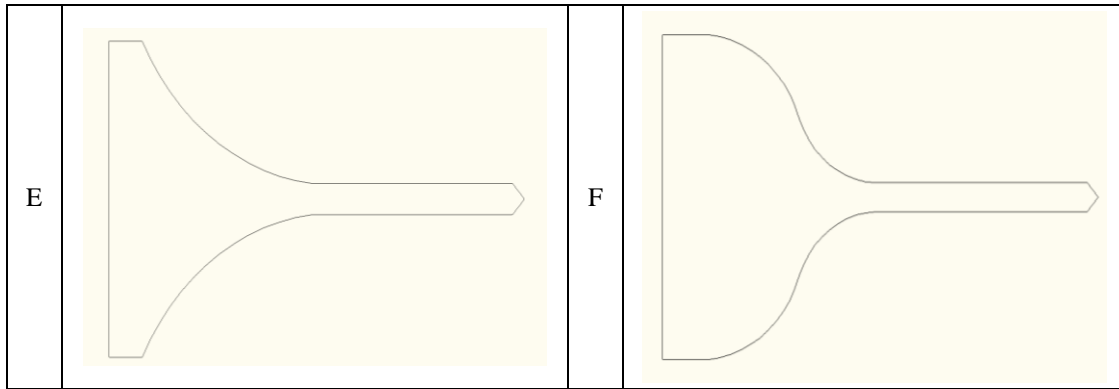
where; Failure load: Critical load.

Design load: Penetration force estimated to be 1mN [189][190][191][79].

The safety factor calculated for silicon electrodes was 23 for layout D with thickness of 50µm, thus, silicon satisfies the mechanical requirements to avoid buckling failure, and similarly for stainless steel. However, the minimum thickness of a polyimide electrode to barely survive buckling was 100µm.

Table 5-2. Proposed electrode layouts

A		B	
C		D	



Thin silicon and stainless steel structures satisfied the mechanical requirements to avoid buckling failure scoring a minimum safety factor of 23 for layout D with thickness of $50\mu\text{m}$. On the other hand; the minimum thickness of a polyimide electrode to barely survive buckling was $100\mu\text{m}$ with a minimum safety factor of 2.2.

Table 5-3. Critical loads [mN] for different layouts: Fixed-free Eigen buckling analysis

	Silicon			Stainless steel			SU-8			Polyimide		
	50μm	100μm	200μm	50μm	100μm	200μm	50μm	100μm	200μm	50μm	100μm	200μm
A	24.8	197.8	970.8	27.5	219.9	1079.1	0.68	5.4	27	0.44	3.5	17.3
B	24.5	195.4	901.6	27.2	217.1	1002.3	0.67	5.4	25	0.435	3.48	16.1
C	22.7	121.6	246.7	25.2	135.9	276.4	0.62	3.3	6.6	0.404	2.2	4.51
D	22.6	180.2	1441.5	25.1	200.3	1602.5	0.62	5	40	0.402	3.2	25.7
E	51.6	412.8	3294.8	57.4	459.0	3663.7	1.4	11	90	0.92	7.4	59
F	47.6	379.8	3032.6	52.9	422.2	3371.5	1.3	10	83	0.85	6.8	54

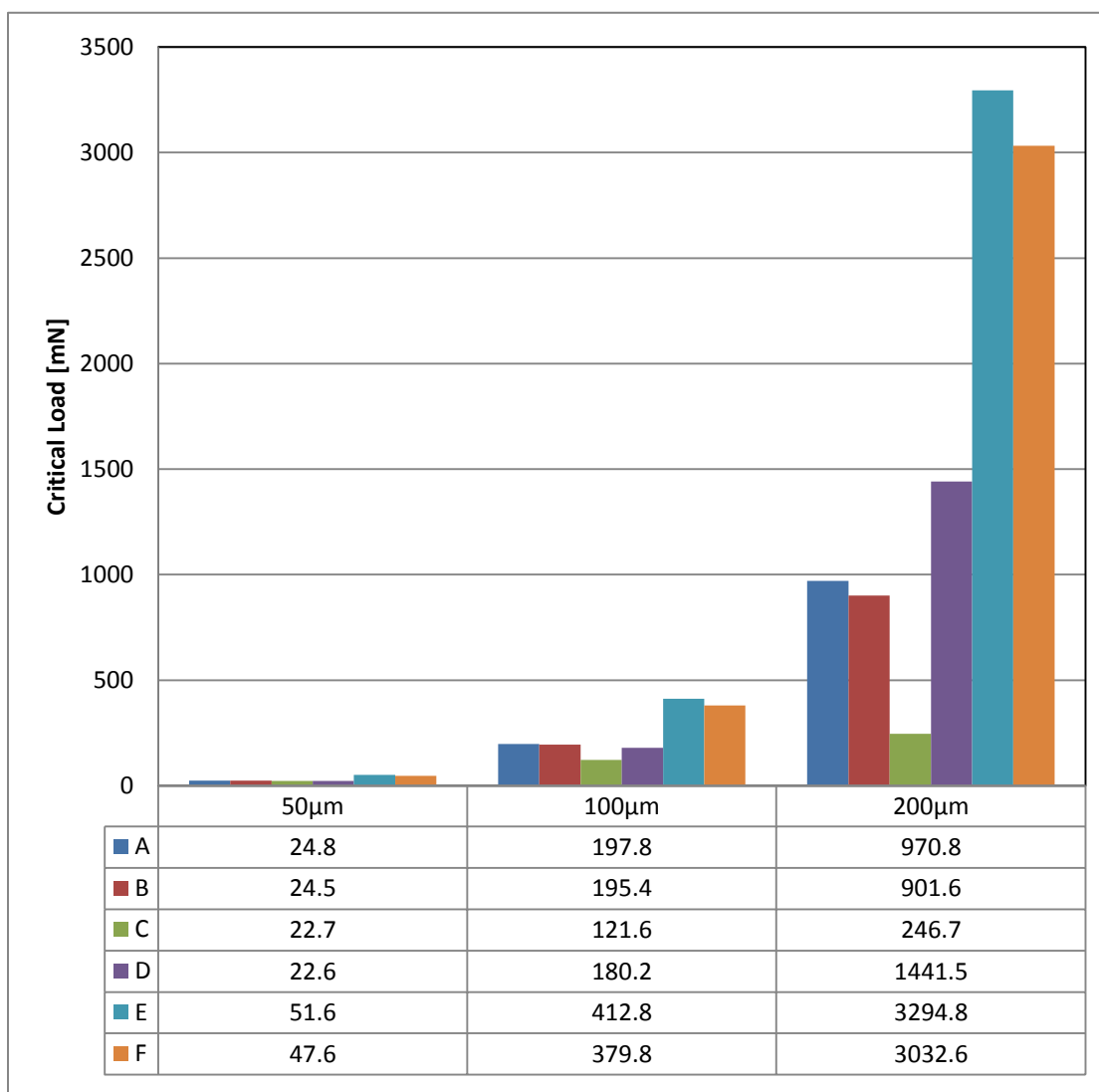
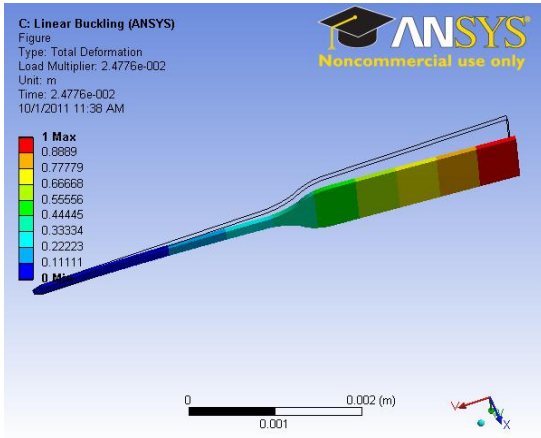
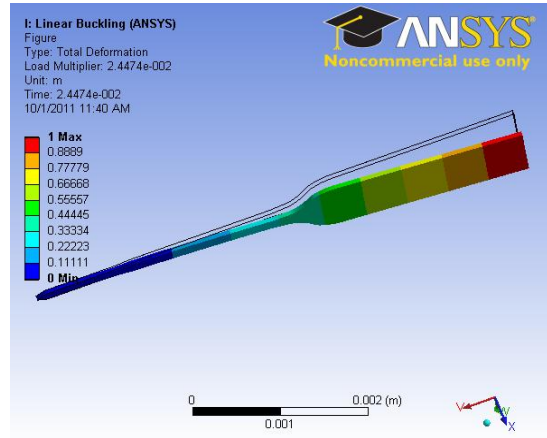


Figure 5-3. Histogram of critical loads for different electrode layouts: Fixed-free Eigen buckling analysis – Silicon

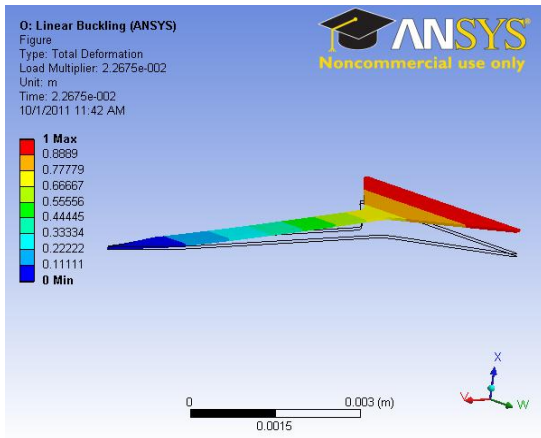
Table 5-4. Eigen buckling analysis: Deformation of different layouts – Silicon



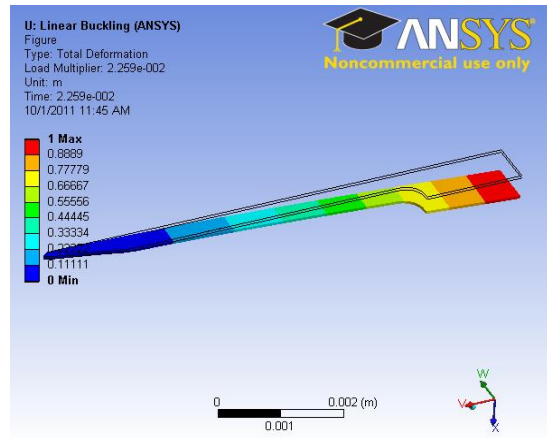
A



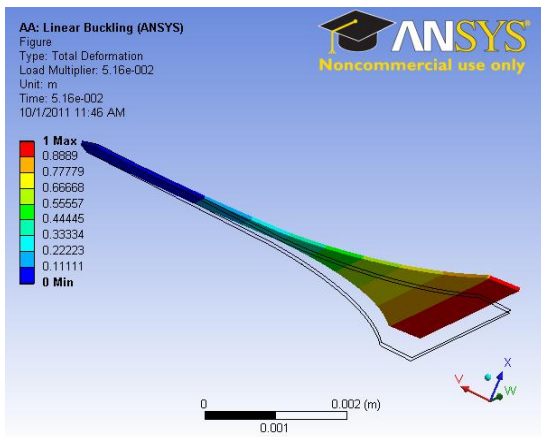
B



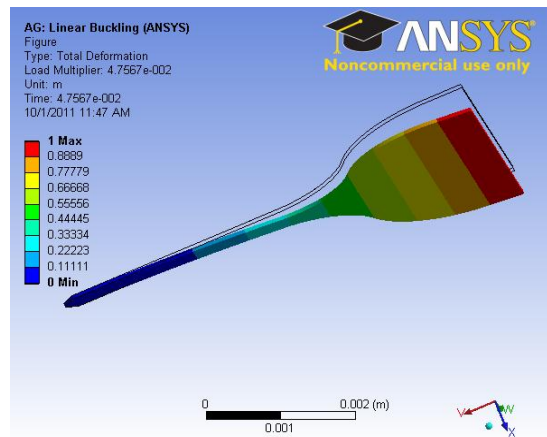
C



D



E



F

5.5 Electrode Fracture

Buckling failure represents one of the failure modes that challenge the electrode mechanical performance. It assumed axial loading, however, the electrode is also subjected to shear forces which would trigger fracture. The maximum principal stress theory (Rankine criterion) was adopted for the analysis of brittle materials. It states that failure occurs when the maximum principal stress reaches the ultimate tensile strength (UTS) determined from uniaxial testing, and similarly for compressive stress. The three principal stresses at any point ($\sigma_1, \sigma_2, \sigma_3$) may comprise tensile and compressive components, and the largest positive value represents the maximum tensile stress, while the smallest negative value is assigned for the maximum compressive stress. This is due to the fact that brittle materials do not yield and undergo plastic deformation, but fail by fracture upon reaching the ultimate tensile stress.

As for ductile materials, the response to axial stresses commences with yielding followed by plastic deformation, necking and finally hardening and cracking. Shear yield strength of ductile materials is approximately half of the tensile (or compressive) yield strength, therefore ductile materials fail through shear rather than tension or compression loading, accordingly; the maximum shear stress is considered the design factor of safety. Ansys 12 stress analysis tool was used for estimating the fracture safety factor utilizing the appropriate criteria according to the material properties, and a safety factor of 5 was considered the minimum safe.

Two sets of analyses were executed to estimate the shear forces exerted on the electrode in response to axial and shear loading. The safety factor was estimated by comparing the failure and design loads using equation 5.2 as defined in Ansys theory manual, and a value equal to or greater than 5 was considered acceptable. Finally, safety factor distribution contours indicating the ratio between maximum stress and maximum strength were plotted for the different models. These plots graphically illustrate the magnitude of shear stresses and identify high stress spots. The provided information assisted in tuning the layouts to avoid points of stress concentrations which act as stress raisers.

$$Safetyfactor = \frac{Failureload}{Designload} = \frac{S_{Limit}}{\sigma_1} \quad \dots (5.2)$$

where; Failure load (S_{Limit}): Tensile ultimate stress, or maximum shear stress.

Design load (σ_1): Maximum tensile stress, or maximum yield strength.

5.5.1 Axial and shear loading

The first analysis was an extension to the buckling failure study and was executed to estimate the maximum principal and shear stresses due to axial loading. Unity force was axially applied and fixed-free end conditions were assumed. The maximum stresses were calculated and compared to the yield and shear strengths according to the material type (ductile or brittle), and a minimum safety factor of 5 was targeted. The simulation model is shown in Figure 5-4, and the analyses were executed for brittle (silicon, SU-8) and ductile (stainless steel, polyimide) structures. During implantation and operation, the electrode is subject to lateral forces normal to the shaft inducing shear stresses which

create off plane deformation. Accordingly, in the second static structural analysis, the electrode was loaded with 1mN shear force equivalent to the value of the force required for electrode insertion and fixed-free support conditions were assumed. The finite element models for both analyses are shown in Figure 5-4.

5.5.2 Simulation results

Axial loading

The simulation results exhibited the superiority of silicon electrodes to resist axial loading. Silicon shafts with thickness of 100 μ m achieved an acceptable safety factor of 15 throughout the critical spots except for layout D. The asymmetry of layout D concentrated the tensile stresses along one of the sides which caused the safety factor to drop below 5 (Table 5-5.D-200 μ m). As for the 50 μ m silicon electrodes, several designs exhibited acceptable performance except for some high stress regions that might cause fracture as shown in layouts A and B (Table 5-5.A-50 μ m, B-50 μ m). Stainless steel electrodes (Table 5-6) followed silicon in failure resistance. Most of the 50 μ m stainless steel structures had minimum safety factor of 5 which would survive axial compression and the minimum required thickness to achieve the targeted safety factor was 100 μ m. On the other hand, polyimide and SU-8 had inferior mechanical properties compared to silicon and stainless steel, and the minimum thickness required for polyimide to survive the mechanical loading was 150 μ m as shown in

Table 5-7.

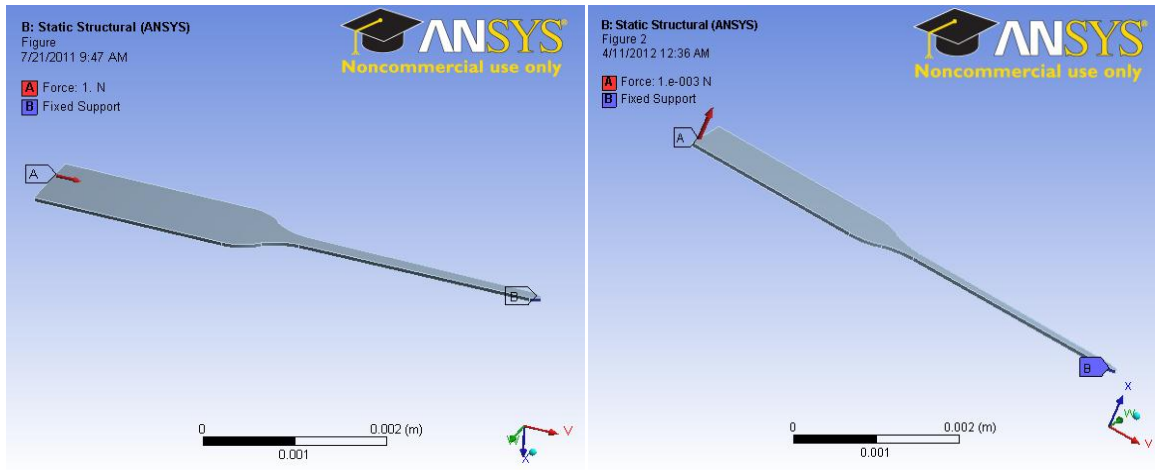


Figure 5-4. Failure analysis models, Left: Axial loading, Right: Shear loading

Although silicon predominated the mechanical performance, but, flexible substrates were preferred for the chronic electrode fabrication. Flexible substrates respond elastically to external stresses with the ability to restore the original shape after the force is withdrawn. Increasing the axial force beyond the yield point would result in permanent deformation without fracture until the ultimate strength is reached. In contrast, brittle (silicon) electrodes would undergo fracture right after crossing the yield point which makes them less attractive for long term in vivo applications. Furthermore, polyimide, easy to process and biocompatible, these properties makes it competent for electrode implementation.

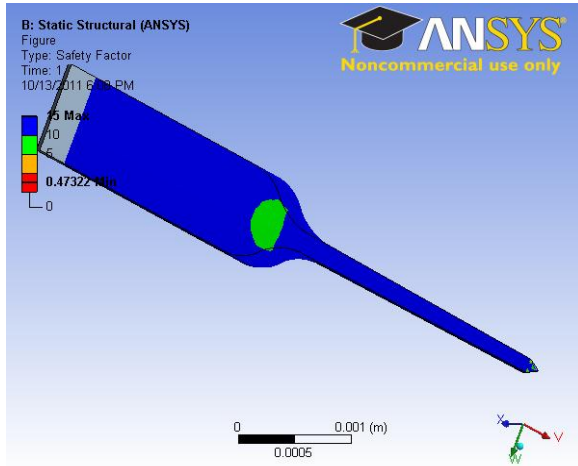
Shear loading

Shear forces applied on the electrode shaft created tensile stresses in one side and compressive stresses along the other. Silicon electrodes analyses showed that the side experiencing compressive stresses did not undergo failure as the ultimate compressive strength for a brittle material was greater than the tensile strength. Consequently, silicon electrodes of different layouts and thicknesses exhibited large safety factors along the compressed side; and the 50 μ m layout A is presented as an example in Table 5-8-A-50 μ m. The results recommend a minimum thickness of 200 μ m to prevent fracture during insertion assuming a single crystal defect free structure. However, layout D exhibited vulnerable response to shear stress at 100 μ m.

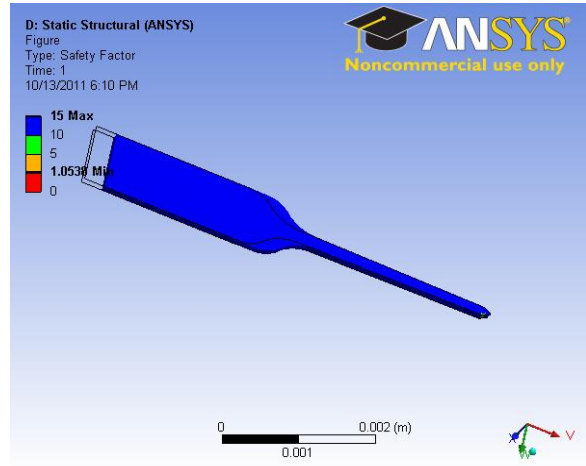
The safety factor distribution contours for axially loaded stainless steel electrodes are plotted in Table 5-6, and in contrast to axial loading, stainless steel surpassed silicon. Stainless steel shafts as thin as 50 μ m demonstrate acceptable performance with a minimum safety factor of 5, and 100 μ m shafts achieved safety factor of 15 throughout the structure. As for polyimide (Table 5-10) and SU-8, they were more vulnerable to shear stresses, and this was rectified by increasing the electrode

thickness beyond 100 μm to realize the required performance. The recommended thicknesses for the different layouts and materials are listed in Table 5-11.

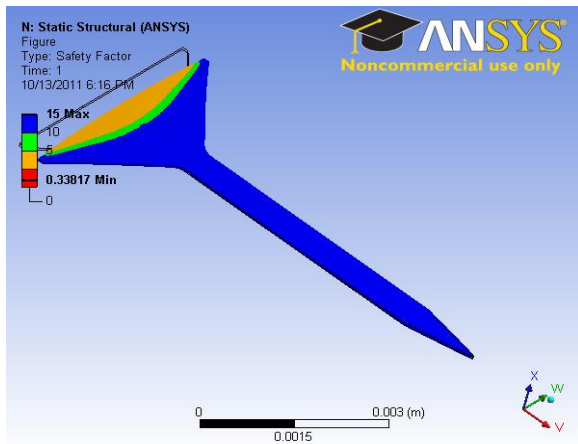
Table 5-5. Safety factor distribution for axial loading – Silicon



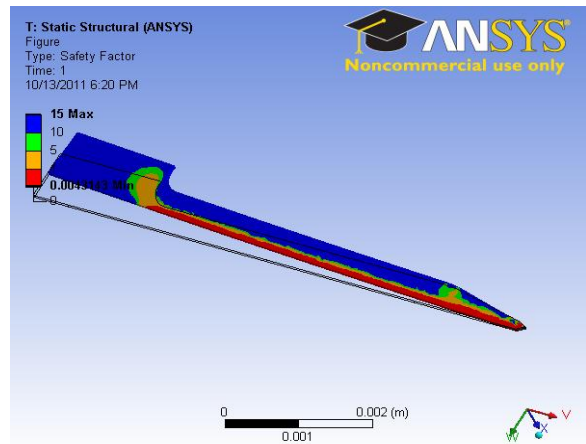
A-50 μm



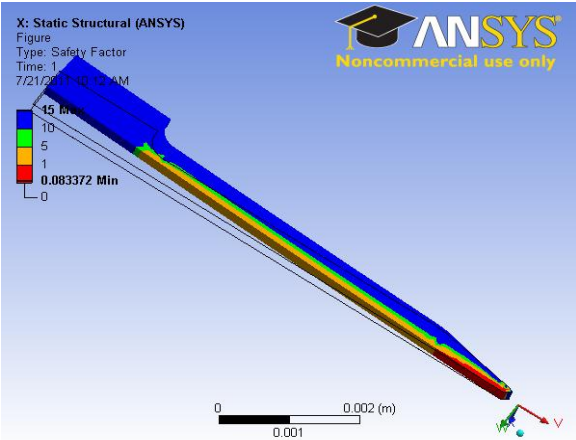
A-100 μm



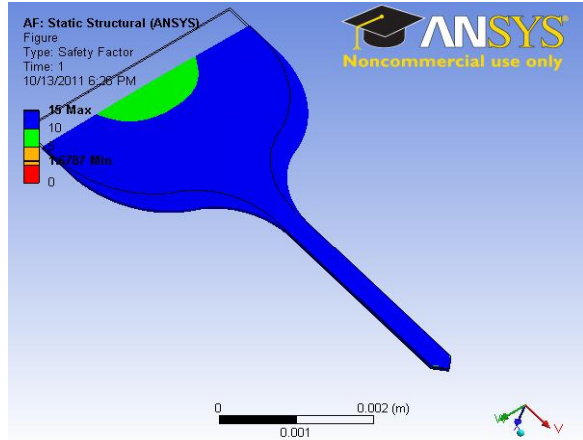
C-50 μm



D-50 μm

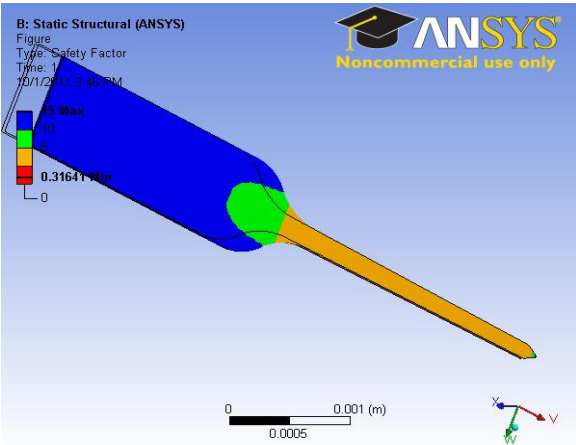


D-200µm

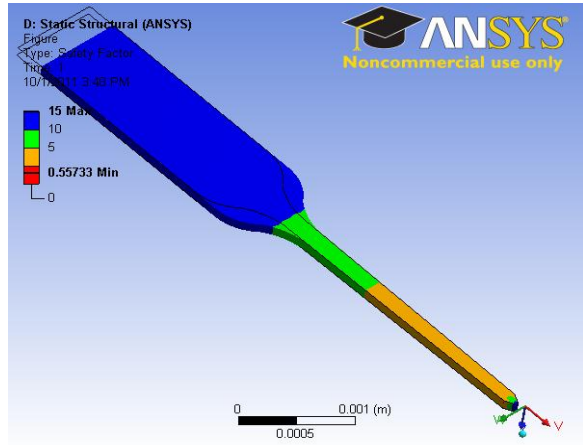


F-50µm

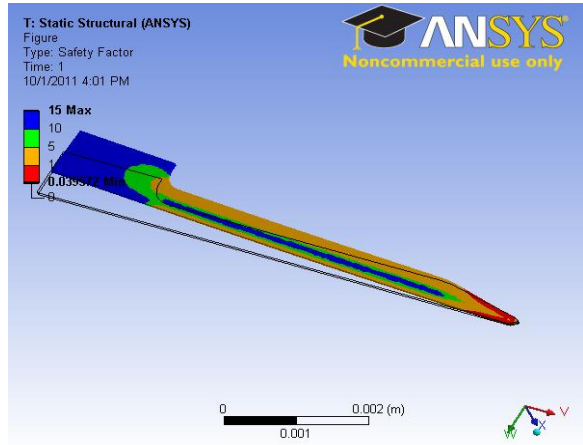
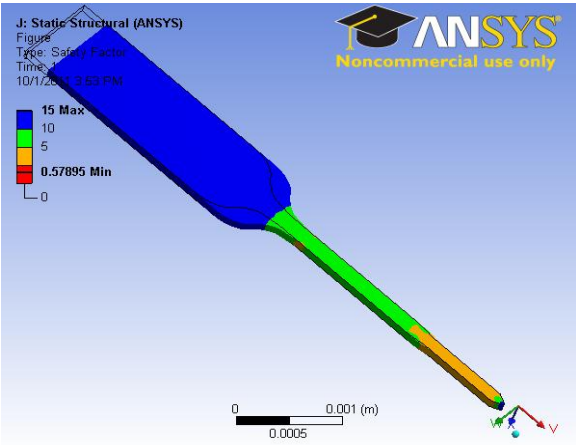
Table 5-6. Safety factor distribution for axial loading – Stainless steel



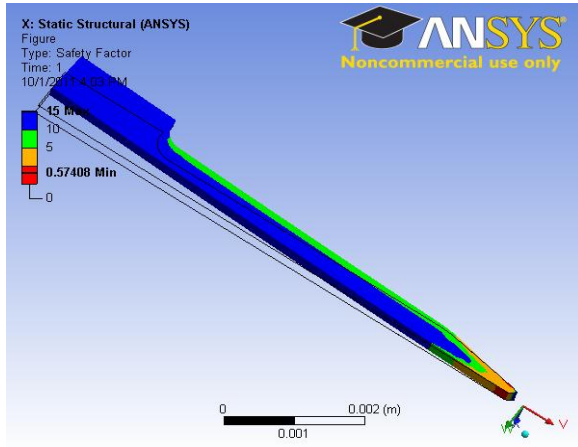
A-50µm



A-100µm

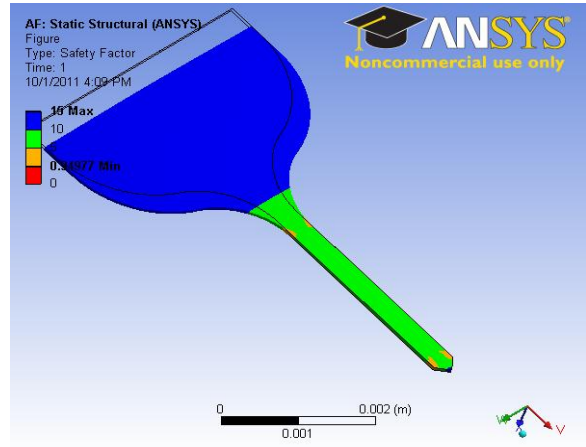


B-100 μ m



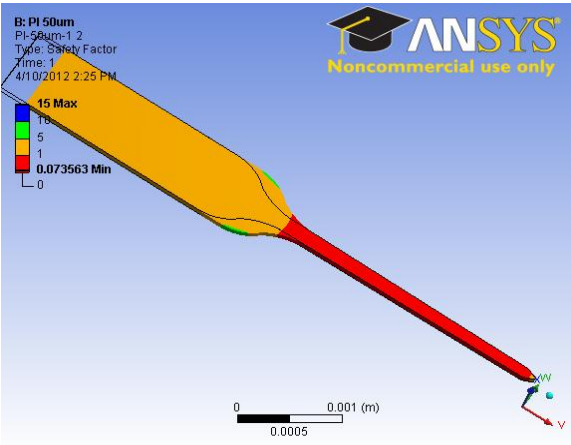
D-200 μ m

D-50 μ m

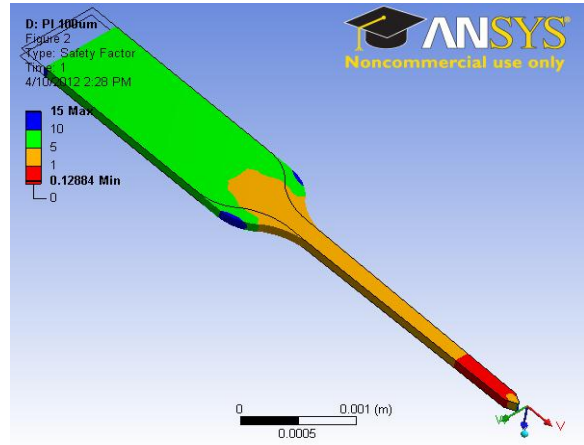


F-50 μ m

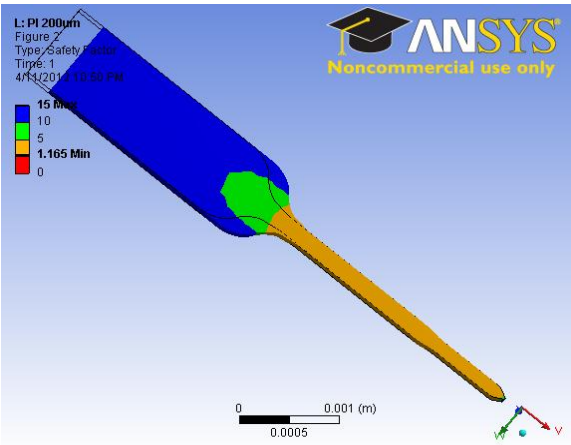
Table 5-7. Safety factor distribution for axial loading – Polyimide



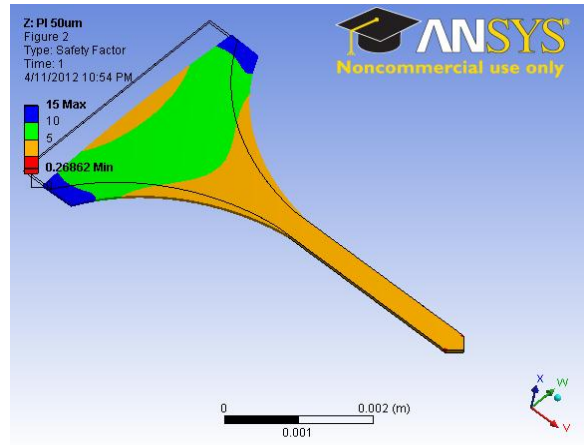
B-50 μ m



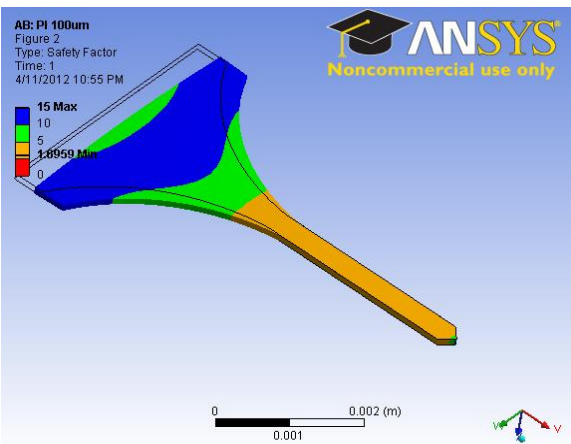
B-100 μ m



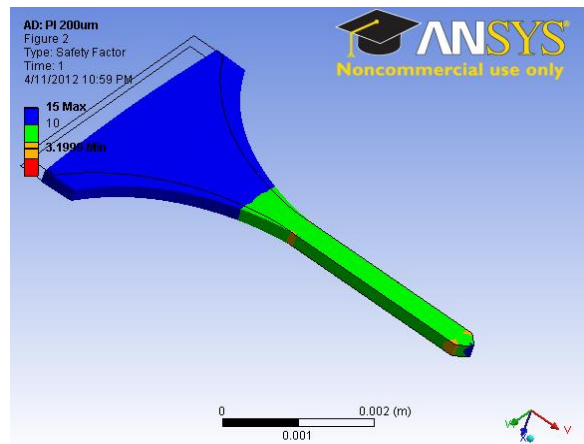
B-200 μ m



E-50 μ m

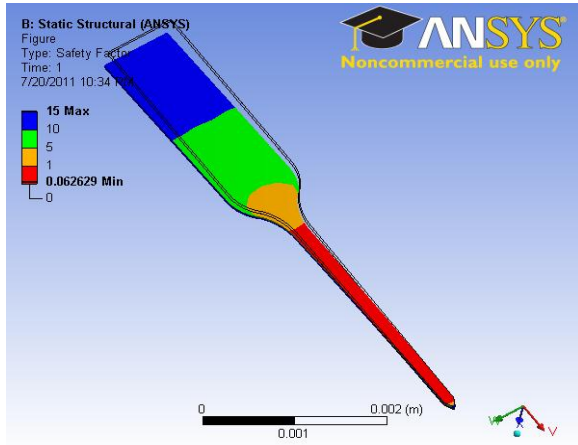


E-100 μ m

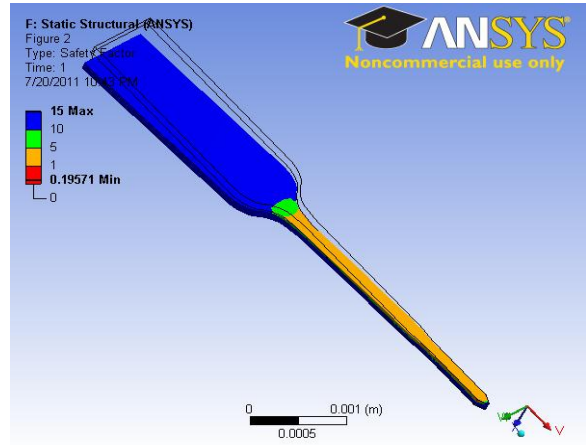


F-200 μ m

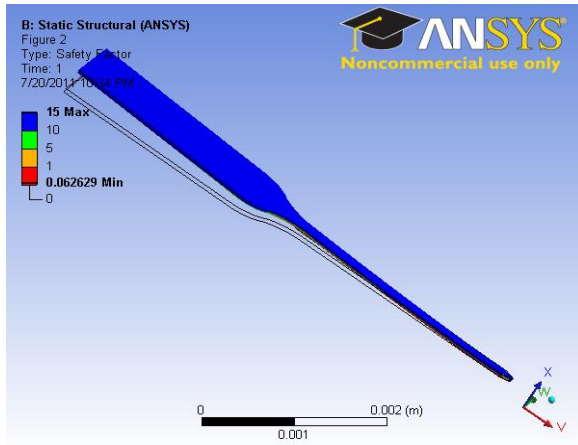
Table 5-8. Safety factor distribution for shear loading – Silicon



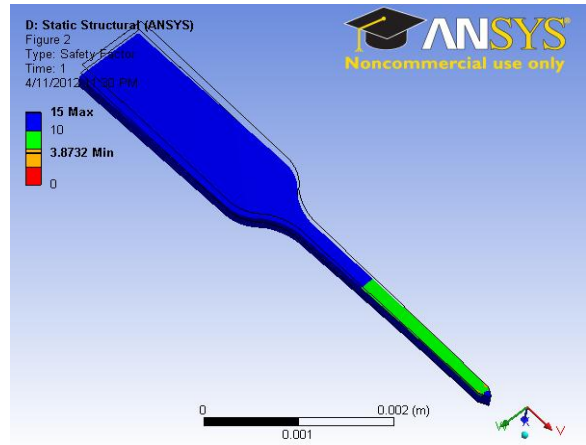
A-50µm



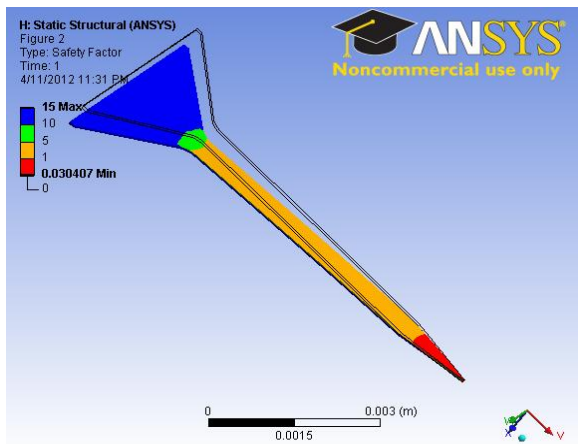
B-100µm



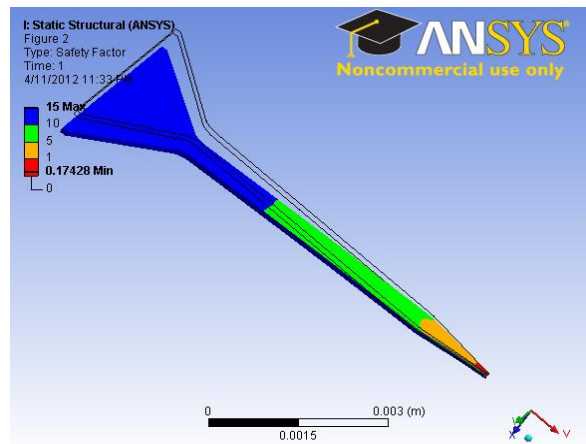
A-50µm (backside)



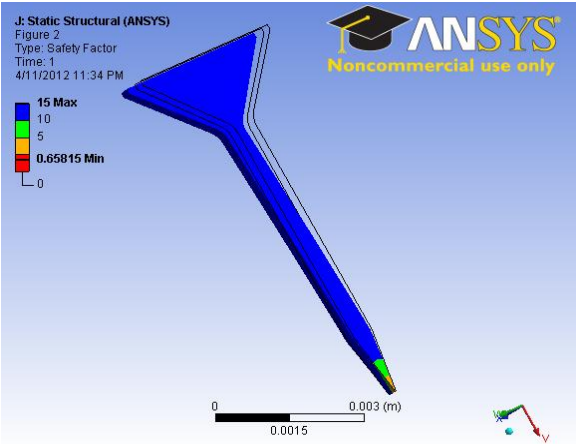
B-200µm



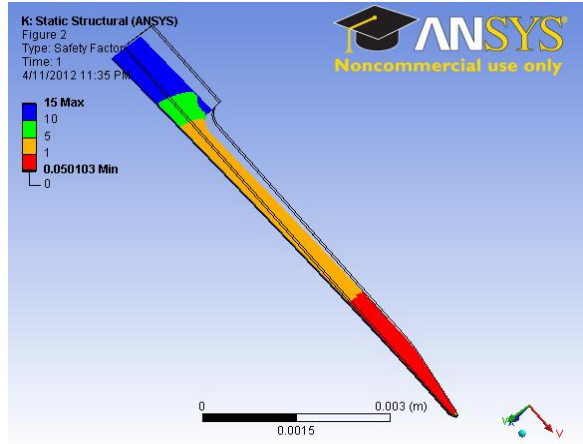
C-50µm



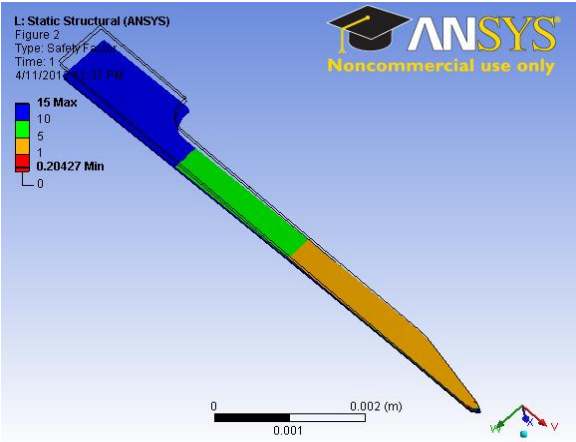
C-100µm



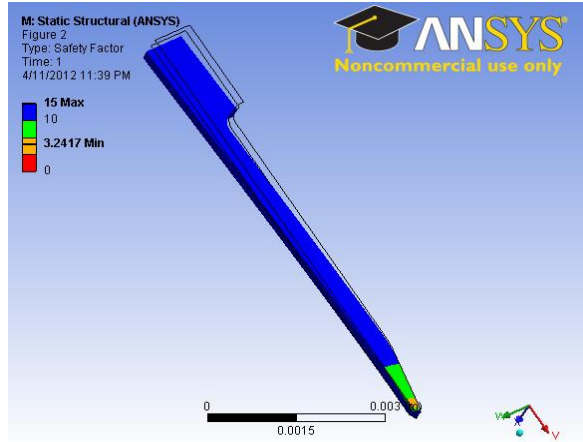
C-200µm



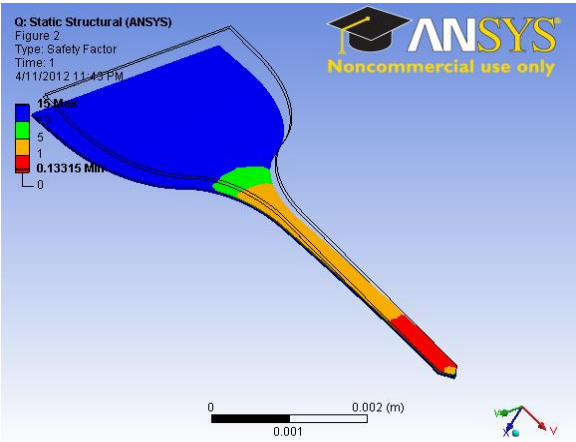
D-50µm



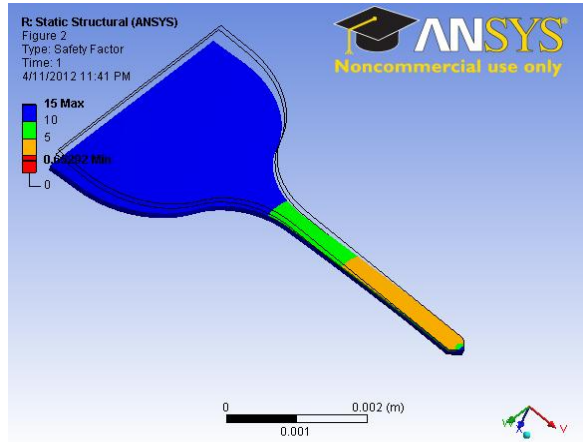
D-100µm



D-200µm

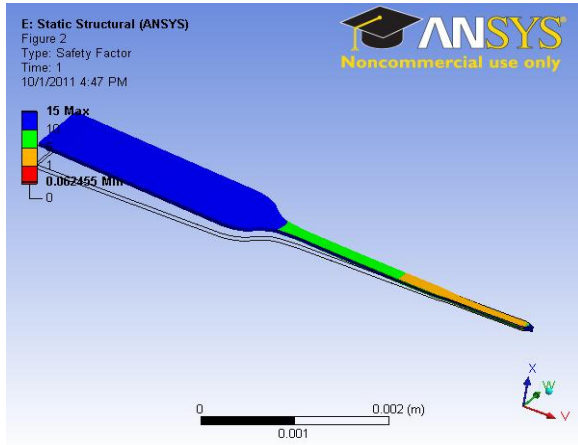


F-50µm

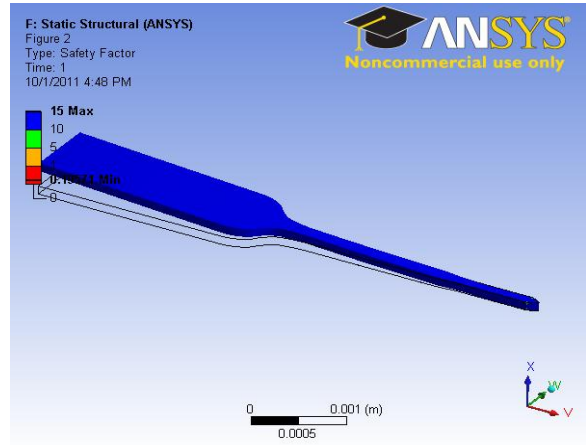


F-100µm

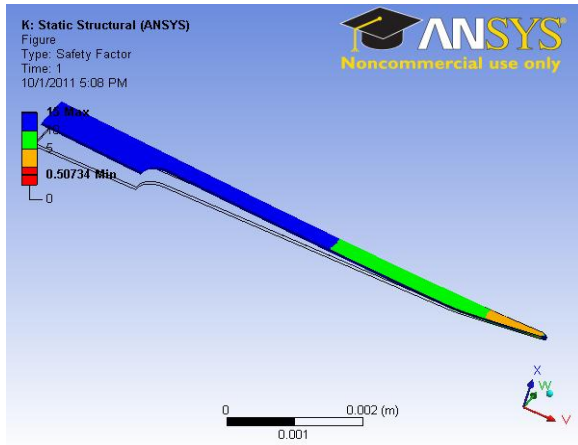
Table 5-9. Safety factor distribution for shear loading – Stainless steel



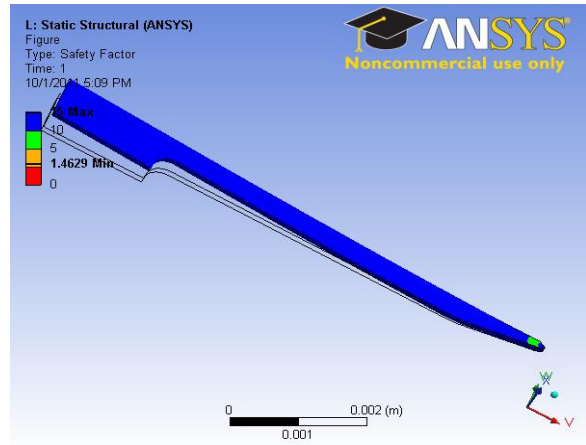
B-50µm



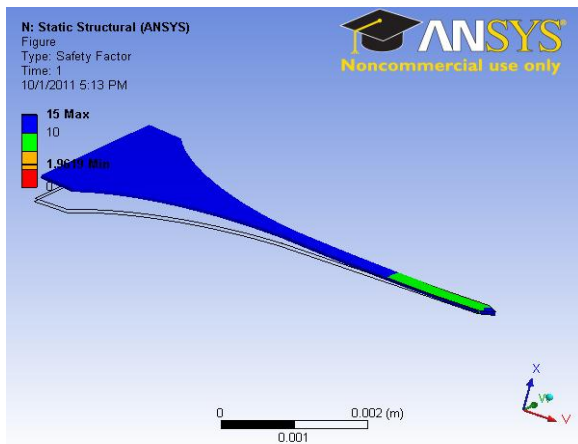
B-100µm



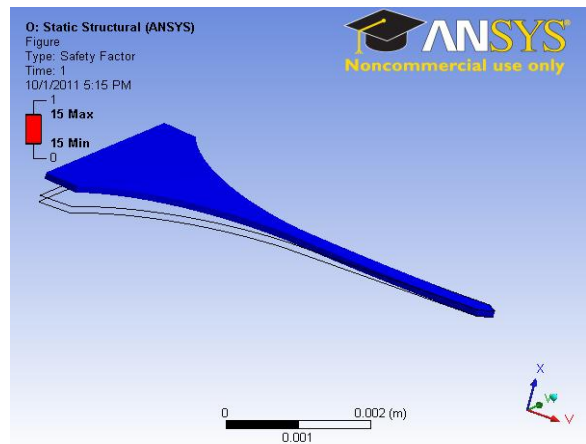
D-50µm



D-100µm

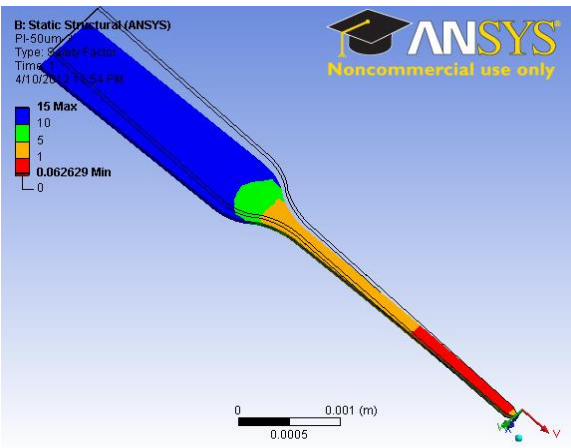


E-50µm

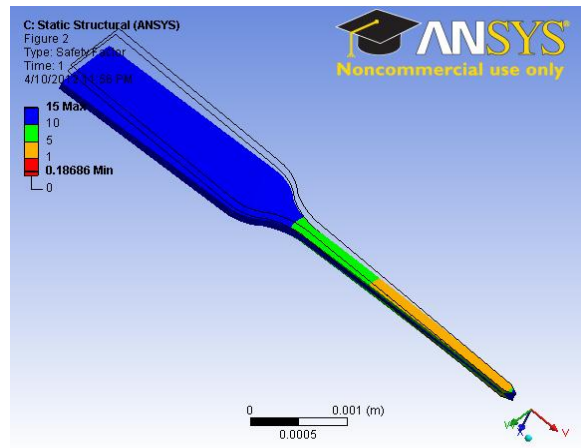


E-100µm

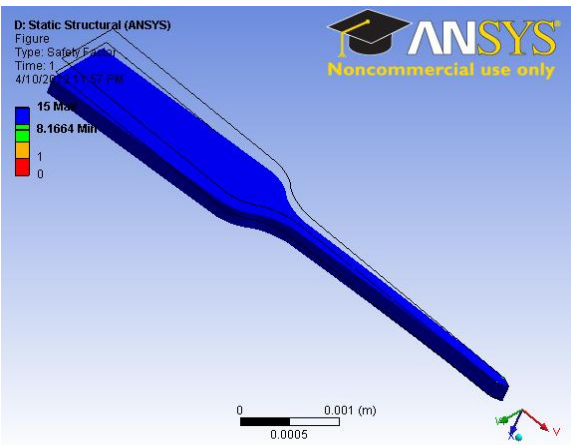
Table 5-10. Safety factor distribution for shear loading – Polyimide



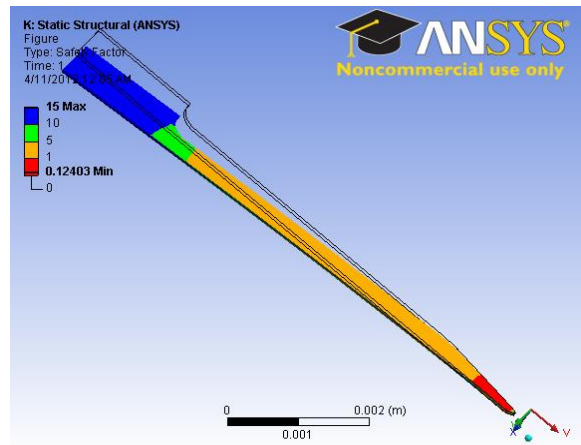
A-50µm



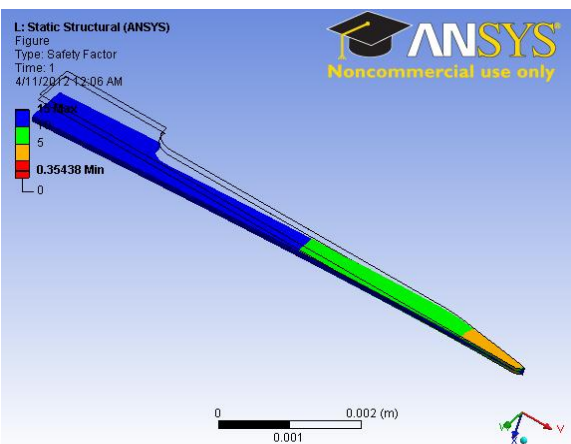
A-100µm



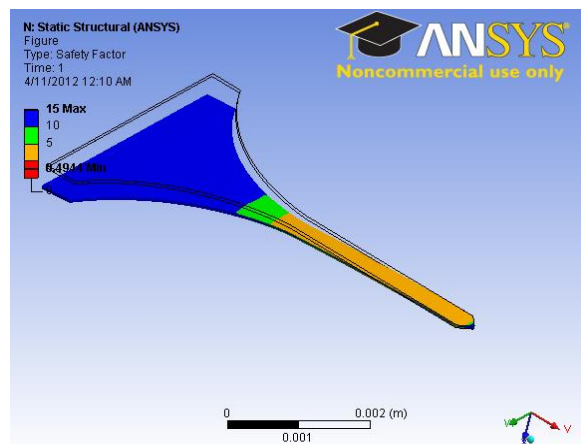
A-200µm



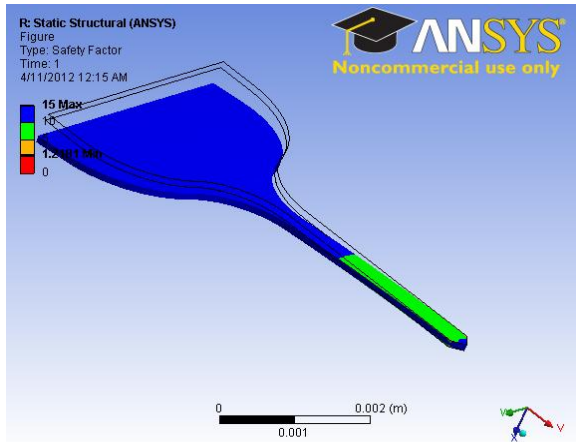
D-50µm



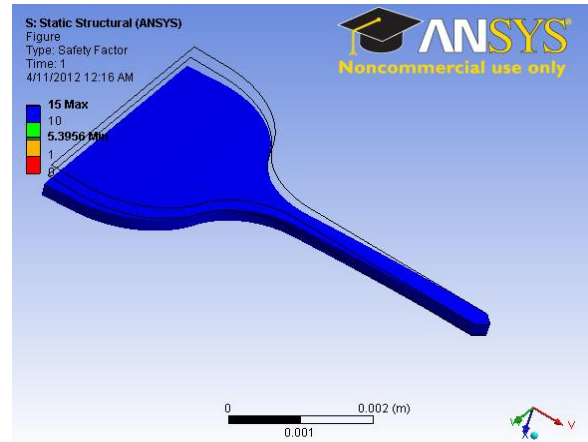
D-100µm



E-50µm



F-100µm



F-200µm

Table 5-11. Minimum thickness recommended for different electrode designs and materials (safety factor = 10)

Layout	Silicon	Stainless steel	Polyimide	SU-8
A	200µm	100µm	>200µm	200µm
B	200µm	100µm	>200µm	200µm
C	100µm	100µm	200µm	100µm
D	200µm	200µm	>200µm	200µm
E	200µm	50µm	200µm	200µm
F	200µm	50µm	200µm	200µm

5.5.3 Array shear loading

Mechanical modeling and simulation of single shaft electrodes exhibited that layouts A and B are competent to satisfy the mechanical requirements and electrode dimensions constraints. Layout B was preferred for microfabrication considerations and was chosen to create the multi shaft electrode which provides 2-D array of interface channels. The array was designed to have four shafts with inter-shaft distance of 1mm. The array was modeled to investigate its response to shear loading and 10mN force was applied normal to the electrode base while the shaft tips were fixed to realize fixed-free support conditions.

Forces were loaded in two different configurations; in the first model, it was applied to the base top edge, and in the second, the force was divided into 2 equal components, each was applied to the one of the base sides as shown in Figure 5-5. Safety factor distribution for silicon, stainless steel and polyimide structures are plotted in Table 5-12, Table 5-13 and Table 5-14 respectively. In comparison to single shaft layouts, the arrays demonstrated slight drop in the resistance to failure. The electrode

arrays experienced lower stresses when the forces were applied along the edge sides and this will influence the design of the insertion mechanism. However, stainless steel achieved the targeted safety factor at a thickness of $100\mu\text{m}$ compared to $200\mu\text{m}$ for silicon, and finally, polyimide demonstrated acceptable performance at $200\mu\text{m}$.

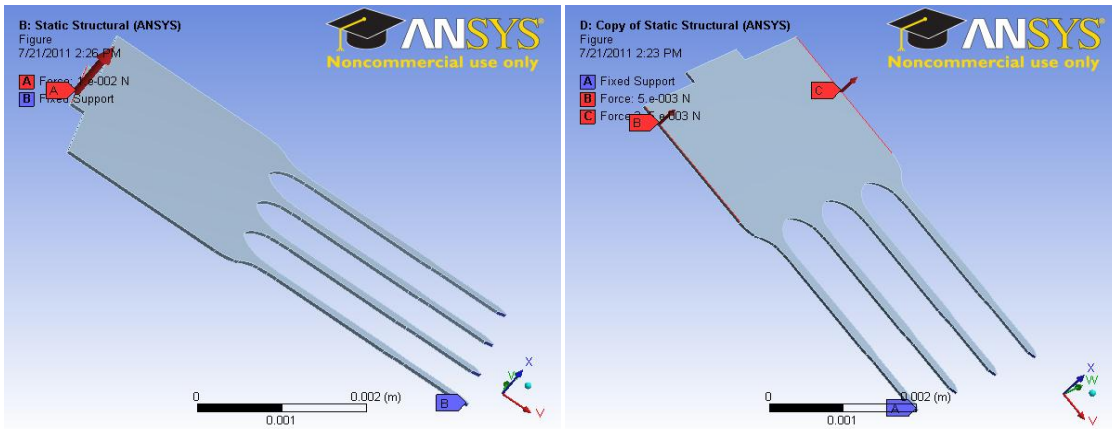
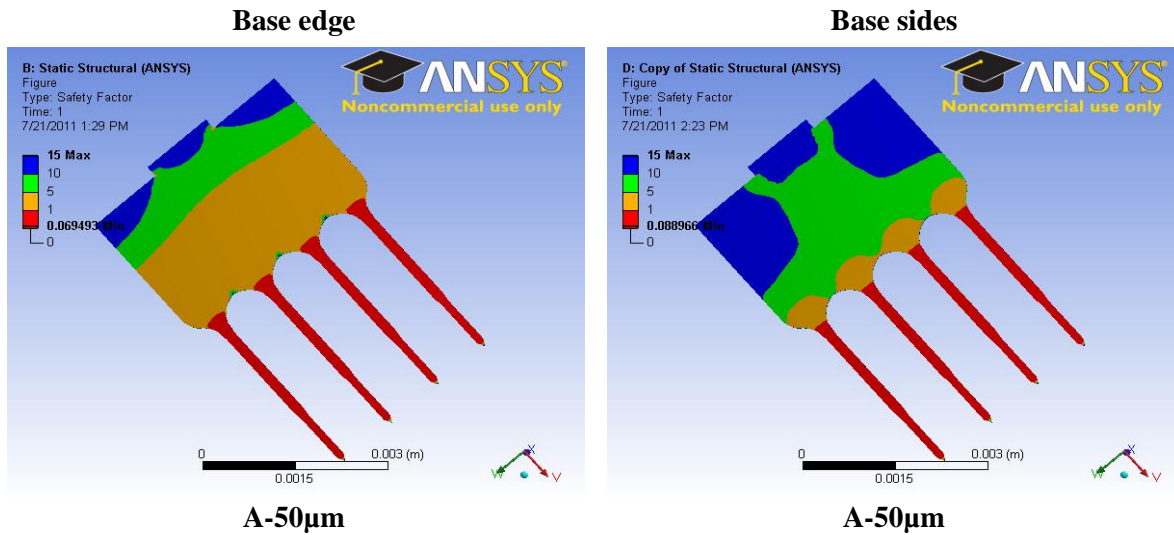
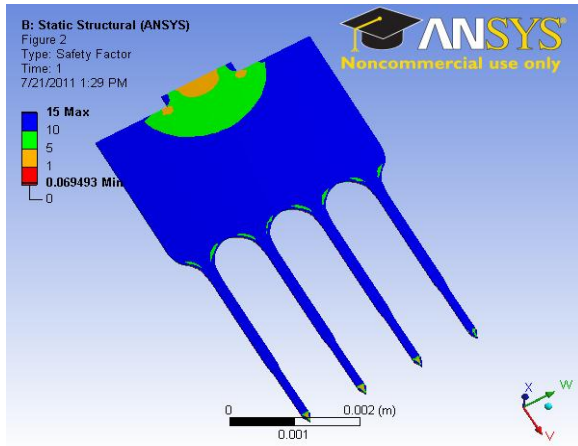


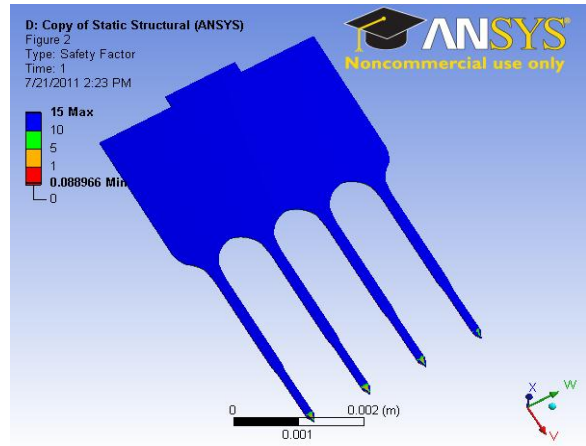
Figure 5-5. Array shear loading model, Left: Base edge loading, Right: Base sides loading

Table 5-12. Safety factor distribution for shear loading of electrode array – Silicon

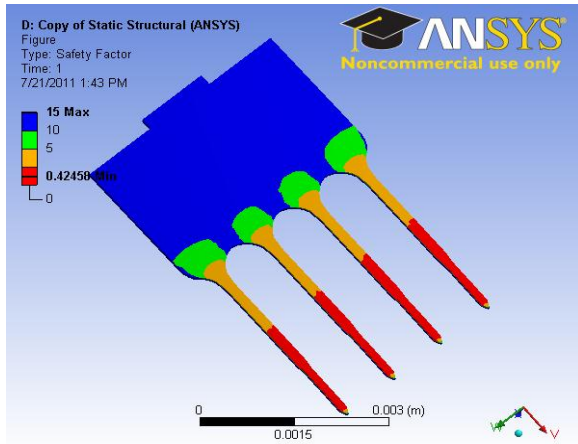




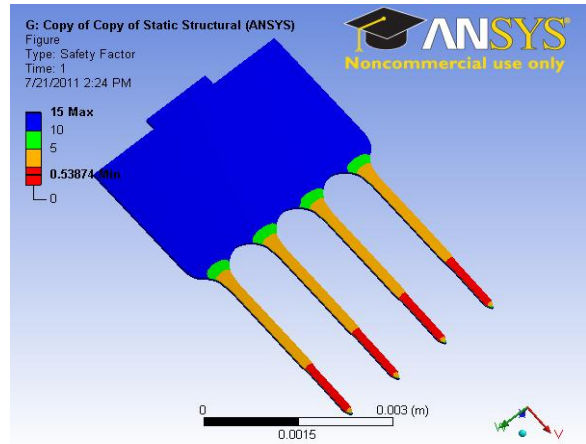
A-50µm – Back side



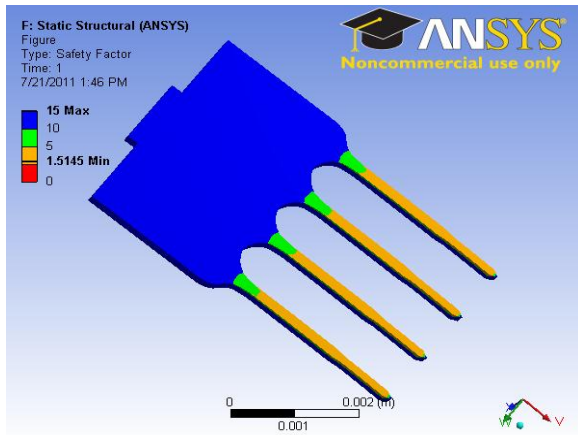
A-50µm – Back side



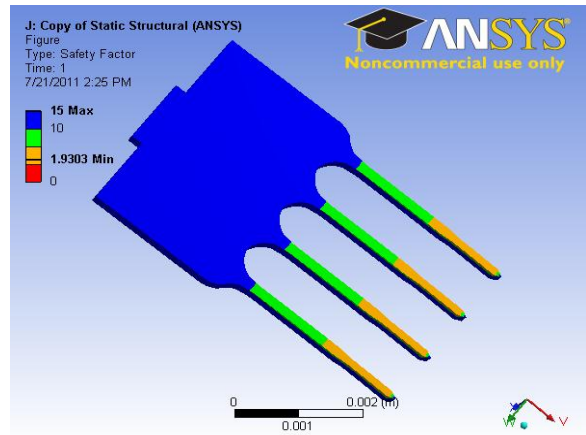
A-100µm



A-100µm



A-200µm

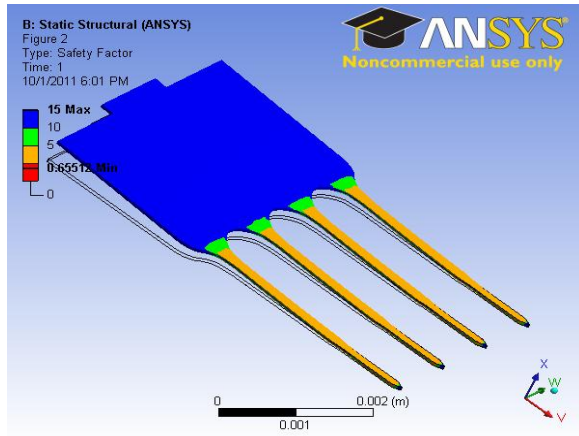


A-200µm

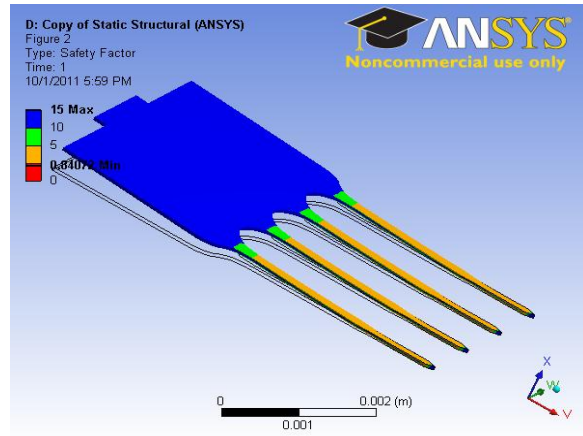
Table 5-13. Safety factor distribution for shear loading of electrode array – Stainless steel

Base edge

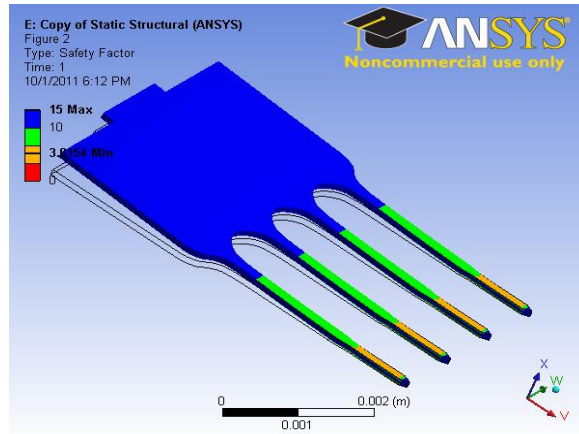
Base sides



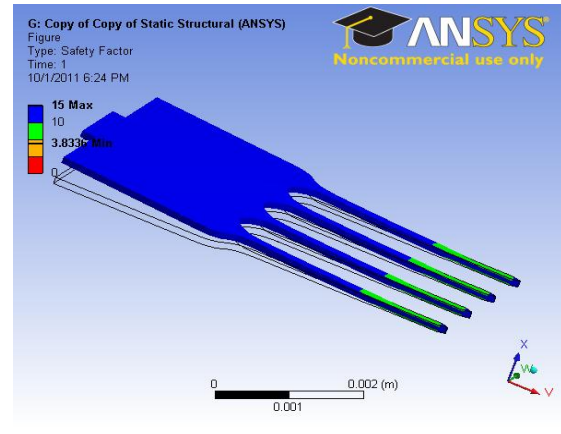
A-50µm



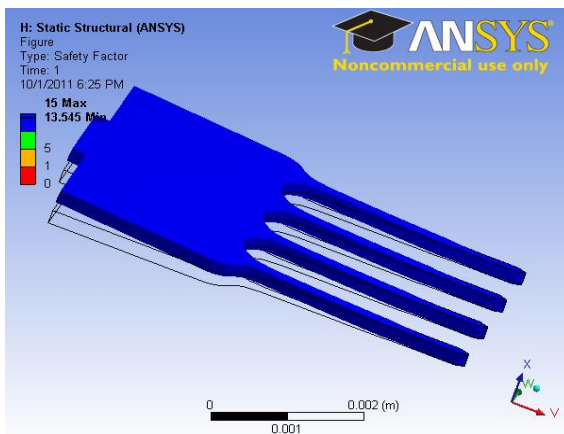
A-50µm



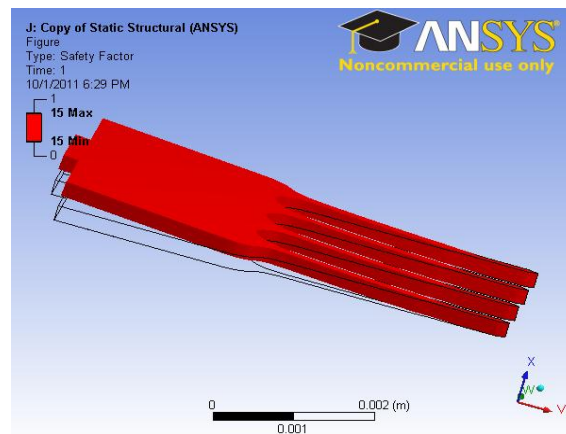
A-100µm



A-100µm

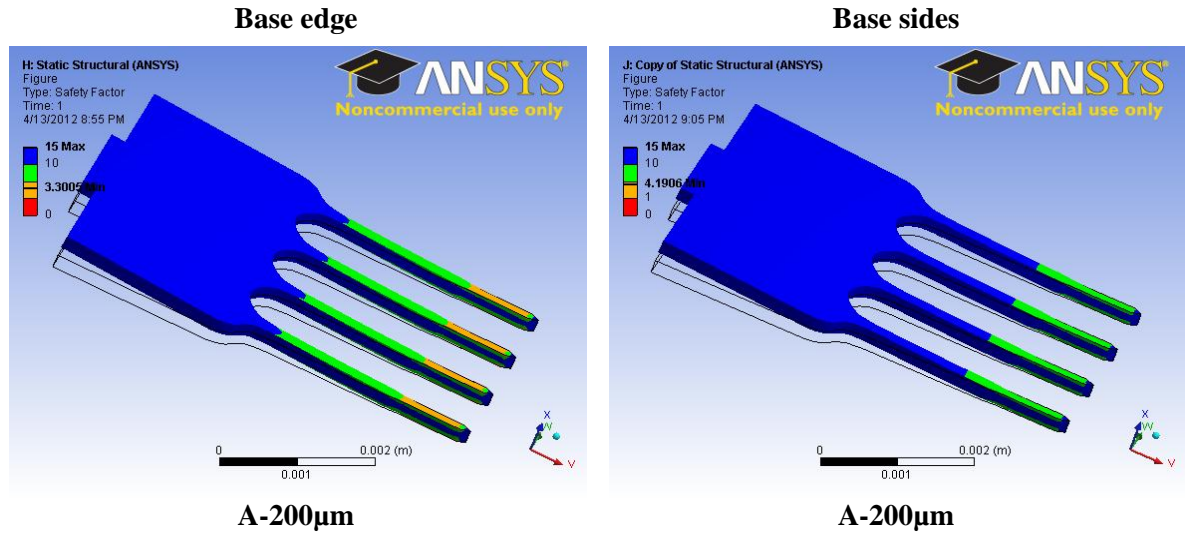


A-200µm



A-200µm

Table 5-14. Safety factor distribution for shear loading of electrode array – Polyimide



5.6 Mechanical Modeling of Brain Tissue

Tissue mechanical modeling was required for studying the electrode behaviour during insertion and the interaction between the electrode and tissue; and provided knowledge required to optimize the electrode mechanical design and the associated insertion mechanism. Human soft tissue is an incompressible material due to the high water content, and exhibits time independent (hyperelastic) and time dependent (viscoelastic) deformations. Hyperelasticity refers to materials which can experience recoverable large elastic strain. The viscoelastic properties can be neglected due to the fast deformation of the tissue in response to stresses [197][198], thus soft and muscle tissue can be modeled as hyper elastic materials, while bones and tendons are linearly elastic. Post-mortem mechanical properties of soft tissue are characterized by increased stiffness which makes in vitro characterization and measurements erroneous [199]. Yet, fresh and stored tissue demonstrates the same stress-strain relation pattern [200].

Brain tissue composition

Brain tissue can be divided into two structure layers; gray matter which is made up of neural cell bodies, unmyelinated processes and neuroglia, and white matter comprising myelinated axonal fibres, supporting cells and blood vessels. The brain is surrounded by meningeal membranes formed of three protective layers: dura matter (outermost layer), arachnoid, and cranial pia matter directly above the brain tissue.

Tissue response to insertion

During insertion, the electrode punctures the pia membrane which causes brain compression, dimpling and trauma [189][190]. Traumatic brain injury (TBI) studies [201] showed that cortical tissue compression between 1 to 5mm causes neural death, release of excitatory neurotransmitters,

significant cognitive deficits, necrosis of cortical tissue at the site of compression, and changes in blood flow. One way to reduce brain trauma is to reduce the pia structural integrity and stiffness of the pia by piercing, this also allows implanting microelectrodes with smaller footprint into the brain.

Rate dependence

The effective modulus of elasticity for viscoelastic materials is a function of rate of stress application which is represented by the electrode insertion velocity. Faster loading (insertion) raises the tissue elastic modulus inducing less strain [202][203][204]. The brain inertia resulting due to its density concentrates the electrode penetration force across the meninges layer; as a result, high insertion speeds can rupture the meninges, while low speeds elastically compress the brain tissue causing incomplete insertion and trauma [31]. Strain rate is considered fast at 500mm/min, medium at 5mm/min, and slow at 0.005mm/min, and the medium insertion rate is commonly used for insertion [200].

Brain tissue modeling

Experimental data were acquired from uniaxial, quasi-static cyclic tension/compression test at a speed of 5 mm/min for fresh brain tissue [200] and the results were processed using Ansys 12 curve fitting tool to identify the appropriate numerical brain tissue model. Several models were tested including polynomial, Mooney-Rivlin, Neo-Hookean, Yeoh and Ogden of different orders. A 3 parameters Mooney-Rivlin hyper elastic model provided the best match and valid material constants; whereas 2nd order polynomial and 5 parameters Mooney-Rivlin model produced good matches but generated negative material constants. The model parameters are listed in Table 5-15 and the data set is provided in Appendix E.

The electrode and skin were modeled to estimate the stresses acting on the electrode shaft during implantation and the FEM model is shown in Figure 5-6. The electrode modeled had a 3mm shaft and a rectangular cross section (50x100 μ m) which represents average dimensions for the actual electrode shaft, and half symmetry was used. The electrode was axially loaded with 1mN which is the force required for skin penetration and the electrode tip was constrained to displace along the direction of the penetration force. The tissue outer boundary was fixed and the electrode-skin interface was modeled as a rough contact. The simulation was executed for silicon and stainless steel electrodes, and the results for silicon are shown in Figure 5-7. The maximum principal stresses were estimated and the safety factor distribution was calculated for the electrode and plotted in Figure 5-7. The results show that the electrode shaft will survive the penetration forces, and similarly for stainless steel and polyimide.

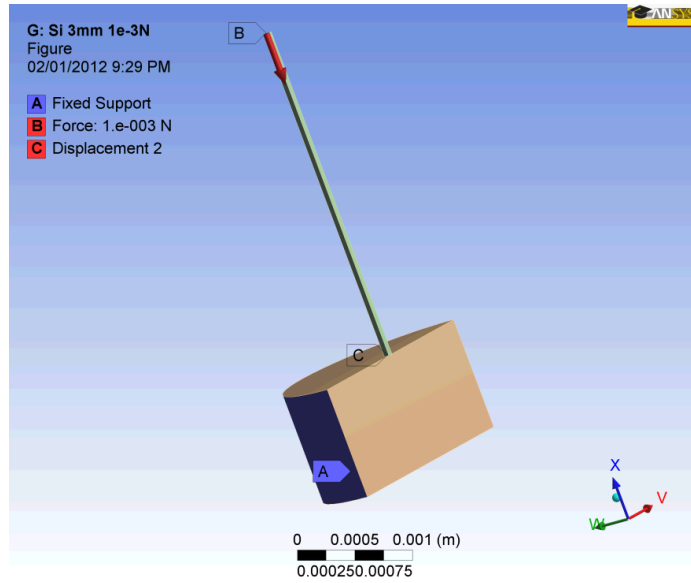


Figure 5-6. Electrode-skin penetration model

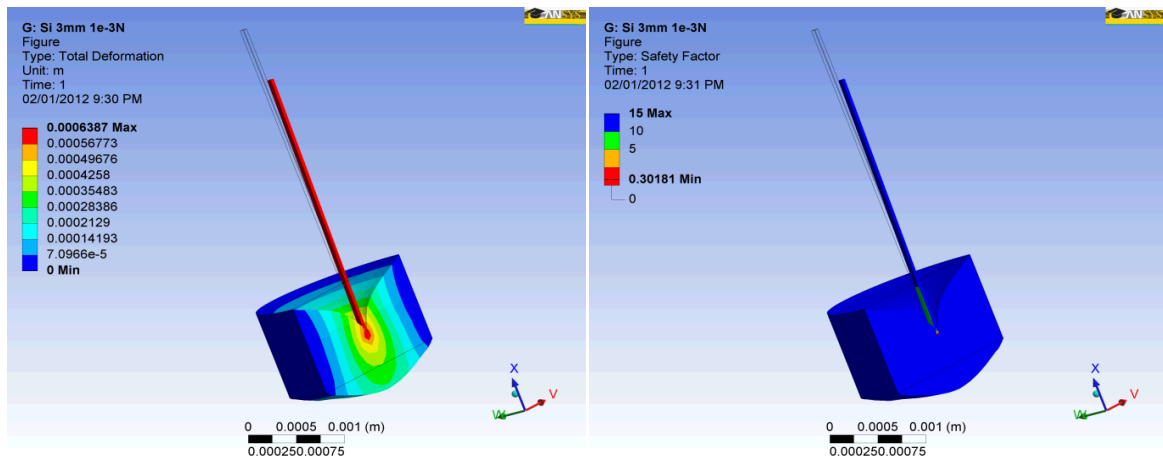


Figure 5-7. Simulation results for silicon shaft, Left: Deformation, Right: Safety factor distribution

Table 5-15. Three parameters Mooney-Rivlin hyper elastic model

C10	151.42	125.68
C01	42.262	51.579
C11	1046.2	2015.6
D1 (incompressibility)	0	0

5.7 Strain Relief Cross-sections

Implanted electrodes are usually tethered to electronic circuits attached to the skull, this makes the electrode shaft susceptible to dislocation and motion artifacts induced by tissue displacement (refer to section 2.4). The tethering effect could be resolved by modifying the electrode design to minimize stress transfer from the base to the shafts. A segment of the electrode stem was thinned to decrease its ability for stress transfer and the tendency to resist bending moments. Several cross-section modifications were proposed in Figure 5-8, and finite element models were created and simulated to estimate the electrodes deformation in response to 1mN shear force and the simulation model is shown in Figure 5-10. The model included a block to model the tissue support against the applied force, and the tissue block was modeled as described previously in section 5.6.

Figure 5-10 demonstrates the deformation of the different electrodes represented by the maximum displacement of the electrode base. The deformation of the original electrode design with a thickness of 125 μm was taken as a reference, and the results showed that design A with 75 μm deep trench exhibited maximum displacement which indicated its low ability to resist deformation and transfer stress to the shafts. The other designs exhibited comparable responses, and Figure 5-11 represents a comparison between the deformation ratio of the different layouts to the original cross-section, and the deformation ratio was calculated as:

$$\text{Deformation ratio} = \frac{\text{Maximum deflection of modified cross-section}}{\text{Maximum deflection of original layout}} \quad \dots (5.3)$$

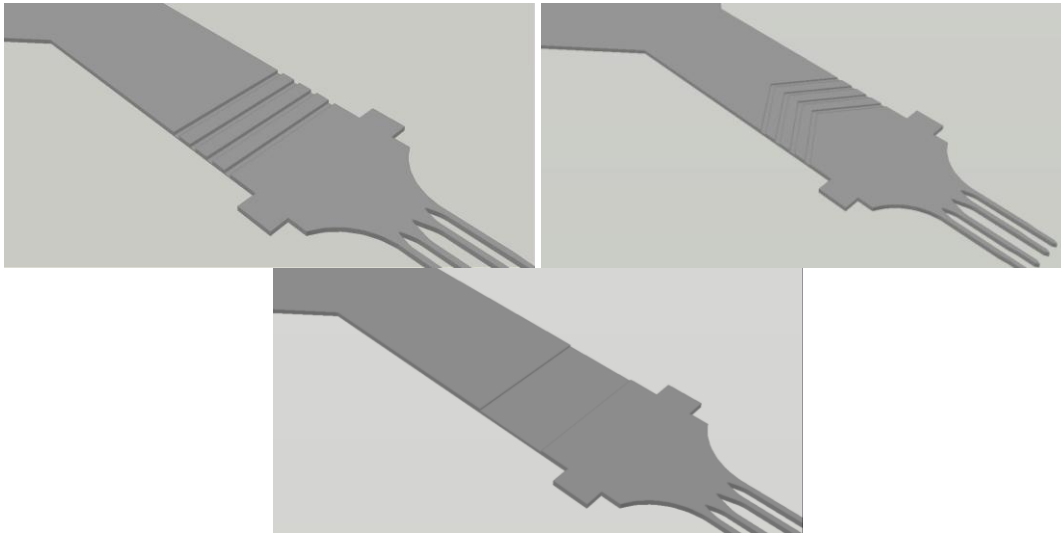


Figure 5-8. Modified cross-sections for strain relief

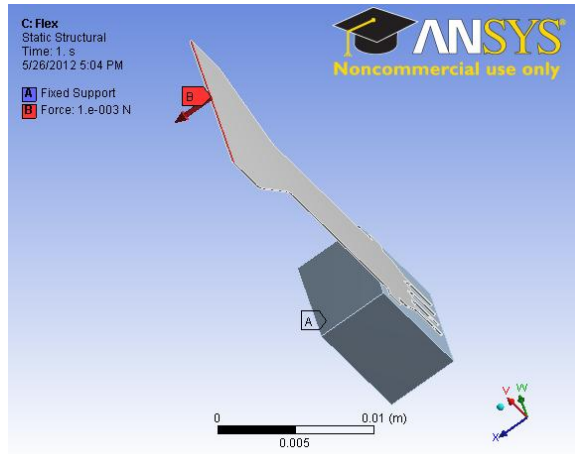


Figure 5-9. Flex cable simulation model

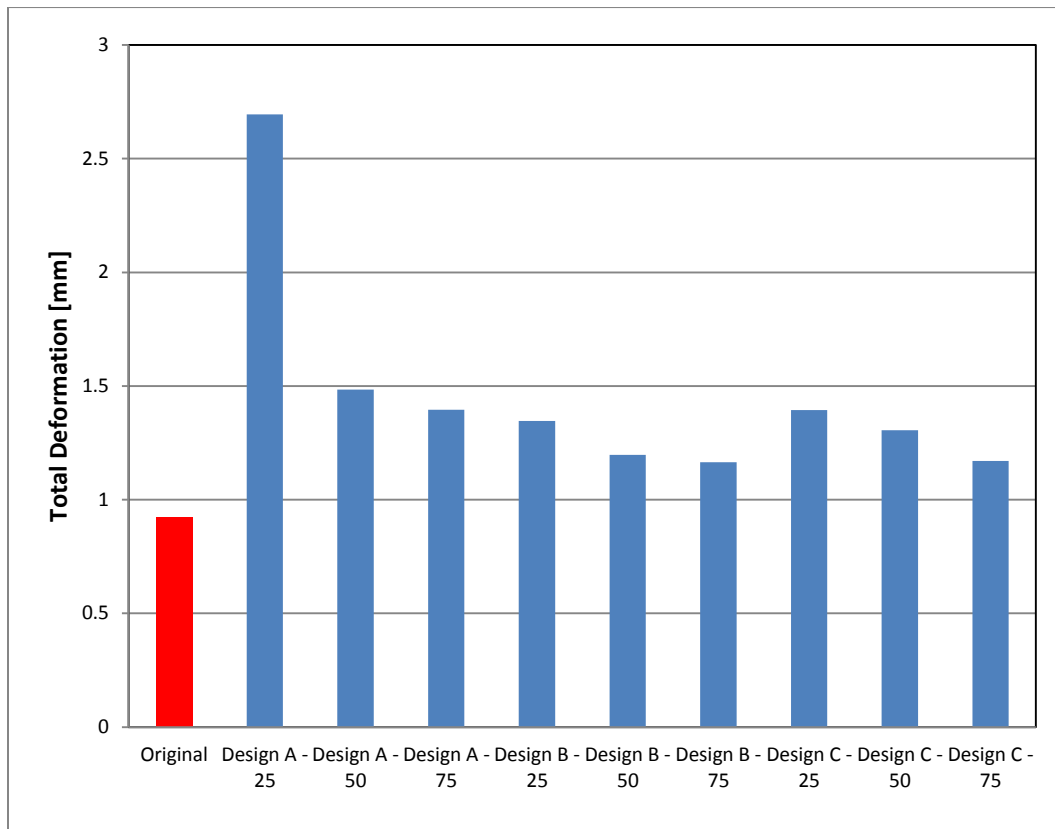


Figure 5-10. Total deformation of different modified cross-sections

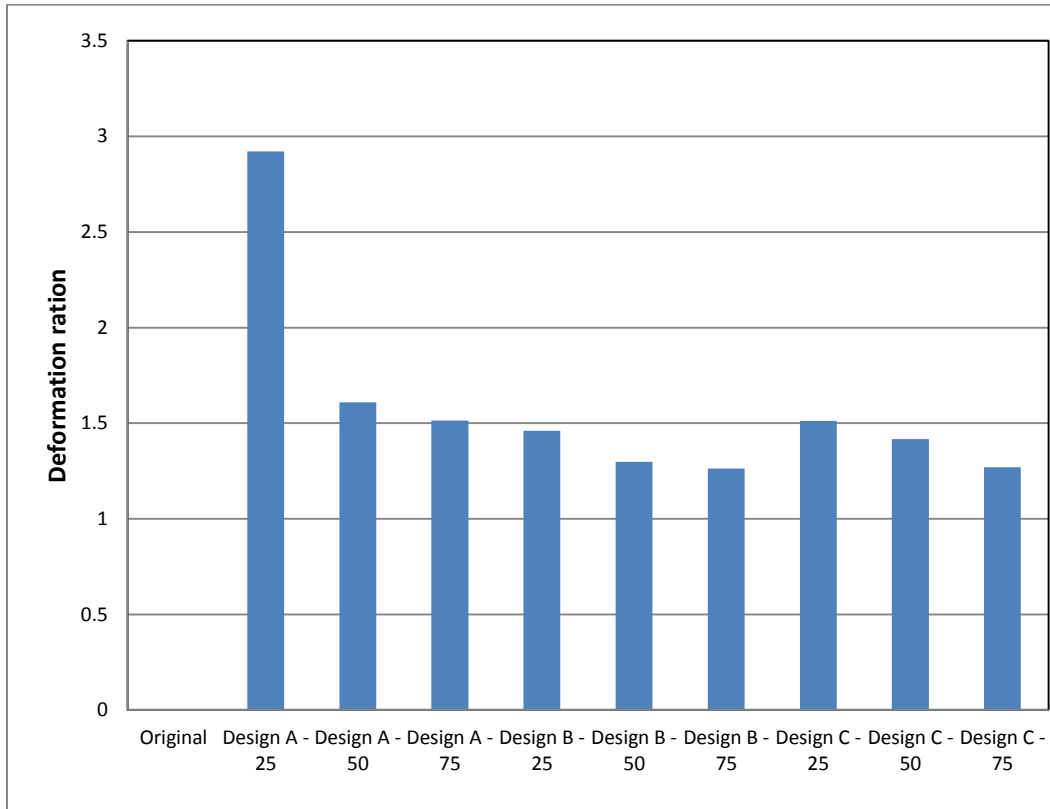


Figure 5-11. Comparing deformation ratios of different cross-section modifications

5.8 Conclusion

This chapter presented an elaborate discussion for the mechanical modeling and analyses of the electrodes and several prototypes were proposed (Table 5-2) and analyzed in pursuit of layouts that would satisfy the design requirements. A competent design would provide shaft surface that suffices accommodating more channels while minimize the footprint to reduce tissue trauma. Finite element models were created for the different layouts, and parametric and sensitivity analyses were executed to scrutinize the effects of the different design parameters on the electrode mechanical performance, including electrode materials, dimensions and geometry. Various analyses techniques were used in evaluating the electrode mechanical performance including: Eigen buckling analysis, linear static analysis with axial and shear loading, and failure analyses for brittle and ductile materials, and the qualified layout was used for the single and multi-shaft electrode implementation.

Silicon exhibited supreme resistance to buckling failure during implantation followed by stainless steel. On the other hand; the minimum thickness of a polyimide electrode to barely survive buckling was 100 μ m with a minimum safety factor of 2.2. Further analyses demonstrated that the electrodes are more vulnerable to failure due to shear loading which induces fractures. Shear analysis results were in favour of stainless steel electrodes due to its ductile properties, and polyimide designs

with thick cross-sections can replace stainless steel. The recommended minimum thicknesses for different layouts and materials were listed in Table 5-11. A quad shaft array electrode was formed using the competent single shaft layout and was modeled to study the effect of different support and loading techniques on the array mechanical performance. Finally, a comprehensive model integrating the electrode and brain tissue was developed to model the electrode-tissue interaction during penetration. In conclusion, the mechanical analyses results provided guidelines for the electrode design and material choice. A competent electrode layout was chosen for the single and multi-shaft electrode implementation. The mechanical modeling and analyses procedures are not limited to the electrodes introduced in this research, and can be customized for a wide range of designs.

Although the flexible electrodes were designed to minimize tissue damage, however, long term (up to 12 months) histological study is required to verify the electrode biocompatibility and the efficacy of the structure design in reducing post implantation trauma.

Chapter 6

Electrode Fabrication

6.1 Introduction

Several electrode designs were proposed to satisfy a range of design requirements and applications. Novel electrode architectures were proposed and required developing appropriate fabrication processes. Electrode fabrication started with simple structures comprising single metallization layer to calibrate the fabrication processes and equipment. The following step was to implement the more complicated designs with multiple layers. Although the objective was to implement the electrodes on flexible; however, the preliminary prototypes were fabricated on silicon substrates to verify the fabrication process. Then the final prototypes were implemented on flexible substrates which introduced several challenges including adhesion, patterning and etching high aspect ratio features on polymers, thermal expansion leading to loss of alignment, and samples handling and processing. Several techniques were developed to tackle practical issues including assembly and interconnection of electrodes to circuits and measurement systems. This required design and fabrication of customized components including carrier wafers, interconnect cables and printed circuit boards. Finally, an array assembly technique was developed to implement 3-D electrode arrays while keeping the overall footprint at its minimal. The presented technique was employed in creating the Waterloo Array demonstrating multi-dimension intra-cortical flexible array designed for long term neuro-interfacing.

6.2 Electrode Materials

Several materials were experimented to fabricate the different electrode components including structural, metallization, insulation and passivation layers. Brittle electrodes were made of silicon, while stainless steel and polyimide were chosen for the flexible structures. Isolation and passivation layers were made of silicon dielectrics (silicon-oxide and nitride) and polyimide thin films. The isolation layer thickness has to allow the reliable formation of the buried via using DC sputtering deposition. Different metals were tested for creating the metallization layers, for example aluminum, copper, chrome, gold and titanium, and the exposed pads were coated with gold or titanium to provide biocompatible tissue contact. The low resistance p-doped silicon wafers were passivated with a dielectric layer prior to metal deposition to eliminate short circuits. Flexible electrodes were fabricated on polyimide and stainless steel sheets, using polyimide thin films as the dielectric layers.

6.3 Simple Single Shaft Recording Electrodes

Simple layout recording electrodes were implemented to characterize and optimize microfabrication equipment and processes. These electrodes were not designed to satisfy the mechanical design requirements or improve the electrode functionality.

Polyimide electrodes

The structural layer of the preliminary electrodes was made of polyimide thin film spin coated on silicon carrier wafer. The carrier wafer was prepared by RCA cleaning and dipping in BHF bath to remove the native oxide layer and facilitate detaching the polyimide electrodes. Metal thin film was deposited and patterned to create the pads and routing tracks, and then polyimide passivation layer was deposited. The passivation layer was patterned to expose the metal pads and form the electrode contour. Polyimide was patterned using dry etching and aluminum hard mask. Metallization layers were made of multiple thin films; chrome (or aluminum) provided the thickness required for achieving low DC resistance, and gold (or titanium) thin film was deposited to provide biocompatible contact. The single shaft electrode presented in Figure 6-1 provided 12 recording channels on 3mm shaft with a width of 550 μm , and the pads were 20x20 μm . The structural polyimide layer was 12 μm which was not thick enough to realize a mechanically competent structure. The electrode shaft was expanded to 830 μm and accommodated 40 recording channels as shown in Figure 6-2. However, this design would not comply with the biomedical design constraints due to the exaggerated shaft dimensions which would yield remarkable tissue trauma.

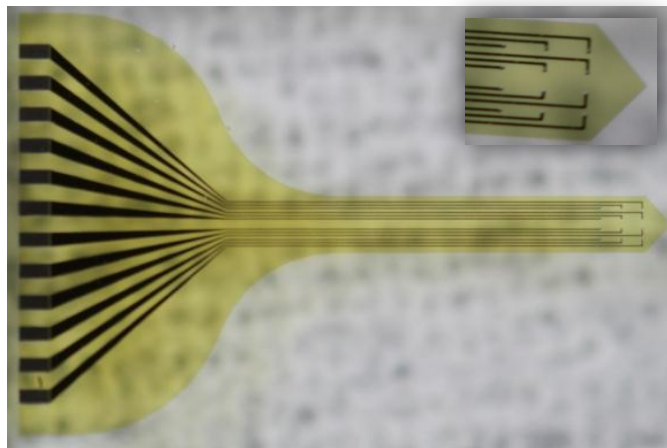


Figure 6-1. Single shaft polyimide recording electrode with 12 channels: $\tau = 12\mu\text{m}$, $w = 550\mu\text{m}$

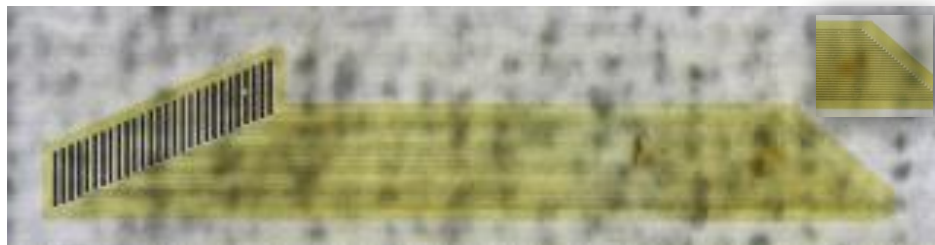


Figure 6-2. Single shaft polyimide recording electrode with 40 channels: $\tau = 12\mu\text{m}$, $w = 830\mu\text{m}$

Silicon electrodes

The simple single shaft layouts were implemented on 385 μm silicon wafers using surface micromachining and silicon bulk processing. Although silicon provided the required mechanical strength; however, its brittle characteristics imposed further mechanical design challenges. The substrate was cleaned and coated with chrome-gold-chrome metallization layer. After patterning the metal layer, dielectric film (silicon-oxide) was coated using plasma enhanced chemical vapour deposition (PECVD) and patterned using ion-assisted plasma etching (reactive ion etching RIE) to expose the interconnect and recording pads. Finally, aluminum hard mask was deposited and patterned to define the electrode contour for deep reactive ion etching (DRIE). After electrode release, the aluminum mask and the top chrome layer protecting the pads were etched to expose the gold pads, and the electrodes are shown in Figure 6-3.

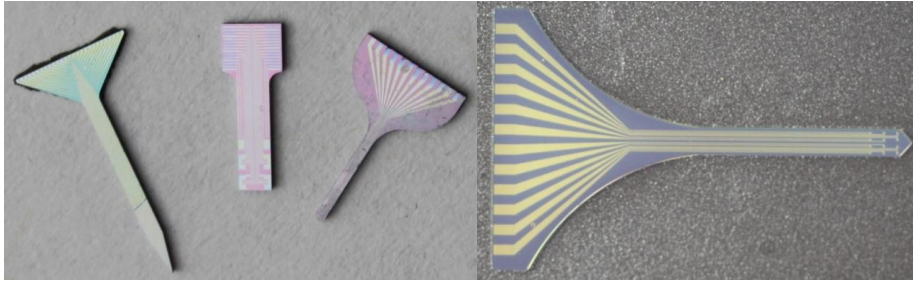


Figure 6-3. Simple single shaft silicon electrodes

An alternative layout with narrow shaft was developed, and two electrodes were designed to have 4 (Figure 6-4) and 7 (Figure 6-5) recording channels. The electrodes were implemented on a silicon-on-insulator (SOI) wafer with a 50 μm device layer. The 6mm shafts were 50 μm in thickness, and had widths of 110 and 200 μm for the 4 and 7 channels respectively (refer to section 3.4 for design details). The electrodes were fabricated using the previously developed silicon electrode process and an extra DRIE step was required to etch the back side of the SOI wafer using the oxide film as an etch stop layer.

6.4 Recording and Stimulation Electrodes

Recording/stimulation electrodes were elaborately discussed in section 3.11. The electrodes were implemented on flexible and brittle substrates using the fabrication procedures in section 6.3. The preliminary recording/stimulation electrode implemented on silicon substrate is shown in Figure 6-6, and the optimized packing layout is illustrated in Figure 6-7.

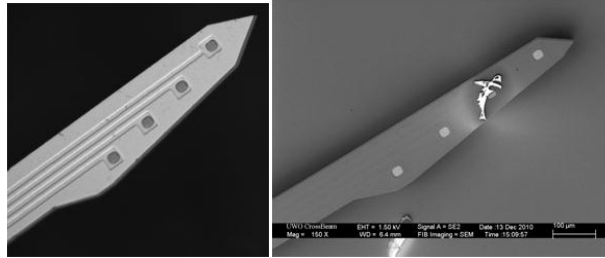


Figure 6-4. Single narrow shaft electrode with 4 channels (Layout A), Top: Before release, Left: Electrode tip, Right: SEM picture for the electrode tip

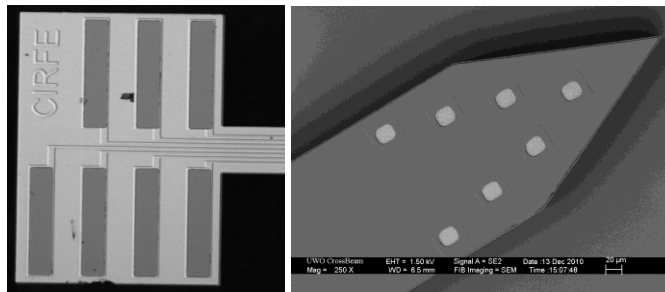


Figure 6-5. Single narrow shaft electrode with 7 channels (Layout B), Top: Before release, Left: Electrode base, Right: SEM picture for the electrode tip

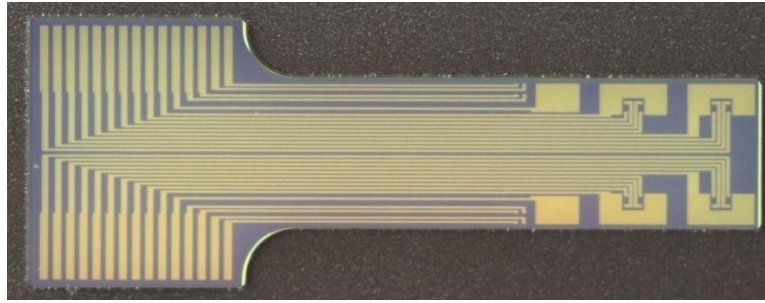


Figure 6-6. Single shaft silicon recording/stimulation electrode with 24 recording and 6 stimulation channels, $w = 1.1\text{mm}$

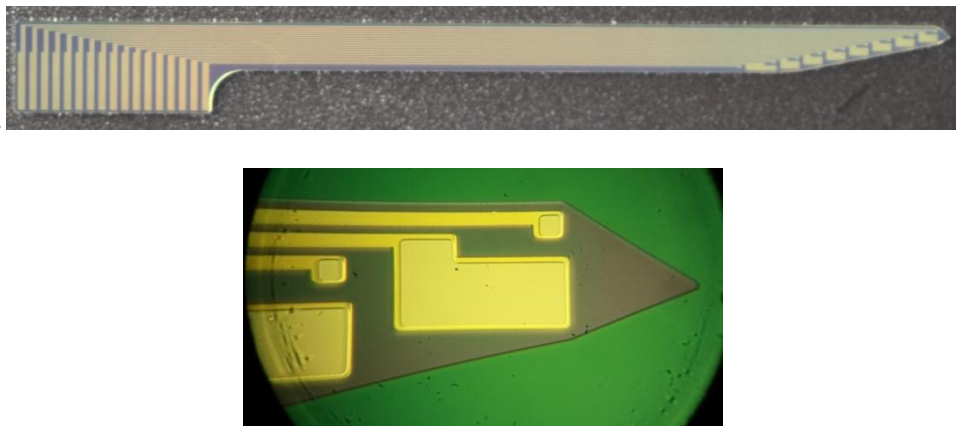


Figure 6-7. Optimized pad layout for stimulation/recording electrodes with 9 recording and 8 stimulation channels, $w = 380\mu\text{m}$, Top: Released electrode, Bottom: Electrode tip

6.5 Double Metallization Layer Stimulation Electrode

The double metallization layer stimulation electrode introduced in section 3.7 was developed to maximize the number of stimulation channels per shaft without increasing the electrode dimensions. The proposed electrode layout was implemented using novel architecture in which the metal structures were divided among two separate layers. The first layer formed the routing tracks and the other carried the pads, and the associated tracks and pads were connected using buried vias formed in the intermediate insulation layer. The electrode was implemented on silicon as well as polyimide substrates.

6.5.1 Silicon electrodes

The silicon electrode was fabricated on $385\mu\text{m}$ p-doped silicon wafer, and the experimental DC resistance measurements (section 6.5.3) stipulated the need to passivate the doped wafer to overcome its low resistance. The wafer was coated with 300nm silicon-oxide (dielectric-1) and the first

metallization layer (metal-1) was deposited and patterned. Metal-1 layer thickness ranged from 300 to 500nm and was made of aluminum. Metal patterning steps are shown in Figure 6-8, Figure 6-8-Left and Middle demonstrate the patterned photoresist mask, and the etched metal tracks are shown in Figure 6-8-Right. The second dielectric layer (dielectric-2) isolated the routing tracks and had a thickness of 350nm. Dielectric-2 was patterned to create the buried vias using RIE and aluminum hardmask, and the vias are shown in Figure 6-9-Left. In another run, the vias were formed using photoresist mask and wet etching in buffered hydrofluoric acid (BHF). However, the oxide vias suffered undercuts observed as colour gradients in Figure 6-9-Right. The over etched vias exposed the underlying tracks causing short circuits after depositing and patterning the second metallization layer. The short circuits were detected by measuring the DC electrical resistance between adjacent tracks which dropped from open circuit to $\sim 3.7\text{K}\Omega$. In conclusion, dry etching using RIE was preferred.

Via design was modified (refer to section 3.8) according to the DC resistance measurements results (refer to section 6.5.3) and was expanded from $6\times 100\mu\text{m}$ to $30\times 100\mu\text{m}$. The routing tracks tips were altered to match the modified via design as shown in Figure 6-10 and the RIE etched vias are demonstrated in Figure 6-11. The second metallization layer (metal-2) comprised multiple thin films; starting with 800nm aluminum film formed using DC sputtering deposition to maintain good step coverage, and followed by deposition of chrome (30nm) and gold (50nm) to provide biocompatible interface. Metal-2 was patterned to create the exposed pads representing each channel, and the pads established contact with the associated tracks on Metal-1 through the buried vias. A final dielectric passivation layer (silicon-oxide or polyimide) can be coated and patterned to expose the pads, provide additional protection to the electrode surface and improve resistance to water uptake and delamination. Finally, the electrode contour was patterned and released using aluminum hardmask and standard Bosch silicon deep reactive ion etching (DRIE) process. Figure 6-12 and Figure 6-13 demonstrate the different components on the electrode shaft including routing tracks, buried vias and stimulation pads. The released electrodes of different designs (single, double and quad shafts) are presented in Figure 6-14 through Figure 6-19.

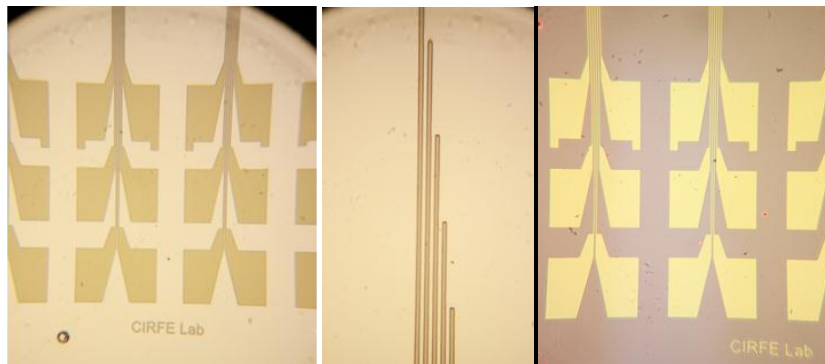


Figure 6-8. Metal-1 patterning, Left and Middle: Photoresist mask (tracks), Right: Metal-1 after etching (interconnect pads)

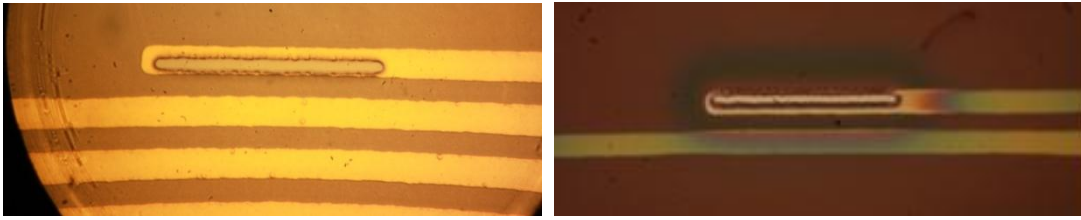


Figure 6-9. Patterned vias, Left: dry etching using RIE, Right: wet BHF etching

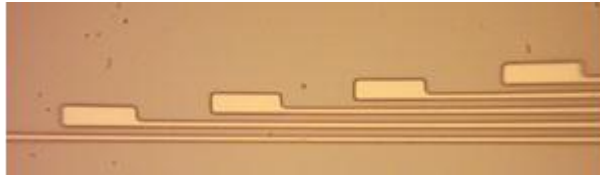


Figure 6-10. Photoresist mask for modified Metal-1 track tips



Figure 6-11. Modified via patterned using RIE in dielectric-2

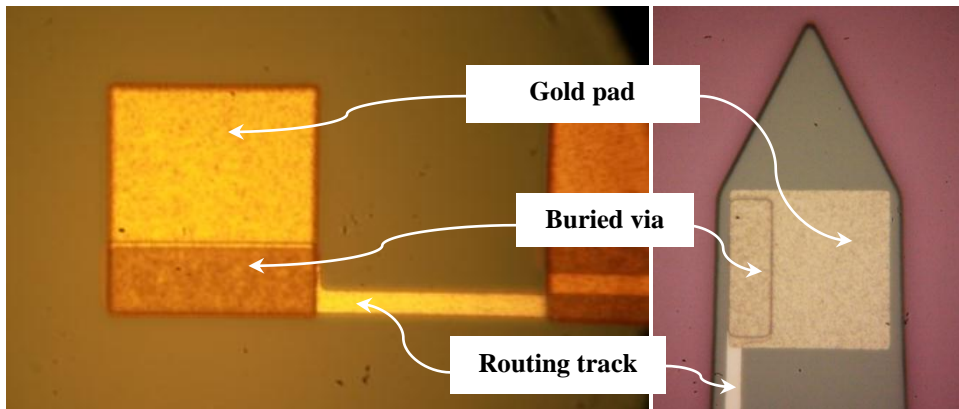


Figure 6-12. Modified vias and patterned pads, Left: Before electrode release, Right: After electrode release

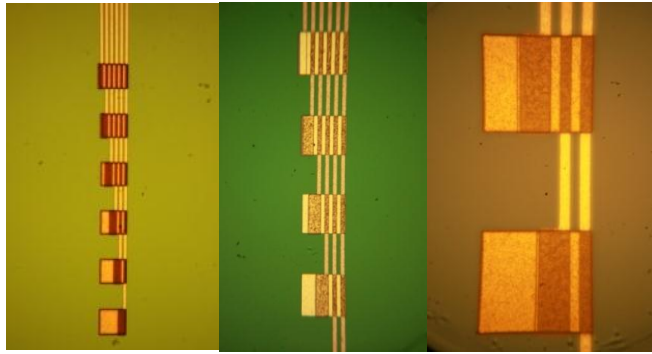


Figure 6-13. Patterned metal layers demonstrating stimulation pads and routing tracks

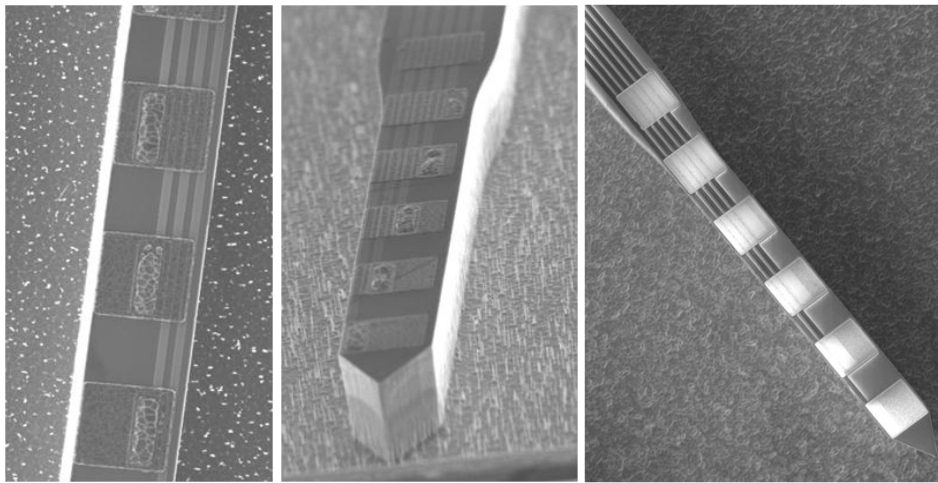


Figure 6-14. Double metallization layer stimulation electrode: SEM pictures for the electrode shaft demonstrating stimulation pads, vias and routing tracks



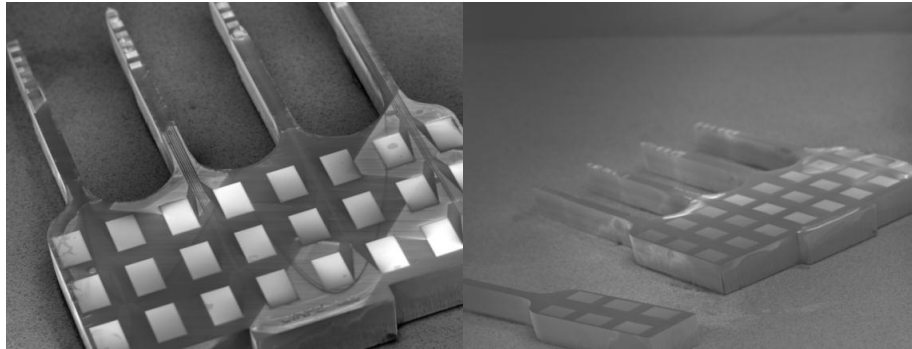


Figure 6-15. Double metallization layer stimulation electrode: SEM pictures

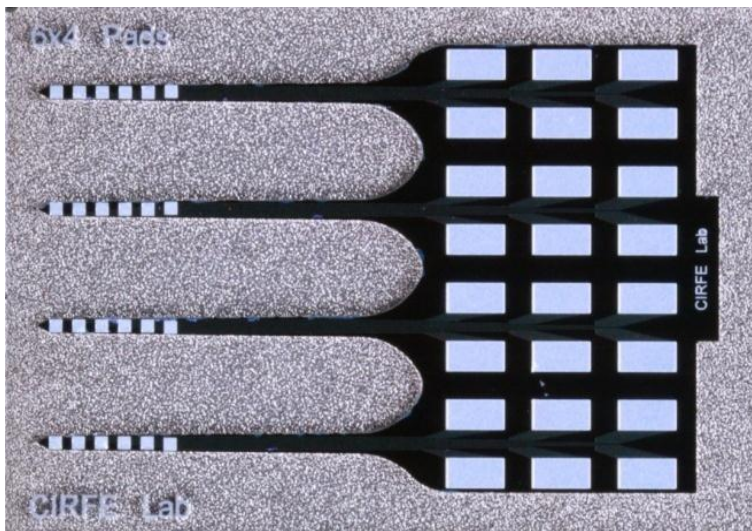


Figure 6-16. Double metallization layer stimulation electrode: Quad shafts (aluminum pads),
 $\ell_{\text{shaft}} = 3\text{mm}$, $w = 130\mu\text{m}$, pads = $110 \times 110\mu\text{m}$

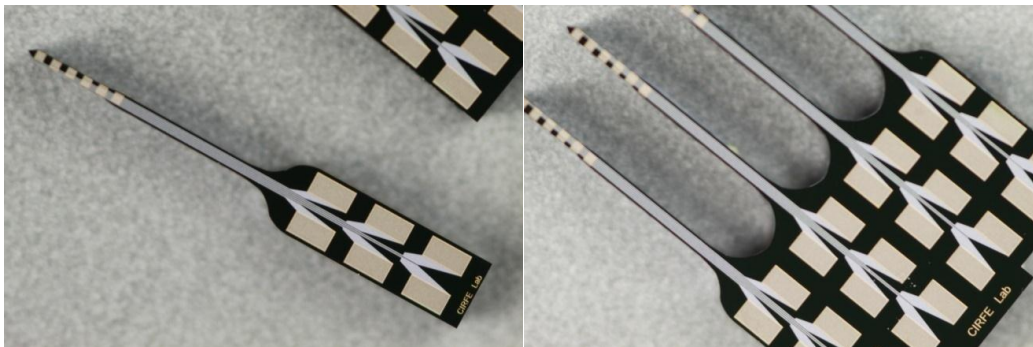


Figure 6-17. Double metallization layer stimulation electrode: Single and quad shafts (gold pads)

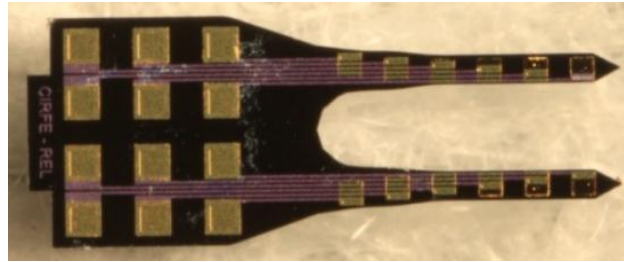


Figure 6-18. Double metallization layer stimulation electrode: Double shaft electrode for small rodents (gold pads), $l_{\text{shaft}} = 1\text{mm}$

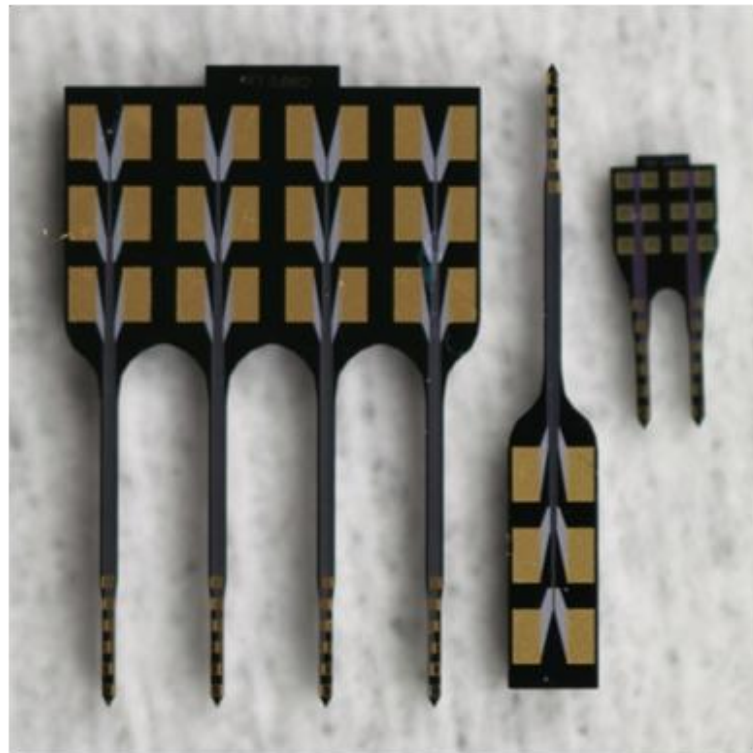


Figure 6-19. Double metallization layer stimulation electrode: Ensemble of different layouts

6.5.2 Stainless steel

Metal sheets were proposed for the flexible electrode implementation to overcome the structural drawbacks of brittle silicon electrodes (refer to Chapter 5). Stainless steel alloy 304 was chosen as the electrode structural layer because of its biocompatibility and mechanical strength. The metal sheet was washed in pure acetone and IPA then a passivation layer of polyimide (PI-2562) was spin coated. The first metallization layer was deposited and patterned to form the tracks, and then the second dielectric layer (polyimide) was spin coated and patterned using RIE and aluminum hard mask to

create the buried vias. Finally, the second metallization layer was deposited and patterned to create the exposed pads. The substrate had rough and shiny surface which camouflaged the patterned alignment marks within the shiny substrate background. Several opaque dielectric coatings were experimented to overcome the metal sheet shiny finish including copper phthalocyanine (CuPc), acrylic paint and polyimide modified with dies. However, the thin spin coated layers were translucent in the bright light of the alignment microscope. Finally, alignment was successfully done using high magnification alignment microscopes (high magnification microscopes were not available when fabrication started).

Metal substrate dicing and electrode release was major unresolved fabrication challenge that terminated the process. Metal thin films can be anisotropically etched using chlorine-based RIE or laser cutting; however, RIE etching depth is limited by the mask thickness and not applicable for 50 μ m sheets. In addition, laser energy required for metal ablation was high enough to damage the patterned features on the electrode surface.

6.5.3 Electrode DC resistance measurement

The electrodes were visually inspected during fabrication and tested for open and short circuit faults using microprobe station, controlled voltage source and ammeter. I-V characteristic curves were plotted to estimate the track resistance, resistance between adjacent tracks and pad-to-substrate resistance. Figure 6-20 demonstrates the I-V characteristic curves of the silicon electrodes fabricated on p-doped silicon wafers and the average DC channel resistance ranged from 1.6 to 2K Ω . The track-to-track resistance was anticipated to be open circuit; however, the measured resistance had an average value of 35K Ω which inferred resistive connectivity between the adjacent tracks through the structural layer. The fabrication recipe was modified and the wafer was passivated prior to metal deposition, and perfect isolation between the tracks was achieved. The double metallization layer electrode architecture was successfully implemented; however, the track DC impedance exhibited unanticipatedly high average resistance of 2.2K Ω . The high resistance was hypothesized to be the result of poor electrical connection between metal-1 and metal-2 layers. This was a result of poor via formation and filling due to the resolution limitation of the photolithography process. This was caused by t during fabrication. The patterned metal-1 layer is shown in Figure 6-8 and a close up picture of the patterned via is shown in Figure 6-9. The buried via design was altered to improve the electrical connectivity between the metallization layers (more details available in section 3.8) and the modified via is shown in Figure 6-10 and Figure 6-11.

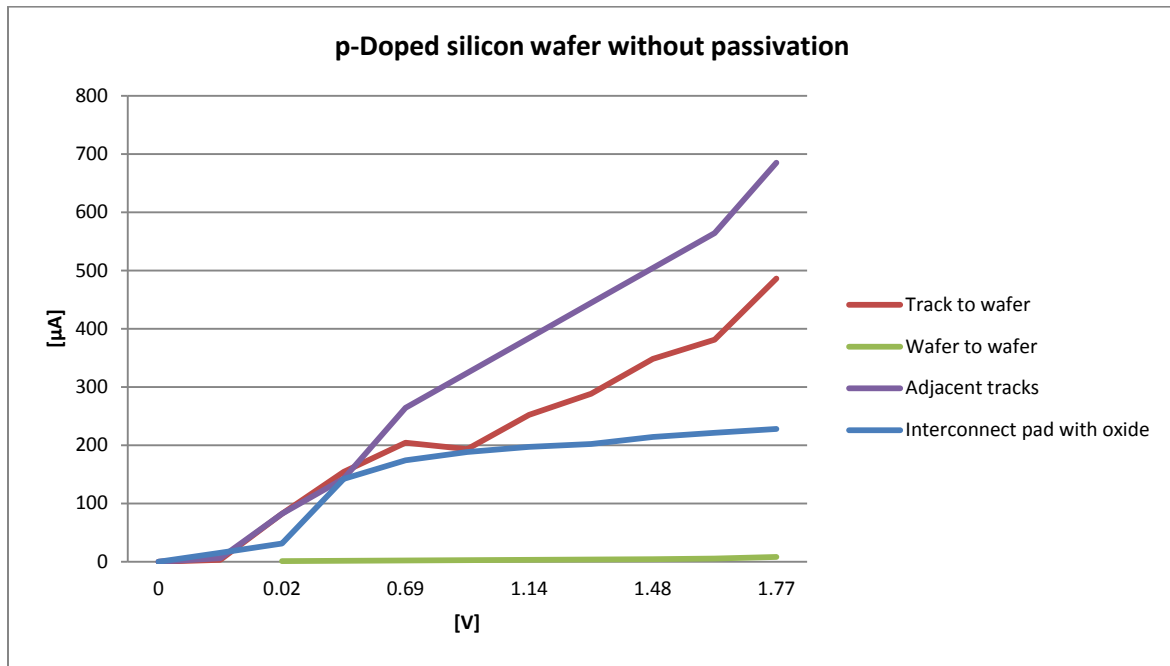


Figure 6-20. I-V characteristic measurements for p-doped silicon wafer without passivation

6.6 Polyimide Electrodes with Integrated Cables (Flex Electrodes)

The Flex electrode was created to include an integrated flexible interconnect cable, and the design was elaborately discussed in section 3.14. Polyimide offers flexibility, chemical stability and biocompatibility, and was chosen to create the structural, dielectric and passivation layers. The electrode was fabricated on 125μm Polyimide sheets, and the substrate was cleaned with acetone and IPA. Thin film of polyimide (PI-2562) was spin coated to provide a clean surface and improve adhesion to subsequent layers. The first metallization layer (Metal-1) was formed of chrome (200nm) and gold (700nm) films and was patterned to create the routing tracks. Chrome was used as an adhesion layer for gold, and a thick film was deposited to overcome surface roughness of the substrate sheet. The second dielectric layer spin was coated and patterned to create the buried vias using RIE and aluminum hardmask. Finally, the second metallization (Metal-2) layer was deposited (chrome-gold: 200-700nm) and patterned to create the exposed pads.

The electrode was released using two different methods: Deep reactive ion etching process was developed to etch deep structures in polyimide. The developed recipe required high vacuum (5mTorr), high ICP power (2KW), temperature controlled electrode (5°C) and 1μm aluminum mask. The process successfully etched through 125μm polyimide substrate maintaining vertical walls with undercut less than 3μm. Laser dicing was also used for releasing the electrodes [207] and it waived the need for patterning a hard mask. Nevertheless, laser alignment had large error margin and the electrode contour was expanded by 30μm to avoid damaging the patterned features by the laser beam heat wave. The size expansion added extra 60μm to the shaft width, which dropped to 30-40μm after

scanning with $\Phi 50\mu\text{m}$ laser beam. The laser diced quad shaft Flex electrode is shown in Figure 6-21, and Figure 6-22 demonstrates close up views of the shaft showing the tracks, pads and vias.

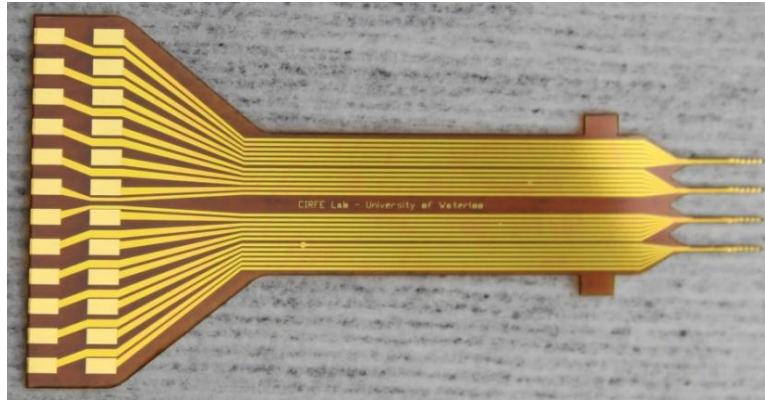


Figure 6-21. Laser diced Flex quad shaft stimulation electrode

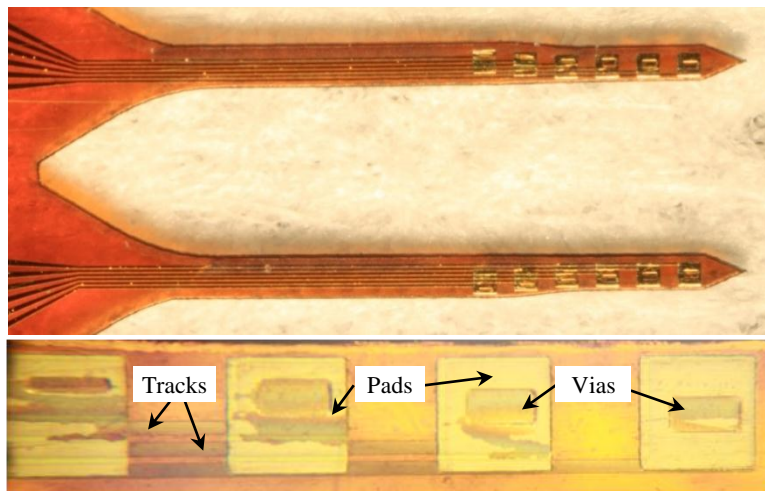


Figure 6-22. Close up views of the electrode shaft, the bottom figure is a dark field image for the shaft showing the pads, tracks and modified vias

6.7 Multi-composite layer Recording Electrodes

The multi-composite layer electrode architecture is a novel design created to multiply the number of channels on recording electrodes without expanding the shaft width, and the electrode design is elaborately discussed in section 3.12.

6.7.1 Fabrication procedure

The electrode was implemented on silicon substrate and the wafer was preconditioned with dielectric passivation (dielectric-1) layer to provide electrical insulation, and this was followed by depositing and patterning the composite layers. Each composite layer comprised multiple metallization thin films and a dielectric coat. The metal layer was made of three thin films, starting with chrome (300nm) as the main metal layer, then gold (50nm) to provide biocompatibility and finally titanium (50nm) as an adhesion layer to the subsequent layer. The metallization layer can also be made of chrome and titanium, and chrome is required to passivate the oxide during titanium wet etching due to the presence of HF acid in titanium etchant. Silicon-oxide (300nm) formed the dielectric layer and could be replaced with silicon-nitride. There were two methods to pattern the dielectric layers and expose the pads, either by patterning each dielectric layer individually or through single patterning step after depositing the topmost dielectric layer. Individual layer patterning is less susceptible to alignment mismatch but adds more photolithography steps, and extra masking steps are required to avoid redeposition of dielectric films on the exposed pads. On the other hand, single step patterning was prone to the propagation of alignment errors throughout the different composite layers. Figure 6-23 demonstrates three groups of patterned tracks and pads, each belonging to a different composite layer. Windows were etched in the oxide layers using aluminum hard mask and RIE as shown in Figure 6-24. Finally, the electrode contour was patterned and etched using DRIE and aluminum hardmask, and the released electrode is presented in Figure 6-25.

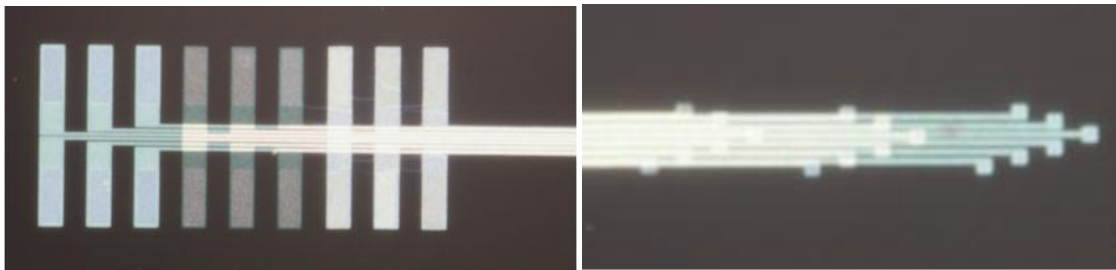


Figure 6-23. Multi-composite layer recording electrode, Left: Interconnect pads, Right: Recording pads

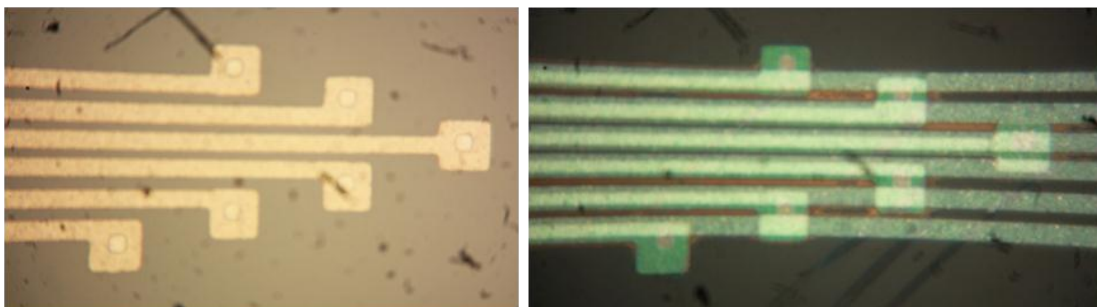


Figure 6-24. Exposed recording pads with etched windows in the oxide layers

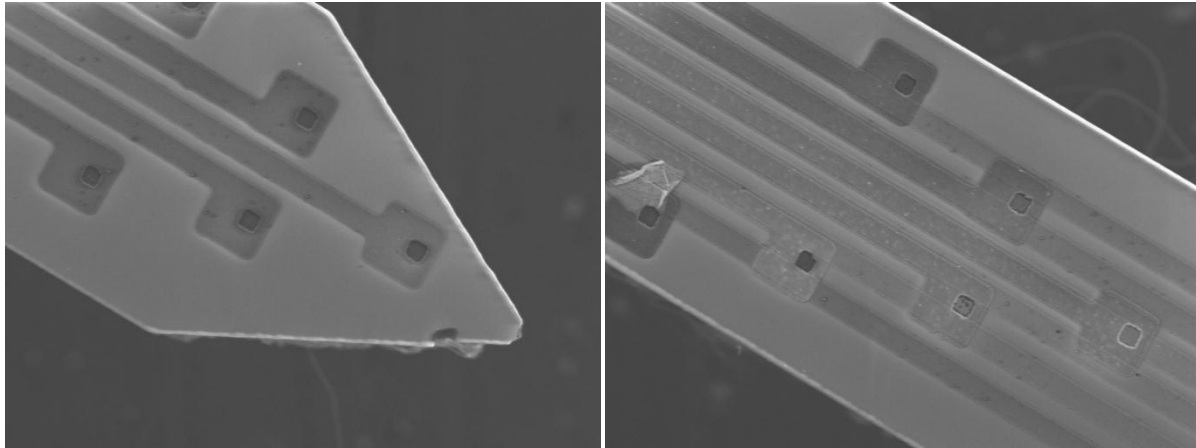


Figure 6-25. SEM pictures for the multi-composite layer electrode, Left: Electrode tip with the bottom most composite layer, Right: Electrode shaft with tracks belonging to the bottom most composite layer and pads of the intermediate layer

6.8 Carrier Wafers and Interconnect Cables

Carrier wafers

Carrier wafers were designed to facilitate electrode handling and mating to circuits, and several designs were implemented for the quad shaft, small rodent dual shaft and flexible electrodes with integrated cables (refer to section 3.13). Silicon was chosen as the substrate material because of its mechanical strength and easy processing.

The quad shaft electrode carrier wafer is shown in Figure 6-26-Left and had 100 μm deep groove for electrode alignment. The wafer had through holes to thread the lead wires and create reliable bonding and the drilling holes markers are shown in Figure 6-26-Right. The wafer was passivated with silicon-oxide and the pads were exposed using RIE etching and hardmask. The wafer dicing and through hole drilling were done using laser micromachining and the design was implemented on 285 μm silicon wafer to be able to drill the high aspect ratio holes. The carrier wafer was fragile and not reliable. The carrier wafer can be implemented on a 385 μm substrate and the fabrication process can be modified by replacing laser dicing with DRIE and the through holes by pads for surface mounting the lead wires or connectors.

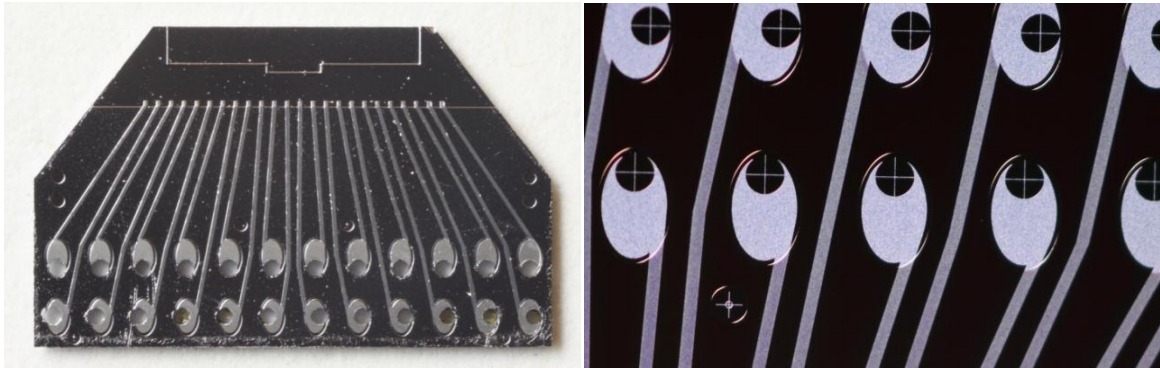


Figure 6-26. Left: Quad shaft electrode carrier with through holes and alignment groove, the electrode surface is passivated with oxide layer, Right: Exposed pads with through holes drilling cross-hair markers

The carrier wafer for the double shaft electrodes was an improved version of the quad shaft electrode carriers and was designed to be released using mechanical saw dicing. This process is low cost and does not require additional patterning steps but limited to orthogonal linear loci. The carrier wafer had a rectangular layout, and Figure 6-27 shows the fabricated wafer with the electrode alignment groove and patterned metallization layer forming the pads and tracks. The electrode was bonded to the wafer using epoxy resin, and the electrode interconnect pads were coupled to the wafer using gold wire bonding.

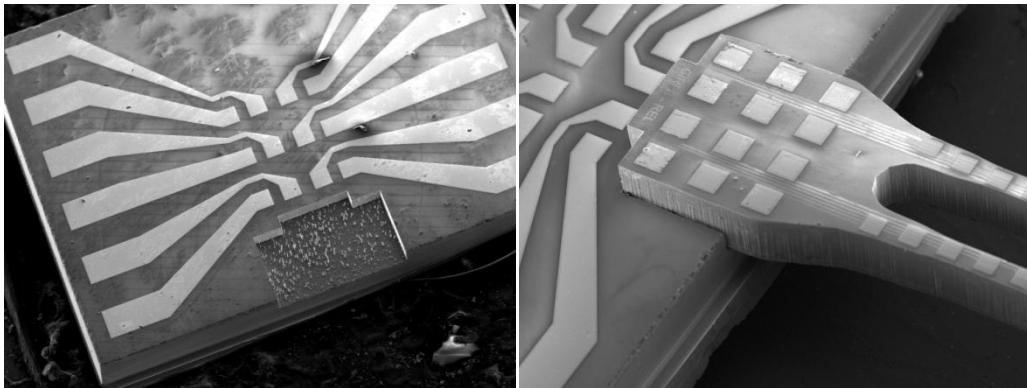


Figure 6-27. SEM pictures of dual shaft electrode carrier wafer, Left: Released carrier wafer with patterned metallization layer and etched alignment groove, Right: Electrode-wafer assembly before gold wire bonding

Flexible cables

Flexible cables were custom designed and fabricated to couple silicon electrodes to external circuits (refer to section 3.13). Different cables were designed to match the various electrodes and carrier

wafers (listed in Table 3-3). The cables were fabricated on 50 and 125 μ m polyimide sheets with copper metallization layers to facilitate soldering to circuits and pcb's using regular solder wires. The cables were designed for release using RIE or laser dicing. The electrode-cable assembly was done using microscope and vacuum stage and the electrode was temporarily attached to a silicon wafer. The cable was attached to the electrode using fast curing epoxy resin, then the electrode pads were bonded to the cable tips using conductive paste (e.g. silver conductive epoxy). The different cable tips are demonstrated in Figure 6-28, and the cable pads had triangular tips to improve spreading the conductive paste and establish reliable bonding. The electrode-cable assemblies for single and quad shaft electrodes are demonstrated in Figure 6-29.

6.9 The Waterloo Array: 3-D Electrodes Arrays

The Waterloo Array is 3-D flexible electrode made by stacking several planar Flex electrodes using custom designed carrier wafers as demonstrated in section 3.14. The Flex electrode with integrated interconnect cable (introduced in section 3.14) was designed for stacking and the electrodes were aligned using the engraved trenches on the carrier wafer and the projections on the electrode. Two carrier wafers were fabricated with different lengths (2.4 and 5mm) as shown in Figure 6-30, and each electrode was glued to the carrier wafer and resided in the etched trench. The electrode was aligned using the engraved notches on the wafer and the projections on the electrode. The gap between the electrodes was manipulated by the wafer thickness and the depth of the trench. The planar electrodes were arranged into a three layers assembly forming a 3-D constellation of 72 pads as demonstrated in Figure 6-31, and more electrodes can be added to the assembly.

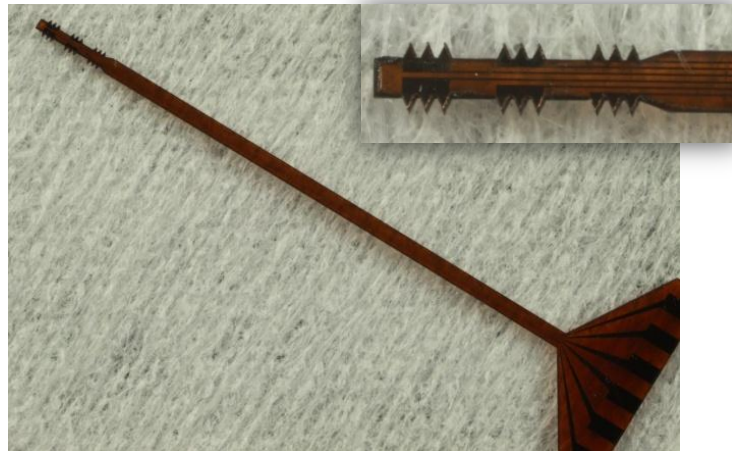




Figure 6-28. Flexible interconnect cables, Top: Single shaft electrode, Bottom left: Quad shaft electrode, Bottom right: Double shaft electrode carrier wafer

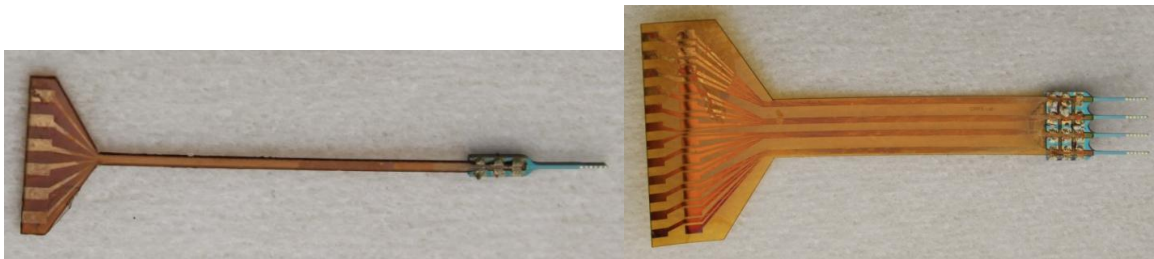


Figure 6-29. Single (Top) and Quad (Bottom) shaft electrode-cable assemblies

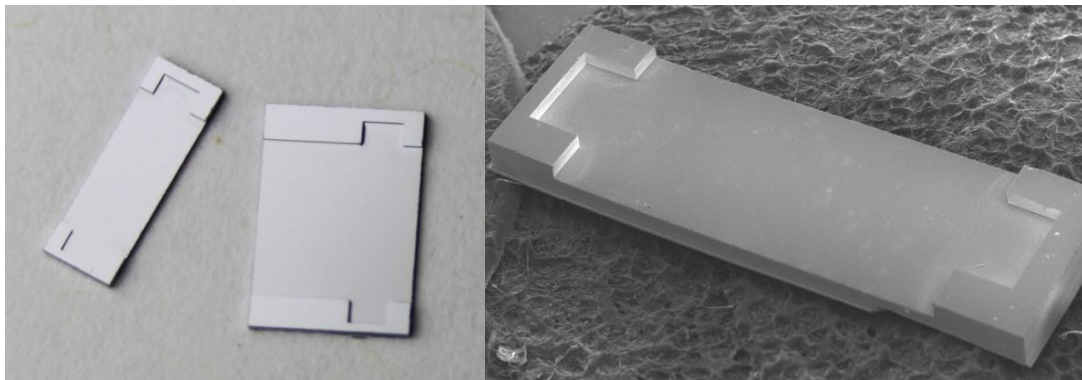


Figure 6-30. Left: 2.4 and 5mm 3-D stacking carrier wafers, Right: SEM picture of the 2.4mm 3-D stacker

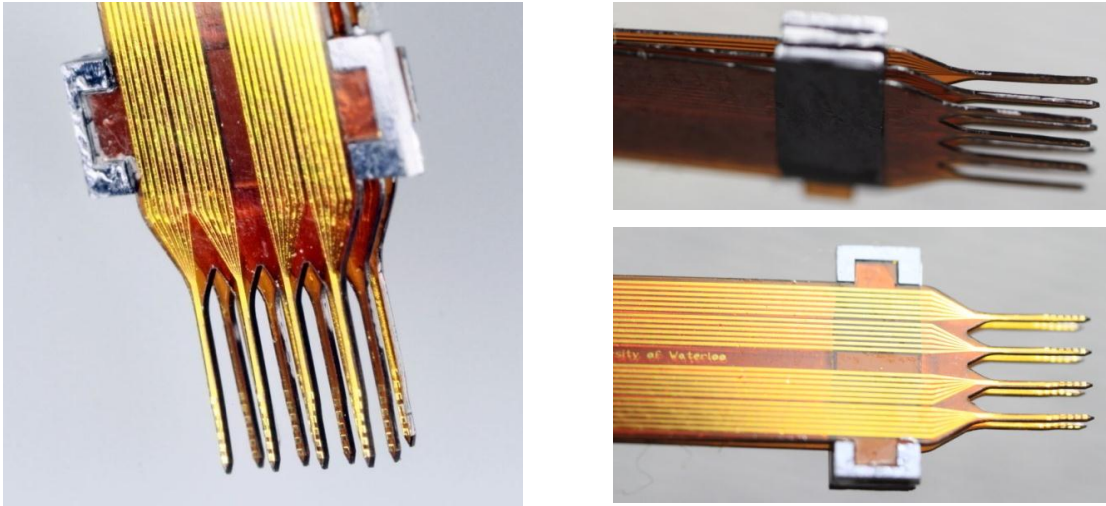


Figure 6-31. The Waterloo Array: 3-D Flex electrode assembly with 12 shafts and 72 stimulation pads

6.10 Pad post processing

Why low impedance

Stimulation is done using controlled current sources, thus lower electrode impedance would help in reducing power consumption. This extends the battery life of implanted systems, and also reduces power dissipation and the associated joule heating. Moreover, lower impedance reduces noise generation. Low cost pad post processing technique was developed using low current pulsed electroplating to deposit a rough gold layer on the neuro-interface pads resulting in significant drop in the interface impedance. The AC electrode impedance is dominated by the electrode-tissue interface which is highly capacitive and proportional to the contact area. The pad post processing increases the surface roughness which expands the surface area yielding lower capacitance. Figure 6-32 illustrates the pad surface for different electrodes including the original Flex, modified Flex with post processed pads, commercial twisted wire, and commercial thin film electrodes. The post processed Flex electrode manifests the highest surface roughness which attributes to the lowest electrode impedance as discussed later in section 7.2.

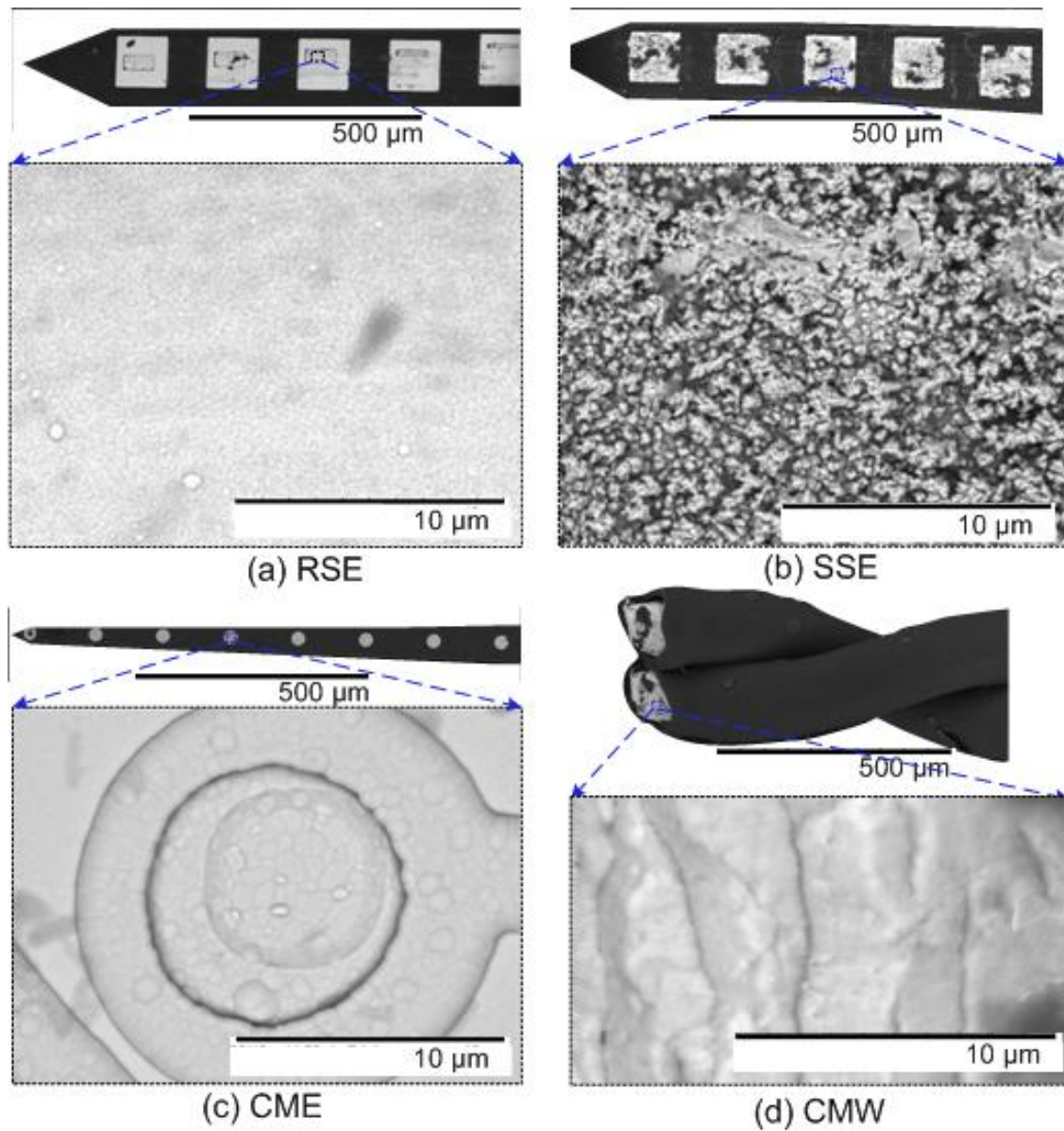


Figure 6-32. SEM pictures of the pads on different electrodes showing the surface roughness. RSE: Rough surface electrode (modified Flex electrode), SSE: Smooth surface electrode (original Flex electrode), CME: Commercial microelectrode (Neuro Nexus), CMW: Commercial microwire electrode

6.11 Conclusion

This chapter demonstrated the fabrication results of the microelectrodes and the different components. Several electrode designs were implemented on brittle (silicon) and flexible substrates (polyimide)

according to different design requirements and applications. Silicon and polyimide electrodes were successfully implemented; however, stainless steel processing was terminated due to unresolved electrode release issues. Silicon substrates were easier to handle and process while polyimide processing required additional steps to manage its flexible structure, lower thermal conductivity and thermal expansion. Silicon is brittle, and mechanical failure will cause fracture and release debris in the body, thus it is suitable for short term animal interfacing (recording/stimulation) applications. On the other hand, flexible electrodes were developed and optimized for chronic in vivo applications. The insertion methodology of flexible electrodes was based on developing a mechanical design that would provide the axial strength required for tissue penetration and waive the need for implantation assistive devices (i.e. stylus or mounting devices) to minimize tissue trauma.

Various materials were tested for fabricating the different electrode layers including metallization, dielectric, and passivation layers. Gold is inert and biocompatible and was chosen for the exposed metal pads that come in contact with tissue. However, platinum causes less metal-metal interface noise than gold and is preferred for recording applications, but it was not available during the research. Other components were also fabricated including carrier wafers, stacking wafers and interconnect flexible cables.

The planar Flex electrode was designed and optimized for stacking using special carrier wafers with alignment trenches. The electrode and carrier wafers were assembled to create the flexible 3-D neuro-interfacing Waterloo Array.

Chapter 7

Electrode Characterization and Testing

7.1 Introduction

This chapter demonstrates the electrode impedance characterization, in vitro and acute in vivo testing of the Flex electrode. The electrode was benchmarked against commercial equivalents including low cost twisted-wire electrode from Plastics One Inc. and thin-film electrodes from NeuroNexus. The original Flex electrode was also compared against the modified design with post-processed pads. Custom printed circuit boards were designed and fabricated to mount the Flex electrode (refer to section 6.6) and facilitate handling and connections to the experimental setups. The electrodes used in this study are labeled as followed: Flex electrode: Smooth surface microelectrode (SME), Modified Flex electrode with post-processed pads: nano-textured microelectrode NME, Twisted wire electrode: Commercial microwire (CMW), and Thin film electrode: Commercial microelectrode (CME).

7.2 Electrode Electrical Characterization

The proper electrode operation and coupling to external circuits require characterizing the electrode impedance. The electrode impedance has DC and AC components, and the latter is dominated by the highly capacitive electrode-tissue interface impedance. DC resistance measurement was done during electrode fabrication for characterization as well as a part of the inspection procedure to identify fabrication defects including open and short circuits. The setting comprised microprobe station, controlled voltage source and ammeter. I-V characteristic curves were plotted to estimate the track resistance, and detailed results are presented in section 6.5.3.

AC impedance was measured using frequency response analysis (FRA) and electrochemical impedance spectroscopy (EIS). Two-electrode standard electrochemical cell was setup using 0.9% sodium-chloride saline solution, platinum counter electrodes, Solatron SI 1287 Electrochemical Interface and Solatron SI 1260 Impedance/Gain-Phase Analyzer. The setup and circuit schematic are demonstrated in Figure 7-1.

Impedance measurement was done by sweeping 10mV signal from 1MHz down to 0.1Hz and the current was recorded. The real and imaginary impedance components as well as Bode plots for the magnitude and phase were plotted. The Flex electrode with 110x110 μ m pads, the commercial twisted wire electrode and the thin-film Neuro Nexus electrode were characterized and the measurements were repeated for different pads and differential channels on several electrodes, where each channel is made up of two interface pads. The electrodes exhibited the anticipated capacitive response attributed to the double layer at the electrode-electrolyte interface. The twisted wire stimulation electrode was considered a benchmark to evaluate the Flex stimulation electrodes and the impedances are plotted in Figure 7-2. The average differential channel impedance recorded was $\sim 5.6\Omega$ M for the Flex and NeuroNexus thin-film electrodes, and $\sim 575\text{K}\Omega$ for twisted wire electrodes. The modified Flex electrode with post-processed pads exhibited remarkable drop in the impedance value and measured

30K Ω . This is attributed to the expanded electrode-electrolyte contact area achieved by the increased pad surface roughness (refer to section 6.10).

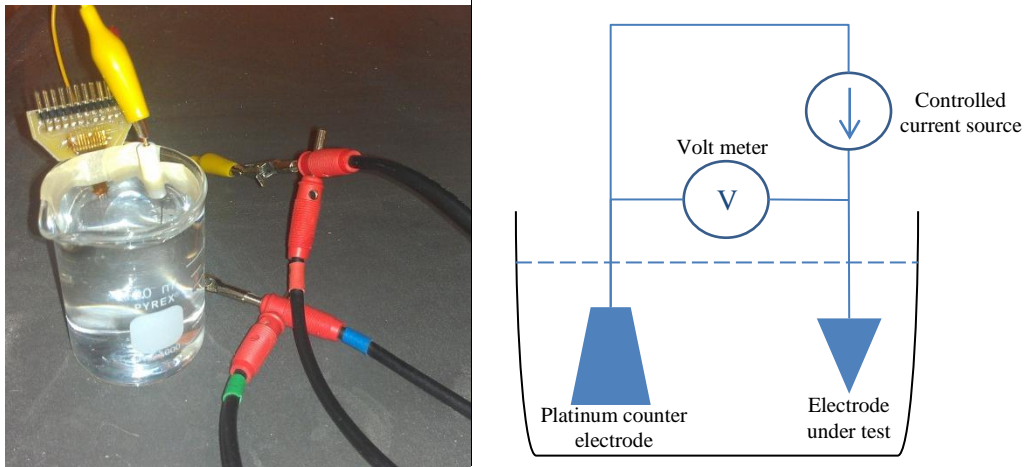


Figure 7-1. Left: AC impedance characterization setup showing the two-electrode standard electrochemical cell, electrolyte and cables. Right: Circuit schematic

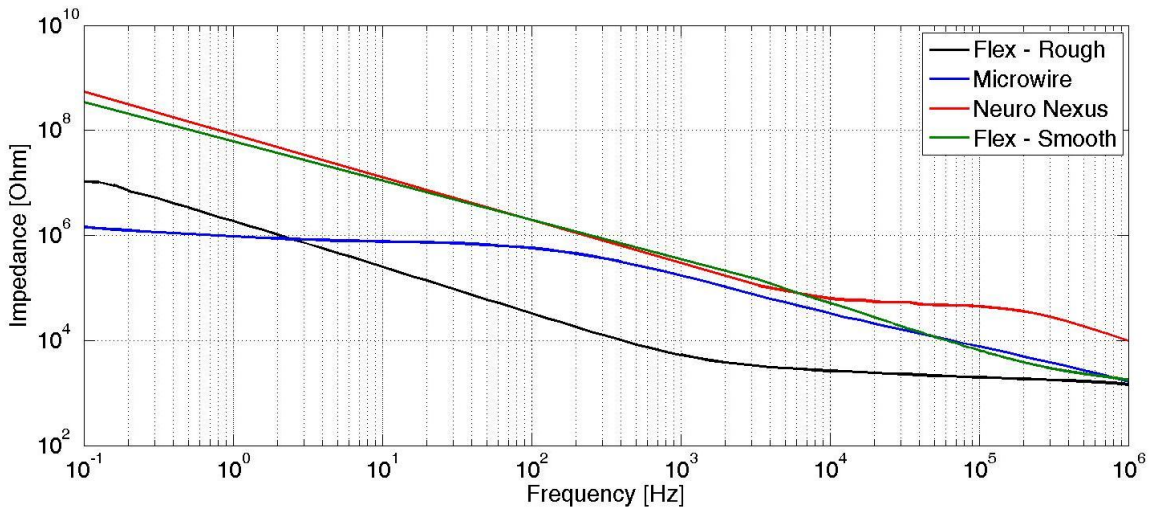


Figure 7-2. FRA of electrode-electrolyte interface: Pad impedance magnitude

7.3 In Vitro Testing of the Flex Electrode

In vitro testing of the stimulation electrodes was done in the Krembil Neuroscience Centre Research, Toronto Western Hospital (TWH) on human hippocampus brain tissue sample. This test verified the proper function of the electrode through stimulating a living brain tissue sample and monitoring the generation of the evoked potential in response to proper stimulation.

The sample was obtained on the same day from resective epilepsy surgery patient and was sliced and prepared for the setup. The electrode was attached to custom designed PCB and two designs were implemented providing access to 12 and 24 channels using 1mil pin header connectors as shown in Figure 7-3. A connection and mounting assembly (Figure 7-4) was custom made to attach the electrode to the micro-manipulator (Figure 7-5). During testing, the tissue sample was secured in place using vacuum stage, and maintained viable in a stream of oxygenated (95%) artificial cerebrospinal fluid (ACSF) and carbon-dioxide (5%) was bubbled through the solution to buffer the bicarbonates in the ACSF. A 0.1mA stimulation current pulse was generated using voltage controlled current stimulator and the charge was delivered to the tissue sample. Signal monitoring was done using standard recording electrodes high gain amplifier (Peak Lab).

The stimulation pulse was first recorded using the same setting without the brain tissue to provide a reference. Then the experiment was executed on the living brain tissue and both the evoked potential and stimulation pulse were detected. The stimulation and recording were repeated multiple times and the captured signals were consistent. The recorded signals are plotted in Figure 7-6 and the exhibiting the stimulation pulse followed by the evoked potential which was identified by medical team as a response to successful stimulation of the hippocampus.

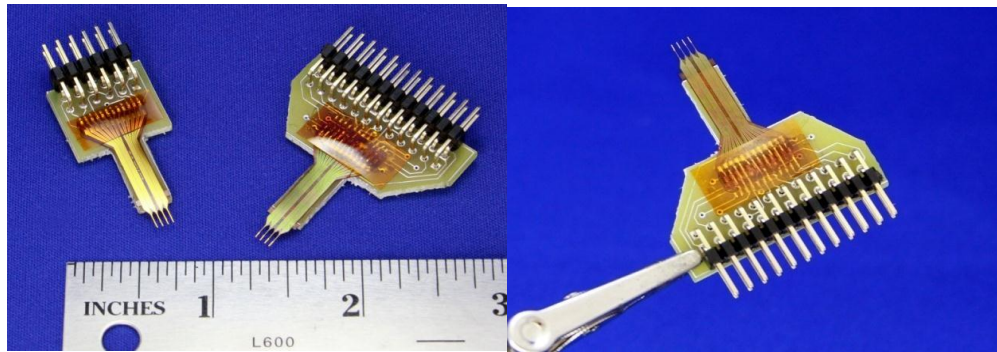


Figure 7-3. Flex electrodes mounted on in vitro PCB's with 12 and 24 channel connections

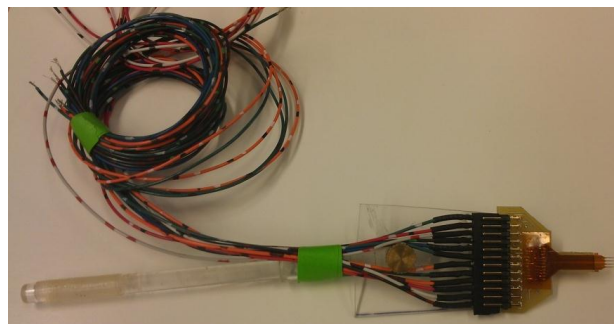


Figure 7-4. Electrode connection and mounting assembly

Table 7-1. FRA of electrode-electrolyte interface impedance: minimum recorded values

	Impedance magnitude	Impedance phase
Smooth pad	2.272M Ω	-67.86 $^{\circ}$
Rough pad	31.9K Ω	-76.016 $^{\circ}$
Sick Kids pad	424K Ω	-58.63 $^{\circ}$
Smooth differential channel	5.59M Ω	-65.7 $^{\circ}$
Rough differential channel	179K Ω	-82.71 $^{\circ}$
Sick Kids differential channel	575K Ω	-27.14 $^{\circ}$

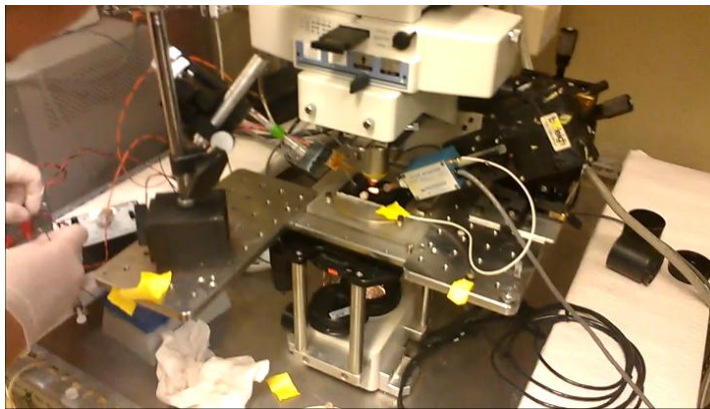


Figure 7-5. In vitro testing setup, Krembil Neuroscience Centre Research Lab, Toronto Western Hospital (TWH)

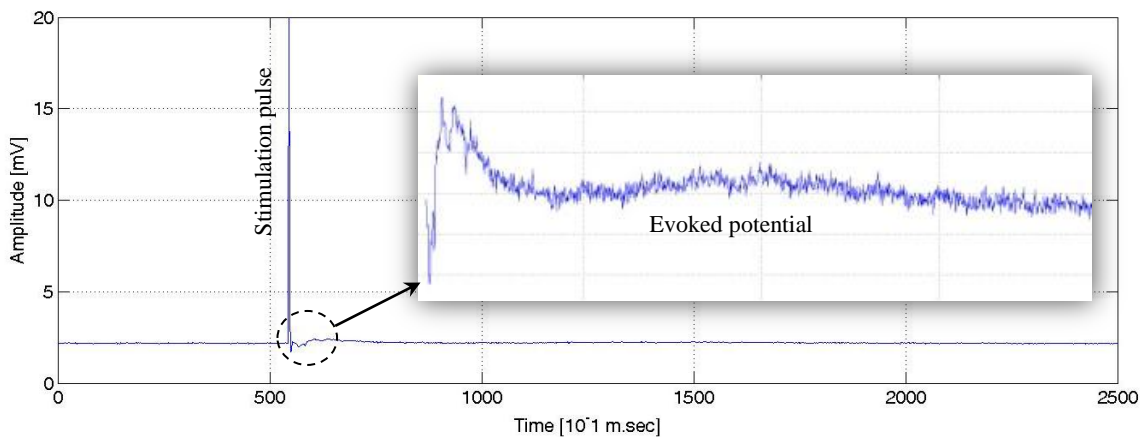


Figure 7-6. Stimulation pulse and the resultant evoked potential

7.4 Acute In Vivo Testing of the Flex electrode

An acute in vivo study was conducted at the Neurosciences & Mental Health Research Institute - the Sick Kids hospital, in which the Flex electrodes (NME and SME) were compared to the commercial microwire (CMW) and the Neuro Nexus thin film microelectrodes (CME) [208]. The study compared the SNR and quality of recorded signals using the different microelectrodes. The electrodes were integrated to a wireless electrotherapeutic implantable system developed for monitoring brain activity and the experiments were repeated to investigate the effect of the effect of the electrodes on the system performance. A modified double-shaft Flex electrode was attached to custom designed PCB with a flexible printed circuit (FPC) header to mate the electrode to the neuro-interfacing system using flat flexible cables (FFC) cable and pin header, the electrode assembly and cable are shown in Figure 7-7.

Noise measurement

Signal to noise ratio (SNR) estimation was done offline using Matlab to analyze the quality of neural signal recordings. SNR rises for higher signal strength and lower system noise, and it was calculated using equation 7.1:

$$SNR = \frac{1}{M} \sum_{i=1}^M \sqrt{\frac{\sum_{k=1}^{N \times F_S} V_{in,i}(k)^2 - V_{msn,i}(k)^2}{N \times F_S}} \quad \dots (7.1)$$

where,

V_{in} : Recorded neural signal

V_{msn} : Microelectrode system noise

F_s : Sampling frequency

M: Number of segments

N: Duration in seconds

$i = 1, 2, 3, \dots M$

$k = 1, 2, 3, \dots N$

Thermal and flicker noise were measured using standard setup with platinum plates. The noise levels recorded for the amplifier (V_{ni}) and reference system (V_{rsn}) were similar ($\sim 7 \mu V_{RMS}$). This was due to the wider surface area in platinum plat and negligible amount noise contribution ($V_{ni} \gg V_{np}$) causing lower electrochemical interaction and thermal noises [209]. Figure 7-8 demonstrates the domination of flicker noise on the V_{ni} in the low frequency band ($< 3\text{Hz}$); however thermal noise is spectrally flat with uniform noise density over the wide frequency band. On the contrary, microelectrode system noise (V_{msn}) remarkably dropped at lower frequency; however, it introduced higher thermal noise due to the higher impedance. Flex electrode with post-processed pads (NME) significantly blocked the low frequency noise and dropped the noise 8 times at 0.1Hz. Also NME introduced ~ 56 times higher thermal noise compared to the V_{rsn} . In conclusion, NME generated lower noise.

Figure 7-8 demonstrates microelectrode noise contributions of the different electrodes. The average oscillation in each band was estimated to evaluate recording performance. The Neuro Nexus electrode (CME) captured the higher noise levels with RMS value of $8.3\mu\text{V}$, followed by $6.64\mu\text{V}$ for the original Flex electrode (SME); while the microwire electrode (CMW) had a value of $4.03\mu\text{V}$ and finally, the post processed Flex electrode (NME) had the best performance with $1.24\mu\text{V}$.

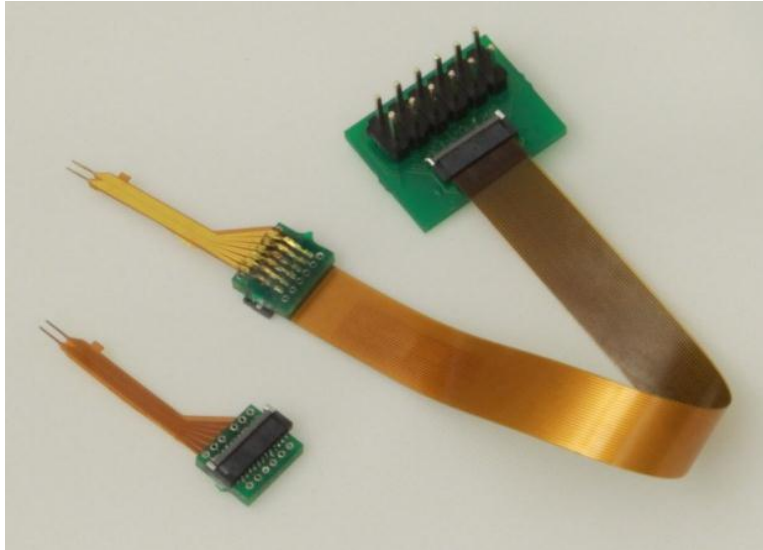


Figure 7-7. Dual shaft Flex electrode in vivo testing assembly

In vivo recording

Acute in vivo recording was done on Sprague–Dawley rats (150–250gm) using craniotomy with general anaesthesia. The electrodes were implanted in the somatosensory area and bipolar recording was done using the implantable system. The recorded signals were analyzed in different frequency bands: delta (0.1 – 4 Hz), theta (4 – 7 Hz), alpha (8 – 13 Hz), beta (13 – 30 Hz) and gamma (30 – 100 Hz).

The neural signals were recorded using different electrodes at 200Hz sampling frequency and divided into 280 segments of 4 seconds for SNR measurement. Figure 7-10 demonstrates spectral densities of recorded neural signals and the associated electrode-electrolyte system noise. SME and CME exhibited more significant low frequency noise compared to NME and CMW. The recordings also demonstrated the higher thermal noise generated by CMW at high frequencies while NME yielded the best signal fidelity. Figure 7-9 shows mean SNR plots for NME, SME, CME and CMW. The presented fabricated microelectrodes (NME and SME) have higher SNRs than commercial CME and CMW.

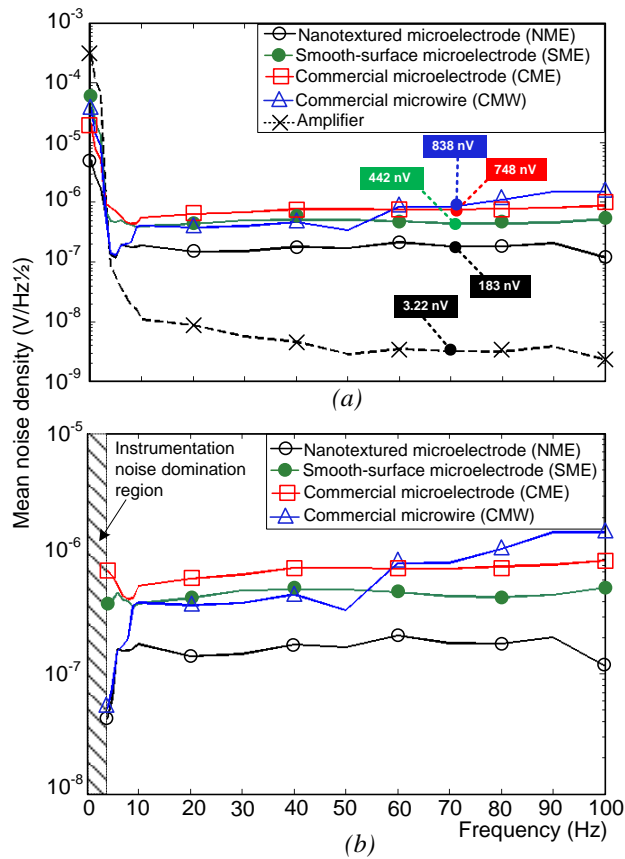


Figure 7-8. Measured noises: (a) instrumentation noise and microelectrodes system noise densities and (b) microelectrodes noise densities of the presented and commercial electrodes [209]

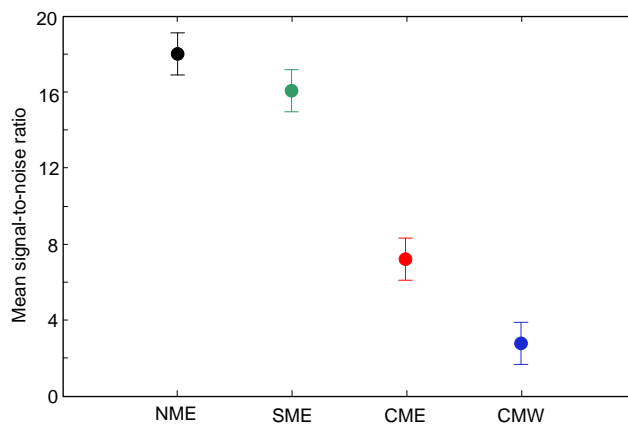


Figure 7-9. Measured mean signal-to-noise ratio for the presented and commercial electrodes [209]

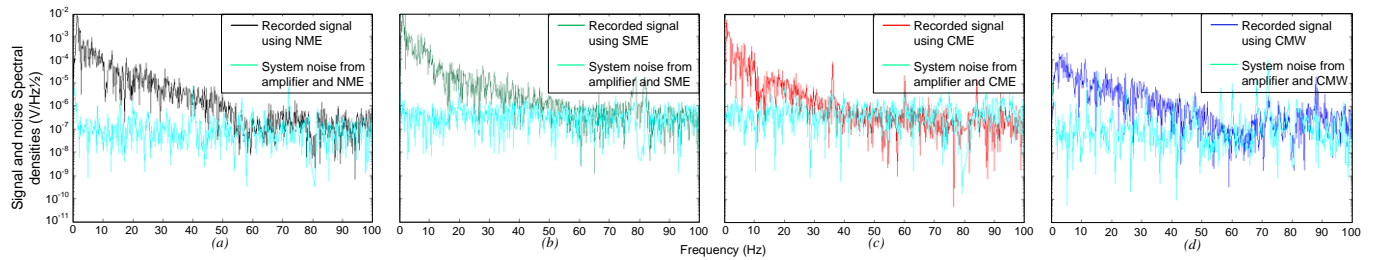


Figure 7-10. Measured neural signal and microelectrodes noise spectral densities of the presented and commercial electrodes [209]

7.5 Conclusion

The electrodes DC resistance and AC impedance were measured to characterize the electrode electrical specifications. The electrode-tissue interface impedance was measured using two-electrode electrochemical cell. The regular and post processed Flex electrodes were benchmarked against commercial equivalents. The regular electrode exhibited an average impedance of $3\text{M}\Omega$ similar to that of the commercial thin film electrode. On the other hand, the post processed electrode demonstrated remarkable drop in the impedance to a value of $30\text{K}\Omega$.

In vitro and in vivo tests were conducted on the Flex electrode to verify its functionality and compare its performance to commercial electrodes. In vitro stimulation test was done on a human hippocampus tissue sample in the Krembil Neuroscience Centre Research Lab, Toronto Western Hospital (TWH) and the evoked potentials were recorded inferring successful tissue stimulation. Acute in vivo recording was done using the dual shaft Flex electrode in the Neurosciences & Mental Health Research Institute, the Sick Kids hospital using a wireless implantable electrotherapeutic device developed for intra-cortical recording and stimulation. The study investigated and compared the effect of several intracortical microelectrodes on the system performance in terms of noise value, signal to noise ratio (SNR) and signal quality. The post processed Flex electrode exhibited the lowest recorded noise and the highest SNR.

In conclusion, the Flex electrode proficiently fulfilled the mechanical, electrical, physiological and biocompatibility design requirements. In vitro and in acute vivo experiments comparing the proposed electrode to commercial alternatives demonstrated the precedence of the Flex electrode in neural recording. The electrode technology will be used to develop customized electrode designs for the clinical research labs collaborating with CIRFE Lab.

Chapter 8

Thesis Conclusion

8.1 Research Summary

The dissertation presented the progress and outcomes of intra-cortical microelectrode design and fabrication. The quest for creating advanced electrodes for neuro-interfacing applications motivated this research. The main objective was to develop, fabricate and test intra-cortical microelectrodes with improved functionality and biocompatibility. This required reworking the conventional electrode technology to create new architectures and layouts capable of satisfying the application requirements. It presented several innovations and novelties capable of improving the electrode functionality and biocompatibility. Electrode development was accomplished through developing design methodology for intra-cortical microelectrodes, creating electromagnetic (EM) and mechanical models for the electrode and brain tissue to study the electrode electric performance and improve its design, and creating novel electrode layouts and architectures to implement proposed designs. The research introduced electrode designs that integrated multiple functions including simultaneous recording and simulation, and current steering. It also presented fabrication processes for the different electrode designs and addressed practical issues including assembly techniques to create 3-D electrode arrays and creating flexible interconnects for external circuits. The research outcomes were concluded by introducing the “Waterloo Array” which is a flexible intra-cortical electrode array with integrated interconnect cable providing high density 3-D constellation of neuro-interfacing channels.

The electrodes were characterized to evaluate their electrical characteristics and their performance was benchmarked against commercial equivalents. In vitro and in vivo tests were carried on to verify their functionality. The electrodes successfully satisfied the design requirements and the Flex electrode with post processed pads manifested superior performance compared to other commercial electrodes.

8.2 Future Work

The design methodologies, optimization procedures and fabrication processes created and developed during this research were applied to create functional prototypes which successfully satisfied the design requirements. Further work and improvements can be applied to the electrode design including:

- Investigate tissue response to chronic implants with different pads types (up to 12 months).
- Experimental evaluation of effect of electrically floating metal layers on controlling electric field distribution within brain tissue (refer to section 4.7).
- Develop fabrication process to implement flexible electrodes on metal substrates.

Appendix A

Acronyms

ACSF	Artificial cerebrospinal fluid
BHF	Buffered Hydrofluoric acid
BMI	Brain-machine interface
CNS	Central nervous system
CME	Commercial microelectrode (NeuroNexus Thin film electrode)
CMW	Commercial microwire (Plastics-One Twisted wire electrode)
DBS	Deep brain stimulation
DCES	Direct cortical electrical stimulation
DRIE	Deep reactive ion etching
ECoG	Electrocorticography
EDM	Electrical discharge machining
EM	Electro-magnetic
ESCS	Epidural spinal cord stimulation
FDA	Food and drug administration
FDTD	Finite difference time domain
FEM	Finite element modeling
FES	Functional electric stimulation
FFC	Flat flexible cables
FPC	Flexible printed circuit
GPi	Globus pallidus
GSA	Geometric surface area
ICP	Inductively coupled plasma
IPA	Isopropanol alcohol
LFP	Local field potential
MINI	Microscale implantable neural interface

NME	Nano-textured microelectrode (post-processed Flex electrode)
OCD	Obsessive-compulsive disorder
PAN etch	Phosphoric, Acetic, Nitric acids etchant
PECVD	Plasma enhanced chemical vapour deposition
PEG	Polyethylene glycol
PGA	Perfect geometric approximation
PVD	Physical vapour deposition
PR	Photoresist
REL	Rehabilitation Engineering Lab (University of Toronto)
RIE	Reactive ion etching
SCC	Stress corrosion cracking
SCS	Spinal cord stimulation
SME	Smooth surface microelectrode (Flex electrode)
SN	Substantia nigra
SOI	Silicon-on-insulator
STN	Subthalamic nucleus
TBI	Traumatic brain injury
TMS	Transcranial magnetic stimulation
TWH	Toronto Western Hospital

Appendix B

Foreign Body Response

1. Foreign Body Response

Neuro-compatibility describes the quality of electrode-tissue interface and its degradation due to the tissue reactive response [98][99][123]. Intra-cortical electrodes are designed for prolonged application and electrode implantation provokes foreign body reaction (FBR) which attempts to dispose of the foreign body through a two phase process [26][91][92][93][94]. The immediate acute phase response employs tissue fluids to dissolve the foreign body [173], followed by the chronic phase response which aims to isolate the foreign body. The implant is encapsulated in an unexcitable tissue layer which increases the contact impedance and degrades the electrode functionality. The chronic response is characterized by the formation of glial scars and activated microglia which attempts to destroy the foreign body through phagocytosis. The capsule can be fully formed within 15 days to four months [95] depending on the provocativeness of electrode material [96], and its thickness capsule depends on the electrode biocompatibility which is a function of electrode material and geometry [97]. The acute phase response delays the operability of electrodes, while the chronic phase response raises the threshold of stimulating electrodes and inhibits signal pick for recording electrodes.

2. Capsule Formation

The capsule formation was elaborately discussed in the literature, and the formation period was estimated to be 12 weeks. A continuous sheath of cells grows in a loosely organized pattern within 2 weeks, and develops a compact and continuous layer in 6 to 12 weeks capable of electrically isolating the electrode. During development, the sheath gets more strongly attached to the surface of the electrode than the surrounding tissue [93]. Metals that invoke high tissue response exhibited formation of thick capsules after 15 days [96]. Furthermore, the electrode geometry and size manipulate the formation of capsules such that micro-sized implants would yield thinner capsules[97].An experiment which demonstrates the body response and formation of capsules using stainless steel electrodes was discussed in [95] and outlined the following observations:

- After 24 hours of implantation: 1mm zone surrounding the electrode contained haemorrhage, necrosis and edema.
- The following 3 days: drop in haemorrhage and necrotic debris.
- The seventh day: 0.1mm layer of capillaries occupied the necrotic zone.
- The 15thday: capillaries replaced the necrotic region, and connective tissue was formed.
- After a month: necrotic debris disappeared, and a capsule surrounded the electrode track.
- After 4 months: and thick capsule was formed.

Appendix C

Brain Tissue Dielectric Properties and Dispersion Modes

1. Conductivity and permittivity

The dielectric properties of a material determine its response to externally applied electric fields. Values for brain tissue conductivity range in literature from 0.05 to 3.3S.m⁻¹, and exhibit anisotropy [148]. The dielectric properties also depend on the type of tissue (e.g. white matter, grey matter, encapsulation tissue and nerve fibers) and the species (e.g. rodents, humans). The low frequency conductivity values used for brain tissue modeling are listed in Table 4-1. Complex permittivity ($\hat{\epsilon}$) was used for modeling the tissue response to time varying fields; and the magnitude (ϵ') and phase shift (ϵ'') were expressed with respect to the polarization field as follows:

$$\hat{\epsilon} = \epsilon' - j. \epsilon'' \quad \dots (D.1)$$

Complex permittivity is a function of frequency and exhibits dispersions through the spectrum. The effective complex permittivity of heterogeneous material was modeled by a four Cole-Cole expression and an additional term represents static conductivity as shown in equation (D.2).

$$\hat{\epsilon} = \epsilon_{\infty} + \sum_{n=1}^4 \left(\frac{\Delta\epsilon_n}{1+(j.\omega.\tau)^{(1-\alpha)}} + \frac{\sigma_s}{j.\omega.\epsilon_0} \right) \quad \dots (D.2)$$

2. Biological tissue parameters database

Based on data published in literature and the work conducted by Gabriel et al, an elaborate database for the dielectric properties of biological tissue was established in 1996 to be used in electromagnetic dosimetry studies. Experimental data was collected from excised animal tissue at 37°C and the database had the following limitations [154]:

- Data was measured on excised not living tissue.
- Model predictions were accurate for frequencies beyond 1MHz due to the presence of sufficient supporting data.
- Data extracted from models at low frequencies (< 1MHz) were only estimates due to lack of detailed data.
- Low frequency data (< 100Hz) was contaminated with electrode polarization errors.
- Data values contributed by Baco et al (1997) were higher than the database due to soaking the brain tissue in saline solution during measurements.
- Data values contributed by Schmidt et al (2003) were higher than the database as the pressure applied by electrodes to hold the samples for elongated measuring periods (150 minutes) seeped fluids from within the cells affecting the measurements.
- Peyman et al (2005) additions to the 1996 database were in good agreement with the model.

- In vitro and in vivo values differ at low frequencies.

The values for relative permittivity, conductivity and loss tangent for white and grey human brain tissue extracted from Gabriel model [152][153] are plotted in Figure D-1 to Figure D-4.

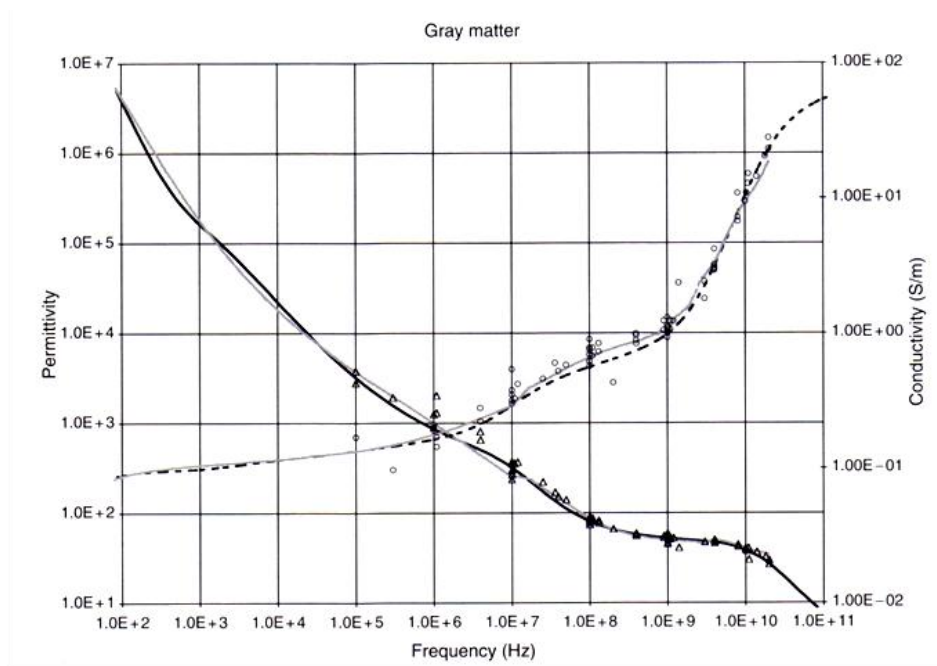


Figure D-1. Dielectric parameters of human brain grey matter based on Gabriel model (solid and dashed lines) and pre-1996 literature (triangles and circles) [154]

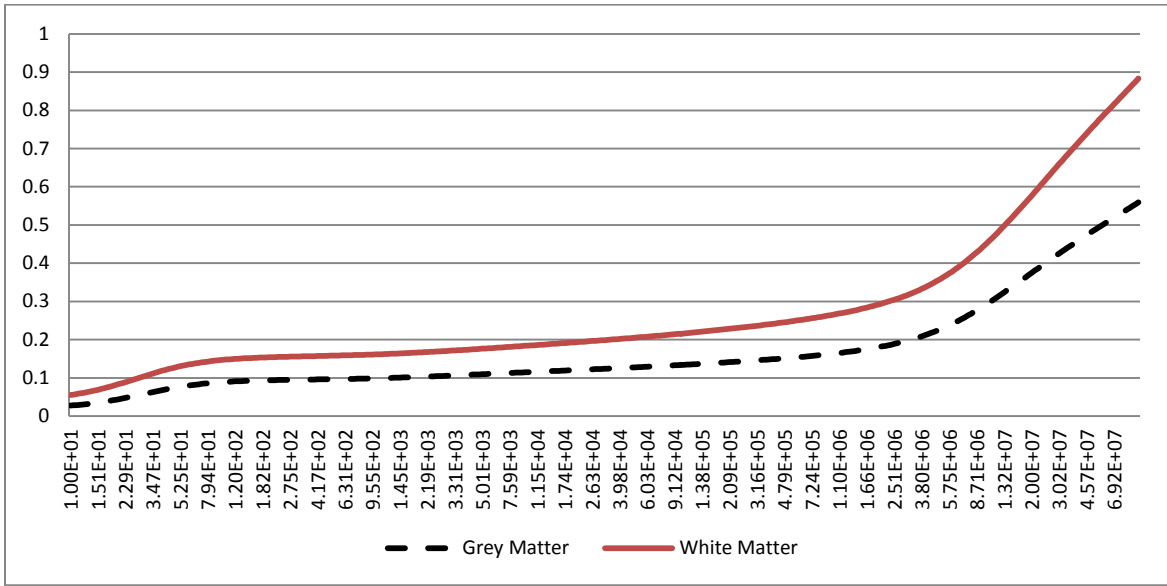


Figure D-2. Conductivity of white and grey matter (10Hz – 100MHz)

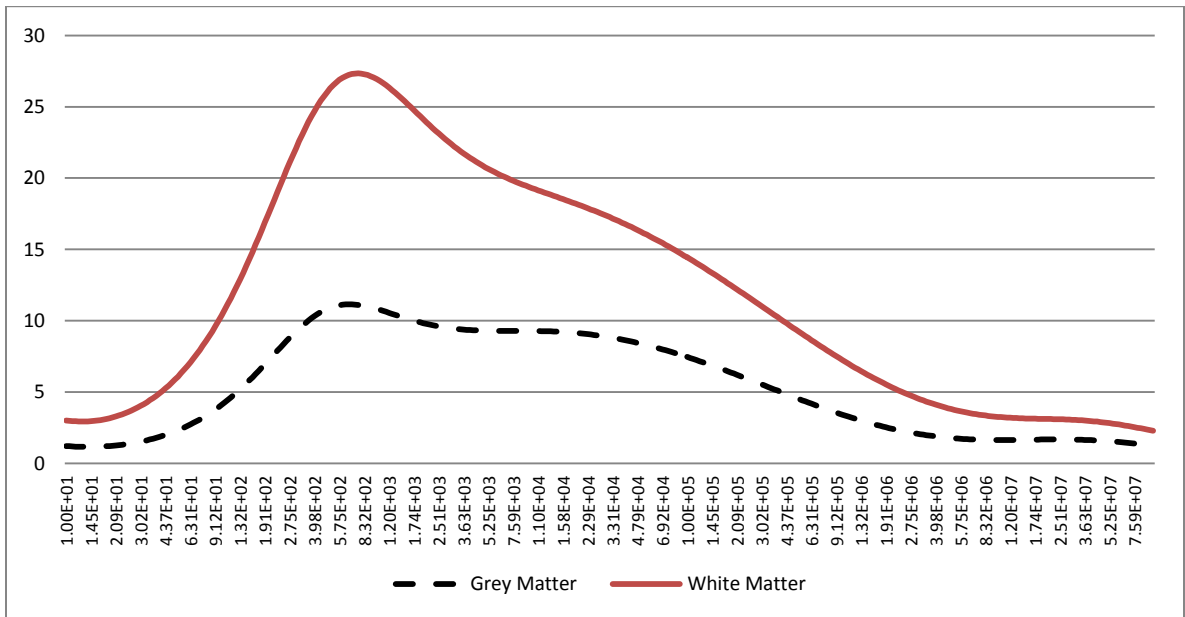


Figure D-3. Loss tangent of white and grey matter (10Hz – 100MHz)

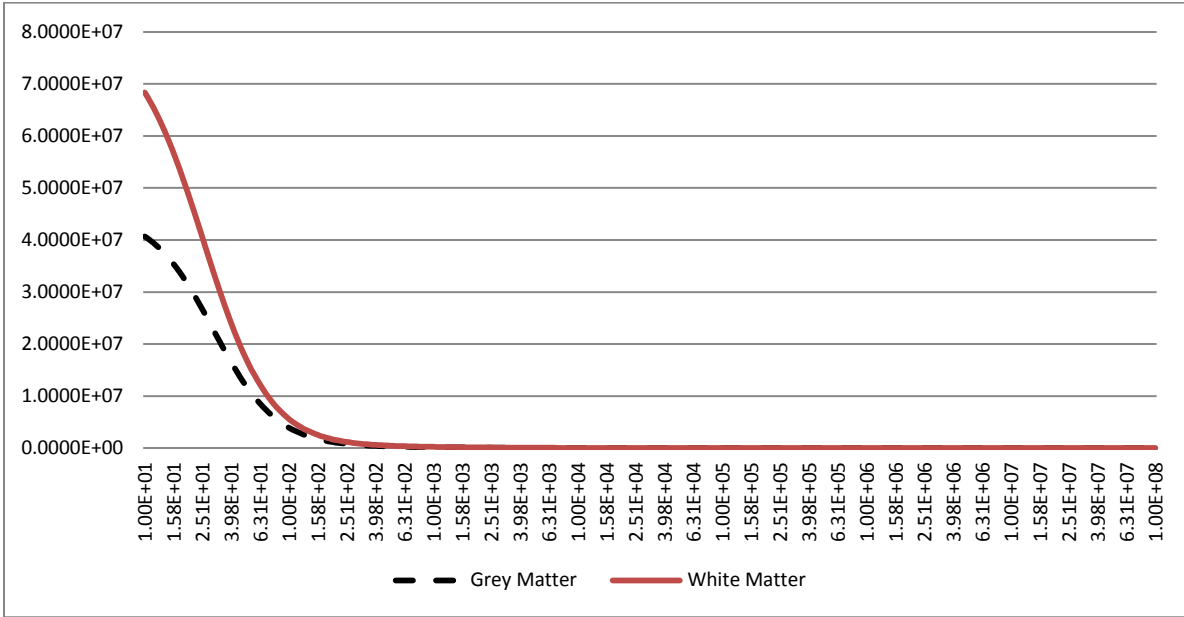


Figure D-4. Relative permittivity of white and grey matter (10Hz – 100MHz)

Appendix D

Material Properties

	Silicon	Polyimide	Gold	Chrome	Aluminum	Stainless steel	Titanium	SU-8
Young's modulus [GPa]	185	3.2	79	289	69	193	116	4.4
Poisson ratio	0.28	0.34-0.42	0.44	0.21	0.35	0.29	0.32	0.22
Density [Kg.m ⁻³]	2330	1430	19300	7190	2700	8030	4506	1200
Ultimate tensile stress [MPa]	35	55	120	83	483	620		55
Shear modulus [GPa]	79.9	0.76	27	115	26	86	44	0.76
Yield stress [MPa]	7000	40			170	205		
Electric conductivity [S/cm]	2.52E-12		4.52E ⁻⁵	8E4	3.5461E5	1.3889E4	2.381E4	
Coeff. Thermal expansion [K]	6	55E-6	14E-6	6.2E-6	24E-6	13E-6	8.6E-6	52
Thermal conductivity [W/m.K]	148	0.52	318	93.9	236	162	21.9	0.2
Specific heat [J/Kg.K]	710	1090	130	460	910	500	140	
Dielectric constant	13 @ 10GHz	3.5 @ 1MHz						4
Loss tangent								0.08

Appendix E

Brain Tissue Mechanical Modeling

The hyperelastic models imposed the following limitations to the stress-strain relation:

1. Stable and independent of cyclic loading.
2. Independent of maximum applied strains.
3. Reversible and does not exhibit hysteresis.
4. Perfectly elastic and does not accommodate permanent strain deformation.

Stress-strain

Uniaxial quasi-static loading of fresh brain tissue is described in [200] and the experimental results are listed in Table L-1. The loading was applied in cyclic tension/compression pattern at a speed of 5mm/min. The data was plotted and modeled using Ansys 12 Curve Fitting Tool and Mooney-Rivlin hyper elastic model with 3 parameters provided the best match and valid material constants. The curve fitting results are plotted in Figure L-1 and the model parameters are listed in Table 5-15.

Table L-1. Fresh brain tissue curve fitted stress-strain curve

Strain [mm/mm]	Stress [Pa]
0	0
0.004	4.23
0.008	8.48
0.0141	14.89
0.0221	23.64
0.0302	32.74
0.0381	42.34
0.046	52.62
0.054	63.73
0.0619	75.87
0.0702	89.23
0.075	98.29
0.0797	107.97

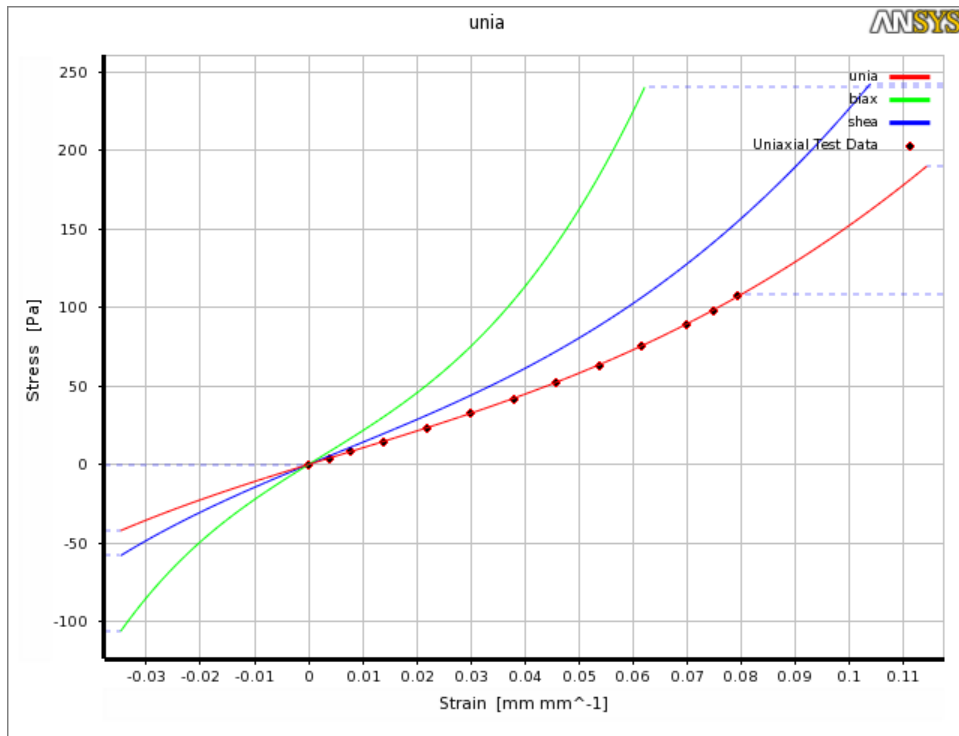


Figure L-1. Curve fitting of the experimental stress-strain of brain tissue

Bibliography

- [1] Liberson, W. T., Holmquest, H. J., Scot, D., Dow, M., 1961, Functional Electrotherapy Stimulation Of The Peroneal Nerve Synchronized With The Swing Phase Of The Gait Of Hemiplegic Patients, Archives of Physical Medicine and Rehabilitation, vol. 42, pp 101-105.
- [2] DiLorenzo, D. J. and Bronzino, J. D., 2007, Neuroengineering, CRC Press.
- [3] House, W. F. and Berliner, K. I., 1986, Safety and Efficacy of the House/3M Cochlear Implant in Profoundly Deaf Adults, Otolaryngologic Clinics of North America Journal, vol. 19, pp 275.
- [4] Simmons, F. B., Epley, J. M., Lummis, R. C., Guttman, N., Frishkopf, L. S., Harmon, L. D., Zwicker, E., 1965, Auditory Nerve Electrical Stimulation In Man, Science, vol. 148, No. 3666, pp 104-106.
- [5] Michelson, R. P., 1971, Electrical Stimulation of the Human Cochlea A Preliminary Report, Archives of Otolaryngology, Head Neck Surgery, vol. 93, pp 317-323.
- [6] McNeal, D. R., 1977, 2000 Years of Electrical Stimulation, in Functional Electrical Stimulation, F. T. Hambrecht and J. B. Reswick, New York Marcel Dekker, pp 3-33.
- [7] Aldini, G., 2004, From Animal Electricity to Human Brain Stimulation, Canadian Journal of Neurological Sciences, vol. 31, pp 576-584.
- [8] Chardack, W. M., Gage, A. A., Greatbatch, W., 1960, A Transistorized, Self-Contained, Implantable Pacemaker For The Long-Term Correction Of Complete Heart Block, Surgery, vol. 48, pp 643-654.
- [9] Bechtereva, N. P., 1972, Therapeutic Electrostimulation of Deep Brain Structures”, Vopr. Neurokhir., vol. 1, pp 7-12.
- [10] Bechtereva, N. P., Bondartchuk, A. N., Smirnov, V. M., Meliutcheva, L. A., Shandurina, A. N., 1975, Method Of Electrostimulation Of The Deep Brain Structures In Treatment Of Some Chronic Diseases. Applied Neurophysiology, vol. 37, pp 136-140.
- [11] Fofonoff, T. A., Martel, S. M., Hatsopoulos, N. G., Donoghue, J. P., Hunter, I. W., 2004, Microelectrode Array Fabrication By Electrical Discharge Machining And Chemical Etching, IEEE Transactions on Biomedical Engineering, vol. 51, issue 6, pp 890-895.
- [12] Higgins, D. and Banker, G., 1998, Primary Dissociated Cell Cultures, In Culturing Nerve Cells, MIT Press, pp 37-78.

- [13] Schwartz, B., 2004, Cortical Neural Prosthesis, *Annual Review of Neuroscience*, vol. 27, pp 453-485.
- [14] Kagoo, K., 2005, Microelectrode Arrays for Neural Recording, School of Engineering, UCSC.
- [15] Najafi, K., Ji, J., Wise, K. D., 1990, Scaling Limitations of Silicon Multichannel Recording Probes, *IEEE Transactions on Biomedical Engineering*, vol. 37, Issue 1, pp 1-11.
- [16] Moxon, K. A., Leiser, S. C., Gerhardt, G. A., Barbee, K. A., Chapin, J. K., 2004, Ceramic-Based Multisite Electrode Arrays for Chronic Single-Neuron Recording, *IEEE Transactions on Biomedical Engineering*, vol. 51, issue 4, pp 647-656.
- [17] Hampson, R. E., Coates, T. D., Gerhardt, G. A., Deadwyler, S. A., 2003, Ceramic-Based Microelectrode Neural Recordings in the Rat and Monkey, *Engineering in Medicine and Biology Society Proceedings of the 25th Annual International Conference of the IEEE*, vol. 4, pp 3700-3703, vol. 4.
- [18] The History of DBS, <http://www.parkinsonsappeal.com>
- [19] Santhanam, G., Ryu, S. I., Yu, B. M., Afshar, A., Shenoy, K. V., 2005, A High Performance Neurally-Controlled Cursor Positioning System, *2nd International IEEE EMBS Conference on Neural Engineering*, pp 494-500.
- [20] Patterson, W. R., Song, Y., Bull, C. W., Ozden, I., Deangelis, A. P., Lay, C., McKay, J. L., Nurmikko, A. V., Donoghue, J. D., Connors, B. W., 2004, A Microelectrode-Microelectronic Hybrid Device For Brain Implantable Neuroprosthesis Applications, *IEEE Transactions on Biomedical Engineering*, vol. 51, Issue 10, pp 1845-1853.
- [21] Mojarradi, M., Binkley, D., Blalock, B., Andersen, R., Ulshoefer, N., Johnson, T., Del Castillo, L., 2003, A Miniaturized Neuroprosthesis Suitable For Implantation Into The Brain, *IEEE Transactions on Neural Systems and Rehabilitation Engineering*, vol. 11, Issue 1, pp 38-42.
- [22] Leuthardt, E. C., Schalk, G., Wolpaw, J. R., Ojemann, J. G., Moran, D. W., 2004, A Brain-Computer Interface Using Electrographic Signals In Humans, *Journal of Neural Engineering*.
- [23] Vetter, R. J., Miriani, R. M., Casey, B. E., Kong, K., Hetke, J. F., Kipke, D. R., 2005, Development of a Microscale Implantable Neural Interface (MINI) Probe System, *27th Annual International Conference of the Engineering in Medicine and Biology Society*, vol. , issue , pp 7341-7344.

- [24] Hofmann, U. G., Folkers, A., Mösch, F., Malina, T., Menne, K. M. L., Biella, G., Fagerstedt, P., De Schutter, E., Jensen, W., Yoshida, K., Hoehl, D., Thomas, U., Kindlundh, M. G., Norlin, P., De Curtis, M., 2006, A Novel High Channel-Count System for Acute Multisite Neural Recordings, *IEEE Transactions on Biomedical Engineering*, vol. 53, issue 8, pp 1672-1677.
- [25] Drake, K. L., Wise, K. D., Farraye, J., Andeson, D. J., Bement, S. L., 2988, Performance of Planar Multisite Microprobes in Recording Extracellular Single-Unit Intra-Cortical Activity, *IEEE Transactions on Biomedical Engineering*, vol. 35, Issue 9, pp719-732.
- [26] Polikov, V. S., Tresco, P. A., Reichert, W. M., 2005, Response Of Brain Tissue To Chronically Implanted Neural Electrodes, *Journal of Neuroscience Methods*, vol. 148, Issue 1, pp 1-18.
- [27] Wood, D. J., 1993, The Characterization of Particulate Debris Obtained From Failed Orthopedic Implants, San José State University, College of Materials Engineering.
- [28] Horbett, T. A., 2002, Biological Activity of Adsorbed Proteins and Biocompatibility, *Journal of Biomaterials Science, Polymer Edition*, pp 367-390.
- [29] Horbett, T. A., 1982, Protein Adsorption On Biomaterials In Biomaterials Interfacial Phenomena and Applications, American Chemical Society.
- [30] Muthuswamy, J., Okandan, M., Jain, T., Gilletti, A., 2005, Electrostatic Microactuators for Precise Positioning of Neural Microelectrodes, *IEEE Transactions on Biomedical Engineering*, vol. 52, Issue 10, pp 1748-1755.
- [31] Rousche, P. J., Pellinen, D. S., Pivin, D. P., Williams, J. C., Vetter, R. J., Kirke, D. R., 2001, Flexible Polyimide-Based Intra-cortical Electrode Arrays with Bioactive Capability, *IEEE Transactions on Biomedical Engineering*, vol. 48, issue 3, pp 361-371.
- [32] Quesney, L. F., Binnie, C. D., Chatrian, G. E., 1998, Electrocorticography Current Trends and Future Perspective, *EEG Clinical Neurophysiology*, suppl. 48.
- [33] Dinner, D. S., Luders, H. O., Klem, G., 1998, Chronic Electrocorticography Cleveland Clinic experience, *Electroencephalography and Clinical Neurophysiology*, suppl. 48, pages 58-69.
- [34] Brindley, G. S. and Lewin, W. S., 1968, The Sensations Produced By Electrical Stimulation Of The Visual Cortex, *Physiology*, vol. 196, pp 479-493.
- [35] Limousin, P., Krack, P., Pollak, P., Benazzouz, A., Ardouin, C., Hoffmann, D., Benabid, A., 1998, Electrical Stimulation Of The Subthalamic Nucleus In Advanced Parkinson's Disease, *The New England Journal of Medicine – Electrical Stimulation of the Subthalamic Nucleus in Advanced Parkinson's Disease*, vol. 339, pp 1105-1111,.

- [36] Kewley, D. T., Hills, M. D., Borkholder, D. A., Opris, I. E., Maluf, N. I., Storment, C. W., Bower, J. M., Kovacs, G. T. A., 1997, Plasma-Etched Neural Probes, Sensors and actuators, vol. 58, pp 27-5.
- [37] Najafi, K., Wise, K. D., Mochizuki, T., 1985, A High-Yield IC-Compatible Multichannel Recording Array, IEEE Transactions on Electron Devices, vol. 32, pp 1206-1211.
- [38] Horch, K. W. and Dhillon, G., 2004, Neuroprosthetics Theory and Practice, World Scientific.
- [39] Gray's anatomy, 1995, 38th edition, Churchill Livingstone.
- [40] Spence, A. P., 1986, Basic Human Anatomy, the Benjamin/Cummings Publishing Company Inc.
- [41] Paxinos, G. and Mai, J. K., 2004, The Human Nervous System, Elsevier Academic Press.
- [42] Warner, J. J., 2001, Atlas of Neuroanatomy, Butterworth Heinemann.
- [43] Patrick, E., Ordonez, M., Alba, N., Sanchez, J.C., Nishida, T., 2006, Design and Fabrication of a Flexible Substrate Microelectrode Array for Brain Machine Interfaces, 28th Annual International Conference of the IEEE Engineering in Medicine and Biology Society, pp 2966-2969.
- [44] Edell, D. J., Toi, V. V., McNeil, V. M., Clark, L. D., 1992, Factors Influencing the Biocompatibility of Insertable Silicon Microshafts in Cerebral Cortex, IEEE Transactions on Biomedical Engineering, vol. 39, issue 6, pp 635-643.
- [45] Moxon, K. A., Kalkhoran, N. M., Markert, M., Sambito, M. A., McKenzie, J. L., Webster, J. T., 2004, Nanostructured Surface Modification of Ceramic-Based Microelectrodes to Enhance Biocompatibility for a Direct Brain-Machine Interface, IEEE Transactions on Biomedical Engineering, vol. 51, issue 6, pp 881-889.
- [46] Wise, K. D., 2005, Silicon Microsystems for Neuroscience and Neural Prostheses, IEEE Engineering in Medicine and Biology Magazine, vol. 24, pp 22-29.
- [47] Hofmann, U. G., Folkers, A., Mosch, F., Malina, T., Menne, K. M. L., Biella, G., Fagerstedt, P., De Schutter, E., Jensen, W., Yoshida, K., Hoehl, D., Thomas, U., Kindlundh, M. G., Norlin, P., De Curtis, M., 2006, A Novel High Channel-Count System for Acute Multisite Neural Recordings, IEEE Transactions on Biomedical Engineering, vol. 53, issue 8, pp 1672-1677.
- [48] Wise, K. D., Anderson, D. J., Hetke, J. F., Kipke, D. R., Najafi, K., 2004, Wireless Implantable Microsystems High-Density Electronic Interfaces to the Nervous System, Proceedings of the IEEE, vol. 92, issue 1, pp 76-97.

- [49] Fofonoff, T. A., Martel, S. M., Hatsopoulos, N. G., Donoghue, J. P., Hunter, I. W., 2004, Microelectrode Array Fabrication by Electrical Discharge Machining and Chemical Etching, IEEE Transactions on Biomedical Engineering, vol. 51, pp 890-895.
- [50] Ratner, B. D. and A. S. Hoffman, A. S., 1996, Thin Films Grafts, and Coatings, an Introduction to Materials in Medicine, Academic Press.
- [51] Ma, H., Hyun, J., Nath, N., Chilkoti, A., 2003, Surface engineering strategies for control of protein and cell interactions, European Conference on Cells and Materials, vol. 6, pp 16.
- [52] Pan, Y. V., Hanein, Y., Scampavia, D. L., Böhringer, K. F., Ratner, B. D., Denton, D. D., 2001, Micromachining of Non-fouling Coatings for Bio-MEMS Applications, Sensors and Actuators.
- [53] Aziz, J. N. Y., Genov, R., Bardakjian, B. L., Derchansky, M., Carlen, P. L., 2007, Brain-Silicon Interface for High-Resolution in vitro Neural Recording, IEEE Transactions on Biomedical Circuits and Systems, vol. 1, issue 1, pp 56-62.
- [54] Neihart, N. M., Harrison, R. R., 2005, Micropower Circuits for Bidirectional Wireless Telemetry in Neural Recording Applications, IEEE Transactions on Biomedical Engineering, vol. 52, Issue 11, pp 1950-1959.
- [55] Akay, M., 2007, Handbook Neural Engineering, IEEE Press Series in Biomedical Engineering.
- [56] Schanne, O. F., Lavalley, M., Laprade, R., Gagne, S., 1968, Electrical Properties of Glass Microelectrodes, Proceedings of the IEEE, vol. 56, Issue 6, pp 1072-1082.
- [57] Wise, K. D., Angell, J. B., Starr, A., 1970, An Integrated-Circuit Approach to Extracellular Microelectrodes, IEEE Trans. Biomed. Eng., vol. 17, pp 238-247.
- [58] Skrzypek, J. and Keller, E., 1975, Manufacture of Metal Microelectrodes with the Scanning Electron Microscope, IEEE Transactions of biomedical engineering, vol. 22, pp 435-438.
- [59] Wise, K. D., Anderson, D. J., Hetke, J. F., Kipke, D. R., Najafi, K., 2004, Wireless Implantable Microsystems High-Density Electronic Interfaces To The Nervous System, vol. 92, pp 76-97.
- [60] Robinson, D. A., 1968, The Electrical Properties of Metal Microelectrodes", Proceedings of IEEE, vol. 56, No. 6, pp 1065-1071.
- [61] Najafi, K., 1994, Solid-state Microsensors for Cortical Nerve Recordings, IEEE Engineering in Medicine and Biology, vol. 13, issue 3, pp 375-387.
- [62] Wise, K. D. and Angell, J. B., 1975, A Low-Capacitance Multielectrode Probe for Use in Extracellular Neurophysiology, IEEE Transactions on Biomedical Engineering, vol. 22, Issue 3, pp 212-219.

- [63] Gritsun, T., Vogt, S., Engler, G., Moll, C. K. E., Engel, A. K., Kondra, S., Ramrath, L., Hofmann U. G., 2007, A Simple Microelectrode Bundle for Deep Brain Recordings, Proceedings of the 3rd International IEEE EMBS Conference on Neural Engineering Kohala Coast, Hawaii, USA.
- [64] Suzuki, T., Mabuchi, K., Takeuchi, S., 2003, A 3-D Flexible Parylene Probe Array For Multichannel Neural Recording, Neural Engineering, First International IEEE EMBS Conference on Conference Proceedings, pp 154-156.
- [65] Tanghe, S. J., Wise, K. D., 1992, A 16-channel CMOS neural stimulating array, IEEE Journal of Solid-State Circuits, vol. 27, pp 1819-1825.
- [66] Hambrecht, F. T., 1984, Natural and Artificial Sensors in Neural Prosthesis, Tech. Digest IEEE Solid-State Sensor Cont., pp 5-7.
- [67] Wise, K. D., Angell, J. B., Starr, A., 1970, An Integrated Circuit Approach To Extracellular Microelectrodes, IEEE Transactions on Biomedical Engineering, pp 238-247.
- [68] Nordhausen, C. T., Maynard, E. M., Normann, R. A., 1996, Single Unit Recording Capabilities of a 100 Microelectrode Array, Brain Research, pp 129-140.
- [69] Prohaska, O., Olcaytug, F., Pfundner, P., Dragaun, H., 1986, Thin-Film Multiple Electrode Probes Possibilities and Limitations, IEEE Transactions on Biomedical Engineering, vol. 33, issue 2, pp 223-229.
- [70] Kuperstein, M. and Whittington, D. A., 1981, A Practical 24 Channel Microelectrode for Neural Recording in Vivo, vol. 28, pp 288-293.
- [71] Mojarradi, M., Binkley, D., Blalock, B., Andersen, R., Ulshoefer, N., Johnson, T., Del Castillo, L., 2003, A Miniaturized Neuroprosthesis Suitable For Implantation Into The Brain, IEEE Transactions on neural analysis and rehabilitation engineering, vol. 11, no. 1.
- [72] Lacour, S. P., Tsay, C., Wagner, S., Yu, Z., Morrison, B., 2005, Stretchable Microelectrode Arrays for Dynamic Neural Recording of in Vitro Mechanically Injured Brain, IEEE Sensors, pages 4.
- [73] Olsson III, R. H., Wise, K. D., 2005, A Three-Dimensional Neural Recording Microsystem With Implantable Data Compression Circuitry, vol. 40, pp 2796-2804.
- [74] Kindlmann, G., Normann, R. A., Badi, A., Bigler, J., Keller, C., Coffey, R., Jones, G. M., Johnson, C. R., 2003, Imaging of Utah Electrode Array, Implanted in Cochlear Nerve", NIH

Symposium on Biocomputation & Bioinformation Digital Biology The Emerging Paradigm, Maryland.

- [75] Boppart, S. A., Wheeler, B. C., Wallace, C. S., A Flexible Perforated Microelectrode Array For Extended Neural Recordings, IEEE Transactions on biomedical engineering, vol. 39, pp 37-42.
- [76] Holman, G., Hanein, Y., Wyeth, R.C., Willows, A. O. D., Denton, D. D., Bohringer, K. F., 2002, Silicon Micro-Needles With Flexible Interconnections, 2nd Annual International IEEE-EMB Special Topic Conference on Microtechnologies in Medicine & Biology, pp 255-260.
- [77] Blum, N. A., Carkhuff, B. G., Charles, H. K., Edwards, R. L., Meyer, R. A., 1991, Multisite Microprobes For Neural Recordings, IEEE Transactions on Biomedical Engineering, vol. 38, issue 1.
- [78] Takeuchi, S., Yoshida, Y., Ziegler, D., Mabuchi, K., Suzuki, T., 2004, Parylene Flexible Neural Probe with Micro Fluidic Channel, 17th IEEE International Conference on Micro Electro Mechanical Systems, pp 208-211.
- [79] Salcman, M. and Bak, M. J., 1976, A New Chronic Recording Intra-Cortical Microelectrode, Medical and Biological Engineering and Computing, vol. 14, Number 1.
- [80] Whittington, R. H., Giovangrandi, L., Kovacs, G., 2005, A Closed-Loop Electrical Stimulation System for Cardiac Cell Cultures, IEEE Transactions on Biomedical Engineering, vol. 52, issue 7, pp 1261-1270.
- [81] Merrill, D. R. and Tresco, P. A., 2004, Impedance Characterization Of Microarray Recording Electrodes In Vitro, Proceedings of the 26th Annual International Conference of the IEEE EMBS.
- [82] Kuncel, A. M. and Grill, W. M., 2004, Selection of Stimulus Parameters for Deep Brain Stimulation", Clinical Neurophysiology, vol. 115, pp 2431-2441.
- [83] Suner, S., Fellows, M. R., Irwin, C. V., Nakata, G. K., Donoghue, J. P., 2005, Reliability Of Signals From A Chronically Implanted, Silicon-Based Electrode Array In Nonhuman Primate Motor Cortex, IEEE Transactions on Neural System Rehabilitation Engineering, vol. 13, pp 525-541.
- [84] Super, H. and Roelfsema, P. R., 2005, Chronic Multiunit Recordings In Behaving Animals Advantages And Limitations, Progress In Brain Research, vol. 147, pp 263-82.
- [85] Abruña, H. D., Electrochemical interfaces", VCH Publishers.
- [86] Lower, S. K., Electrochemistry, Simon Fraser University.

- [87] McKenna, 1939, Theoretical Electrochemistry, Macmillan and Co..
- [88] Beebe, X. and Rose, T. L., 1988, Charge Injection Limits Of Activated Iridium Oxide Electrodes With 0.2 Ms Pulses In Bicarbonate Buffered Saline, IEEE Transactions on Biomedical Engineering, vol. 35, pp 494-495.
- [89] Brummer, S. B. and Turner, M. J., 1977, Electrochemical Considerations for Safe Electrical Stimulation of the Nervous System with Platinum Electrodes, IEEE Transactions on Biomedical Engineering, vol. 24, pp 59-63.
- [90] Cogan, S. F., 2008, Neural Stimulation and Recording Electrodes, Annual Review of Biomedical Engineering, Vol. 10, pp 275-309.
- [91] Geddes, L. A., Roeder, R., 2003, Criteria for the Selection of Materials for Implanted Electrodes, Annuals of Biomedical Engineering, pp 879-890.
- [92] Fournier, E., Passirani, C., Montero-Menei, C. N., Benoit, J. P., 2004, Biocompatibility of Implantable Synthetic Polymeric Drug Carriers Focus On Brain Compatibility, Biomaterials, vol. 24, pp 3311-3331.
- [93] Turner, J. N., Shain, W., Szarowski, D. H., Anderson, M., Martins, S., Isaacson, M., Craighead, H., 1999, Cerebral Astrocyte Response To Micromachined Silicon Implants, Experimental Neurology, pp 33-49.
- [94] Szarowski, D. H., Andersen, M. D., Retterer, S., Spence, A. J., Isaacson, M., Craighead, H. G., Turner, J. N., Shain, W., 2003, Brain Responses To Micro-Machined Silicon Devices, Brain Research, vol. 983, issues 1-2, pp 23-35.
- [95] Collias, J. C. and Manuelidis, E. E., 1957, Histopathological Changes Produced By Implanted Electrodes In Cat Brains. Journal of Neurosurgery, vol. 14, pp 302-328.
- [96] Robinson, F. R. and Johnson, M. T., 1961, Histopathological Studies of Tissue Reactions to Various Metals Implanted In Cat Brains, ASD Technical Report, Aeronautical Systems Div Wright-Patterson Afb Ohio Aerospace Medical Div.
- [97] Campbell, P. K., Jones, K. F., Huber, R. J., Horch, K. W., Normann, R. A., 1991, A Silicon-Based, Three-Dimensional Neural Interface, IEEE Transactions on Biomedical Engineering, vol. 38, pp 758-768.
- [98] Satish, L., Gandhi, D., Rousche, P. J., 2004, Preliminary Study Of Neurite Outgrowth Within Polyimide Microtubes, Proceedings of the 26th Annual International Conference of the IEEE EMBS, vol. 2, pp 4306-4309.

- [99] Satish, L., Gandhi, D., Das, R., Rousche, P. J., 2005, Analysis of In-vitro Neurite Extension for Neurotrophic Electrode Design, Proceedings of the 2nd International IEEE EMBS Conference on Neural Engineering, pp 385-387.
- [100] Patrick, E., Ordonez, M., Alba, N., Sanchez, J. C., Nishida, T., 2006, Design and Fabrication of a Flexible Substrate Microelectrode Array for Brain Machine Interfaces, Proceedings of the 28th IEEE EMBS Annual International Conference New York City, USA, pp 2966-2969.
- [101] Rubinstein, J. T., Spelman, F. A., Soma, M., Suesserman, M. F., 1987, Current Density Profiles of Surface Mounted and Recessed Electrodes for Neural Prostheses, IEEE Transactions on Biomedical Engineering, vol. 34, issue 11, pp 864-875.
- [102] Loeb, G. E., Bak, M. J., Salcman, M., Schmidt, E. M., 1977, Parylene as a Chronically Stable, Reproducible Microelectrode Insulator, IEEE Transactions on Biomedical Engineering, vol. 24, issue 2.
- [103] Fassbender, F., Schmitt, G., Schoning, M. J., Luth, H., Buss, G., Schultze, J. W., 2000, Optimization of Passivation Layers For Corrosion Protection Of Silicon-Based Microelectrode Arrays, Sensors and Actuators B Chemical, vol. 68, pp 128-133.
- [104] Agnew, W. F. and McCreery, D. B., 1990, Neural Prostheses, Prentice Hall.
- [105] Stensaas, S. S. and Stensaas, L. J., 1978, Histopathological Evaluation of Materials Implanted In The Cerebral Cortex, Acta Neuropathology, vol. 41, pp 145-155.
- [106] Garca-de-Quirs, F. J., Bonomini, M. P., Ferrndez, J. M., Ferrndez, E., 2003, Validation of a Cortical Electrode Model for Neuroprosthetics Purposes, Lecture Notes in Computer Science, pp 81-88.
- [107] Dodge, H. W., Petersen, C., Sem-Jacobsen, C. W., Sayre, P., Bickford, R. G., 1955, The Paucity Of Demonstrable Brain Damage Following Intracerebral Electrography Report Of A Case, Proceedings of Staff Meeting, Mayo Clinic, vol. 30, pp 215-221.
- [108] Babb, T. L. and Kupfer, W., 1984, Phagocytic And Metabolic Reactions To Chronically Implanted Metal Brain Electrodes, Experimental Neurology, vol. 86, pp 171-184.
- [109] Fischer, G., Sayre, G. P., Bickford, R. G., 1957, Histologic Changes In The Cat's Brain After Introduction Of Metallic And Plastic Coated Wire Used In Electroencephalography, Proceedings of Staff Meeting, Mayo Clinic, vol. 32, pp 14-22.
- [110] Weiland, J. D., Anderson, D. J., 2000, Chronic Neural Stimulation with Thin-Film, Iridium Oxide Electrodes, IEEE Transactions on Biomedical Engineering, vol. 47, pp 911-918.

- [111] Stieglitz, T., Beutel, H., Keller, R., Schuettler, M., Meyer, J., 1999, Flexible, Polyimide-Based Neural Interfaces, Proceedings of the Seventh International Conference on Microelectronics for Neural, Fuzzy and Bio-Inspired Systems, MicroNeuro '99, pp 112-119.
- [112] Dymond, A. M., Kaechele, L. E., Jurist, J. M., Crandall, P. H., 1970, Brain Tissue Reaction to Some Chronically Implanted Metals, *Journal of Neurosurgery*, vol. 33, pp 574-580.
- [113] Schmidt, S., Horch, K., Norman, R., 1993, Biocompatibility Of Silicon-Based Electrode Arrays Implanted In Feline Cortical Tissue, *Journal of Biomedical Materials*, vol. 27, pp 1393-1399.
- [114] Stieglitz, T., Beutel, H., Schuettler, M., Meyer, J. U., 2000, Micromachined, Polyimide-based Devices for Flexible Neural Interfaces, *Biomedical Microdevices*, vol. 2, pp 283-294.
- [115] Stokes, K. B., Bornzin, G. A., Weabusch, W. A., 1983, A Steroideselecting, Low-Threshold, Low Polarizing Electrode, in *Cardiac Pacing*, edited by D. Steinkoff. Verlag Darnstadt, pp 369.
- [116] Stelzle, M., Wagner, R., Jagermann, W., Frohlich, R., 1997, Ultrathin Organic Films For Biocompatible Low Impedance Pacemaker Electrodes, Proceedings of the 18th annual international conference of the IEEE on bridging disciplines for biomedicine, vol. 1, pp 114.
- [117] Dario, P., Carrozza, M. C., Benvenuto, A., Menciassi, A., 2000, Microsystems in Biomedical Applications, *Journal of Micromechanical Micro engineering*, pp 235-244.
- [118] Pan, Y. V., Hanein, Y., Scampavia, D. L., Böhringer, K. F., Ratner, B. D., Denton, D. D., 2001, A Precision Technology For Controlling Protein Adsorption And Cell Adhesion In bioMEMS, The 14th IEEE International Conference on Micro Electro Mechanical Systems, pp 435-438.
- [119] Rubinstein, J. T., Miller, C. A., Mino, H., Abbas, P. J., 2001, Analysis of Monophasic and Biphasic Electrical Stimulation of Nerve, vol. 48, pp 1065-1070.
- [120] E. D. L., 1998, Self-Assembly And Steric Stabilization At Heterogeneous Biological Surfaces Using Adsorbing Block Copolymers, *Chemistry and Biology*, pp 177-183.
- [121] Harris, J. M., 1992, *Poly-Ethylene Glycol Chemistry, Bio-Technical and Bio-Medical Applications*, Plenum.
- [122] Sharma, S., Johnson, R. W., Desai, T. A., 2002, Poly (Ethylene Glycol) Interfaces for the Control Of Biofouling In Silicon-Based Microsystems, 2nd Annual International IEEE-EMB Special Topic Conference on Microtechnologies in Medicine & Biology, pp 41-45.
- [123] Lopez, G. P., Ratner, B. D., Tidwell, C. D., Haycox, C. L., Rapoza, R. J., Horbett, T. A., 1992, Glow Discharge Plasma Deposition of Tetraethylene Glycol Dimethyl Ether for Fouling-Resistant Biomaterial Surfaces, *Journal of Biomedical Materials*.

- [124] Mar, M. N., Ratner, B. D., Yee, S. S., 1999, An Intrinsically Protein-Resistant Surface Plasmon Resonance Biosensor Based Upon a RF-Plasma-Deposited Thin Film, *Sensors Actuators*.
- [125] Lu, H. B., Homola, J., Pan, Y. V., Ramer, B. D., Campbell, C. T., Yee, S. S., 2000, Surface Functionalization for Self-referencing Surface Plasmon Resonance Biosensors by RF-plasma-deposited Thin Films and Self-assembled Monolayers, *Society for Biomaterials Transactions of the 6th World Biomaterials Congress*, pp 151.
- [126] Böhringer, K. F., 2003, Surface Modification and Modulation in Microstructures Controlling Protein Adsorption, Monolayer Desorption, and Micro-Self-Assembly, *Journal of Micromechanical Microengineering*.
- [127] Bonham, B. H. and Litvak, L. M., 2008, Current focusing and steering Modeling, physiology, and psychophysics, *Hearing Research*, vol. 242, pp 141-53.
- [128] Butson, C. R. and McIntyre, C. C., 2008, Current Steering To Control The Volume Of Tissue Activated During Deep Brain Stimulation, *Journal Of Brain Stimulation*, vol. 1, pp 7-15.
- [129] McIntyre, C. C., Mori, S., Sherman, D. L., Thakor, N. V., Vitek, J. L., 2004, Electric Field And Stimulating Influence Generated By Deep Brain Stimulation Of The Subthalamic Nucleus, *Clinical Neurophysiology*, vol. 115, pp 589-95.
- [130] Muthuswamy, J., Gilletti, A., Jainl, T., Okandan, M., 2003, Microactuated Neural Probes To Compensate For Brain Micromotion, *Proceedings of the 25th Annual International Conference of the IEEE Engineering in Medicine and Biology Society*, vol. 2, pp 1941-1943.
- [131] Oweiss, K. G., Anderson, D. J., Papaefthymiou, M. M., 2003, Optimizing Signal Coding In Neural Interface System-On-A-Chip Modules, *Proceedings of the 25th Annual International Conference of the IEEE Engineering in Medicine and Biology Society*, vol. 3, pp 2216-2219.
- [132] Wise, K. D., 2006, Wireless Integrated Microsystems - Coming Breakthroughs in Health Care, *International Electron Devices Meeting*, pp 1-8.
- [133] Irazoqui, P. P., Mody, I., Judy, J. W., 2005, Recording brain activity wirelessly, *IEEE Engineering in Medicine and Biology Magazine*, vol. 24, Issue 6, pp 48-54.
- [134] Guillory, K. S. and Normann, R. A., 1999, A 100-Channel System For Real Time Detection And Storage Of Extracellular Spike Waveforms, *Journal of Neuroscience Methods*.
- [135] Wagenaar, D. A. and Potter, S. M., 2002, Real-Time Multi-Channel Stimulus Artifact Suppression by Local Curve Fitting, *Journal of Neuroscience Methods*, vol. 120, pp 113-120.

- [136] Gnadt, J. W., Echols, S. D., Yildirim, A., Zhang, H., Paul, K., 2003, Spectral Cancellation of Microstimulation Artifact for Simultaneous Neural Recording In Situ, *IEEE Transactions on Biomedical Engineering*, vol. 50, Issue 10, pp1129-1135.
- [137] Hashimoto, T., Elder, C. M., Vitek, J. L., 2002, A Template Subtraction Method For Stimulus Artifact Removal In High-Frequency Deep Brain Stimulation, *Journal of Neuroscience Methods*, vol. 113, pp 181-186.
- [138] Jimbo, Y. and Kawana, A., 1992, Electrical Stimulation And Recording From Cultured Neurons Using A Planar Electrode Array, *Bioelectrochemistry and Bioenergetics*, vol. 29, pp 193-204.
- [139] Grumet, A. E., 1999, Electrical Stimulation Parameters for an Epi-Retinal Prosthesis, PhD thesis, Massachusetts Institute of Technology.
- [140] Thorn, B. E., Applegate, L., Jones, K., 1994, The relative efficacy of monopolar vs. bipolar electrodes in stimulation-produced analgesia, *Experimental Brain Research*, Springer Berlin / Heidelberg, vol. 79, Number 2, pp 266-270.
- [141] Temel, Y., Visser-Vandewalle, V., Wolf, M. V. D., Spincemaille, G. H., Desbonnet, L., Hoogland, G., Steinbusch, H. W. M., 2004, Monopolar Versus Bipolar High Frequency Stimulation In The Rat Subthalamic Nucleus - Differences In Histological Damage, *Neuroscience Letters*, vol. 367, no. 1, pp 92-96.
- [142] Robblee, L. S. and Rose, T. L., 1990, Electrochemical Guidelines for Selection Of Protocols And Electrode Materials For Neural Stimulation, in *Neural Prostheses—Fundamental Studies*, Prentice-Hall.
- [143] Shannon, R. V., 1992, A Model of Safe Levels for Electrical Stimulation, *IEEE Transactions on Biomedical Engineering*, vol. 39, pp. 424-426.
- [144] Twardoch, U. M., 1994, Integrity of Ultramicro-Stimulation Electrodes Determined From Electrochemical Measurements, *Journal of Applied Electrochemistry*, vol. 24, pp 835-857.
- [145] McIntyre, C. C. and Grill, W. M., 2002, Extracellular Stimulation of Central Neurons Influence of Stimulus Waveform and Frequency on Neural Output, *The Journal of Neurophysiology*, vol. 88, no. 4, pp 1592-1604.
- [146] Gabran, S. R. I., 2008, Subdermal Dry EEG Spike-Array Electrodes Design and Optimization Methodology, VDM publishing, Germany.

- [147] Butson, C. R. and McIntyre, C. C., 2006, Role of Electrode Design On The Volume of Tissue Activated During Deep Brain Stimulation, *Journal of Neural Engineering*, vol. 3, pp 1-8.
- [148] Geddes, L. A. and Baker, L. E., 1967, The specific resistance of biological material - A compendium of data for the biomedical engineer and physiologist, *Journal of Medical and Biological Engineering and Computing*, vol. 5, No. 3, pp 271-293.
- [149] Stinstra, J. G., Peters, M. J., 1998, The volume conductor may act as a temporal filter on the ECG and EEG, *Medical and Biological Engineering and Computing*, Springer Berlin / Heidelberg, vol. 36, Number 6, pp 711-716.
- [150] Schwan, H. P., 1981, Dielectric Properties of Biological Tissue and Physical Mechanisms of Electromagnetic Field Interaction, *Biological Effects of Nonionizing Radiation*, ACS Symposium Series 157, Karl H. Illinger, the American Chemical Society.
- [151] Schmid, G., Neubauer, G., Mazal, P. R., 2003, Dielectric Properties Of The Human Brain Measured Less Than 10 Hours Post Mortem, *Journal of Bioelectromagnetics*, vol. 24, Issue 6, pp 423-430.
- [152] Gabriel, C., Gabriel, S., Corthout, E., 1996, The dielectric properties of biological tissues I. Literature survey, *Physics in medicine and biology*, vol. 41, pp 2231-2249.
- [153] Gabriel, S., Lau, R. W., Gabriel, C., 1996, The dielectric properties of biological tissues III. Parametric models for the dielectric spectrum of tissues, vol. 41, No. 11, pp 2271-d2293.
- [154] Barnes, F. S. and Greenebaum, B., 2007, *Bioengineering and Biophysical Aspect of Electromagnetic Fields*, Taylor and Francis.
- [155] Butson, C. R., Maks, C. B., McIntyre, C. C., 2006, Sources and effects of electrode impedance during deep brain stimulation, *Journal of Clinical Neurophysiology*, vol. 117, Issue 2, pp 447-454.
- [156] Sotiropoulos, S. N. and Steinmetz, P. N., 2007, Assessing The Direct Effects Of Deep Brain Stimulation Using Embedded Axon Models, *Journal Of Neural Engineering*, pp 107-119.
- [157] Salvador, R., Miranda, P. C., Roth, Y., Zangen, A., 2007, High-Permeability Core Coils for Transcranial Magnetic Stimulation of Deep Brain Regions, *IEEE EMBS 2007 Conference Proceedings*, pp 6653-6656.
- [158] Goncalve, S., De Munck, J. C., Verbunt, J. P. A., Heethaar, R. M., Da Silva, F. H. L., 2003, In vivo measurement of the brain and skull resistivities using an EIT-based method and realistic models for the head, *IEEE Transactions in Biomedical Engineering*, vol. 50, pp 754-767.

- [159] Nicholson, P. W., 1965, Specific impedance of cerebral white matter, *Experimental Neurology*, vol. 13, pp 386-401.
- [160] Apollonio, F., Paffi, A., Parazzini, M., Maggio, F., Novellino, T., Ravazzani, P., D'Inzeo, G., 2007, Fundamental Electrical Quantities in Deep Brain Stimulation Influence of Domain Dimensions and Boundary Conditions, *IEEE EMBS 2007 Conference Proceedings*, pp 6669-72.
- [161] McIntyre, C. C., Mori, S., Sherman, D. L., Thakor, N. V., Vitek, J. L., 2004, Electric field and stimulating influence generated by deep brain stimulation of the subthalamic nucleus, *Clinical Neurophysiology*, vol. 115, Issue 3, pp 589-595.
- [162] Moro, E., Esselink, R. J. A., Xie, J., Hommel, M., Benabid, A. L., Pollak, P., 2002, The Impact on Parkinson's Disease of Electrical Parameter Settings in STN Stimulation, *Neurology*, vol. 59, pp 706-13.
- [163] Rousche, P. J. and Normann, R. A., 1990, A System For Impact Insertion Of A 100 Electrode Array Into Cortical Tissue, *Proceedings of the Twelfth Annual International Conference of the IEEE Engineering in Medicine and Biology Society*, vol. 1, pp 494-495.
- [164] Kim, H., 2004, Fabrication and analysis of plastic hypodermic needles by micro injection moulding, *Masters Thesis*, Georgia Institute of technology.
- [165] Chandrasekaran, S. and Fraizer, B., 2003, Characterization of surface micromachined metallic microneedles, *Journal of Microelectromechanical Systems*, vol. 12, pp 289-295.
- [166] Henry, S., McAllister, D. V., Allen, M. G., Prausnitz, M. R., 1998, Micromachined needles for the transdermal delivery of drugs, *The 11th Annual International Workshop on Micro Electro Mechanical Systems*, pp 494-498.
- [167] Hendriks, F. M., *Mechanical Properties of Different Layers of Human Skin*, Dept. of Materials Technology, Eindhoven Univ. of Technology, <http://www.bmt.tue.nl/pdf/postersonderzoekdag2001/fhendriks.pdf>
- [168] Oomens, C. W. J., 2001, Deformation Analysis of a Supported Buttock Contact, *Bioengineering Conference ASME*, Vol. 50.
- [169] Hendriks, F. M., Brokken, D., Van Eemeren, J. T. W. M., Oomens, C. W. J., Baaijens, F. P. T., Horsten, J. B. A. M., 2003, A numerical experimental method to characterize the non-linear mechanical behaviour of human skin, *Skin Research and Technology*.
- [170] Gere, J. M., Timoshenko, S. P., 1999, *Mechanics of Materials*, Stanley Thornes Ltd.

- [171] Kim, H. and Colton, J. S., 2005, Fabrication and analysis of plastic hypodermic needles, *Journal of Medical Engineering & Technology*, Taylor & Francis, vol. 29.
- [172] Perez-Duarte, A., Van der Veen, S., Rhenalu, P., France, I., Muzzolini, R., Ehrstrom, J., 2002, On Material Models for Static Sizing of Compression Driven Airframe Structure, 43rd AIAA/ASME/ASCE/AHS/ASC Structures, Structural Dynamics, and Materials Conference.
- [173] Hibbler, R. C., 1991, *Mechanics of Materials*, Macmillan.
- [174] Oogarah, T. B., 2008, Low Temperature RF MEMS Inductors Using Porous Anodic Alumina, M.A.Sc. Thesis, University of Waterloo.
- [175] Chut, W., Mehregany, M., Mullen, R., 1993, Analysis of tip deflection and force of a bimetallic cantilever microactuator, *Journal of Micromechanical Microengineering*, vol. 3, pp 4-7.
- [176] Dahimann, G. W., Yeatman, E. M., 2000, Fabrication, RF characteristics and mechanical stability of self-assembled 3D microwave inductors, 8th IEEE International Symposium on High Performance Electron Devices for Microwave and Optoelectronic Applications, pp 128-133.
- [177] McCreery, D., Lossinsky, A., Pikov, V., Liu, X., 2006, Microelectrode Array for Chronic Deep-Brain Microstimulation and Recording, *IEEE Transactions in Biomedical Engineering*, vol. 4, pp 726-736.
- [178] Rousseau, L., Lissorgues, G., Verjus, F., Yvert, B., 2009, Microfabrication of high-density microelectrode arrays for in vitro applications, 13th International Conference on Biomedical Engineering, vol. 23, pp 790-793.
- [179] Du, J., Riedel-Kruse, I. H., Nawroth, J. C., Roukes, M. L., Laurent, G., Masmanidis, S. C., 2009, High-Resolution Three-Dimensional Extracellular Recording of Neural Activity with Microfabricated Electrode Arrays, *Journal of Neurophysiology* vol. 101, pp 1671-1678.
- [180] Du, J., Roukes, M. L., Masmanidis, S. C., 2009, Dual-side and three-dimensional microelectrode arrays fabricated from ultra-thin silicon substrates, *Journal of Micromechanics and Microengineering*, vol. 19.
- [181] Motta, P. S., 2005, Multielectrode Microprobes for deep-brain stimulation fabricated using a novel 3-d shaping electroplating process, *IEEE Transactions on Biomedical Engineering*, issue 5, pp 923-933.
- [182] EMPIRE XCcel Manual, IMST GmbH, Germany, November 12, 2008 <http://www.empire.de/>

- [183] Gabriel, S., Lau, R. W., Gabriel, C., 1996, The dielectric properties of biological tissues II. Measurements in the frequency range 10Hz to 20 GHz, *Physics in medicine and biology*, vol. 41, pp 2251-2269.
- [184] Italian national research council, Institute for Applied Physics <http://niremf.ifac.cnr.it/tissprop>
- [185] Gabran, S. R. I., Saad, J. H., Salama, M. M. A., Mansour, R. R., 2009, Finite Difference Time Domain (FDTD) Modeling of Implanted Deep Brain Stimulation Electrodes and Brain Tissue, 31st IEEE Engineering in Medicine and Biology Society, Minnesota, USA, pp 6485-6488.
- [186] Gabran, S. R. I., Saad, J. F. H., Salama, M. M. A., Mansour, R. R., 2011, Electromagnetic Modeling and Design Optimization of Intra-Cortical Microelectrodes, The 5th International IEEE EMBS Conference on Neural Engineering.
- [187] Saad, J. F. H., Gabran, S. R. I., Salama, M. M. A., Mansour, R. R., 2011, Quantitative Modeling of Electric Field in Deep Brain Stimulation Study of Medium Brain Tissue and Stimulation Pulse Parameters, The 5th International IEEE EMBS Conference on Neural Engineering.
- [188] Miocinovic, S., Lempka, S. F., Russo, G. S., Maks, C. B., Butson, C. R., Sakaie, K. E., Vitek, J. L., McIntyre, C. C., 2009, Experimental and theoretical characterization of the voltage distribution generated by deep brain stimulation, *Journal of Experimental Neurology*, vol. 216, pp 166-176.
- [189] Paralikar, K. J., Lawrence, J. K., Clement, R. S., 2006, Collagenase-aided insertion of intracortical microelectrode arrays evaluation of insertion force and chronic recording performance, *Conference Proceedings of the International Conference of IEEE Engineering in Medicine and Biology Society*.
- [190] Paralikar, K. J., Clement, R. S., 2006, Collagenase-Aided Intracortical Microelectrode Array Insertion Effects on Insertion Force and Recording Performance, 2008, *IEEE Transactions on Biomedical Engineering*, vol 55, issue 9, pp 2258-2267.
- [191] Najafi, K., Hetke, J. F., 1990, Strength characterization of silicon microprobes in neurophysiological tissues, *IEEE Transactions on Biomedical Engineering*, vol 37, issue 5, pp 474-481.
- [192] Petersen, K. E., Silicon as a mechanical material, 1982, *Proceedings of the IEEE.*, vol. 70, no. 5.
- [193] Sooriakumar, Chan, Savage and Fugate, A comparative study of wet vs. dry isotropic etch to strengthen silicon micro-machined pressure sensor, *Electrochemical Soc. Proc.*, vol. 95-27.

- [194] Yi, T., Li, L., Kim, C. J., 2000, Microscale material testing of single crystalline silicon, *Sensors And Actuators*, vol 83, issue 1-3, pp 172-178.
- [195] Tsuchiya, T., Tabata, O., Sakata, J., Taga, Y., 1997, Specimen size effect on tensile strength of surface-micromachined polycrystalline silicon thin films, *IEEE Proceedings on Tenth Annual International Workshop on Micro Electro Mechanical Systems MEMS '97*, pp 529-534.
- [196] Ansys theory manual
- [197] Lapeer, R. J., Gasson, P. D., Karri, V., 2011, A Hyperelastic Finite-Element Model of Human Skin for Interactive Real-Time Surgical Simulation, *IEEE Transactions on Biomedical Engineering*, vol 58, issue 4, pp 1013-1022.
- [198] Zhijiang, M. W., Du, Z., 2007, A Physically Based Model to Simulate Orthopedic Surgery from 3D CT Image, *International Conference on Complex Medical Engineering*, pp 507-512.
- [199] Samur, E., Sedef, M., Basdogan, C., Avtan, L., Duzgun, O., 2007, A robotic indenter for minimally invasive measurement and characterization of soft tissue response, *Medical Image Analysis*, vol 11, issue 4, pp 361-73.
- [200] MacLean, S., 2010, Brain tissue analysis of mechanical properties, Department of Mechanical Engineering at The Ohio State University.
- [201] Rennaker, R. L., Street, S., Ruyle, A. M., Sloan, A. M., 2005, A comparison of chronic multi-channel cortical implantation techniques manual versus mechanical insertion, *Journal of Neuroscience Methods*, vol 142, issue 2, pp 169-176.
- [202] Miller, K., Chinzei, K., 2001, Mechanical properties of brain tissue in tension, *Journal of Biomechanics*, vol 35, issue 4, pp 483-490.
- [203] Kauer, M., Vuskovic, V., Dual, J., Szekely, G., Bajka, M., 2002, Inverse Finite Element Characterization of Soft Tissues, *Medical Image Analysis*, vol 6, issue 3, pp 275-287.
- [204] Miller, K., 1998, Constitutive model of brain tissue suitable for finite element analysis of surgical procedures, *Journal of Biomechanics*, vol 32, issue 5, pp 531-537.
- [205] Lee, K. K., He, J., Singh, A., Massia, S., Ehteshami, G., Kim, B., Raupp, G., 2004, Polyimide-based intracortical neural implant with improved structural stiffness, *J. Micromech. Microeng.*, vol. 14, pp. 32-37.
- [206] Stice, P., Gilletti, A., Panitch, A., Muthuswamy, J., 2007, Thin microelectrodes reduce GFAP expression in the implant site in rodent somatosensory cortex, *J. Neural Eng.*, vol. 4, pp. 42-53.

- [207] Gabran, S. R. I., Mansour, R. R., Salama, M. M. A., 2012, Maskless pattern transfer using 355 nm laser, *Journal of Optics and Lasers in Engineering*, vol. 50, pp. 710-716.
- [208] A. Bagheri, S. R. I. Gabran, M. T. Salam, J. L. Perez Velazquez, R. R. Mansour, M. M. A. Salama, and R. Genov, A Nanostructured Microelectrode for Simultaneous Wireless Neural Signal Recording and Electrical Stimulation System, *Biomedical Circuits and Systems Conference*, 2012, Taiwan, accepted.
- [209] A. Hassibi, R. Navid, R. W. Dutton, and T. H. Lee, "Comprehensive study of noise processes in electrode electrolyte interfaces," *Journal of Applied Physics*, vol. 96, N. 2, 2004.